Synthèse en milieux supercritiques de nanoparticules à base de BaTiO3 : étude des mécanismes de formation, mise en forme des poudres et ferroélectricité

Gilles Philippot

THÈSE EN COTUTELLE PRÉSENTÉE

POUR OBTENIR LE GRADE DE

DOCTEUR DE

L'UNIVERSITÉ DE BORDEAUX

ET DE TU DARMSTADT

ÉCOLE DOCTORALE DES SCIENCES CHIMIQUES

ÉCOLE DOCTORALE DE GENIE ELECTRIQUE ET INFORMATIQUE

SPÉCIALITÉ Physico-chimie de la matière condensée

Par Gilles PHILIPPOT

Supercritical fluid synthesis of $BaTiO_3$ based nanoparticles

Study of the particles growth mechanisms, powder processing and ferroelectric properties

Sous la direction de Cyril AYMONIER, Catherine ELISSALDE
et Rolf JAKOBY

Soutenue le 16 Octobre 2014

Membres du jury :

M. MAGLIONE Mario	Directeur de recherche CNRS, ICMCB, France	Président
M. ALGUERO Miguel	Directeur de recherche CSIC, ICMM, Espagne	Rapporteur
M. WALTON Richard	Professeur, Warwick University, Royaume-Uni	Rapporteur
M. AYMONIER Cyril	Chargé de recherche CNRS, ICMCB, France	Examinateur
Mme. ELISSALDE Catherine	Directeur de recherche CNRS, ICMCB, France	Examinateur
M. IBANEZ Alain	Directeur de recherche CNRS, Institut Néel, France	Examinateur
M. JAKOBY Rolf	Professeur, TU Darmstadt, Allemagne	Examinateur
M. ROUGE Fabien	Directeur général, Polyrise, France	Examinateur
M. ETOURNEAU Jean	Professeur émérite, Université de Bordeaux, ICMCB, France	Invité

Acknowledgements

This PhD research work was carried out in the framework of the International Doctoral School in Functional Materials (IDS FunMAT) through a collaboration between, the Supercritical Fluids group at the Institut de la Chimie et de la Matière Condensée de Bordeaux (ICMCB – CNRS – France), the Institut für Mikrowellentechnik und Photonik at Technische Universität Darmstadt (Germany) and an industrial partner, Polyrise (Bordeaux – France). First, I would like to thank all the people who have been involved in this project.

I would like to thank Claude Delmas who was the director of the ICMCB when I started my project and Mario Maglione who took over the ICMCB direction for welcoming me over the last three years. Similarly, I would also like to thank Rolf Jakoby (TU Darmstadt) and Fabien Rougé (Polyrise) for keeping the doors of their laboratories opened to me, for they kindness and availability. Moreover, I would like to thank Jean Etourneau, Laurent Servant and Marianne Delmas for welcoming me into the IDS FunMAT program.

I would like to thank Richard Walton (Warwick University) and Miguel Alguero (Instituto de Ciencia de Materiales de Madrid) for the assessment of my PhD thesis manuscript and join Alain Ibanez (Institut Néel) to this acknowledgement for joining the assessment committee of my PhD defense.

I have a special though towards my advisors, Cathy Elissalde and Cyril Aymonier (ICMCB) and Rolf Jakoby (TU Darmstadt), who have been following me over these last three years, thank you very much for everything! Of course from a scientific point of view but not only, this step made me grow up and I am happy to say that, after this first collaboration, you became more than colleagues to me and I would be more than happy to keep in touch with both of you and why not to collaborate in the coming years!

Many thanks to those who have been involved across the different steps of this project. At ICMCB, I have special thanks to Marjorie Albino who was of great help for the ceramic processing and characterizations (and thank you for coming from Le Mans for my defense!), Christine Labrugère for the XPS measurements, Yannick Petit for the SHG analyses, Sonia Buffière for the electronic microscopy images, Eric Lebraud for the XRD measurements, Michael Joss for his contribution concerning the behaviors of the nanostructured ceramics, Dominique Denux for the thermal analyses and Jean Macaigne who was my MSc student during the six last months of my PhD and help me with the experiments.

This project being pluridisciplinary, thus many people from outside ICMCB were involved. I would like to thank Bo Iversen, Kirsten Jensen and Espen Bojensen from Aarhus University (Denmark) for the *in situ* WAXS studies. I would like to thank Claude Estournes, Geoffroy Chevalier, Romain Epherre, Alicia Weible and Alain Peigney from the CIRIMAT at Toulouse for their help in the processing step of the BST nanopowders into dense and nanostructured ceramics. I would also like to thank, Isabelle Bord Majek and Massar Wade from the Laboratoire de l'Intégration du Matériau au Système (IMS - Bordeaux), Yuliang Zeng and Donghang Lu from TU Darmstadt, Mélanie Louarn and Matthieu Buet from Polyrise for their help developing and characterizing hybrid materials.

Again, many thanks to everybody at ICMCB where I spent most of my PhD with a great atmosphere. I want to warmly thank everyone from the supercritical fluids group, past and present, for their welcoming, their help and kindness. I have a special thank for Manuel Théodet who was the first to train me and made me earn a lot of time! He is not a colleague anymore but a friend! This can also be directed for the other people who passed through the group, among them: Thomas, Amaury, Blanca, Bruno, Ricardo, Cédric, José, Oana, Lucile, Sam, Cyril. Q, Stéphane.

When I arrived here in Bordeaux, I did not know anybody, and after three years I am leaving with many friends. A special though to the Barbecue team, Mailys, Lucie, Baptiste, Mathieu, Quentin and Mathias with whom I have great memories and I am sure that even if I am leaving to the great north we will keep in touch! Hopefully they will not be the only ones, I am thinking, in particular, to Stéphanie, Isabelle, Lucile C, Madhu, Cyril C, David, Laurent, Johan, Alex, Carole, Oliv', Quentin S, and everyone else I may forget!

Finally, I would like to thank my parents, my sister, Aurélien, all my other friends for supporting me over these three years where I might have been, from time to time, a "little bit" annoying! My thoughts are also directed to Sophie who has joined me during this adventure and was able to support me even though I was not always the most smiling guy!

Many thanks, again, to everyone who have been around me during those three years!

Content

Elaboration en milieux fluides supercritiques de nanoparticules du type $BaTiO_3$

Etude des mécanismes de formation des nanoparticules, mise en forme de céramiques nanostructurées denses et caractérisation de leurs propriétés diélectriques

L'électronique faisant partie intégrante de notre société, ce domaine concentre beaucoup d'efforts en recherche et développement afin de continuellement améliorer les technologies dont nous disposons. Si nous prenons comme exemple le cas des téléphones portables, en quelques années, les améliorations en termes de taille, performances et fonctionnalités ont été remarquables pour finalement arriver aux « smartphones » que l'on utilise quotidiennement. Actuellement, afin de continuer à améliorer ce type d'appareils, une des stratégies est de se concentrer sur la diminution en taille des composants électroniques des circuits imprimés, et plus particulièrement, des composants passifs, tels que les condensateurs, et cela tout en préservant, voire en améliorant, leurs performances. En effet, les composants passifs représentent jusqu'à 80% de la totalité des composants et occupent 40% de l'espace. De ce fait, une sensible diminution en taille peut rapidement avoir un effet significatif, libérant ainsi de l'espace pour augmenter les fonctionnalités ou diminuer la taille des appareils considérés. Dans le cadre de cette thèse, nous nous sommes focalisés sur le cas particulier des condensateurs. Ce type de composant, dont la fonction est de réguler le flux électrique dans un circuit imprimé, présente une structure relativement simple et ainsi plus facile à miniaturiser. Ils sont constitués d'un matériau dit diélectrique, qui est positionné entre deux électrodes conductrices. La capacité [$C = (\mathcal{E}.S)/e$ en Farad (F)] dépend de $\mathcal{E}$ la permittivité diélectrique du matériau (en F/m), de S la surface des électrodes (en m^2) et de e l'épaisseur du diélectrique (en m) ; on peut en déduire que les performances du composant vont aussi bien dépendre des propriétés intrinsèques du matériau diélectrique utilisé ($\mathcal{E}$) que de sa géométrie. Il doit être le plus fin possible (e) tout en présentant une surface la plus étendue possible (S). Une option est donc de développer des condensateurs multicouches (Figure 1) où l'on alterne les couches conductrices qui serviront d'électrodes et les couches de matériau diélectrique. Dans le cadre de cette

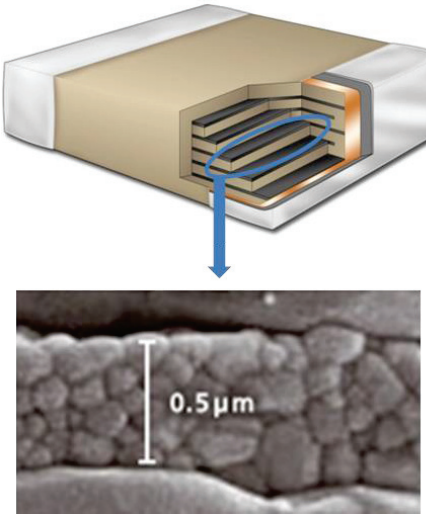

Figure 1: Illustration d'un condensateur multicouche

étude, le choix du diélectrique s'est porté sur les matériaux du type $BaTiO_3$ et de ses solutions solides $Ba_{1-x}Sr_xTiO_3$ ($0 \leq x \leq 1$ - BST) et $BaTi_{1-y}Zr_yO_3$ ($0 \leq y \leq 1$ – BTZ). Ces derniers présentent une structure Perovskite : le baryum est en site A, à savoir sur les sommets de la maille, le titane en site B, dans un octaèdre d'atomes d'oxygène qui se trouvent au centre des faces (Figure 2).

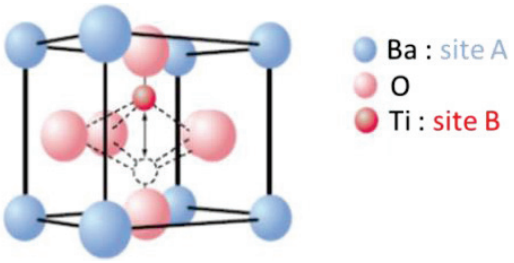

Figure 2: Illustration de la structure Perovskite

A température ambiante la structure est quadratique (non centrosymétrique) et présente ainsi une polarisation spontanée qui peut être orientée via l'application d'un champ électrique externe. Néanmoins, en chauffant le matériau au-delà de 120°C, la structure devient cubique (centrosymétrique) et perd cette polarisation spontanée ; cette température associée à cette transition de phase est appelée la température de Curie (T_{Curie}).

En utilisant du $BaTiO_3$, il est possible de nos jours d'atteindre des épaisseurs de couche diélectrique de l'ordre de 500 nm dans le cas des MLCCs (Figure 1). Néanmoins, pour continuer à diminuer cette épaisseur, il est nécessaire de développer des voies de synthèse permettant de produire des nanoparticules d'une dizaine de nanomètres entièrement cristallisées, tout en maintenant un coup de production raisonnable. De ce fait, le procédé de synthèse en voie supercritique peut être considéré comme une alternative intéressante. En effet, en plus de répondre aux attentes en terme de qualité des nanomatériaux, ce procédé peut fonctionner en continu offrant ainsi la possibilité d'un transfert à l'échelle industrielle. Néanmoins, il a été démontré dans la littérature que pour des tailles de particules inférieures à 150 nm, les propriétés féroelectriques intrinsèques de ce type de matériaux changent avec notamment un diminution de la T_{Curie}. Les objectifs de ce projet de thèse étaient donc, dans un premier temps, (i) de comprendre la formation de nanocristaux de $BaTiO_3$ et de ses solutions solides (BST et BTZ) en conditions supercritiques, puis, (ii) d'étudier leur mise en forme en céramiques nanostructurées denses afin d'avoir accès aux effets de taille sur les propriétés ferroelectriques.

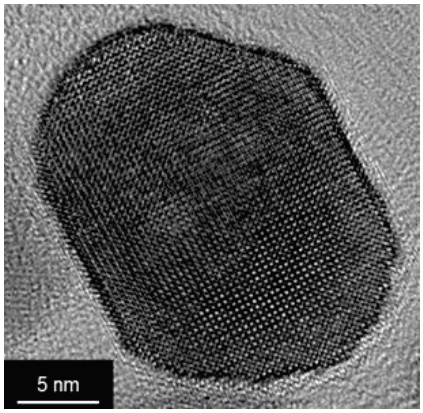

Figure 3: Nanocristal de $BaTiO_3$

Pour ce faire, nous nous sommes donc concentrés dans un premier temps sur l'étude de la formation de nanoparticules de $BaTiO_3$. L'utilisation de techniques d'analyse *ex situ* telles que la diffraction des rayons X et la microscopie électronique en transmission nous a

permis de démontrer la production en continu de nanocristaux purs de 20 ± 6 nm (Figure 3), validant ainsi la mise au point de la synthèse en continu en milieux supercritiques. Une fois cette étape maîtrisée, nous avons pu nous intéresser à l'étude des mécanismes de formation de ce type de matériau en milieux supercritiques.

Pour cela, nous avons utilisé d'autres techniques d'analyse *ex situ* telles que les spectroscopies infrarouge, Raman et de photoélectrons X afin d'avoir des informations complémentaires aussi bien sur la structure et les défauts des nanocristaux mais aussi sur leur chimie de surface. A ces résultats, nous avons associé des analyses *in situ* synchrotron de diffraction des rayons X aux grands angles, permettant de suivre en temps réel la formation des particules en conditions supercritiques. Ceci permet d'observer directement les effets des conditions expérimentales, telles que la température ou la concentration des précurseurs, sur la taille et la structure des particules. La combinaison de ces deux types d'analyses (*in situ* et *ex situ*) permet donc de cibler les conditions expérimentales optimales à utiliser pour produire des nanoparticules avec des morphologies répondant aux spécifications. Une fois cette étude complétée, nous l'avons étendue, aux solutions solides BST et BTZ. Un des résultats forts de cette étude est la synthèse, pour la première fois, de la totalité de la solution solide de BTZ en milieux fluides supercritiques (Figure 4). De plus, à notre connaissance, seulement un autre groupe de recherche a également reporté la synthèse de la totalité de la solution solide de BTZ en utilisant un procédé sol-gel modifié et basé sur la diffusion de vapeurs.

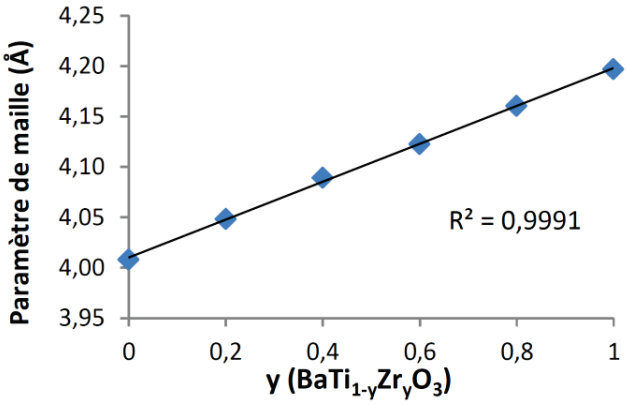

Figure 4 : Variation linéaire du paramètre de maille pour la phase BTZ en fonction de la composition

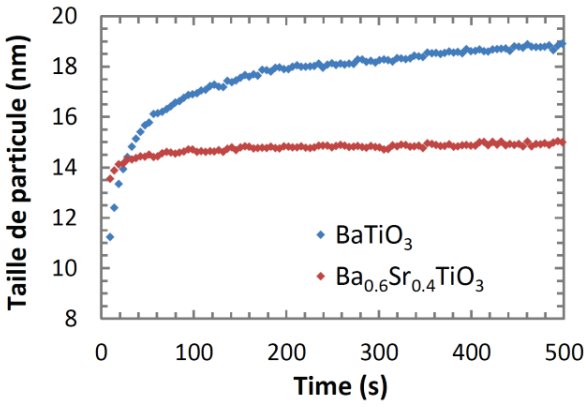

Figure 5 Etude *in situ* de l'influence de la substitution du baryum avec du strontium sur la croissance des particules.

Après être parvenu à synthétiser l'ensemble des solutions solides BST et BTZ, nous nous sommes intéressés à l'étude des mécanismes de formation. Si nous prenons l'exemple du BST (Figure 5), nous avons constaté qu'à condition expérimentale

identique, la taille des particules synthétisées varie avec la stoechimétrie. En effet, les particules de $BaTiO_3$ sont plus grosses que celles de $Ba_{0.6}Sr_{0.4}TiO_3$. De plus, nous nous sommes également aperçus que l'état de surface, en particulier la quantité de défauts –OH, change aussi ; leur quantité tend à diminuer en augmentant la quantité de baryum substitué par du strontium. De cela, nous avons alors pu proposer un mécanisme de formation de ces nanoparticules basé sur la densité des groupes hydroxyles en surface. Le mécanisme pouvant être associé à une réaction du type sol – gel, plus il y aura de défaut –OH à la surface des particules, plus le précurseur va pouvoir se condenser à la surface pour faire croître les particules. C'est pourquoi la taille des particules de $BaTiO_3$, pour des conditions expérimentales identiques, sera plus grande que pour les particules de $Ba_{0.6}Sr_{0.4}TiO_3$.

Au niveau des applications, il est important de savoir que pour ce type de matériau, la taille des nanoparticules impacte directement les propriétés diélectriques (notamment le T_{Curie}). De ce fait, nous nous sommes intéressés à la mise en forme de ces poudres afin d'étudier, notamment, les effets de taille. Le premier challenge était de parvenir à préparer des céramiques denses et nanostructurées tout en préservant la taille initiale des nanoparticules. Ceci a été possible via l'utilisation du Spark Plasma Sintering (SPS) qui est une technique de frittage associant des cinétiques de chauffe très rapides (jusqu'à 1000 °C/min) à des pressions élevées (jusqu'à 1 GPa) ; cette technique permet des frittages très rapides (de l'ordre de la minute) à des températures modérées (≤ 1200 °C), limitant la croissance granulaire. Grâce à cela, nous avons pu réaliser, dans le cas du système BST, des céramiques à densité élevée (densité ≥ 85 %) tout en préservant la taille initiale des particules (Figure 6). Ceci nous a donc permis d'étudier, d'une part, les effets de taille sur les propriétés intrinsèques ainsi que l'impact des conditions de frittage, en particulier les pressions appliquées, sur les propriétés.

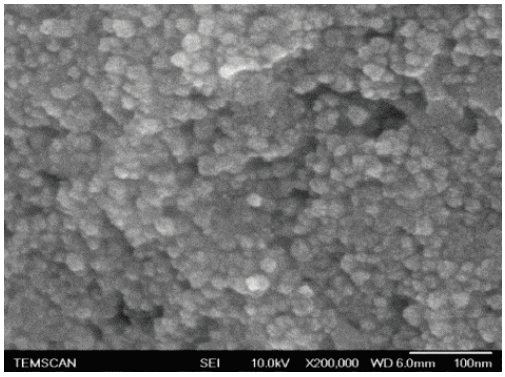

Figure 6 : Céramique dense et nanostructurée de $Ba_{0.6}Sr_{0.4}TiO_3$

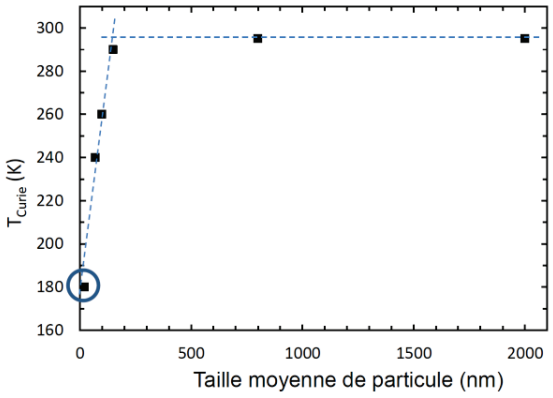

Figure 7 : Variation de la T_c avec la taille des grains.

Concernant les effets de taille, nous avons d'abord mesuré les propriétés diélectriques de la céramique nanostructurée avant de lui faire subir des

traitements thermiques afin de faire croitre les grains et comparer les propriétés correspondantes à la littérature. Ceci nous a permis dans un premier temps de confirmer la précision de la synthèse et de compléter les données de la littérature en déterminant, par exemple, la T_{Curie} pour des céramiques présentant des grains de 20 nm (Figure 7).

Pour ce qui est des effets de pression, nous avons pu constater qu'en augmentant la pression appliquée de 300 jusqu'à 400 MPa, il était possible de faire varier les propriétés diélectriques, en particulier la T_{Curie}, et ceci dans un sens contraire à l'effet de taille étant donné que cette dernière augmentait avec la pression appliquée (Figure 8). Néanmoins, en augmentant encore plus la pression appliquée (jusqu'à 600 MPa), on a constaté qu'il n'y avait plus d'impact, ceci probablement dû à un effet de compensation entre l'effet de taille et la pression appliquée. Concernant le système BTZ, nous nous sommes appuyés sur cette technologie afin de démontrer la précision de la synthèse, notamment sur la composition des matériaux, via les variations des propriétés des céramiques en fonction de la stœchiométrie.

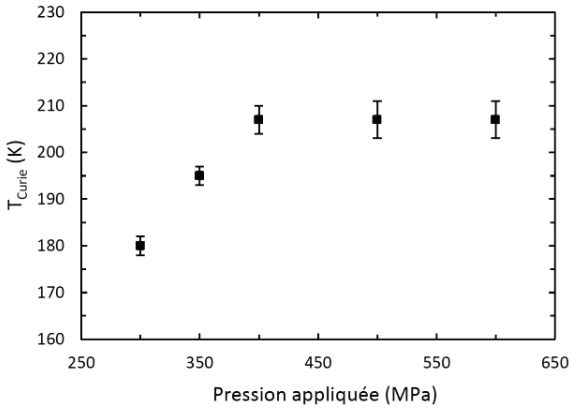

Figure 8 : Effet de la pression appliquée durant l'étape de SPS sur la température de Curie du matériau.

Enfin, une fois que nous sommes parvenus à maîtriser la synthèse et à caractériser les propriétés intrinsèques de ces nanomatériaux, nous avons abordé un nouvel aspect qui est le développement de matériaux hybrides présentant des propriétés diélectriques élevées. Il s'agissait donc de disperser des nanoparticules de type $BaTiO_3$ dans des matrices polymères du type polyester et d'en étudier les propriétés diélectriques. Le but étant toujours de viser des applications dans l'électronique, mais plutôt sur l'aspect flexibles des appareils.

Introduction

This PhD thesis is registered in the framework of the International Doctoral School in Functional Materials (IDS-FunMat) which is a program funded by the European Union. Such PhD is carried out between two universities from different countries and an industrial partner. This work which, is a first step towards hybrid technology, was achieved through collaborations between Bordeaux University (France), Technische Universität Darmstadt (Germany) and Polyrise which is a startup company specialized in hybrids materials.

Nowadays, the industry, which always pushes away boundaries in terms of device size, performance, functionalities and reliability, expects more and more the use of low cost and high quality components, especially ferroelectric ones for microelectronic and communication devices. As illustration, multi-layer ceramic capacitors (MLCCs) have undergone a remarkable size reduction over the last 30 years. To be able to achieve high capacitance in a smaller volume (increase of the volumetric efficiency), the dielectric layers thickness has to be reduced while increasing their number. Now, the thickness of a dielectric layer ranges from 2.0 down to 0.8 μm and the grain size within each layer should become less than 100 nm [1–6]. However, this size diminution has a direct impact on the materials dielectric properties. That is why it is now critical to produce well crystallized particles with a narrow size distribution in order to control the permittivity and reduce the creation of defects during the processing and integration of these powders into electronic devices [7].

Based on the mentioned challenges, the following PhD thesis presents a study concerning the synthesis and characterization of ferroelectric nanomaterials such as barium titanate based ones. For decades, the high potential of these materials in terms of industrial applications has been dragging intensive researches in order to better understand and improve their properties. In addition to be lead free, barium titanate based materials show very interesting ferroelectric, piezoelectric, pyroelectric and dielectric properties. These strengths make them usable for information and communication technologies, especially in common microelectronic devices like capacitors, dynamic random access memories, sensors and waveguides [8–11].

Currently there are three main synthesis routes to produce such materials: the solid-state, the sol-gel and the hydrothermal ones. Nevertheless, in the context of such size down scaling, these conventional synthesis routes reach their limits in terms of material characteristics and production costs or time, triggering the development of alternative processes. A promising approach is the synthesis of ferroelectric nanopowders using supercritical fluids. This scalable technology enables a single step synthesis of high quality monocrystalline particles at moderate temperatures (<400°C) and in tens of seconds fitting with the environmental expectations.

The two main challenges to be faced in this PhD thesis can be defined as following:

- The supercritical fluid synthesis enabling to fulfill the industrial expectations in terms of nanomaterials quality, the first goal is to improve the understanding of the $BaTiO_3$ based nanoparticles formation, in such conditions, for a better control. To do that we combined conventional *ex situ* analyses like X-ray diffraction, electronic microscopy and different types of spectroscopy with *in situ* synchrotron powder X-ray diffraction ones. This is first done on $BaTiO_3$ nanoparticles and then extended to the solid solutions $Ba_{1-x}Sr_xTiO_3$ (with $0 \leq x \leq 1$ - BST) and $BaTi_{1-y}Zr_yO_3$ (with $0 \leq y \leq 1$ - BTZ).

- The size reduction for these materials affecting their ferroelectric behavior, the second goal is to process them into dense and nanostructured ceramics keeping the starting grains size using fast sintering methods, such as the spark plasma sintering (SPS) one. This will enable us to characterize their intrinsic ferroelectric properties at the nanoscale to (1) improve basic knowledge on the size effect and (2) evaluate their potential applications in electronic, and especially for capacitors. Finally, in the specific case of embedded capacitors, the processing of bulk ceramics being challenging, the discussion will be open to the development and characterization of hybrids composites which are easier to process. In our case we looked at $BaTiO_3$ particles produced in supercritical fluids and dispersed into a polymeric matrix.

The first chapter of this manuscript will enable to define the context of the study. It will start with an introduction to the capacitor technology: its history, principle, interests and challenges in modern technology. Then, the ferroelectricity being the key property in such devices, a presentation of its origin, principle and tunability will be done using the example of $BaTiO_3$, which is the most used material for this type of application. This will be followed with a description of the most well-known synthesis routes with their advantages and limitations in terms of expected materials characteristics (size, size distribution, composition, homogeneity, etc.) and cost. Finally the supercritical fluid technology principle, interests and field of applications will be developed and presented as a potential alternative to the conventional synthesis routes, especially with the example of $BaTiO_3$ based nanoparticles synthesis (BST and BTZ) and characterizations.

The second chapter will consist in a presentation of the methods used to synthesize, characterize and process barium titanate based nanoparticles. It will first describe the supercritical fluid flow reactor used and the key parameters to control the synthesis. This will be associated with *ex situ* techniques used to characterize the powders in terms of size, homogeneity, crystallinity and purity. This will be followed with a presentation of the apparatus used to make *in situ* synchrotron powder X-ray diffraction analyses to monitor the particles growth in supercritical fluid conditions. The last part will deal with a presentation of the technologies used to process the powders into ceramics or composite and how do we perform their ferroelectric characterizations.

The third chapter will present the supercritical fluid synthesis of barium titanate based nanoparticles and its solid solutions; $Ba_{1-x}Sr_xTiO_3$ with $0 \leq x \leq 1$ (BST) and $BaTi_{1-y}Zr_yO_3$ with $0 \leq y \leq 1$ (BTZ). In each cases, a combination of *ex situ* analyses such as the Fourier transform infrared spectroscopy (FTIR), Raman spectroscopy, X-ray photoelectron spectroscopy (XPS), X-ray diffraction (XRD) and high resolution transmission electron microscopy (HRTEM) with *in situ* synchrotron wide angle X-ray scattering (WAXS) will be done. This will first enable (1) to deeply characterize the materials in terms of internal structure, morphology, size and size distribution, crystallinity and surface properties and (2) to understand the formation mechanisms of these particles in supercritical fluids.

The fourth and last chapter will start with the processing of BST nanoparticles into dense and nanostructured ceramics using spark plasma sintering (SPS) with the specific case of $Ba_{0.6}Sr_{0.4}TiO_3$ nanoparticles. The material size effect onto its intrinsic ferroelectric properties will be studied and discussed with other published works. In the meantime, a study of the SPS processing effects onto the material structure and the consequences on its ferroelectric properties will be also investigated. In the case of the BTZ solid solution, the properties going from ferroelectric to relaxor according to the composition, another section will concern the processing of these particles, at different compositions, into ceramics and their characterizations. This will allow us demonstrating the accuracy of the synthesis route through the variation of the BTZ intrinsic properties with the composition as reported in the literature. Finally, an opening section concerning hybrid materials and more precisely the dispersion of barium titanate nanoparticles into a polymeric matrices will be presented. It will consist in the development and validation of a method for the characterization of such composites in order to, later on, be able to classify the best ones prior their integration as embedded capacitors in printed circuits boards (PCBs).

Chapter I. Dielectric materials for passive electronic components: from synthesis to processing, a state of the art

I.1 Electronic and passive components: the case of capacitors

I.1.1 Challenges

As presented in Figure I-1, we can see that most of the components on a printed circuit board (PCB) are passives. They represent up to 80% of the total components quantity and occupy around 40 % of the surface, which limits a further size reduction of the electronic devices [12].

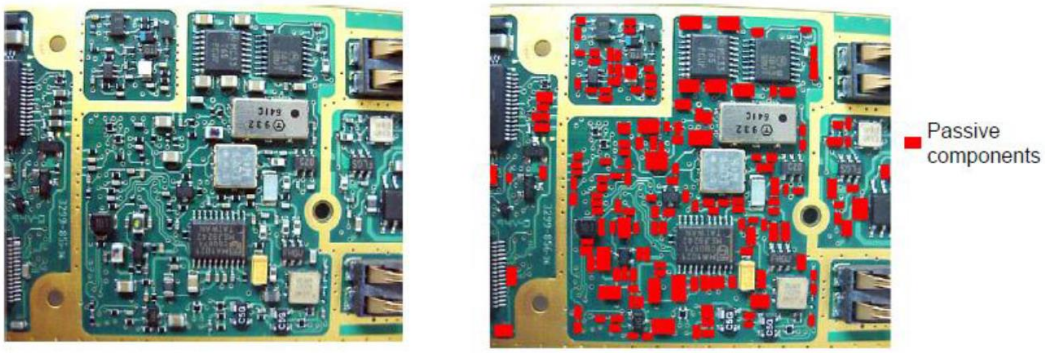

Figure I-1. Illustration of the number of passive components and their density on a printed circuit board (PCB).

It is thus necessary to improve the passives volumetric efficiency which will also enable to use more of them and make faster, more complex, power efficient and compact portable devices. However the industry reaches a point where they encounter more and more problems to further decrease the components size while keeping their efficiency [13,14].

In order to answer to the down scaling challenges we are going to focus on the capacitor case which is the most used passive in electronic, and especially on two of its most promising configurations: (1) the multi-layer ceramic capacitors (MLCCs) which are already well known but facing issues getting smaller and (2) the promising case of embedded capacitors, and more precisely the hybrids (ceramic / polymer) ones which not only enable the device miniaturization but also open the new market of flexible electronics.

I.1.2 History of capacitors

The history of capacitors starts in 1745 when the German Ewald Georg von Kleist (Germany) evidenced for the first time that is was possible to store and release charges at will with the so-called Leyden jar experiment. In this experiment he partially filled a glass jar with water and connected the fluid to a generator using a conductive wire (electrode) in order to load the setup. Once the loading was achieved, he disconnected the generator and, holding the jar in one hand, he touched the electrode as presented in Figure I-2 [15].

Figure I-2. First Illustration of a Leyden Jar experiment [15].

This resulted in a so painful discharge of the device through his body that he said he "would not take a second shock for the kingdom of France". Even though von Kleist was the first, at his expense, to observe this phenomena, the experiment was called the Leyden jar because, independently to von Kleist's study, Pieter van Musschenbroek from the University of Leyden (Netherlands) did a similar experiment one year later and reported it clearly enough to be mimicked by other scientists [16].

Later on, in the 19th century, Benjamin Faraday investigated again this device. He was able to bring a major contribution proving that the charges were not stored in water, as it was supposed, but in the glass jar. Indeed, he managed to observe the same phenomenon putting a glass sheet in between two electrodes. From this experiment he introduced the notion of dielectric constant within materials. His work on the capacitor technology was awarded giving his name to the unit for capacitance. However, as presented in Figure I-3, from the discovery of the phenomena in 1745 by von Kleist up to the early 20th century, the capacitors evolution was quite slow. It is only in the 1920s, with the radio technology, that the evolution of such devices really took off through the elaboration of new designs. Thanks to these developments, capacitors became an essential component in the evolution of modern technologies. Nowadays, this type of component is one of the most used in electronics [14].

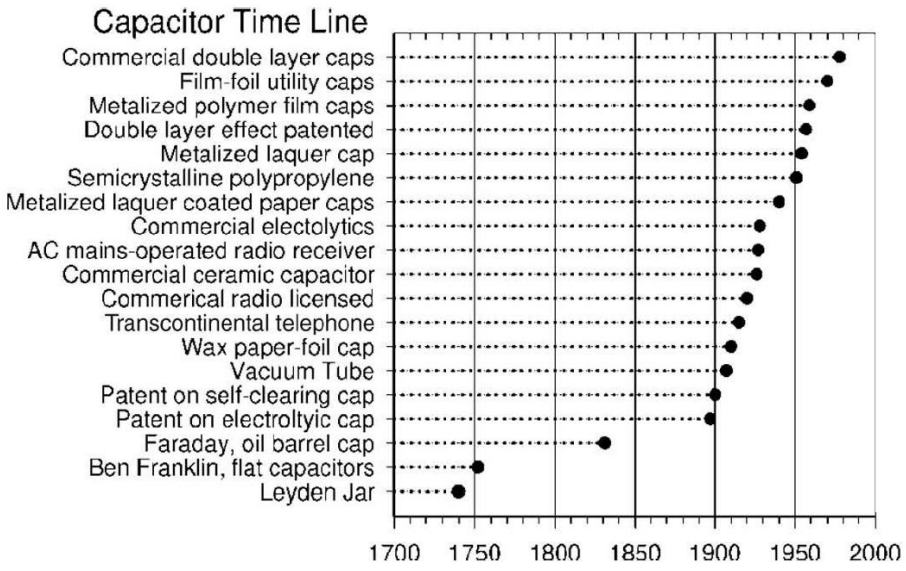

Figure I-3. Development of the capacitors technology with years [14] Copyright © 2010, IEEE.

I.1.3 Principle

Many types of capacitors are available in the market, but their operating principle remains simple (Figure I-4).

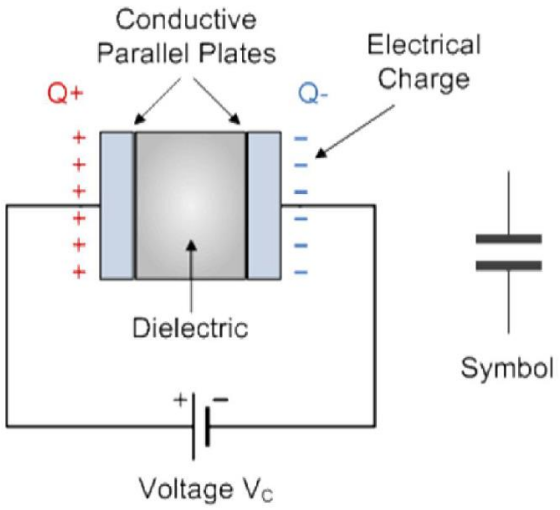

Figure I-4. Operating principle of a capacitor.

A capacitor is made of two parallel conductive plates (electrodes) separated with a nonconductive material called dielectric. When a voltage is applied between the electrodes an electric field appears inside the dielectric material which is going to store the electric energy which can then be realized. This operating principle enables to store, filter and regulate electrical energy into the electronic circuit.

In such devices, the ratio of the electrodes charge Q (in coulombs, C) over the voltage V (in volts V) across the capacitor is called the capacitance C (in Farads, F), see equation (1).

$$C = \frac{Q}{V} \quad (1)$$

This represents the capacity to "hold" the charges for a given applied voltage. It is important to note that one Farad is a very large unit that is why, typically, the capacitance values are in the range from µF to pF. This value directly depends on to the nature of the dielectric material between the electrodes.

A good dielectric material is defined by the presence of localized charges which can be poled applying an external voltage enabling the charges storage. This polarizability is defined with the relative permittivity ε_r which is the ability of a material to develop a polarization applying an electric field. In addition to be dependent of the materials intrinsic properties, the capacitance value can change according to the geometry of the electrodes used to measure it. The equation (2) presents the simplified formula to determine it:

$$C = \frac{\varepsilon . S}{e} \quad (2)$$

Where *S* is the surface of the electrodes (in m^2), *e* is the thickness of the dielectric in between the electrodes (in m) and *ε* the dielectric permittivity (in F/m) which can be expressed as in equation (3):

$$\varepsilon = \varepsilon_0 . \varepsilon_r \quad (3)$$

Where $\varepsilon_0 = 8.854187.10^{-12}$ F/m is the vacuum dielectric permittivity.

Another critical aspect defining a good capacitor is the value of the dielectric losses expressed as tan δ. This represents the overall electric losses of the component in operating conditions. If these losses are too high, the resulting energy dissipation can then impact the performances of the entire device. The origins of these losses can be extrinsic and / or intrinsic to the dielectric material. First it depends on the components structure and defects, especially at the electrodes / dielectric material interfaces. Then, it is also directly related to the dielectric material itself through the ohmic losses which are intrinsic to the dielectric material itself. These losses can be divided into two contributions: (1) a stationary contribution related to the electronic resistance and (2) a dynamic one related to the energy loss during electronic charges and dipoles motion. Indeed, these dipoles and

charges present a frequency dependent inertia to react to an external electric field. This results in a phase shift of the response according to the applied voltage leading to a complex expression of the dielectric permittivity depending on the pulse (ω) of the applied electric field (equation (4)).

$$\varepsilon_r(\omega) = \varepsilon'(\omega) + i\varepsilon''(\omega) \quad (4)$$

In this case the capacitor is no longer considered as ideal and we use the tangent of the phase shift angle (tan δ) to define the associated loss (equation (5)).

$$tan\,\delta = \frac{\varepsilon''(\omega)}{\varepsilon'(\omega)} \quad (5)$$

The objective is to have the highest (ε) possible while keep the losses (tan δ) as low as possible.

I.1.4 Multi-Layer Ceramic Capacitors (MLCCs)

I.1.4.1 Market

The development of MLCCs started in the 50s but it is only these last decades that it was considered as a huge breakthrough, meeting the expectations of the electronic industry to make more compact and power efficient devices [17]. Because the MLCCs cover a wide range of current capacitor applications (Figure I-5), in 2008, their manufacture represented around 90% of the total market in volume for only 40 % of its total value, making it the most used configuration of capacitor.

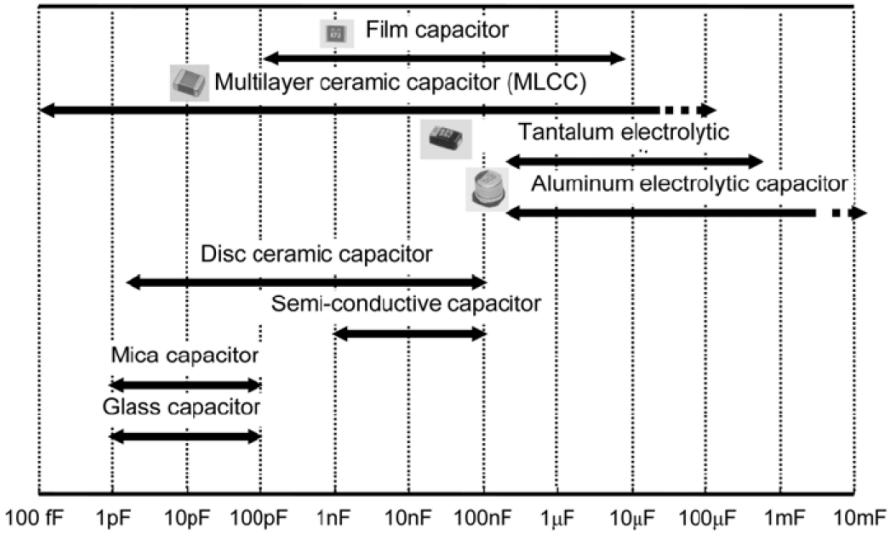

Figure I-5. Types of capacitors capacity and their range of application [18].

Knowing this and because hundreds of capacitors are required in the everyday life devices, such as cell phones, around 1.5 trillion of components were manufactured in 2009 and the volume production is predicted to exceed the Moore's law for the coming years [19].

I.1.4.2 MLCCs Configuration

As presented Figure I-6, a MLCC is made of a stack of several dielectric thin films intercalated with conductive layers acting as interdigitated electrodes connected at the opposite ends of the component with termination electrodes [19].

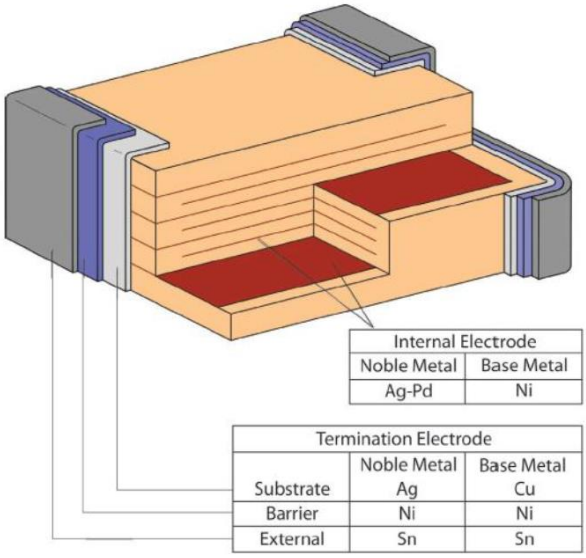

Figure I-6. Configuration of a MLCC [19] Copyright © 2010, IEEE.

In such configuration, the combination of high dielectric thin films with their number and the large electrode surface area enables to produce components with a high dielectric efficiency compared to conventional one layer capacitors. As a consequence the expression of the capacitance described in equation (2) becomes equation (6):

$$C = N \frac{\mathfrak{E}.S}{e} \tag{7}$$

Where N is the number of dielectric layers.

I.1.4.3 MLCCs manufacturing

Figure I-7 summarizes the different steps which are necessary in the fabrication of MLCCs. The first one consists in making a homogeneous dispersion of the dielectric ceramic powder mixing it with solvents and organics such as dispersant, binder and plasticizers. The ceramic slurry can then be tape

casted into thin and continuous films using doctor blade. This technique enables the formation of films with well-defined thicknesses. It works by placing a sharp blade at a fixed distance from the substrate to coat it. The dispersion is then placed in front of the blade, which is then moved linearly across the substrate, leaving a thin and wet film [20].

The thin film is then dried to make a flexible dielectric tape and electrodes are patterned on top of it using screen printing. This technique enables to make 2D patterning of the printed layers. A squeegee is used to fill a patterned screen with the electrode paste. The wet electrodes surface and thickness are defined by the design of the screen [20].

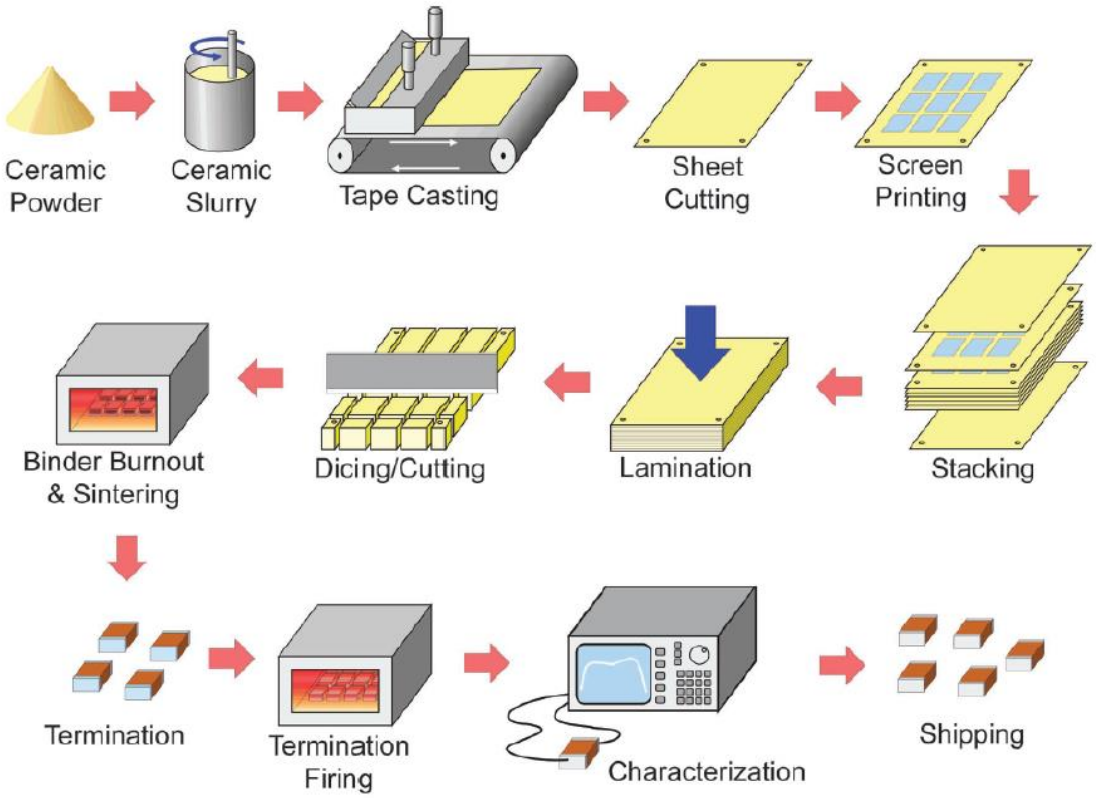

Figure I-7. MLCCs fabrication steps [19] Copyright © 2010, IEEE.

The dielectric tapes with patterned electrodes are then stacked layer by layer and precisely aligned during the lamination. The next step is to cut the stack into individual MLCCs which are heat treated to burn out the binder and sintered to transform the dielectric tape and electrode paste into a dense structure. Finally, a metal termination is connected to the inner electrodes on opposite ends of the components and fired to consolidate the structure. Once the components validation tests are achieved they are ready to be integrated in PCBs.

I.1.4.4 Challenges

To increase the volume efficiency of such structure it is necessary to increase the number of dielectric layers while decreasing their thickness. Nowadays MLCCs can have up to 1000 layers of a submicron thickness while becoming smaller and smaller. As an illustration, you can see in Figure I-8 that MLCCs can now be even smaller than an automatic pencil of 500 µm having dielectric layers of 500 nm thick.

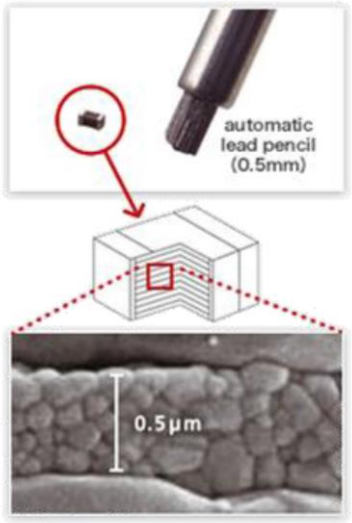

Figure I-8. Submicron layer of a MLCC.

However, to reach such thickness it is necessary to use other deposition processes such as spin casting for the dielectric and physical vapor deposition for the electrodes. These technological issues are not the most challenging ones. To make such thin dielectric layers, or even thinner, the building blocks, which are the particles, have to be very small (tens of nanometers) and with a narrow size distribution to make homogeneous deposits (Figure I-9).

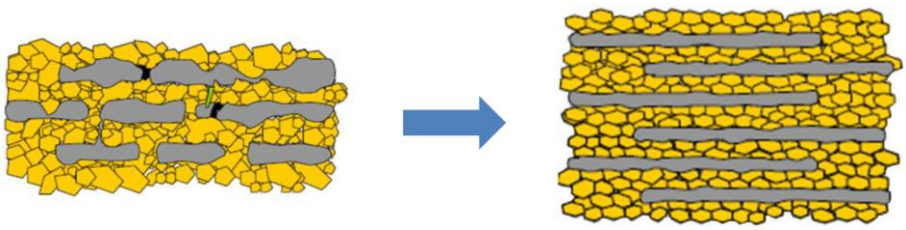

Figure I-9. Illustration of the powder quality necessary to achieve a successful MLCC downscaling.

If the quality of the powder is not good enough then the devices will present a lot of defects affecting their efficiency. In addition, the powder has to be monocrystalline to lower the quantity of defects at the grain boundaries and thus control the permittivity. The size effect on the dielectric

properties of the materials and the notion of critical size will be discussed later in this chapter. It is important to note that the co-sintering of dielectric with electrodes is a technological problem that industries also try to solve.

In addition to the well-known MLCCs structure, a new type of capacitors has been focusing attention for few years: the embedded capacitors.

I.1.5 Embedded capacitors

I.1.5.1 Concept

The concept of embedded capacitors is very different from the one of MLCCs. This type of structure has been studied for only few years and is far away from the MLCCs level of development. Nevertheless it remains a very promising alternative to make more compact devices embedding passives inside the PCBs substrates (Figure I-10).

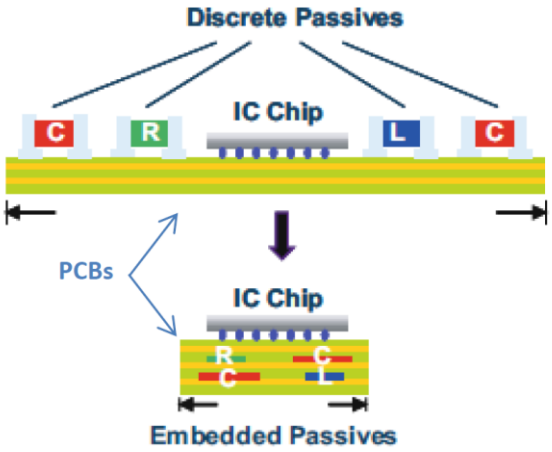

Figure I-10. Potential advantages in terms of size reduction with embedded passives [21] Copyright © 2008, Springer Science + Business Media.

This strategy presents many advantages; of course there is the size reduction, but it can also enable a weight reduction and, the components being protected, an increase in reliability to improve the overall performances at a competitive cost [21,22].

I.1.5.2 Configuration of embedded capacitors

As presented in Figure I-11 the configuration of an embedded capacitors remains similar to the basic principle of a capacitor where there is a dielectric material in between two electrodes.

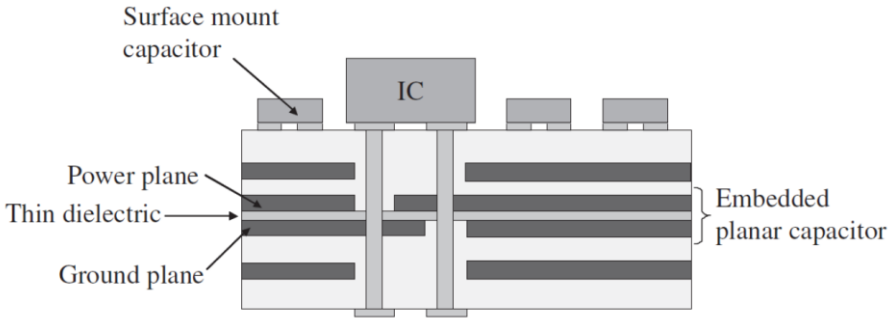

Figure I-11. Illustration of an embedded capacitor configuration [23] Copyright © 2011, Elsevier.

However, in this case, it consists in making a cavity inside the substrate, designing the bottom electrode, filling the cavity with the dielectric material, designing the top electrode and buried it with an additional layer of substrate. For this type of component, the main challenges concern the dielectric materials processing, deposition and interfaces adhesion with the substrate. The dielectric has to exhibit good intrinsic properties while being processable at low cost. That is why many efforts are devoted from the researchers to develop so called “high-k materials”, meeting the expectations in terms of performances, mechanical strength and processability.

I.1.5.3 Development of the dielectric material

This intensive work led to the development of three different types of materials with interesting potential: (1) ceramics, (2) ceramic / polymer composites and (3) conductive filler / polymer composites.

I.1.5.3.1 Ceramics

Similarly to conventional capacitors, it is possible to use only a ceramic as dielectric. As you can see in Figure I-12, the thin ceramic layer is directly embedded into the substrate.

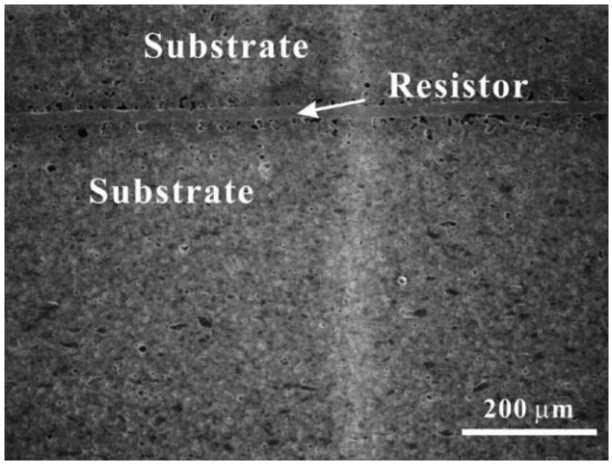

Figure I-12. Illustration of an embedded ceramic resistor made by co firing of the dielectric and substrate [24]

The dielectric properties of such components are, by far the best. However, their processing cost makes them expensive. For example, it is necessary to sinter the material above 600°C making it unsuitable for a direct processing into low cost organic substrates. In addition, shrinkage due to the sintering can induce strain and adhesion issues between the ceramic and the substrate [24–26]. These aspects make this type of structure quite difficult and expensive to process: it is thus necessary to develop new types of dielectric materials easy to process, such as ceramic / polymer composites.

I.1.5.3.2 Ceramic / polymer composites

The idea of this type of dielectric is to combine the advantages of the ceramics in terms of dielectric properties with the processability of the polymer for a low cost integration. Table I-1 presents different types of composites existing with their properties.

Table I-1. Examples of ceramic / polymer composites

Materials	Dielectric permittivity (Ɛ)	Loss (tan δ)	Filler size (nm)	Loading (vol%)	Ref
$BaTiO_3$/epoxy	40 (1 kHz)	0.035	100 - 200	60	[27]
PZT/PVDF	50		20000	50	[28]
$Pb(Mg_{1/3}Nb_{2/3})O_3$-$PbTiO_3$/P(VDF-TrFE)	≈ 200 (10kHz)	0.1 (10 kHz)	500	50	[29]
PMN-PT+$BaTiO_3$/high-k epoxy	≈ 150 (10 kHz)		900 / 50	85	[30]
$CaCu_3Ti_4O_{12}$/P(VDF–TrFE)	243 (1 kHz)	0.26 (1 kHz)		50	[31]
$BaTiO_3$/P(VDFHFP)	37 (1 kHz)	< 0.07 (1 MHz)	30 - 50	50	[32]
$Ba_{0.55}Sr_{0.45}TiO_3$/cyclic olefin copolymer	6 (1GHz)	0.0009 (1 GHz)		25	[33]

In this case the problem lies with the very low dielectric properties of the polymeric matrices. It is necessary to use a large volume fraction of inorganic filler making the composite more difficult to process and inhomogeneous in terms of particles dispersion [27–33]. Following the same idea of hybrids materials, it is also possible to use composites made of conductive fillers dispersed in a polymeric matrix to make composites with high dielectric permittivities.

I.1.5.3.3 Conductive filler / polymer composites

This is possible when filler loading comes close enough to the percolation threshold. As illustrated in Figure I-13 the percolation threshold appears when the loading is high enough to have particles in contact across the in dielectric layer, creating a conductive network, opening ways for charges to move between the electrodes, leading to short cut and component failure.

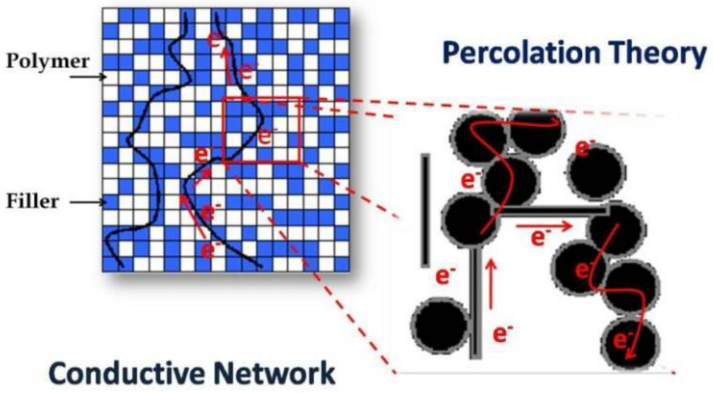

Figure I-13. Illustration of the percolation theory [34].

This type of structure is called the “supercapacitor network”. It is interesting because the loading does not have to be as high as in the ceramic / polymer composite case. Table I-2 presents different types of composites existing with their properties.

Table I-2. Examples of conductive filler / polymer composites

Materials	Dielectric permittivity (Ɛ)	Loss (tan δ)	Filler size (nm)	Loading	Ref
Ni-$BaTiO_3$/PVDF	300 (10 kHz)	0.5 (10kHz)	Ni: 200 BT: 1000	Ni: 23 vol% BT: 20 vol%	[35]
Carbon black/epoxy	13000 (10 kHz)	3.5 (10kHz)	≈ 30	15 vol%	[36]
Al/epoxy	109 (10 kHz)	0.02 (10kHz)	3000	80 wt%	[37]
Ag/epoxy	≈ 300 (1 kHz)	0.05 (1kHz)	40	22 vol%	[38]
Al/Ag-epoxy	160 (10 kHz)	0.045 (10kHz)	Al: 3000 Ag < 20	Al: 80 wt%	[39]
Ag/carbon black/epoxy	2260 (10kHz)	0.45 (10kHz)	Ag: 13	Ag: 3.7 wt% C: 30 wt%	[40]
Ag@C/epoxy	> 300 (1kHz)	< 0.05 (1kHz)	80 – 90 (core)	25 – 30 vol%	[41]

The problem with such structure is that it requires a high precision and control of the conductive filler dispersion otherwise high losses will appear [40,42–52].

I.1.5.4 Challenges

Among the different options the one of ceramic / polymer composites remains the most interesting one, especially in the specific case of nanocomposites. Similarly to MLCCs, the use of nanodielectrics as filler could enable the elaboration of thin films for an increase of the capacitance. Nevertheless, it is necessary to get a very good control of the nanometric filler dispersion inside the matrix. Indeed, the agglomeration of the particles can lead to undesirable properties in terms of material processability or components efficiency. It is thus necessary to use surfactants to get controlled and homogeneous dispersions.

This motivated great efforts over the last years, however, the "perfect" dielectric material has not been produced yet. Indeed, improvements still need to be done in terms of: (1) inorganic filler synthesis to precisely control the size, size distribution and functionalization to later obtain homogeneous particle dispersions, (2) composite loading and homogeneity and (3) processing methods to reliably make thin films.

I.1.6 Conclusion

Even if the phenomenon responsible for the operating principle of a capacitor has been discovered in the 18th century, it is only in the 20th with the apparition of the radio that the interest towards this type of components took off. **To face the industrial challenges to make more compact and multifunctional devices, two configurations are very promising: (1) MLCCs and (2) embedded capacitors. However in both cases it requires the development of ferroelectric materials synthesis processes enabling the controlled production of high quality nanomaterials.**

The operating principle of a capacitor is based on the polarizability of the dielectric material, also known as ferroelectricity. In the following part we are going to present the origin and principles of the ferroelectricity to discuss the issues we can encounter while decreasing the ferroelectric material size to meet the aforementioned specifications.

I.2 Ferroelectricity: origin and principle

The history of ferroelectric materials began in the 17th century when Elie Seignette synthesized a salt of sodium potassium tartrate tetrahydrate (or Rochelle salt) for medical applications. It is only several decades later that other interesting properties were discovered like the piezoelectricity in 1880 [53], the pyroelectricity in 1824 [54] and finally the ferroelectricity in the early 1900s [55–57]. The Second World War was at the origin of a major progress with the discovery of ferroelectricity in perovskite based ceramics. Among the different ceramics studied, the lead free barium titanate ($BaTiO_3$ or BT) appeared as one of the most promising candidate with a dielectric permittivity (ε_r > 10 000 at room temperature) much higher than the one for others ceramics such as TiO_2 and $CaTiO_3$ (ε_r < 100 at room temperature) [8,58–61]. Even if this material was discovered by Bourgeois in the 19th century [62] it is only in the 1940s that Wul and Goldman evidenced its dielectric properties [63] and von Hippel its ferroelectric ones [64].

The crystal structures describing the materials arrangement can be divided into 32 classes, or point groups, according to the number of rotational axes and mirror planes they exhibit (Figure I-14).

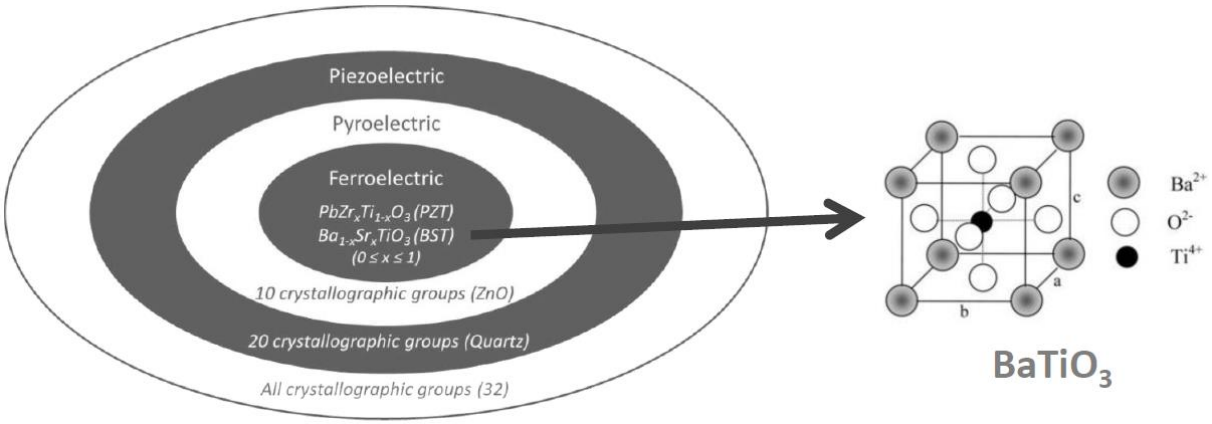

Figure I-14. Classification of the various properties based on their crystal structure with the example of the paraelectric cubic perovskite structure of $BaTiO_3$ [65] Copyright © 2014, Elsevier.

Among the thirty-two crystal classes, twenty-one are non-centrosymmetric and of these, twenty exhibit piezoelectricity. Only 10 of the 32 point groups are polar, having a dipole in their unit cell, and exhibiting pyroelectricity. Finally, inside these ten classes few of them are going to present the ferroelectric property which is the ability of tuning the material polarization according to different stable directions applying an external electric field [8,66]. One of the most well-known crystal structure fulfilling the requirements to be ferroelectric is the perovskite one.

The unit cell of the perovskite structure (ABO_3) is presented in Figure I-14 through the example of $BaTiO_3$ where the titanium atom occupies the B site within an oxygen octahedron, the barium atoms occupy the A sites at the corners and the oxygen atoms are at the center of faces.

I.2.1 Phase transitions and dielectric permittivity

Figure I-15 shows an overview of the $BaTiO_3$ dielectric permittivity evolution as a function of temperature in the case of a bulk ceramic. At high temperature $BaTiO_3$ has a paraelectric cubic perovskite phase. As the temperature decreases, it undergoes three successive transitions ferroelectric phases with tetragonal, orthorhombic and rhombohedral symmetries at 120, 0 and -90°C, respectively. The maximum of permittivity occurs at T = 120°C which is called the Curie temperature (T_{Curie}). Above 120°C, the barium titanate has a cubic structure exhibiting a centrosymmetry with no spontaneous polarization. Below 120°C, it turns into a tetragonal phase, with a displacement of the titanium atoms inside the oxygen octahedra [19].

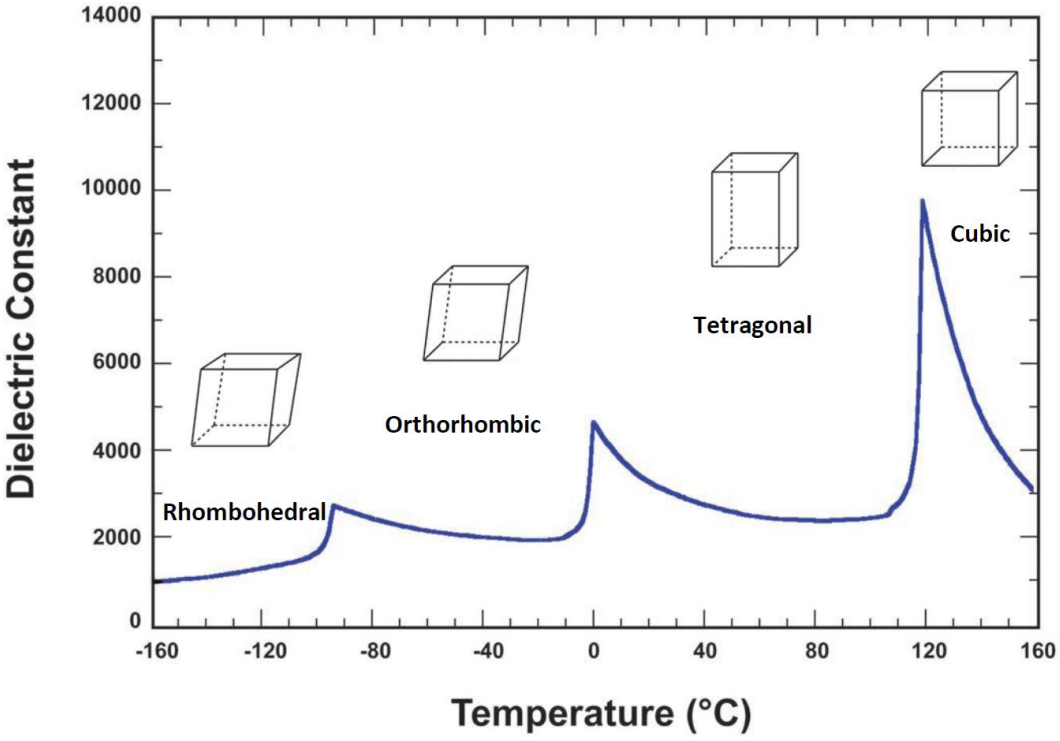

Figure I-15. Evolution of $BaTiO_3$ dielectric permittivity as a function of temperature [19] Copyright © 2010, IEEE.

I.2.1.1 Paraelectric state

If $T > T_{Curie}$ the $BaTiO_3$ structure will present an ideal perovskite structure, in the Pm3m cubic space group, which is centrosymmetric and where the ratio of the lattice parameters c / a = 1. In this

symmetry the material cannot present a spontaneous polarization and is called apolar. As you can see in Figure I-16 without any external field applied there is no polarization within the material.

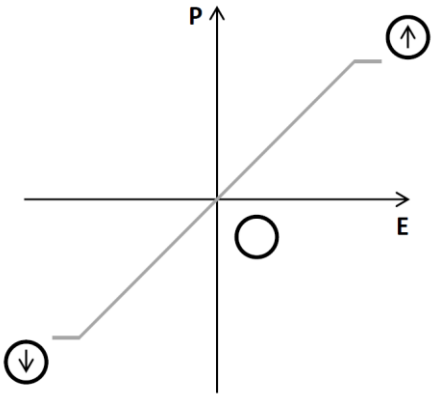

Figure I-16. Polarization of a paraelectric material under an external electric field.

However, the Ti^{4+} cation (r_{Ti} = 0.75 Å) being much smaller than the Ba^{2+} one (r_{Ba} = 1.49 Å) [67], the titanium atom remains mobile inside its octahedral cage. This enables the creation and alignment of dipoles within the material under the application of an external field making it paraelectric.

I.2.1.2 Ferroelectric state

If T < T_{Curie} the $BaTiO_3$ structure will change to the P4mm tetragonal space group, non centrosymmetric and with a ratio c / a > 1 making it ferroelectric. As presented in Figure I-17, this cell distortion results in a displacement of the Ti^{4+} cations and O^{2-} anions in opposite directions and the apparition of a non centrosymmetric octahedron within the cell leading to the apparition of local dipoles. These dipoles interact constructively creating a spontaneous polarization.

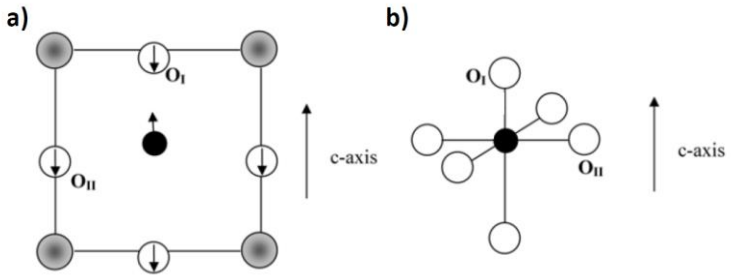

Figure I-17. Apparition of spontaneous polarization with cell distortion in P4mm space group : a) displacement of the Ti^{4+} cation and O^{2-} anions in opposite directions and b) non centrosymmetric octahedron [18].

This distortion can occur along the three crystallographic axes of the cell leading to the formation of ferroelectric domains where the polarization is uniform. This enables to minimize the deformation and so the strain within the material. The domains are separated from each other with “domain walls”. As presented in Figure I-18, there are two main types of domain walls: (1) domain walls at

180° where the vectors are parallel on each side of the wall and (2) domain walls at 90° where the vectors of polarization are perpendicular to the side of the wall (head to tail or head to head). However, the head to head configuration is not energetically stable in terms of charges and tends to be transformed in the head to tail one [68–70].

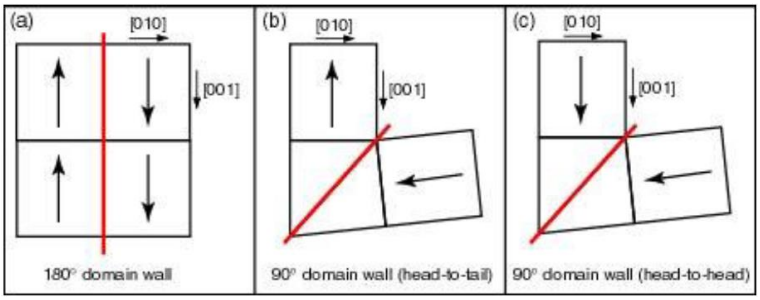

Figure I-18. Different types of domains configuration: (a) 180°-domain wall, (b) 90°-domain wall (head to tail) and (c) 90°-domain wall (head to head) [71].

The domains at 90° are not only ferroelectric but also ferroelastic which enable to relax the strain within the material due to the lattice distortion along the c axis in the tetragonal phase. However, the domains at 180° are only ferroelectric.

As illustrated in Figure I-19, it is then possible to switch the orientation of the domains within the material applying an external electric field, inducing the apparition of a hysteresis loop.

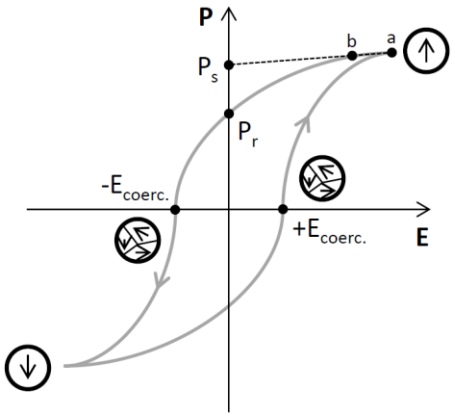

Figure I-19. Ferroelectric hysteresis loop with the representation of the polarization state in the circles [65] Copyright © 2014, Elsevier.

The remanent polarization (P_r) corresponds to the material polarization without external electric field (E) and the saturation polarization (P_S) is reached in the high field range. Finally, the coercive field ($E_{Coerc.}$) is the field to apply in order to switch off the spontaneous polarization [72].

I.2.1.3 Conclusion

The transition from the ferroelectric tetragonal state to the paraelectric cubic one at 120°C, for the $BaTiO_3$, cancels the spontaneous polarization within the material. This leads to a greater sensibility of the dipoles towards an external electric field illustrated with the apparition of a maximum of permittivity (Figure I-15). Unfortunately this is not the most suitable for electronic applications which usually operate at room temperature and require a high tunability of the dielectric material in addition to low losses and high permittivity.

I.2.2 Tunability of the ferroelectricity: T_{Curie} adjustment

It is well established that the dielectric permittivity variation applying an external electric field can be divided into two contributions, a linear and a nonlinear one which are temperature dependent. This nonlinearity being the highest around T_{Curie}, it is thus necessary to have a material with a T_{Curie} close to the device operating temperature in order to combine high permittivity and high tunability. In addition, to avoid the hysteresis loop effect, an asymmetric effect, it is preferable to use a material in the paraelectric state [73]. Meaning that we have to make a material presenting a T_{Curie} just below the operating temperature of the considered device, which is usually the room temperature.

I.2.2.1 Site substitution

The barium titanate based materials presenting an ABO_3 perovskite structure, it is possible to proceed to an ionic substitution of either, the cations in sites A and / or B. This results in a variation of the phase transition temperatures and so of the T_{Curie} position.

I.2.2.1.1 Substitution of the cation in site A

The most well-known substitution is the one of barium cations with strontium ones. The cationic radius of Sr^{2+} (r_{Sr} = 1.32 Å) being smaller than the Ba^{2+} one (r_{Ba} = 1.49 Å) [67] the substitution is easily accessible. Indeed, it does not require a lattice expansion for the strontium insertion into the cell. As shown in Figure I-20, we can see that the tetragonal to cubic phase transition, and so the T_{Curie}, can be tuned across a wide range of temperatures, enabling an adjustment of permittivity maximum (ε_{max}) at room temperature [74].

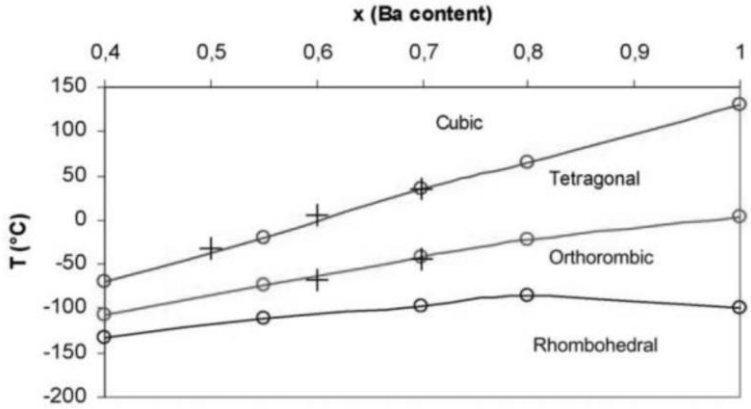

Figure I-20. Effect of barium substitution with strontium on phase transition temperatures [74] Copyright © 2005, Elsevier.

In parallel to the strontium substitution effect, Ishidate et al [75] experimentally demonstrated that applying an external pressure on the material has a similar effect to the strontium substitution. As presented in Figure I-21, according to the applied force direction on the material, the geometry of the cell is modified from a tetragonal to a cubic phase at a given temperature.

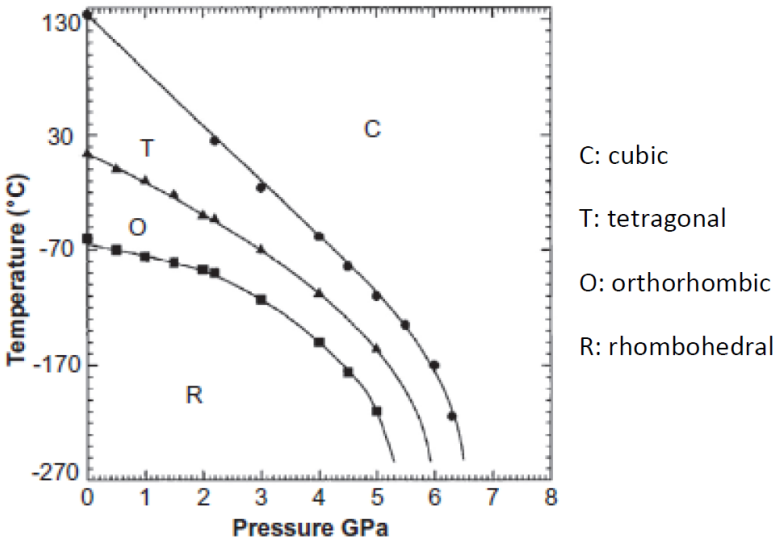

Figure I-21. $BaTiO_3$ pressure – temperature phase diagram [75] Copyright © (1997), American Physical Society.

For example, with a pressure of 2.3 GPa, they observed a phase transition from the tetragonal to the cubic one at room temperature. The lattice contraction was estimated at 0.023 Å which is comparable to the one in the case barium substitution with strontium. Indeed, when 30 % of barium is replaced with strontium, the same phase transition will also occur at room temperature with an associated lattice contraction of 0.03 Å. These two values being close they conclude that the strontium substitution and the pressure applied play an equivalent role on the lattice contraction inducing variations in phase transition temperatures.

I.2.2.1.2 Substitution of the cation in site B

Similarly to the A site substitution, it is also possible to proceed to the B site one. In this case, one of the most interesting cation is the zirconium (IV). Indeed, $BaTi_{1-y}Zr_yO_3$ (with $0 \leq y \leq 1$) is a very attractive material for applied and fundamental research presenting a versatile behavior according to its composition. As presented in Figure I-22, we can see that the T_{Curie} decreases with the increase of zirconium substitution. However the variation of the phase diagram differs from the barium substitution with strontium. In this case, with $y > 0.15$, the three main phase transitions at 120, 0 and -90°C (identified in the section I.2.1) merge together in a single one called T_m.

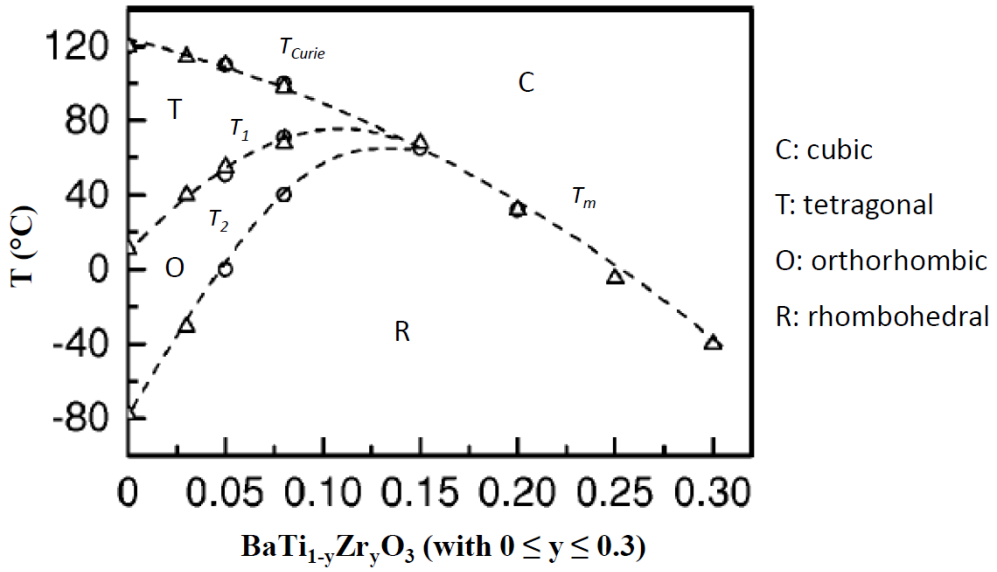

Figure I-22. Phase diagram for $BaTi_{1-y}Zr_yO_3$ ceramics with $0 \leq y \leq 0.3$ (data were taken at 1 kHz) [76] Copyright © (2002), AIP Publishing LLC.

In terms of properties, with y below 0.10 the phase transition from ferroelectric to paraelectric is sharp, increasing the substitution rate from 0.10 to 0.25 broader the transition. Increasing further the amount of substituted titanium cations from 0.25 to 0.40 turns the material into a relaxor where its maximum of dielectric permittivity becomes frequency dependent as presented in Figure I-23 [77–83]. That is why we move from the notion of T_{Curie} where the maximum of permittivity is constant towards T_m where the maximum is frequency dependent. Such material with tunable dielectric constant and high permittivity presents an interesting potential in terms of applications. Of course it can be used as MLCCs, piezoelectric transducers and chemical sensors, but also as microwave electric-field tunable materials [78,83,84].

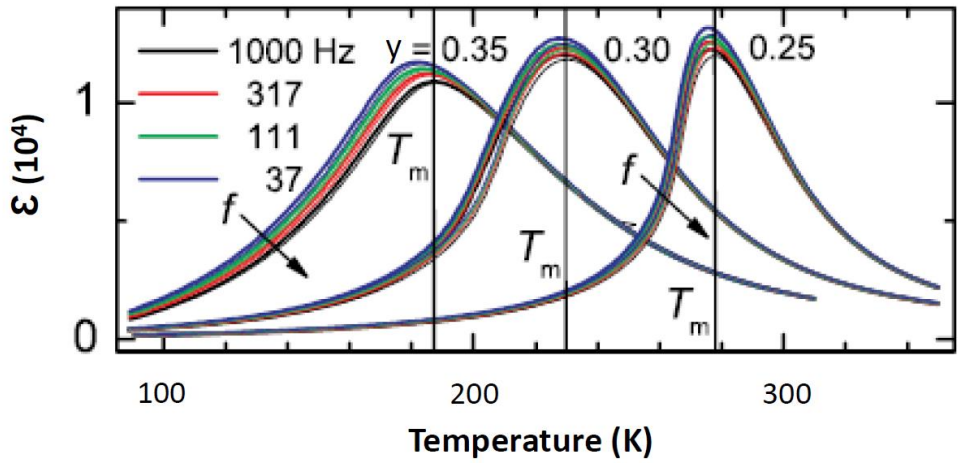

Figure I-23. Illustration of the relaxor effect for $BaTi_{1-y}Zr_yO_3$ with y = 0.25, 0.30 and 0.35 [85] Copyright © (2013), AIP Publishing LLC.

However, it is difficult to replace more than 40 % of titanium with zirconium because the cationic radius of Zr^{4+} (r_{Zr} = 0.86 Å) is bigger than the Ti^{4+} one (r_{Ti} = 0.75 Å) [67] which creates strain and lattice distortion inside the material [76].

The cationic substitution is not the only parameter which influences the T_{Curie}, decreasing the size of the particles also tends to shift it towards lower temperatures.

I.2.2.2 Size effect

The properties of ferroelectric materials are intimately related to their crystal structure which can be intimately linked to their size. Indeed we can see that the permittivity of ferroelectric ceramics is also strongly dependent on the grain size. Figure I-24 reports several literature works regarding the grain size effect on materials permittivity underlining, in the case of $BaTiO_3$, a spreading of the values with a strong influence of both the synthesis and sintering methods [86].

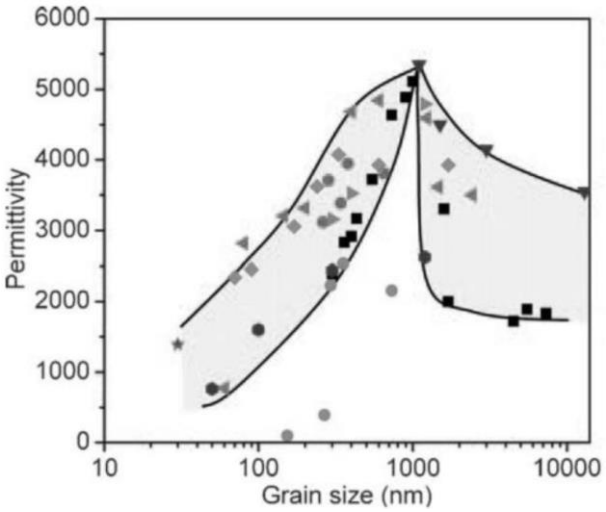

Figure I-24. Evolution of $BaTiO_3$ dielectric permittivity (ε) as a function of ceramics grain size [86] Copyright © 2011, Elsevier.

We can see that Ɛ decreases decreasing the grain size and because we tend to lose the ferroelectric properties; it is usually reported that below a particle size around 100 nm, the structure is no longer considered as tetragonal at room temperature but adopting the so called “pseudo cubic” structure [87,88].

Such size effect on the material structure has been explained by three different models:

- The internal stress model based on the change in domain structure. In this case it is supposed that this size effect impacts the ferroelectric domains organization with the disappearance of the domain walls at 90° (Figure I-25).

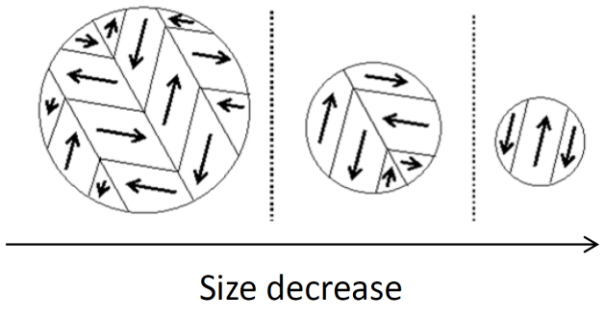

Figure I-25. Size effect on domain walls organization.

As already mentioned, these domains at 90° being also ferroelastic, they enable the relaxation of the strain resulting from the tetragonal distortion. If there are only domains at 180° remaining which are not ferroelastic, the strain induced from the tetragonal distortion will not be relaxed, which will block the phase transition and lead to the apparition of the pseudo cubic structure [89–91].

- The surface stress model is based on the existence of a cubic “dead layer” at the surface of the particles [2,92,93]. In this case, the model is a correlation between the material size and its synthesis route. According to the type of synthesis, a part of barium from the material can be solubilized creating –OH defects. The presence of these barium vacancies tends to stabilize a cubic phase at the surface of the particles in order to maintain the electroneutrality of the structure [94–96]. As presented in Figure I-26a, the size of the particles decreasing, the proportion of the cubic shell increases compared to the tetragonal core, leading to a progressive loss of the ferroelectric behavior [2,92,93,97,98].

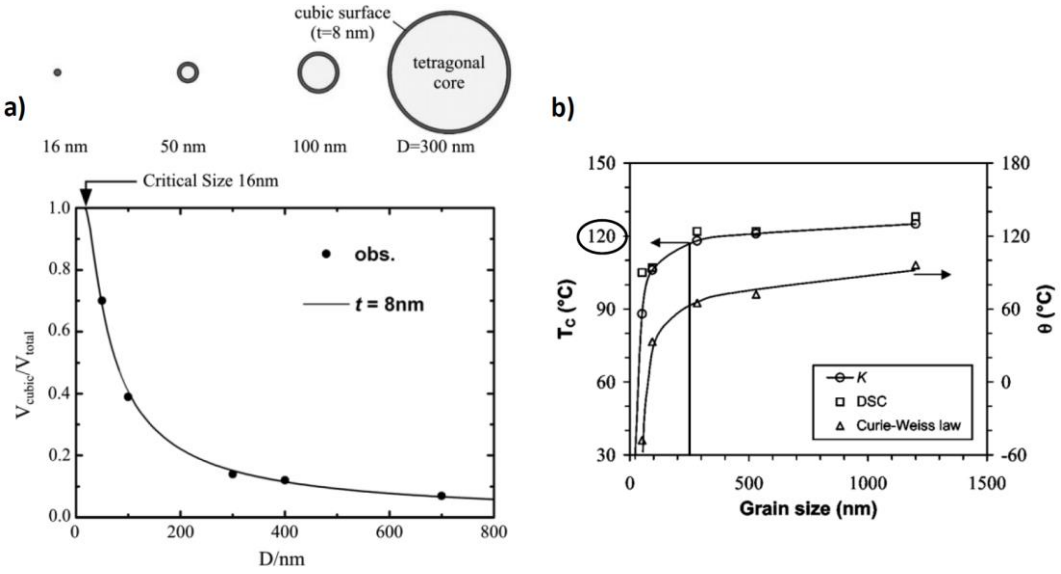

Figure I-26. $BaTiO_3$ grain size effect on (a) the volume ratio of the cubic component to the entire $BaTiO_3$ nanopowder at 300 K, V_{cubic}/V_{total} and (b) T_{Curie} adapted from ref. [92,99] Copyright © 2005, Springer-Verlag/Akadémiai Kiadó & Copyright © (2004), American Physical Society.

As shown in Figure I-26b a notion of critical size in terms of particle dimensions was then established. This corresponds to the smallest particle size where the T_{Curie} remains at 120°C, in this case around 200 – 300 nm. Below this, a competition between the influence of the cubic phase surface over the tetragonal one impacts and decreases the position of T_{Curie} [1,2,4,93,100–102].

- The nanoparticles composite structure is an evolution of the dead layer theory. In this case it consists in an inner tetragonal core, a gradient lattice strain layer (GLSL), and a cubic layer at the surface [97,98]. Its origin can be similar to the dead layer one, there is only an additional “transitional” layer between the core and the shell which has to be considered (Figure I-27).

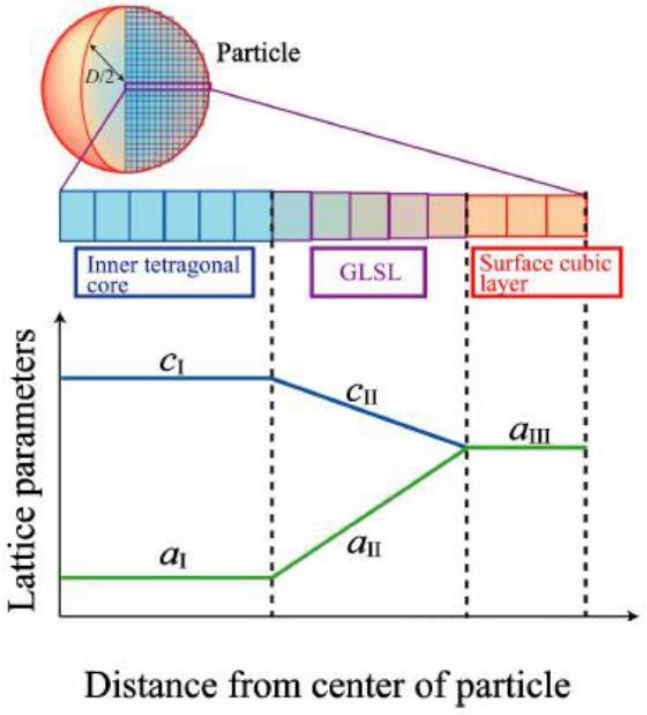

Figure I-27. Composite structure model of a $BaTiO_3$ nanoparticle [98] Copyright © 2013 The Ceramic Society of Japan.

Many theoretical and experimental researches have been carried out in order to define this critical size where the T_{Curie} drops but they led to contradictory results predicting critical sizes going from few nanometers to several tens of nanometers [61,87,99,100,103–105]. These differences highlight the influence of both; the synthesis and sintering conditions. That is why these different models and their origin will be discussed later on in the specific case of our synthesis. However, being focused on powder processing, the ferroelectricity in nanocrystals etched from bulk crystals will not be addressed here [106].

I.2.3 Size effect and dielectric permittivity

It is also important to keep in mind that the size decrease does not only impact the T_{Curie} but also the dielectric permittivity of the material. Figure I-28 presents the variation the dielectric permittivity of $BaTiO_3$ particles at different sizes. At 1200 nm the profile is similar to the bulk material one with a T_{Curie} around 120°C associated to a sharp transition from the ferroelectric to the paraelectric phase and a ε_{max} reaching 5000. Decreasing the particle size down to 300 nm the T_{Curie} drops, with a broader phase transition and a ε_{max} around 3500. Finally at 50 nm we do not see any more the phase transition and ε_{max} goes below 1000.

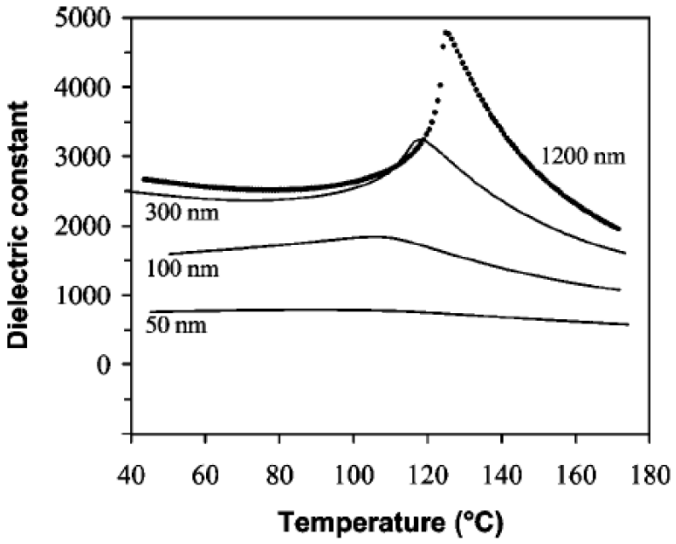

Figure I-28. Variation of the T_{Curie} and dielectric permittivity at 100 kHz according to $BaTiO_3$ grains size evolution [99] Copyright © (2004), American Physical Society.

This is a very critical aspect which as to be carefully taken into account according to the targeted application. Indeed, a broader phase transition from ferroelectric to paraelectric phase can be good in terms of temperature stability of devices. However the permittivity has to remain high enough to fulfill its initial function.

I.2.4 Conclusion

Based on a description of its origin and principle, we have shown that the ferroelectricity was dependent to the material crystalline structure. Then, we presented the two ways to tune the crystalline structure and so the properties through the cations substitution or the size effect. The last one is very important because it also fits to the industrial expectations in terms of size downscaling towards the nanometer scale. It is thus important to develop synthesis methods enabling a high level of control on the material characteristics (size, size distribution, composition, purity, etc.) from the early stage of its processing. Nevertheless it is important to keep in mind the impact of this downscaling on the value of permittivity.

In the following part a state of the art concerning the main synthesis routes is presented and illustrated keeping the example of $BaTiO_3$ synthesis.

I.3 $BaTiO_3$ main synthesis routes

The challenge is to have a process for the large scale synthesis of the material fulfilling the expectations in terms of characteristics while keeping in mind the economic and environmental requirements.

This section summarizes the most well-known synthesis routes described in the literature to produce metal oxide materials. They can be divided in two categories; (1) the dry processes with the deposition (chemical vapor deposition, atomic layer deposition or physical vapor deposition) [107–113], molten salts [114–119] and solid-state [8–10,18,120–123] methods and (2) the wet processes with the sol-gel [99,124–126], hydrothermal [127–142] and bio-inspired methods [143–146]. With in-between the supercritical fluids technology [147–160]. In this section a focus will be done on three of these techniques: the solid-state, the sol-gel and the hydrothermal routes for the $BaTiO_3$ based materials synthesis.

I.3.1 The solid state process

The solid state process is one of the oldest and simplest synthesis route enabling the large scale production of a wide range of oxides. It consists in mixing various carbonates or oxide powders and calcined them for several hours at high temperatures (> 1000 °C). In the case of $BaTiO_3$ synthesis, the barium precursor first reacts at the surface of the titanium oxide and the reaction is propagated toward the center by diffusion to produce single phase $BaTiO_3$ particles [18].

The main strengths of this process are the low cost of the precursors and the ability to produce a large amount of material at once, however it presents some weaknesses. The final product can present $BaCO_3$ and TiO_2 pollutions from unreacted precursors and a Ba_2TiO_4 secondary phase resulting from the high temperature reaction [120–123]. The mechanism being based on a diffusion process, the final size of the powder depends on the precursors size and on the thermal treatment. Usually the resulting grain sizes are hundreds of nanometers with a wide size distribution. An accurate control in terms of stoichiometry within the produced material is hardly achieved, this can be critical in the case of more complex oxides such as barium strontium titanate. As a result, defects and compositional inhomogeneity can occur during further processing steps leading to a poor reliability toward materials integration into devices. To limit these drawbacks and improve the homogeneity, the different precursors have to be as small as possible and particularly well mixed. This leads, as a preliminary step, to the compulsory use of techniques such as ball milling [161–164]. The production of $BaTiO_3$ nanoparticles from $BaCO_3$ and TiO_2, using high energy milling applied on

the precursors to obtain nanocrystals, led to the synthesis of 70 nm nanoparticles with a narrow size distribution [165]. However the remaining problems, beside the supplementary milling step, are the time duration and the occurrence of additional pollutions in the final material. Moreover, heating the powders above 1000 °C during several hours presents an important energy cost. Researches have been achieved in order to overcome these problems leading to the elaboration of versatile approaches: for example the coating of $BaCO_3$ with amorphous titania in the case of $BaTiO_3$ synthesis. This method enables a synthesis at lower temperature (around 600 °C) with a better control of the final particles size and size distribution (100 – 200 nm with narrow size distribution) [166]. However this process is not straight forward and is still time consuming making it difficult to be industrialized [8–10].

I.3.2 The sol-gel process

Another main synthesis route is based on the sol-gel process which is divided in two different approaches: (1) gelation of a powder colloidal solution or (2) hydrolysis and condensation of precursors such as alkoxides or nitrate salts followed by a drying step. The first step consists in mixing the suspension of colloidal powders adjusting the pH to prevent the precipitation in the case of the approach (1) or mixing the precursors with water to start the hydrolysis of the precursors in the case (2) to produce a sol. Then, according to the targeted application, the sol can be deposited on a substrate using various methods such as spin coating or screen printing. With time the gelation of the sol appears due to the polycondensation of the colloidal powders or of the precursors. The gel is then dried to get the amorphous material and a final annealing step at 700-1000 °C is compulsory to crystallize it. It enables a better control of the produced nanoparticles in terms of size (< 100 nm), stoichiometry, homogeneity and purity (slight $BaCO_3$ contamination). In this case the problem is more focused on the use of cost effective and hazardous chemicals and on the process duration. Moreover, the compulsory annealing step increases the particles size. Finally, unlike the solid state synthesis which is a dry process, the synthesis being achieved in a wet media; such materials present –OH defects [99,124–126]. This last point has to be carefully taken into account because it can affect the material properties.

I.3.3 The hydrothermal process

The hydrothermal term was introduced for geological purpose in the 1800s by Sir Roderick Murchison as the action of water at elevated temperature and pressure. The first hydrothermal system was set up in 1845 by Schafthaul to simulate the hydrothermal phenomena occurring within the earth. However it is only during the 20th century that this technology was recognized as being an

important process towards material synthesis. Such reactions are mainly carried out in sealed stainless steel autoclaves heated above room temperature which consequently increases the pressure within the setup [127,128].

Table I-3. Summary of the different synthesis processes with the associated material characteristics [65] Copyright © 2014, Elsevier.

Processes	Process duration	Post synthesis step	Average size (nm)	Defects	Aggregation	Homogeneity	Stoichiometry
– Dry							
Solid state	Long	Milling	>1000	$BaCO_3$, Ba_2TiO_4	Low	Low	Low
Molten salts	Long	Washing	>500	$BaCO_3$	Low	Moderate	Moderate
		Drying					
		Milling					
Deposition	Long	Annealing	<100	$BaCO_3$	Moderate	Moderate	Moderate
– Supercritical fluids	Short	Drying	<100	OH^-	~Moderate	High	High
– Wet							
Sol–gel	Long	Drying	<100	~$BaCO_3$, Ba_2TiO_4 OH^-	Moderate	High	High
		Annealing					
Hydrothermal	Moderate	Drying	20–200	~$BaCO_3$ OH^-	~Moderate	High	High
Bio-inspired	Long	Drying	<100	$BaCO_3$ Polymer	~Moderate	High	High

Usually the reaction mechanism involved in this synthesis is based on the precursors dissolution followed by a precipitation / crystallization of the product. Walton et al. were the first to follow in real time the formation of metal oxide nanoparticles in hydrothermal conditions using *in situ* neutron powder diffraction measurements. In this study they focused on the $BaTiO_3$ synthesis starting from $Ba(OD)_2$,$8D_2O$ or $BaCl_2$ precursors mixed with amorphous or crystallized TiO_2 particles. They were able to observe first; the dissolution of the barium precursor, followed by the titanium one before the crystallization of the $BaTiO_3$. As evidenced in Figure I-29 this showed that the driving force of this synthesis is based on the solubility of the less soluble precursor (here TiO_2) compared to the insolubility of the product ($BaTiO_3$) [129,130].

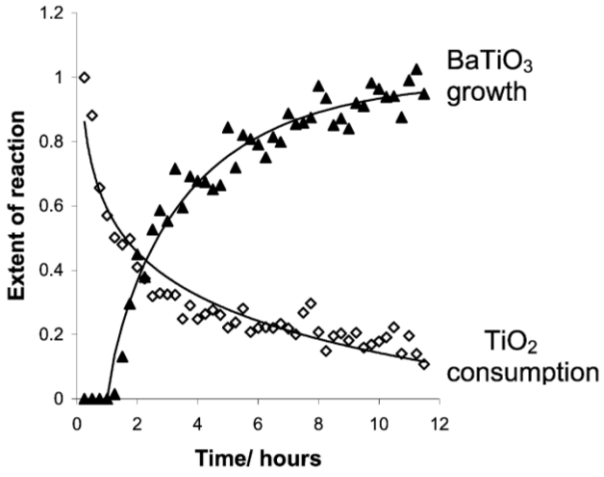

Figure I-29. *In situ* neutron diffraction experiment showing of the consumption of TiO_2 and growth of $BaTiO_3$ with time [129] Copyright © 2001, American Chemical Society.

The most important parameters for these syntheses are (1) the nature and concentration of mineralizers, (2) the temperature and (3) the solvent. (1) Usually the mineralizers are alkaline hydroxides or alkaline carbonates and the most often used are the sodium or potassium hydroxides ones. According to their nature and / or concentrations they can affect the synthesis yield. It is important to be careful with the use of mineralizers because sometime the cation can also act as a dopant in the resulting material. (2) According to the nature of the precursors, acetate or nitrate, and so the reaction mechanism, the temperature will or will not have an impact on the growth behavior. (3) Finally the type of solvents used can play an important role, the reaction occurring under pressure and temperature; the variation of these two parameters changes the fluid properties. For example the use of methanol or ethanol instead of water will change the viscosity and the thermal conductivity of the media leading to chemical reactivity variations [128,131–136].

This technology presents different advantages: (1) it enables the synthesis of various kinds of metal oxide nanoparticles with a good control over their size (from few to several nanometers), size

distribution and morphology at temperatures below 200 °C and pressures below 1.5 MPa, (2) it is environmentally friendly because the solvents are generally not hazardous and the operating temperature is low (< 200°C) and (3) it is low cost and reliable so it is possible to scale up this technology toward industrial production. However in some cases the apparition of a slight $BaCO_3$ contamination can be observed. In addition, as in the case of the sol-gel process, the reaction being achieved in a wet media the presence of –OH defects is reported [128,133,137–142].

I.3.4 Conclusion

Each of these processes presents different strengths and drawbacks which are limiting to fulfill the down scaling expectations (Table 1) in terms materials quality and production cost. That is why it is necessary to develop new synthesis processes such as the supercritical fluid technology in order to suitably answer the industrial demand. This technology combines aspects from the solid state synthesis such as its large scale production ability with others from the wet synthesis such as the quality of produced material thanks to a good control of their size and size distribution, crystallinity, purity and homogeneity.

I.4 The supercritical fluid technology, an alternative

The supercritical fluid method of advanced material design can be considered as an extension of the usual synthesis routes, coupling advantages of the "conventional" methods with some additional inputs making it even more attractive. One of the most valuable one is the enhancement of the chemical reactivity leading to a fast synthesis (tens of second) enabling the use of continuous processes favoring the scaling up ability towards industry.

I.4.1 What is a supercritical fluid?

I.4.1.1 General considerations

A supercritical fluid is a single phase domain which appears crossing the critical pressure and temperature of the considered fluid. For example in the case of water (Figure I-30) this domain appears for pressures over 22.1 MPa and temperatures higher than 374 °C. It is important to know that the supercritical domain is not a proper phase; it is a continuous change from the liquid phase to the gas one. Varying the pressure and temperature it is possible to adjust the density, viscosity, diffusivity or surface tension of the media leading to the apparition of very interesting properties not only for the materials synthesis [147,148,150,152,154,156,167–169] but also for their recycling [170].

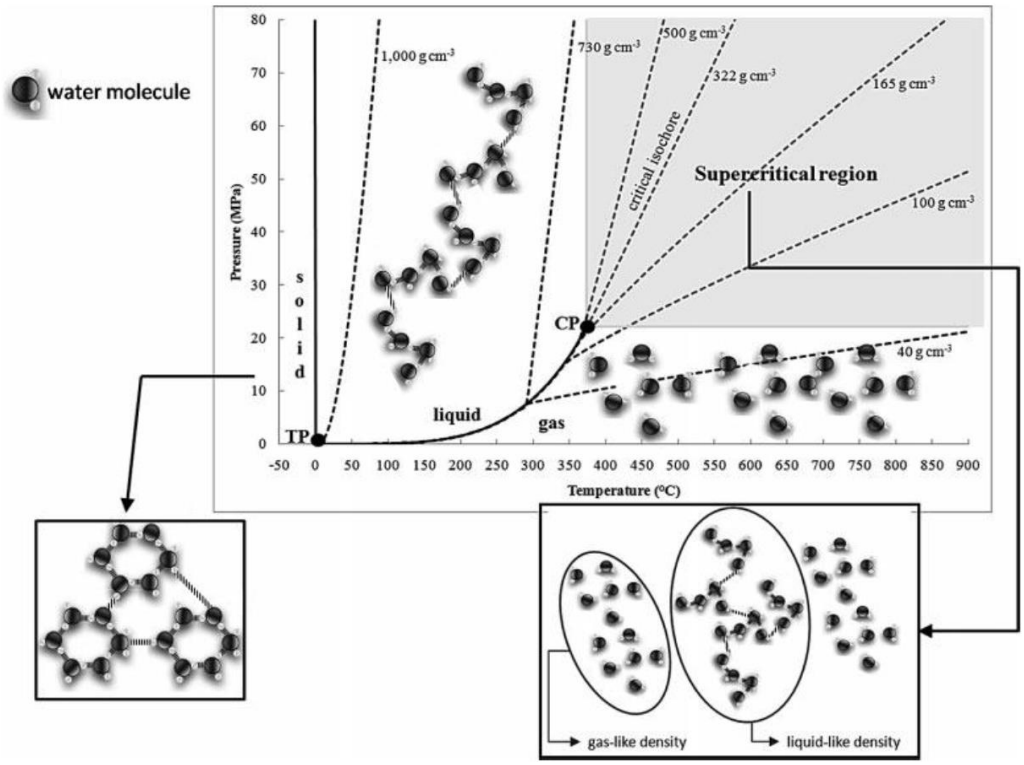

Figure I-30. Pressure–temperature phase diagram of pure water. TP is the triple point (TTP = 0 °C, PTP = 612 Pa) and CP is the critical point (TCP = 374 °C, PCP = 22.1 MPa). Some isochoric curves are drawn (dotted lines) [171] Copyright © 2010 Society of Chemical Industry.

To summarize, this domain combines some properties of the liquid phase to the ones of the gas phase [171]. These properties are intrinsic to the nature of the solvent and can be tuned by mixing together different types solvents.

I.4.1.2 Case of mixtures

In the case of mixtures the interactions between the molecules induce the modification of the critical pressure and temperature of the considered fluids. These properties are then going to be specific for a given mixture at a well-defined composition. For example in the case of water / ethanol mixtures, which are interesting in the case of ferroelectric nanomaterials synthesis in supercritical fluids, the polarity of each species will generate hydrogen bonding between the two types of molecules: the ethanol molecules are going to affect the water molecules structure leading to changes on the critical pressure and temperature of the mixture [172]. In the Figure I-31 Bazaev et al [173] combined theoretical and experimental data from literature [174–176] in order to predict the evolution of the critical temperature and pressure as a function of the water / ethanol composition.

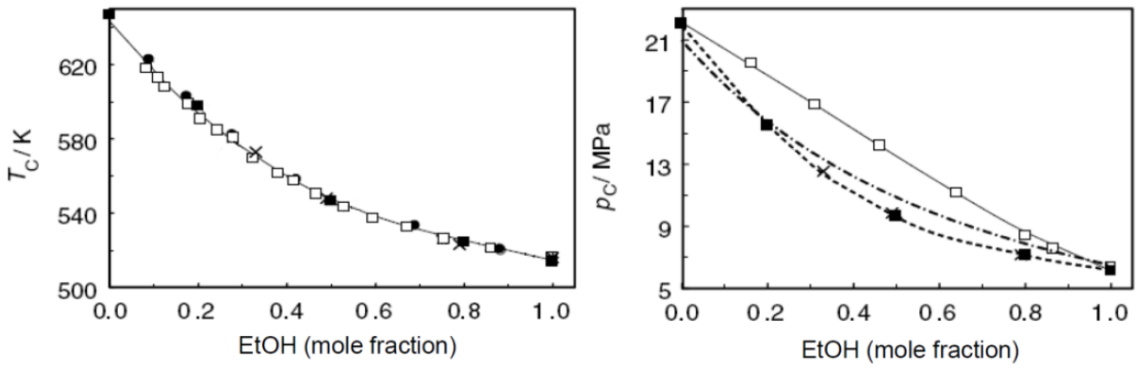

Figure I-31. Evolution of the critical pressure and temperature according to water / ethanol mixture composition where: ● Marshal et al [174] □ Griswold et al [175] × Barr-David et al [176] ■ Bazaev et al [173] Copyright © 2007, Elsevier.

The different studies concerning the critical temperatures evolution with the media composition were in very good agreement. Concerning the critical pressures, except the study of Griswold et al [175] assuming a linear evolution, the different results were also in good agreement.

Nevertheless, there are not a lot of data concerning other or more complex solvent mixtures in the literature. That is why our research group at ICMCB investigates this aspect to develop models, validated with experiments, for predicting the critical points for other and / or more complex mixtures through the PhD work of B. Pinho.

I.4.2 Nanomaterials synthesis in supercritical fluids

Even if the supercritical domain is known for a long time it is only in the early 1990s that Adschiri et al. first reported the synthesis of metal oxide nanoparticles using supercritical water with the synthesis of cerium oxide nanoparticles [177].

In thus conditions, a chemical reaction occurs leading to the material nucleation and growth. According to the nature of the reagents and solvents used, there are four main kinds of chemical reactions which can occur in supercritical conditions: (1) hydrothermal reactions of metal salts or metal precursors in supercritical water leading to their hydrolysis and dehydration [147,148,154,178–180], (2) the thermal decomposition of metal precursors [152,181,182], (3) the reduction / oxidation reactions of metal salts or metal precursors [183–188] and (4) the hydrolysis / condensation reactions known as sol-gel [159,189,190].

In terms of process, the chemical reaction, nucleation and growth are performed into a high pressure and high temperature reactor and feed with high pressure pumps (Figure I-32). The produced material can be recovered whether as a powder using a particle filter positioned before the back pressure regulator valve or in suspension at the outlet of the process.

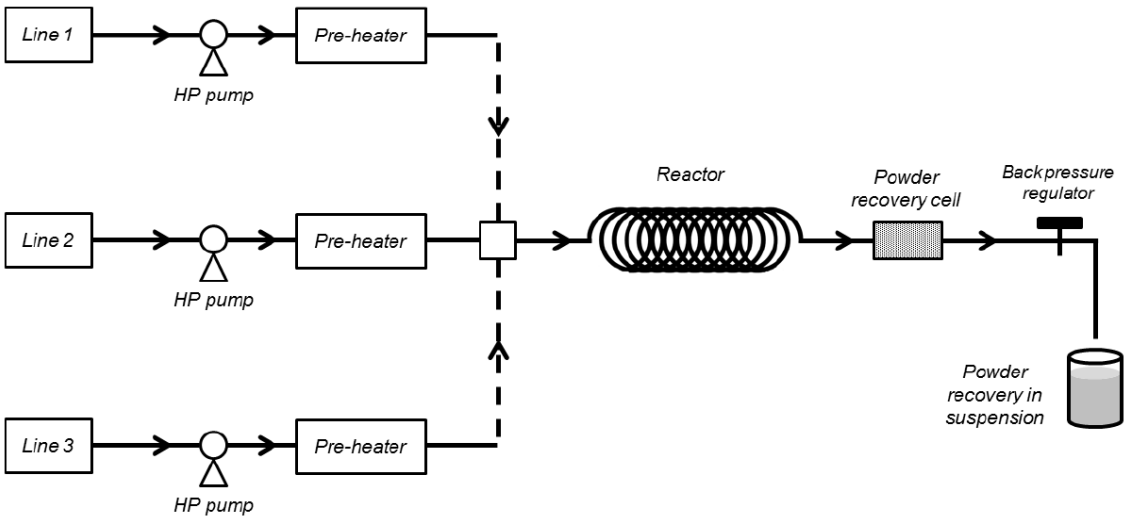

Figure I-32. General sketch of a supercritical fluid process for nanomaterials synthesis [65] Copyright © 2014, Elsevier.

This type of setup is very flexible and can be tuned at will. In its simplest configuration the process will present a single line to inject the precursor dissolved into the solvent. For example Slostowski et al [191] synthesized cerium oxide from ammonium cerium(IV) nitrate solubilized in different alcohols. In this case the heat was only increased by the heating system of the reactor. It can be more complex, for example Hakuta et al developed another design to produce cerium oxide adding a second preheated line [192]. The first line feeding the reactor with the precursors and the second one bringing preheated solvent to the reactor. The two flows are mixed at the inlet of the reactor. There the heating is mainly done by the solvent line. The heating system of the reactor is mainly used to keep the temperature. In other cases the setup can present several lines according the nature of the precursors and their solubility in the solvents used [156,159] or to make more complex structures like hybrids [157,193]. Playing with the main process operating parameters such as reactor's pressure and temperature, precursors nature and their concentration, type of solvents and residence time within the reactor, it is then possible to control the inorganic or hybrids (inorganic / organic) nanoparticle design in terms of size, morphology, structure, composition, crystallinity and surface properties [150,169].

The main interests of this technology can be summarized as follow:

- The properties of the fluids in supercritical conditions enable to the carry out reactions with very fast reaction kinetics (tens of seconds). It is thus possible to operate in continuous leading to the possibility of a better control over the process.

- Using this process it is also possible to reliably synthesize high quality nanoparticles (well crystallized, narrow size distribution, pure, stoichiometric, etc.) in a single step. In comparison with the sol-gel process, it is generally necessary to have a post thermal treatment to crystallize the particles.

- This technology is also versatile enabling a controlled synthesis of various kinds of nanoparticles such as metals (Cu, Ag, Pt, Pd, etc.) [184–188,194–199], oxides ($Ba_xSr_{1-x}TiO_3$ with $0 \leq x \leq 1$, TiO_2, ZrO_2, CeO_2, Fe_2O_3, Cu_2O, Cr_2O_3, Al_2O_3, ZnO, AlOOH, Co_3O_4, CuO, NiO, $CoAl_2O_4$, $MgFe_2O_4$, etc.) [159,182,189,190,199–207] or nitrides (Ni_3N, Cu_3N, Co_2N, Cr_2N, Fe_4N, etc.) [182]. In these conditions of synthesis the nucleation is favored over the growth, leading to the production of nanopowders with high specific surface area which can be very interesting for catalysis or gas capture [208].

- It is a sustainable process which operates at relatively low temperature (< 400 °C) and mainly uses green solvents such as water or alcohols.

- Finally, it is a scalable technology towards industrial production and the first commercial plant is already running (Figure I-33) producing 1 000 tons per year of $LiFePO_4$ [207].

Figure I-33. First commercial plant (1000 tons per year) for the continuous supercritical hydrothermal synthesis of $LiFePO_4$; plant was constructed by Hanwha Chemical [207] Copyright © 2011, Royal Society of Chemistry.

I.4.3 Conclusion

All these aspects show that the supercritical fluid method leads to a good compromise between the solid state and the sol-gel syntheses and enhance the hydrothermal one. On one side it enables the production of a large amount of material in a reasonable amount of time like in the case of the solid

state process. On the other hand it offers a good control on the synthesized particles in terms of size and size distribution, characteristic of the wet syntheses. In addition it fits with an environmentally friendly policy through the use of green solvents and the moderate amount of energy needed [7,207].

In the next part, a state of the art concerning the supercritical fluid synthesis of $BaTiO_3$ / $Ba_xSr_{1-x}TiO_3$ (with $0 \leq x \leq 1$) nanoparticles will be presented, highlighting the advantages of the process in terms of the quality of the produced materials.

I.5 Supercritical fluid synthesis of $Ba_xSr_{1-x}TiO_3$ (with $0 \leq x \leq 1$ - BST)

Only few papers (around 10) report the synthesis of $BaTiO_3$ based materials in supercritical fluids and are mainly shared between two research groups, the supercritical fluid research center at the national institute of Advanced Industrial Science and Technology (AIST – Senday – Japan) and the Supercritical Fluid group at the Institute of Condensed Matter Chemistry of Bordeaux (ICMCB – CNRS – France). From these 10 papers two main approaches are presented towards the synthesis of $BaTiO_3$ based nanoparticles in supercritical fluids: (1) the "supercritical hydrothermal like synthesis" based on hydroxide ($Ba(OH)_2$), oxide (TiO_2) or nitrate ($Ba(NO_3)_2$) precursors or (2) the "supercritical sol-gel like synthesis" based on alkoxides precursors which not only enable the synthesis of $BaTiO_3$ (as in the case (1)) but also the barium strontium titanate (BST – $Ba_{1-x}Sr_xTiO_3$ with $0 \leq x \leq 1$) entire solid solution one.

I.5.1 Supercritical hydrothermal synthesis of $BaTiO_3$ (BT)

Hayashi et al reported the continuous synthesis of $BaTiO_3$ in supercritical water based on different types of precursors ($Ba(NO_3)_2$, $Ba(OH)_2$, [$Ba(OH)_2$, $8H_2O$] and TiO_2). For these syntheses they chose the setup configuration where a preheated line of water is used to heat the media in order to faster the reaction and have a homogeneous nucleation when it is mixed with the precursors at the inlet of the reactor [149,153,155–158]. The precursor line is not preheated to avoid side reactions. The $BaTiO_3$ crystallizes inside the reactor which is under supercritical conditions and the powders are recovered after the back pressure regulator.

One type of precursors was a mixture of TiO_2 nanoparticles dispersion with a solution of $Ba(OH)_2$. According to the flow rate, the conditions of pressure and temperature, the BT nanoparticles were produced in time ranging from few milliseconds to tens of seconds. The $BaTiO_3$ nanoparticles average size was comprised between 10 to 50 nm; an increase of the mean size increased the size distribution. In the case of 50 nm particle, the size distribution was spread from 10 to 150 nm. These syntheses displayed aggregated particles with high crystallinity. According to the conditions of pressure and temperature they claimed that they change the crystal phase from the cubic to the tetragonal one. To get a tetragonal phase, the temperatures ranged from 400 to 420°C and the pressure from 20 to 35 MPa. They based their investigation on XRD analyses of the powders and more precisely on the full width at half maximum (FWHM) of the XRD peaks at (111) and (200). They estimated that since the FWHM for the (200) peak, characteristic of the tetragonal phase, was larger than the one of the (111) peak, the phase was tetragonal. Nevertheless, we have to be very careful with such interpretation since we do not actually observe the splitting of the 200 and 002 peaks.

Moreover, based on Figure I-21, the variation of pressure is far too low to have any consequences on the material's structure. Finally they have not done any ferroelectric characterization to further prove their hypothesis.

Two reaction mechanisms similar to the most well-known ones of hydrothermal syntheses were proposed [130]: (1) dissolution of TiO_2 precursor followed by crystallization of $BaTiO_3$ as demonstrated by Walton et al [129] or (2) *in situ* crystallization based on barium diffusion into TiO_2 nanocrystals [149,153,155,158].

$BaTiO_3$ was also obtained mixing $Ba(NO_3)_2$ with a dispersion of TiO_2 nanocrystals and using a residence time of 8 milliseconds leading to nanoparticles of 10 nm with narrow size distribution. The particles were well crystallized in the cubic phase. Again the presence of –OH defects was detected. In this case, the proposed mechanism was based on the hydrolysis and precipitation of the precursors [157].

With the use of these types of precursors only the synthesis of $BaTiO_3$ nanopowders was reported but they did not verify the accuracy of the synthesis measuring their ferroelectric properties and comparing them to the literature. However, as introduced in the following part, the use of alkoxides enables the production of barium strontium titanate nanopowders over the entire solid solution.

I.5.2 Supercritical sol-gel like synthesis of barium strontium titanate

Bocquet et al. were the first to report the synthesis of $BaTiO_3$ starting with a double alkoxide ($BaTi(O\text{-}iC_3H_7)_6$) in supercritical water / isopropanol mixture [151]. In this study, an extra preheated line was used and the temperature was fixed only by the heating system of the reactor. However, because the alkoxides are not stable in water, two lines were used: one for the precursors dissolved in isopropanol, the other for the water. The reactor was divided in two parts: the first one was in vapor phase to hydrolyze the alkoxides and the second one in supercritical conditions to thermally treat the produced nanoparticles. These nanoparticles presented an average size of 10 nm with a narrow size distribution and a specific surface area of 80 to 90 m^2/g. The infrared measurements showed –OH defects.

Based on these results, Reverón et al. from our group combined both syntheses using alkoxide precursors reacting in water / alcohol mixtures and a preheated line. They first synthesized $BaTiO_3$ nanopowders and then demonstrated for the first time the synthesis of the entire solid solution of BST nanoparticles in supercritical fluids [159,189,190,209].

Barium, strontium and titanium isopropoxides were dissolved in ethanol. The flow reaction system was made of two injection lines: one for the precursors dissolved in ethanol and the second one for water in order to proceed to the hydrolysis of the precursors at the mixing point. The entire system was pressurized at 26 MPa using a back pressure regulating valve. The water line was preheated at 150°C to faster the reaction, however the injection line of precursors was kept at room temperature to avoid side reactions. The two lines were mixed at the inlet of a height meter length tubular reactor with 16 cm^3 of inner volume. The first four meters were heated at T_1 = 150°C to enhance the hydrolysis of the precursors and the four last meters were heated at T_2 = 380°C above the critical point of the water / ethanol mixture to promote the crystallization. Using this setup the experimental parameters were tuned for the $BaTiO_3$ synthesis [159]. One of the most important parameter, beside the pressure and temperature, was the ethanol molar ratio. For an ethanol molar ratio of 0.29 pure $BaTiO_3$ nanoparticles with a crystallinity higher than 90 % were obtained. The particles presented an average size of 41 nm with a size distribution of ± 13 nm. For all the materials the presence of –OH defects was detected.

After the optimization of the experimental conditions for $BaTiO_3$ synthesis, the process was transferred to $Ba_{1-x}Sr_xTiO_3$ (with $0 \leq x \leq 1$) solid solution synthesis [189,190]. Increasing the strontium amount leads to a decrease of the mean particle size. As shown in Figure I-34 the average size went from 41 ± 13 nm in the case of $BaTiO_3$, to 25±6nm for x = 0.5 and to 19 ± 5nm in the case of $SrTiO_3$.

These materials were then uniaxially pressed into pellets and sintered 4 four hours at 1325 °C in order to measure their ferroelectric properties according to their composition (Figure I-34).

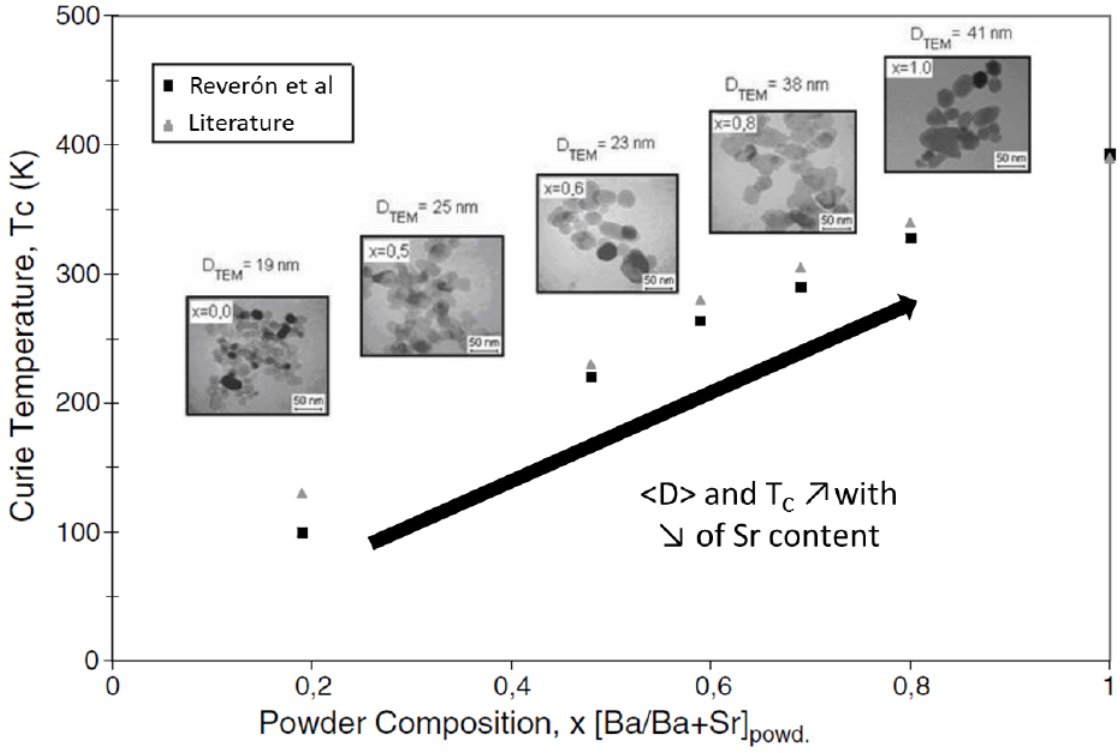

Figure I-34. Effect of barium substitution with strontium on particles size T_{Curie} evolution [189].

The variation of the T_{Curie} according to the strontium content being in agreement with the literature it exhibits the synthesis accuracy in terms of materials composition and stoichiometry [189,209]. However, it is also possible to observe correlation between the composition and the average particles size. Indeed, it appears that the increase of strontium amount tends to decrease the particles size. But so far no precise explanations were found to justify this trend.

I.5.3 Conclusion

Although this process enables the synthesis of high quality and well crystallized nanoparticles with narrow size distribution as expected by the industry, there are still just few papers reporting the supercritical synthesis of $BaTiO_3$ or BST nanomaterials. Two main synthesis routes can be used according to the nature of the precursors leading to different reaction mechanisms. The one based on alkoxide precursors enables more flexibility than the other with the possibility to produce the entire solid solution between $BaTiO_3$ and $SrTiO_3$ ($Ba_{1-x}Sr_xTiO_3$ with $0 \leq x \leq 1$). In both cases it is important to note that even if the syntheses are achieved under pressure (around 25 MPa) it is too low to have any consequences on the material's structure (Figure I-21) even if Hakute et al. study claimed that a variation pressure can modify the $BaTiO_3$ crystal structure from cubic to tetragonal phase [155]. **It is thus necessary to achieve a deeper study to understand and control the**

nucleation and growth mechanisms, especially in the case of the BST solid solution, where the size variation with the composition remains unexplained and to get a better control on the synthesis.

I.6 Conclusion of Chapter I

Passive components being space consuming on PCBs, they focus great attention from the industry because they limit the ability to produce more compact and multifunctional electronic devices. The case of capacitors is especially targeted because a large amount of them is necessary in a single device. For example, a cell phone uses hundreds of them to operate. To face this challenge, two types of capacitor configurations are very promising, the MLCCs which are already well known but can be improved and the embedded capacitors which are still at the development stage.

In both cases, the operating principle relies on the use of ferroelectric materials such as perovskite $BaTiO_3$ based materials. Such materials have gained a lot of attention from researchers for decades because they present high dielectric permittivity. However the ferroelectricity is very sensitive to the grains size when they reach tens of nanometers. That is why, if we want to maintain a certain level of device performance, it is necessary to use high quality dielectric nanomaterials in terms of size, crystallinity, purity, and homogeneity, while keeping a large amount of production at low cost and following the environmental policy. So far, the main synthesis routes reach their limits and new processes have to be developed. An alternative is the supercritical fluid technology.

In addition to bring an answer to the materials quality expectations, this scalable technology enables a fast and reliable materials production using green solvents. Moreover this technology is versatile and not only enables the production of oxide nanoparticles but also metals, nitrides and more complex structures such as core shell ones. The example of the $BaTiO_3$ synthesis is really well illustrating the contribution which can be brought by this technology to the industrial production of metal oxide nanomaterials with the ability to produce in tens of seconds high quality $BaTiO_3$ based nanoparticles.

However, if we want to use it for a large scale production of nanomaterials, it is first necessary to understand their formation in supercritical fluids conditions in order to control their design. Moreover, as already discussed, at the nanoscale it becomes essential to understand the link between the materials structure and their ferroelectric properties. This will be possible with an in depth study of the material structure and surface properties correlated to a characterization of their intrinsic ferroelectric properties.

To do that, this PhD work is divided in two parts:

- Study of the supercritical fluid synthesis of barium titanate based nanoparticles and its solid solutions; $Ba_{1-x}Sr_xTiO_3$ with $0 \leq x \leq 1$ (BST) and $BaTi_{1-y}Zr_yO_3$ with $0 \leq y \leq 1$ (BTZ) combining *ex situ*

analyses like X-ray diffraction, electronic microscopy and different types of spectroscopy with *in situ* synchrotron powder X-ray diffraction.

- Process these powders into ceramics for studying either their bulk or intrinsic properties. For the study of bulk properties, we are going to use the “conventional” sintering process enabling the grain growth. However, to study the intrinsic properties it is necessary to make dense and nanostructured ceramics keeping the starting grains size. This is possible using fast sintering methods, such as the spark plasma sintering (SPS) one. This will enable us to improve the knowledge concerning the size effect on their properties and to evaluate their potential application in electronic, especially for capacitors. This part will be conclude with an opening study concerning the development and dielectric characterization of hybrid nanocomposites (nanoparticles / polymer).

Chapter II. Nanomaterials synthesis, processing and characterization: experimental setups and methods

In the following chapter we are going to present the different methods we used across this PhD, starting with a presentation of the ones to produce and characterize the barium titanate based nanoparticles, where a focus in done on the *in situ* synchrotron powder diffraction setup enabling to follow in real time the nanoparticles formation in supercritical fluid conditions. Finally, the techniques to process these powders into ceramics or composites and their characterization tools will be described.

II.1 Nanoparticles synthesis

To synthesize our particles, we chose to work with a reactor that operates in a continuous mode because it enables to have a good control of the process operating parameters such as pressure, temperature and residence time, while producing a reasonable amount of material to perform both, the characterization and processing steps of the powders. In this first part we will describe the setup and the various characterization tools we used.

II.1.1 Setup

The experimental setup used for this work is based on a former one developed at the ICMCB, in the "supercritical fluids" group (Figure II-1). Indeed it has already been successfully operated to synthesize barium titanate and barium strontium titanate monocrystalline particles [150,159,189,190,209–211]. The strength of this setup lies in its versatility, indeed, such system is quite easy to transform at will.

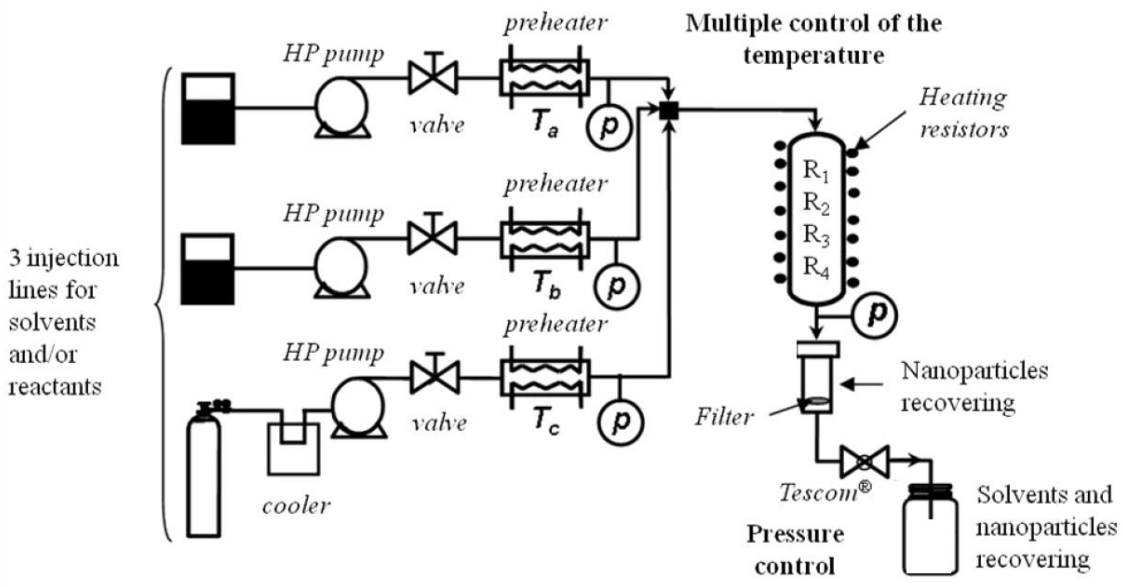

Figure II-1. Sketch of the experimental setup developed at ICMCB [150,210] Copyright © 2006, Elsevier.

The experimental setup consists in two high pressure pumps (flow up to 15 mL.min^{-1}). For this study, one is dedicated to the injection of the alkoxide precursors solubilized in ethanol, the other one for the injection of water. A third pump can be used equally for the injection of a second solution of metal precursors, a solution of functionalizing agents or even of CO_2, depending of the type of study carried out. The injected solutions can also be preheated independently (T_a, T_b, T_c) before being mixed. The pressure is equal in the whole system, verified with manometers (*p*) and controlled with a back pressure regulator (Tescom®) (see image of the actual setup Figure II-2). For security reasons, security valves adjusted at 40 MPa are located right after the high pressure pumps.

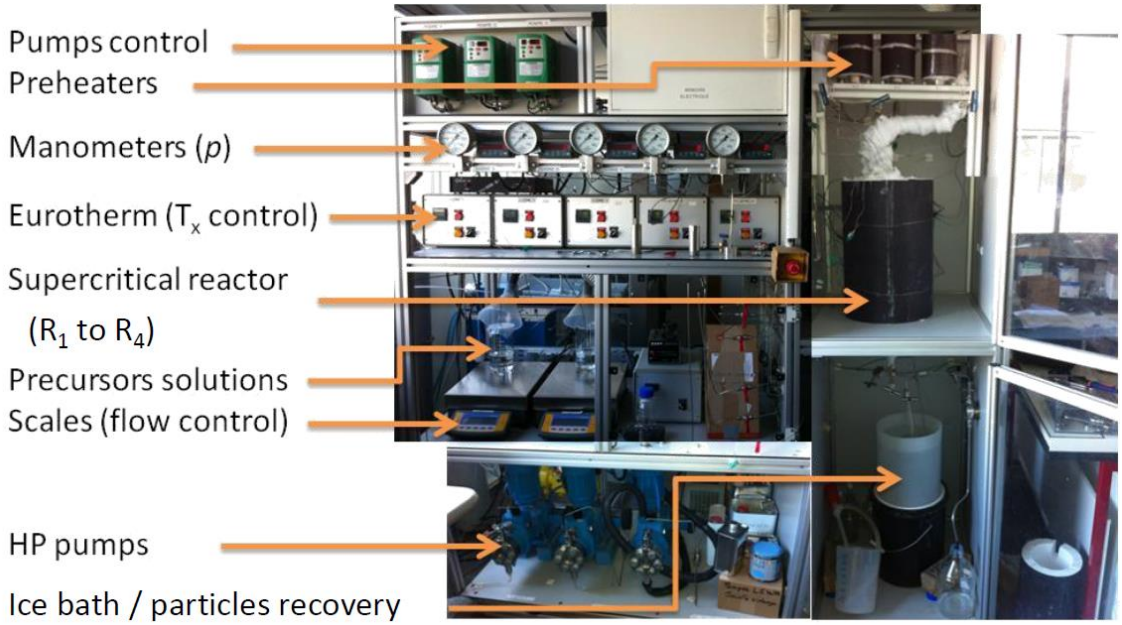

Figure II-2. Photography of the continuous flow experimental setup used for the synthesis of nanoparticles in supercritical fluids.

The tubular reactor in which the reaction, the nucleation and growth and the crystallization of the nanoparticles take place, is made of stainless steel tube (type 316L, inner diameter of 1.57 mm) and consists in four independent parts of 6 m long each (R_1 to R_4). This was made in a view of exploring different configurations of reactions (total length of the reactor, split-up of the hydrolysis and the crystallization, etc.). They are maintained at constant temperature with the use of four heating resistors (Thermocoax®) (T_1 to T_4). K type thermocouples are positioned all along the reactor to enable the visualization of the temperature profiles during the synthesis reaction. An insulation layer minimizes the heat radiation of the reactor and the whole system is put into a Plexiglas box for a safe protection.

The nanoparticles are recovered either with a filter that blocks them on the streamline, or directly in suspension after the back pressure regulator. At the outlet of the reactor, a part of the circuit is

deepened in iced water to quench the growth of the nanoparticles on the one hand, and on the other hand to prevent the back pressure regulator from being overheated and damaged by the hot fluid going through it.

The setup is operated and controlled with the help of an interface programmed on the software Labview®.

II.1.2 Fluid hydrodynamic

For such setup, it is of main importance to control the hydrodynamic of the flow within the reactor. First, it enables to adjust the residence time for the reaction, but also, the size distribution of the particles.

To do that, we use the Reynolds number (equation (7)) which considers the viscosity and the mass flow of the fluid according to the reactor diameter to define three different regimes: laminar, intermediate or turbulent.

$$Re = \frac{\rho . v . D}{\eta} = \frac{4 . d_m}{\pi . D . \eta} \quad (7)$$

Where ρ is the density of the fluid (kg.m^{-3}), v the fluid speed (m.s^{-1}), η the dynamic viscosity (Pa.s), D the reactor inner diameter (m) and d_m the mass flow of the fluid (kg.s^{-1}).

It is important to note that the density and viscosity of the fluid depend on the system temperature and pressure. The density can be estimated with *Refprop©* developed by the National Institute of Standards and Technology (NIST) and the viscosity with *AspenTech©* software.

II.1.2.1 Laminar flow

When Re < 2000, the flow is considered as laminar and the speed profile is parabolic (Figure II-3b). The linear speed $v\ (r)$ (in m.s^{-1}) of an element of fluid located at a distance r (in m) from the axe of the reactor can be expressed as equation (8):

$$v(r) = 2 . v \left[1 - \left(\frac{2 . r}{D} \right)^2 \right] \quad (8)$$

The linear speed is then faster on the axis of the tube (r = 0) and is equal to 2 v than on the wall of the reactor where the speed is theoretically equal to zero. The shortest residence time can therefore be estimated from equation (9):

$$t_s > \frac{L.\pi.R^2.\rho}{2.d_m} \quad (9)$$

In this case, unlike the plug flow type, the reaction duration will not be constant. It will be faster at the center of the reactor than at its wall. This will directly impact the produced particles size and broader their size distribution.

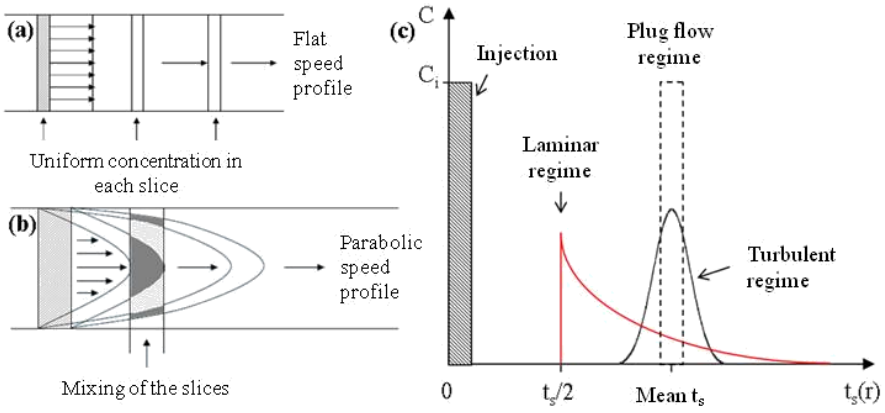

Figure II-3: a) plug flow, b) laminar flow, c) comparison of reaction time with the type of regime.

In addition, because the speed is equal to zero at the side of the reactor, this will favor the deposit of the produced material on the reactor surface. The material having a much longer residence time will grow up to a point where it will be took off from the reactor by the flow. This will lead to the apparition of a secondary population of particles in terms of size.

II.1.2.2 Intermediate flow

For 2000 < Re < 3000, the flow is intermediate between the turbulent and the laminar ones (Figure II-3c), and the Equation (9) is still valid to calculate the shortest residence time. In terms of particles morphology, the size distribution may adopt an intermediate profile too.

II.1.2.3 Turbulent flow

When Re > 3000, the flow is considered as turbulent and the reactor can be associated to the plug flow type reactor model (Figure II-3a). The speed and the precursor concentrations are uniform in each “slice” of the fluid and the relation time = distance / speed is valid across the entire reactor section. The residence time can therefore be calculated according to equation (10):

$$t_s = \frac{L.\pi.R^2.\rho}{d_m} \quad (10)$$

Where t_s is the residence time (s), L the length of the reactor (m) and R the inner radius of the reactor (m). The residence time being constant for each particles, they present a narrow size distribution.

II.1.3 Conclusion

Thanks to its versatility, this setup is very interesting because it enables to carry out different types of tests playing on various experimental parameters such as the temperature, pressure, reactor length, multi injection, flow rate and so on, in order to optimize the materials synthesis. One of the critical parameters is the control of the fluid hydrodynamic which mainly impacts the residence time during the synthesis. If it is not constant across the entire reactor section, the produced powders will present a broad size distribution. It is thus preferable, if possible, to carry out the syntheses in a turbulent flow regime to have a plug type reactor, leading to a constant residence time and so to a better control over the size and size distribution of the produced nanoparticles. However it is not the only important one. Changing the pressure, temperature, solvent nature and precursor concentrations can also directly impact the properties of the nanoparticles.

In the next section we are going to present the various methods we used to characterize the nanoparticles in terms of structure, morphology, size and surface properties.

II.2 Powder characterization methods

Crossing information from different *ex situ* and *in situ* characterization techniques is necessary to describe the produced powders and improve the understanding of mechanisms occurring in the supercritical fluid reactor (Figure II-4).

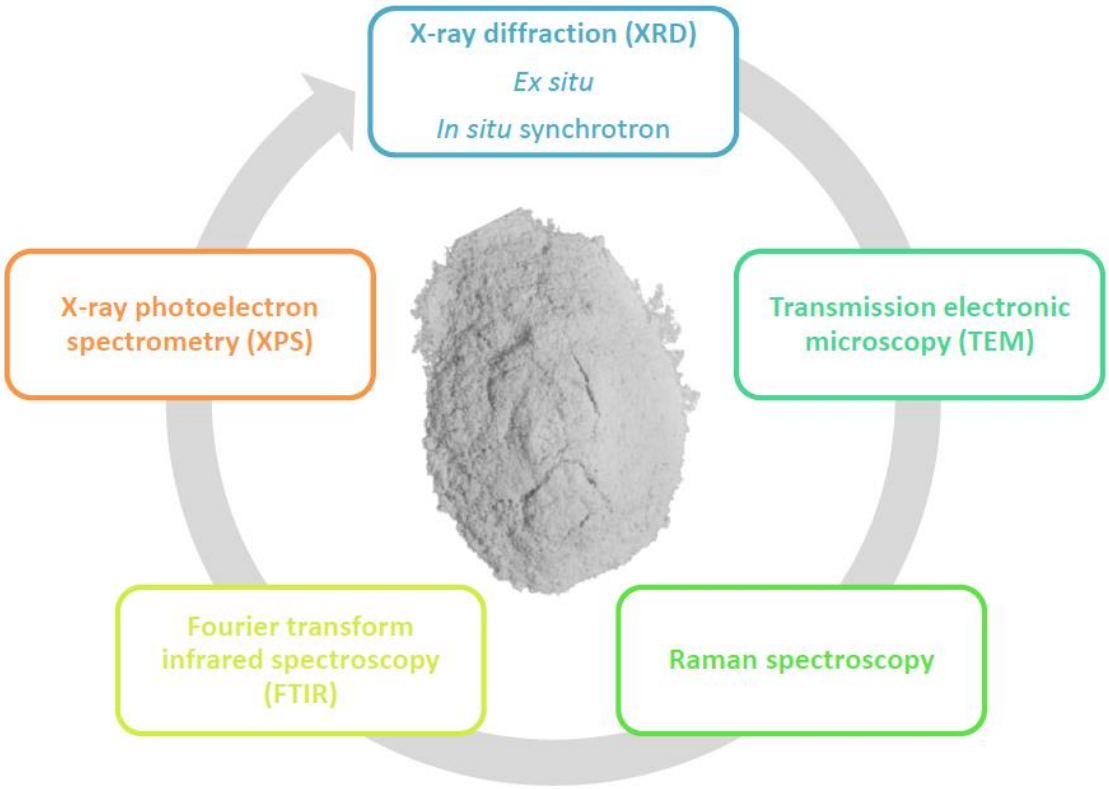

Figure II-4. Characterization techniques.

Many characterization techniques are available at ICMCB and at the "Plateforme Aquitaine de Caractérisation des MATériaux" (PLACAMAT) in Bordeaux or through a collaboration with Prof. B. Iverson at Aarhus University (Denmark) and the following will present the different ones we used, associated with the type of information they provide, to achieve a deep characterization of the produced material.

II.2.1 Powder X-ray diffraction (PXRD)

Across this study, the use of X-ray diffraction is of main interest. We performed both, conventional *ex situ* powder X-ray diffraction measurements but also *in situ* synchrotron wide angle X-ray scattering (WAXS) ones using an adapted reactor.

II.2.1.1 Ex situ PXRD measurements

The analyses were carried out by E. Lebraud and S. Pechev from ICMCB internal service, and two types of apparatus were used according to the nature of information we were looking for:

- A PANalitycal X'pert MPD Bragg-Brentano θ-θ geometry diffractometer equipped with a secondary monochromator over an angular range of 2θ = 8-80°. The Cu $K_{\alpha1,\alpha2}$ (λ_1 = 1.54060 Å, λ_2 = 1.54441 Å) radiations are generated at 40 KV and 40 mA.

- A PANalytical X'Pert MPD-PRO powder diffractometer equipped with a germanium monochromator to be perfectly monochromatic. We observe only the diffraction of the Cu $K\alpha_1$ radiation at λ_1 = 1.54060 Å generated at 45 KV and 40 mA.

The difference between these two apparatus lies in the quality of the expected XRD patterns. The second being perfectly monochromatic, it is possible to carry out a much more precise analysis than with the first one. Indeed, the first one having the contribution of two wavelengths, leads to the superposition of two XRD patterns mingled at low diffraction angles but which tend to split at higher angles. However, the analysis with the first equipment being much faster (around 30 minutes) compared to the second one (several hours or days), it is very convenient to use it to make a first selection of samples which are then measured with the second one.

II.2.1.2 In situ WAXS measurements

The *in situ* experiments were carried out in collaboration with Prof. B. Iversen team, especially Dr. K. M. Jensen and E. D. Bøjesen, from Aarhus University (Denmark) at the beamline i711 at MAXII, MAX-lab, Lund, Sweden.

MAX laboratory has three storage rings (MAX I, MAX II and MAX III) and a fourth one (MAX IV) which is under construction. We used the MAX II ring which is, at the moment, the largest one with a circumference of 90 meters. The electrons are injected in the ring with an energy of 400 MeV and accelerated inside the storage ring. In the case of this ring, the electrons can reach an energy of 1500 MeV. At this energy, the electrons present a speed of 99.99999 % of the light speed and a mass around 300 times higher than their resting mass. The maximum stored current is 300 mA and the number of electrons in circulation is estimated at 500 billion.

In the case of this study we used the beamline i711 which enables single crystal and powder diffraction. The beam energy is comprised between 12.6 keV (λ = 0.98 Å) and 8.8 keV (λ = 1.4 Å) with a monochromator selecting photon flux with an energy of 12 keV (λ = 1.03 Å). A four circles

diffractometer Newport kappa is located at 5.5 meters form the monochromator and the detector is a an Oxford Diffraction Titan CCD camera [212,213].

The reactor is a single crystalline sapphire capillary with an internal diameter of 700 µm and a wall thickness comprised between 6 to 80 µm. Such capillary can withstand tens of MPa and is thermally stable up to 450°C while being chemically inert. Finally, the sapphire being made of light elements (α-Al_2O_3), the X-ray transmission makes possible to observe the diffraction from the particles inside the reactor with a good resolution.

As presented in Figure II-5a, the capillary is tighten into a shoe using Swagelok© stainless steel tube fittings and graphite ferrules. The shoe enables to protect the capillary, preventing any external mechanical strain which could break it while under pressure and temperature. It is also possible to insert a thermocouple within the capillary in order to precisely know the temperature during the experiment. The setup is pressurized using a high-performance liquid chromatography (HPLC) high pressure pump, which could reach 40 MPa, connected to the capillary with a 1/16 inch diameter stainless steel tube. The heating is provided by a jet of hot air. The air is preliminary heated at the expected temperature then focused on the capillary using a pneumatic shutter system which controls the direction of the flow (Figure II-5a and b).

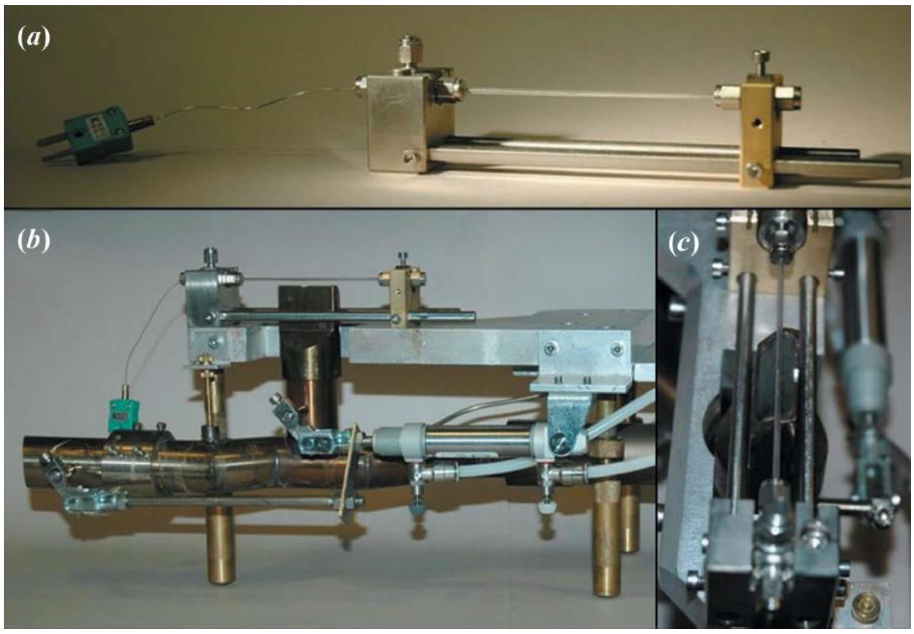

Figure II-5. a) Sapphire capillary tighten into the shoe, b) shoe mounted on the heating system and c) top view of the setup [214] .

Once the capillary is mounted into the shoe and pressure tested, it is filled with the precursor mixture using a syringe. One end of the capillary is then caped and the other connected to the high

pressure pump. After, the capillary is pressurized using a high pressure pump, and subsequently heated with a jet of hot air. Simultaneously with the onset of the heating, sequential X-ray exposures are initiated (Figure II-6). The synchrotron beam energy was 12.3 keV and powder diffraction patterns were collected with the CCD detector every five seconds. The experiments were allowed to run for at least 20 minutes.

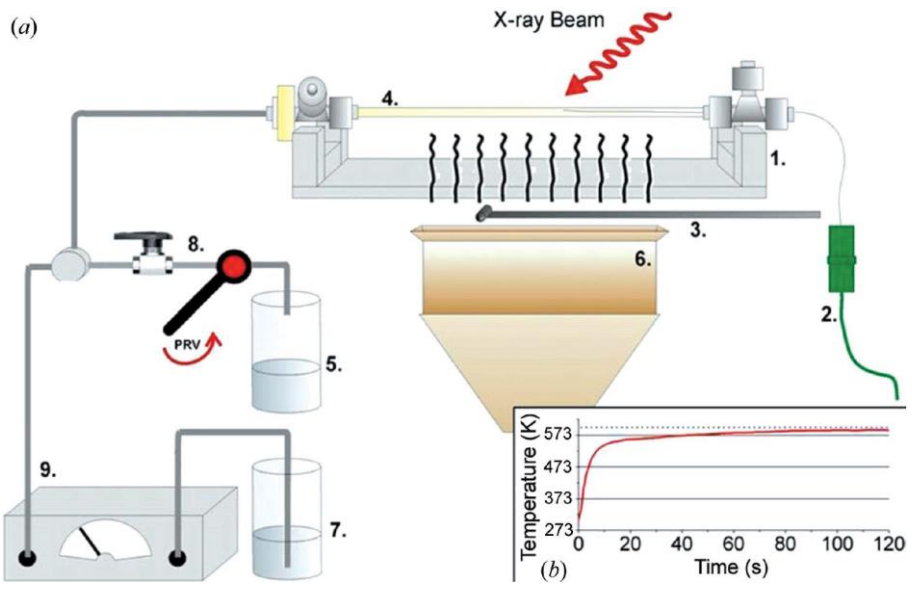

Figure II-6. Sketch of the entire system: 1, fastening shoe; 2, thermocouple; 3, beams top; 4, capillary; 5, waste container; 6, heater mouthpiece; 7, solvent; 8, valves (ball-valve and PRV); 9, HPLC pump (including manometer) [214].

It is important to note that, this setup being different than the one used for the flow synthesis described in section II.1, we cannot directly compare the results obtain with each apparatus. The idea is more to compare the trends to get additional insights concerning the materials formation.

II.2.1.3 Interest for this PhD project

The diffraction phenomenon consisting in an interaction between an electromagnetic wave (such as X-ray) with the periodic medium of a crystallized material, the resulting X-ray diffraction (XRD) pattern will depend on the X-ray wavelength and on the internal atomic arrangement intrinsic to the material analyzed.

Using the software *DIFFRACT^{plus} EVA*, it is thus possible to identify the different phases present in the analyzed material comparing the measured diagram with the ones from the powder diffraction files (PDF) reported in the JCPDS-ICDD database. We can then get more precise information on the materials internal structure such as the lattice distortion, the site occupancy or the internal disorder and strain refining the patterns with the software *FullProf.*

With these profile refinements we can calculate parameters such as the crystallites size using the area below the diffraction peaks. The profile refinements being achieved with the Thomson Cox Hastings – pseudo Voigt approximation, the profiles are described by a convolution of Gaussian (normal distribution, G(x)) and Lorentzian (Cauchy distribution, L(x)) components. Those normalized components (L'(x) and G'(x)) will then give information concerning the peaks broadening (FWHM or H'). Each distribution has a different FWHM: H_G and H_L and the shape of the Voigt function depend on the relative importance of both contributions, see equation (11):

$$V(x) = V(x, H_G, H_L) \tag{11}$$

The pseudo Voigt function, pV(x), approximates the Voigt function where H_L and H_G are replaced by the pair (η, H), equation (12):

$$pV(x) = \eta \mathrm{L}'(\mathrm{x}) + (1 - \eta)\mathrm{G}'(\mathrm{x}) \; with \; 0 \leq \eta \leq 1 \tag{12}$$

Equation (12) can then be numerically calculated as equation (13):

$$H = \begin{pmatrix} {H_G}^5 + 2.69269\,.\,{H_G}^4\,.\,H_L + 2.48243\,.\,{H_G}^3.\,{H_L}^2 \\ + 4.47163\,.\,{H_G}^2.\,{H_L}^3 + 0.07842\,.\,H_G.\,{H_L}^4 + \; {H_L}^5 \end{pmatrix}^{1/5} \tag{13}$$

With equations (14) and (15)

$$H_G = \frac{\sqrt{I_G}}{\cos(\theta)} \tag{14}$$

$$H_L = \frac{Y}{\cos(\theta)} \tag{15}$$

Leading to equation (16)

$$H = \frac{1}{\cos(\theta)} \begin{pmatrix} \sqrt{I_G}^5 + 2.69269\,.\,\sqrt{I_G}^4\,.\,Y + 2.48243\,.\,\sqrt{I_G}^3\,.\,Y^2 \\ + 4.47163\,.\,\sqrt{I_G}^2\,.\,Y^3 + 0.07842\,.\,\sqrt{I_G}\,.\,Y^4 + \; Y^5 \end{pmatrix}^{1/5} \tag{16}$$

Which can be then inserted in the Scherrer formula, equation (17):

$$< D >= \frac{K \,.\, \lambda}{H \,.\, \cos(\theta)} \tag{17}$$

The uncertainties (σ_D) were calculated with the equations (18) and (19) where σ_{IG} and σ_Y are the uncertainties on I_G and Y determined through the profile refinement.

$$\sigma_D = \left(\frac{0.94\lambda}{H^2}\right) . \sigma_H \tag{18}$$

$$\sigma_H = \frac{\pi}{180} . \sqrt{\frac{Y}{16\, {I_G}^{2/3}} . {\sigma_{I_G}}^2 + \frac{\sigma_{I_G}}{4\, Y} . {\sigma_Y}^2} \tag{19}$$

II.2.2 Transmission electron microscopy (TEM)

Two different apparatus were used:

- A HITACHI H7650 with an accelerating voltage from 80 to 120 kV which can operate in high contrast or high resolution. Such apparatus enable to have a resolution of 1 nm according to the nature of the material analyzed. In our case, we worked in high resolution mode where the magnification can reach x600 000. The detector is a *ORIUS SC1000 11MPx (GATAN)* camera and we used the *Digital Micrograph (GATAN)* software to acquire the images.

- A JEOL 2200FS with an accelerating voltage of 200 kV and equipped with a high resolution camera. In this case, the resolution is 0.23 nm. Again, the *Digital Micrograph (GATAN)* software was used to acquire the images.

The first TEM is located at the Bordeaux Imaging Center (BIC) on which I was trained and autonomous to do the analyses and the second one is located at PLACAMAT and the high resolution analyses were carried out by S. Buffière.

This technique, based on the interaction between the electrons from the microscope beam going through the sample and the ones from the sample itself to create an image, enables to observe the nanoparticles in terms of size (to determine their size distribution) and morphology. It is also possible, in high resolution mode (HRTEM) to observe the atomic arrangement. This enables to discuss the crystallite size calculated from the XRD measurements and see if the nanoparticles are monocrystalline. Finally, such analysis gives information concerning the homogeneity of the powder.

II.2.3 Spectroscopy

II.2.3.1 Raman spectroscopy

The Raman used is a *DXR dispersive microscope* with a 532 nm wavelength excitation laser operating at 8 mW output power. The focus is made with a confocal microscope with a x10 objective, leading to a surface analysis of 3.5 μm^2. The resolution was 3 cm^{-1} over a window from 15 to 3550 cm^{-1}.

The Raman spectroscopy was very important in the case of our study. Indeed, as presented in the previous chapter (section I.2.2.2) for the $BaTiO_3$ case, at the nanometer scale, the materials structure is modified due to the surface strain leading to a pseudo cubic structure. Contrary to the XRD analysis, which represents an average response of the materials diffraction, the Raman technique enables a much more local analysis. It is a very sensitive tool to characterize crystal structures and phase transitions. Measuring the vibration frequency of a crystal lattice or a molecule (phonons), it detects the local dynamic symmetry in small regions (coherence length lower than 2nm) making it useful to prove non centrosymmetric local structure in an apparent pseudo-cubic nanopowders.

II.2.3.2 Fourier transform infrared spectroscopy (FTIR)

The FTIR measurements were carried out with a *Bruker Equinox 55 spectrophotometer*. The absorption spectra were acquired through 32 scans in a window from 400 to 4000 cm^{-1}, with a resolution of 4 cm^{-1}.

Similarly to the Raman analysis, through the vibration of atomic bonds, it is possible to identify the materials fingerprint and so its purity. However, in the present study it is mostly interesting to use it in order to characterize the surface properties of our materials.

II.2.3.3 X-ray photoelectron spectrometry (XPS)

Two different apparatus were used in this study:

- ESCALAB VG 220i-XL using Mg K_α as X-Ray source of 1253.6 eV which is not monochromatic. The vacuum chamber was set at 10^{-7} Pa and the analyzed area is a disc with a diameter of 150 µm. This equipment only compensates the electronic charges.

- K-ALPHA using Mg K_α as X-Ray source of 1486.6 eV which is monochromatic. The vacuum chamber was set at 10^{-7} Pa and the analyzed area was a disc with a diameter of 200 µm. This equipment which compensates both, the electronic and ionic charges offers a better resolution.

In both case the measurements were carried out by C. Labrugère at the PLACAMAT platform and the spectra were analyzed with the software *AVANTAGE (ThermoFisher Scientific)*.

This technique enables an analysis of the materials surface properties through measurement of the kinetic energy and number of electrons released after the atomic ionization due to a X-ray exposition. Making it complementary to the observation we can do using the FTIR spectroscopy.

II.2.4 Conclusion

Combining these different types of analyses, such as XRD, TEM, Raman, FTIR and XPS, which have different levels of resolution enables to make complete analysis of the material. In addition, to characterize the structure and surface properties of the nanoparticles, we can follow in real time their formation in supercritical conditions with the *in situ* WAXS setup.

Once the particles are produced and characterized, the next step is to study the ferroelectric properties to first improve the basic knowledge and then, see if such material can answer the industrial demand in terms of properties. To do these measurements we first have to densify the powders into ceramics.

II.3 Powders processing and characterizations

II.3.1 Ceramics

Performing ceramics will allow us to determine dielectric properties of the ferroelectric nanopowders synthesized by supercritical fluids. The choice of the sintering process depends on the aimed objectives: reaching the highest density, keeping the initial grain size of the nanopowder, controlling composition and defects.

There is an intimate link between the crystal structure of the particles, the nano/microstructure of the ceramics and their dielectric properties. It is thus possible in ceramics to correlate the microstructural and dielectric features. The dielectric characteristics depend on the porosity (which decreases the dielectric permittivity), the grain size (which can affect the transition temperature, the permittivity and losses values), thus the density and the quality of grain boundaries which can be considered as defects rich regions. Besides, by its ability to act at several scales, the ceramic technology can be a key strategy. Through different adjustable parameters (such as the temperature, atmosphere, heating and cooling rates), it is possible to control during the thermal treatment the diffusion process, composition gradients, grain growth and defects chemistry.

According to the solid solution studied and to our objectives, we used either; conventional sintering or spark plasma sintering (SPS). The efficiency of SPS to sinter nanomaterials has been fully demonstrated. In this fast sintering process the combination of pulsed electric current and uniaxial pressure leads to efficient heat transfer. As a result, sintering kinetics are increased. In addition, temperature and duration treatment can be significantly reduced compared to conventional sintering limiting the available time for grain growth.

This work was achieved in close collaboration with Dr. C. Elissalde team at ICMCB and Dr. C. Estournes team at the “Centre Interuniversitaire de Recherche et d’Ingénierie des Matériaux - Plateforme Nationale CNRS de Frittage Flash” (PNF2 / CIRIMAT) from the University Paul Sabatier in Toulouse (France).

II.3.1.1 Powders sintering

II.3.1.1.1 Conventional sintering

The first step to make a pellet is to carefully mill the powder in order to break as much as possible the aggregates which could later on lead to inhomogeneity and further differential sintering within the ceramic. A binder, which is a polymer is added (few weight % of the powder) to enhance the

mechanical strength of the raw pellet. The mixture is then poured in 8 mm diameter die and uniaxially pressed with a pressure around 1 T/cm^2 using a hydraulic press.

The pellet is then sintered in a furnace under air atmosphere. A first temperature dwell is realized at few hundreds degrees (around 500°C) for one hour in order to gently burn out the binder used to make the pellet and let the powder self-reorganize to fill the voids created from the binder. Then the temperature is increased up to 1200°C or more for several hours (at least four hours) in order to densify the ceramic through a grain growth before cooling the furnace down.

In such process, the heating and cooling rates are generally around 100 to 300°C/h and the overall cycle takes several hours.

II.3.1.1.2 Spark plasma sintering (SPS)

As already mention, in comparison to the conventional sintering process, for which the main limitation for nanopowders consolidation is the duration of the thermal cycle, SPS enables very high heating rates and short dwell times of few minutes, leading to enhanced sintering kinetics. Using this technique it is possible to make dense materials keeping the initial grain size of the nanoparticles enabling thus to determine size effect, grain boundaries and defects influences on the final dielectric properties of the ceramics.

The powder (without any binder) is loaded in a graphite die, an uniaxial pressure is applied and a pulsed electrical current is allowed to pass via electrodes through the die. The heating source is not external but the die acts as a heating source (Figure II-7). The sintering is generally carried out under reducing conditions (low oxygen partial pressure). A post annealing in air is usually performed to remove surface carbon contamination and to eliminate oxygen vacancies if necessary. However it is possible to work in inert atmosphere (argon, nitrogen) and in some very specific cases in air as it is actually in development in CIRIMAT –PNF2 Toulouse.

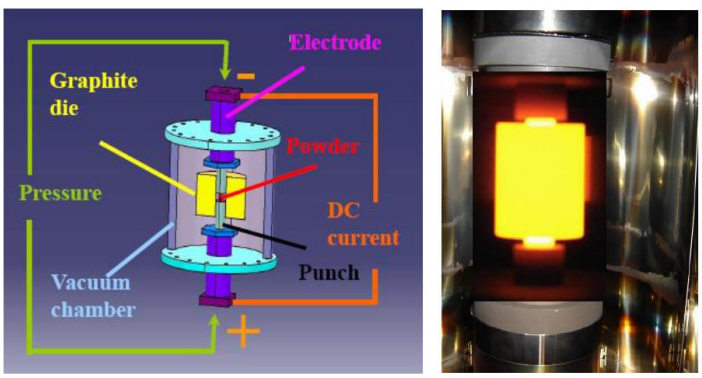

Figure II-7. Sketch and image of a SPS apparatus.

Similarly to conventional furnace, it is possible to adjust the sintering atmosphere. However, the difference lies in the heating principle. In this case it is brought by a high electric current going through the die. This current can be either continuous or pulsed. This enables to quickly reach high temperatures (hundreds of °C.min^{-1}) while applying high pressure (hundreds of MPa) leading to sintering cycles of few minutes which is much shorter than the conventional case.

We had access to two different SPS apparatus to carry out the different experiments:

- At the ICMCB we used a Dr. Sinter 515S machine manufactured by the society SPS Syntex Inc and operated by Dr. U-C. Chung. This apparatus has an output pulsed current of 1500 A, a voltage ranging from 2 to 20 V and can apply a pressure up to 200 MPa.

- At the "Centre Interuniversitaire de Recherche et d'Ingénierie des Matériaux - Plateforme Nationale CNRS de Frittage Flash" (PNF2 / CIRIMAT) from the University Paul Sabatier in Toulouse (France) in a collaboration with Dr. C. Estournes team and, especially G. Chevalier and Dr. R. Epherre. The equipment is a Dr Sinter 2080 manufactured by the society SPS Syntex Inc. which can deliver a pulsed current of 8000 A with a voltage of 15 V and can apply a pressure up to the GPa.

II.3.1.2 Ceramic characterization

Similarly to the powder characterization, XRD is the first analysis to be performed on the ceramic in order to see if there are any variations in terms of purity, composition and grain size resulting from the sintering. Then, it is also necessary to determine the ceramics density, using a pycnometer. Dielectric measurements and microstructural studies using scanning electron microscopy (SEM) are then performed.

II.3.1.2.1 Dielectric measurements

The measurements were carried out with an automatic Wayne-Kerr 6425 impedance bench developed at ICMCB in a frequency range from 100 Hz to 200 kHz. Gold electrodes are deposited on two parallel faces of the ceramic and the real and imaginary contributions of the permittivity; Ɛ' and Ɛ", are respectively determined from the measured values of capacitance (C) and losses (tan δ) from equations (20) and (21):

$$\varepsilon' = \frac{C.e}{\varepsilon_0.S} \tag{20}$$

$$\varepsilon'' = \varepsilon'.tan\,\delta \tag{21}$$

Where ε_0 is the vacuum permittivity (ε_0 = 8.854187.10^{-12} F.m^{-1}), S is the surface of the electrodes (in m^2), e the thickness of the dielectric material (in m). The contribution from the measurement apparatus is removed through its calibration in open circuit.

The first step is the deposit of thin layer of gold on the ceramic, using physical vapor deposition, to make the electrodes. Then we used the setup described in Figure II-8.

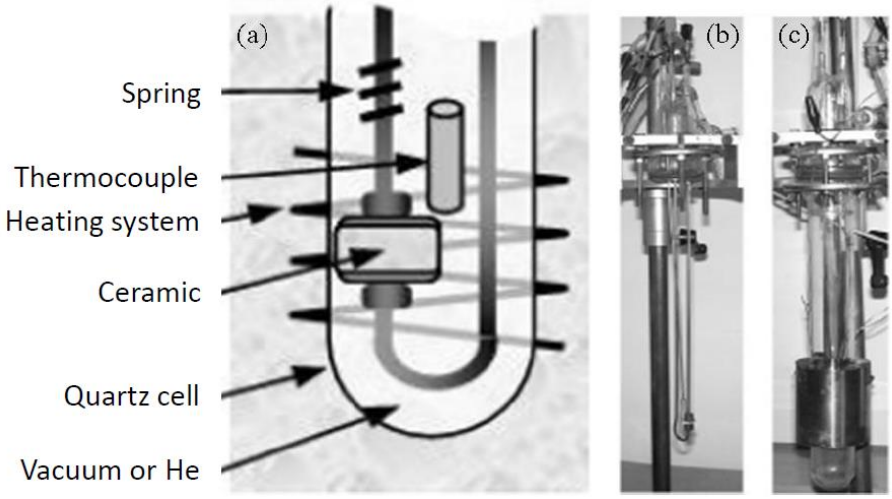

Figure II-8. a) sketch of the dielectric measurement cell, b) image of the open cell and c) image of the closed cell.

After the calibration the ceramic is placed between the two nickel electrodes in a quartz cell to control the atmosphere during the measurements. It can either be vacuum or helium, which is more conductive, enabling to start the measurements from a lower temperature (≈ 100 K). The sample is preliminary heated up to 150°C to evaporate, and absorbed with a nitrogen trap, any traces of water which can parasite the measurements. The cell is then cooled down putting it into a liquid nitrogen bath and progressively heated up using a tubular oven mounted on it, with a heating rate of 1°C.min^{-1}. The measurements are performed for different frequencies while the sample is heated.

For this work, the characterization setup was mainly operated by M. Albino and J. Macaigne at ICMCB.

II.3.1.2.2 Microstructure analysis with scanning electron microscopy (SEM)

There were four apparatus accessible: (1) a JEOL 6360A at ICMCB with an accelerating voltage from 0.5 to 30 kV and a magnification up to 30000 operated by M. Albino, (2) a JEOL JSM 6700F which is a high resolution one with an accelerating voltage from 0.5 to 30 kV and magnification up to 650000 at PLACAMAT and operated by S. Buffière, (3) another JEOL JSM 6700F operated by A. Weibel and A. Peigney at the Toulouse center of micro characterization(UMS Raimond Castaing) and (4) a JEOL JSM

7800F Prime which is a high resolution one with an accelerating voltage from 1 to 30 kV and magnification up to 1000000 6700F operated by A. Weibel and A. Peigney at the Toulouse center of micro characterization(UMS Raimond Castaing).

This technique, based on the interaction between the electrons from the microscope beam and the sample enables to observe the microstructure and homogeneity of ceramics in terms of grains size, composition and porosity. This is possible through different types of electron – material interactions:

- Secondary electrons providing information concerning the material morphology.

- Backscattered electrons, giving a chemical contrast which enables to observe the ceramics homogeneity in term of composition. Indeed, the lighter elements providing less backscattered electrons, appear darker.

- Photon X, with characteristic energies for each element, enables also to see the homogeneity within the ceramic. This analysis is known as energy dispersive spectrometry (EDS).

II.3.2 Nanocomposites

For this part of the study, the processing and characterization of the composites were performed in collaboration with Dr. I. Bord-Majek and M. Wade at the institute of Integration Materials to System in Bordeaux (IMS - CNRS) and with Prof. R. Jakoby, Dr. Yuliang Zheng and L. Donghang at TU Darmstadt in the Institute for Microelectronic and Photonic (Germany).

II.3.2.1 Strategy

This part is a preliminary work in order to develop a method to easily characterize the ferroelectric properties of the produced nanocomposites. Unlike ceramics, making coplanar capacitors with the composites may not be the best strategy. Indeed, the electrodes cannot be deposited using the sputtering methods because the temperature during the process tends to melt the polymer making inhomogeneous electrodes. The idea is thus to deposit the composite on the electrodes before stacking them. However, with such method, two main issues appear; (1) the control of the nanocomposite thickness and (2) we often traps air bubbles at the interfaces. To overcome these problems we chose to work on inter digital capacitors (IDC) structures. In this case, the two electrodes being on the same substrate, we deposit the composite on top of them using screen printing enabling a deposit with a controlled thickness and without any air bubbles. Nevertheless, we obtain with this type of structure, results which are a combination of the material and substrate contributions. It is thus necessary to use a substrate with the lowest dielectric contribution possible

and the best candidate is glass (Ɛ ≈ 3). It was compulsory to first measure the structure alone before making the deposit.

II.3.2.2 Composite processing

At this step of the study, the elaboration process of the composite is very simple. It consists in mixing together a known amount of powder with a polymer and use ultrasounds during 30 minutes to get a homogeneous dispersion.

II.3.2.3 Composite characterization

A thin layer of metal, such as gold, is deposited on a substrate using physical vapor deposition and patterned with the photolithography process to make the IDC structure. Then, using a mask, the composite is deposited on the IDC structures using screen printing. The mask has a thickness of 50 µm patterned to leave an open space to make the deposit on the IDC structure while protecting an access to the electrodes for the measurements.

Once the capacitor is made we can then perform room temperature measurements scanning both, the voltage and the frequency up to 100 GHz (Figure II-9). The experiment is carried out at TU Darmstadt in the research group of R. Jakoby by Y. Zheng and D. Lu.

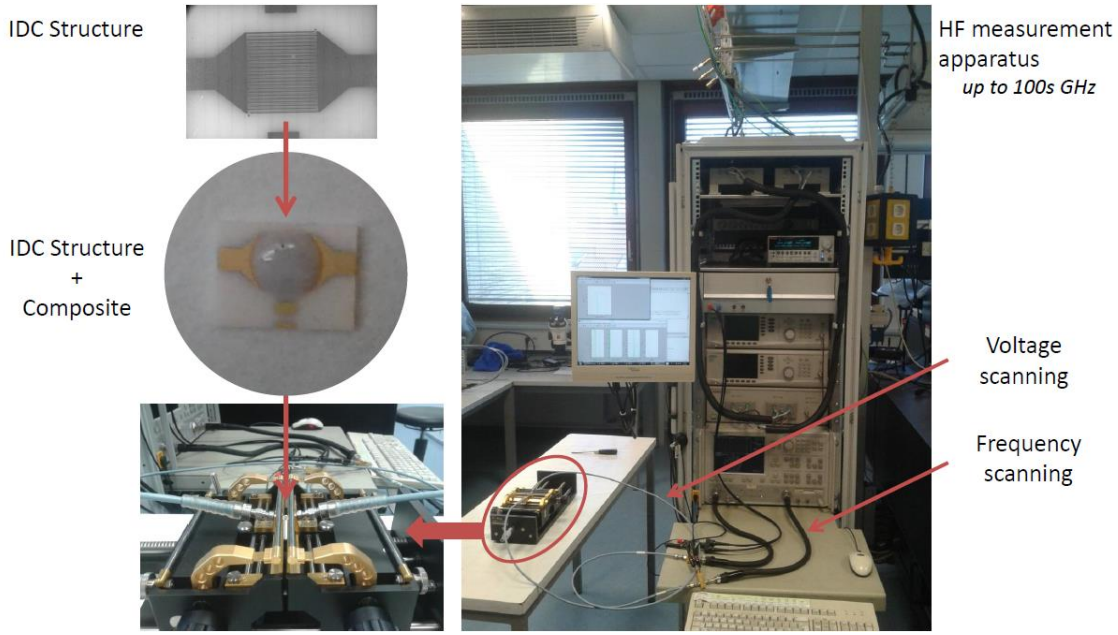

Figure II-9. Illustration of the high frequency (HF) apparatus to measure the composites using a IDC structure.

In this case the IDC structure is in gold and the substrate in alumina and not glass. In addition, the composite is only dropped on the structure we thus do not control the layer thickness.

With such capacitor configuration, it can be difficult to extract precisely the exact value of the composite dielectric constant knowing that the measurement gives a combination of both: the substrate and the composite. It is thus necessary to use substrates with the lowest dielectric properties like the glass.

II.3.3 Conclusion

Having access to both type of sintering, conventional and fast, enables us to perform a wide and complete study of the produced powders. On one side, using the conventional sintering we can prove the accuracy of the synthesis comparing the dielectric properties of the ceramics to the bulk ones from the literature. On the other hand, we can use fast sintering to produce nanostructured ceramics keeping the starting grain size. After checking the microstructure with HRSEM we can study the effect of grains size and, ceramic density and homogeneity on the dielectric properties.

Thanks to this fast sintering technology, it is then possible to move towards the development of hybrids nanocomposites since we know the starting value of the permittivity brought by the nanoparticles. The process presented for characterizing the nanocomposite properties is a method enabling a first and reliable analysis of the different types of composites we can make. It is thus easy to rank them according to their performances and determine which ones are the best before going to the integration step.

II.4 Conclusion of Chapter II

Putting together all these methods we can achieve a deep study of both, nanopowders and ceramics. Using different analyses such as XRD, FTIR, Raman, TEM, XPS we can do a complete study of the materials characteristics in terms of size, size distribution, morphology, purity, crystallinity, defects and surface properties. This also gives us information concerning the internal strain due to the size effect. Combining both, these results with *in situ* WAXS synchrotron analyses which enable to follow in real time the particles formation, we can then get a good understanding of the nanomaterials formation mechanisms in supercritical fluid conditions.

Once this step is achieved we can then move towards the nanopowder processing as a ceramic. This enables to either characterize the bulk properties of the materials using conventional sintering or to study the intrinsic properties of the materials at the nanoscale using fast sintering. We can then achieve a preliminary study on composites made with the produced particles. To do that we chose to use the IDC structure instead of the coplanar one which was the one used for the ceramics characterizations. With this structure it is more difficult to get a precise value of the composite properties as we also measure the substrate. However, using every time the same design we can then easily rank the different types of composites.

Chapter III. Barium titanate based nanoparticles in supercritical fluids: towards an understanding of formation mechanisms

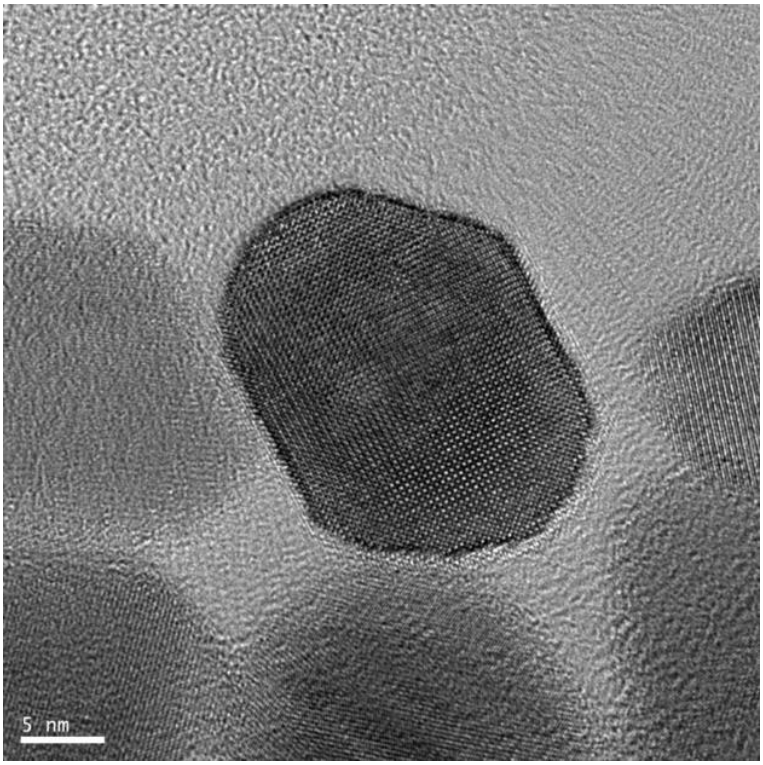

As already discussed in chapter I, at the nanoscale, it becomes essential to identify, understand and control the correlation between the material characteristics and their ferroelectric properties. That is why, in the following chapter, we are first going to investigate the synthesis part with two main objectives:

- Based on previous researches achieved in our group concerning $BaTiO_3$ and BST syntheses in supercritical fluids [159,189,190,209,215] we are going to study their formation mechanisms coupling *ex situ* characterizations such as XRD, FTIRD, Raman and TEM with *in situ* synchrotron wide angle X-ray scattering (WAXS) analyses.

- Then we are going to extend this study towards the synthesis of the entire solid solution from $BaTiO_3$ to $BaZrO_3$. In this case it is the site B which is impacted by the substitution of the titanium cation with the zirconium one, which is bigger and more refractory. That is why using conventional syntheses routes it is difficult to replace more than 40 % of titanium with it. Nevertheless, we were the first to demonstrate the synthesis of the entire solid solution using the supercritical fluid technology.

III.1 Synthesis of $BaTiO_3$ nanoparticles

III.1.1 Experimental conditions

III.1.1.1 Materials

The choice of solvent and metal precursors is of critical importance. Based on the knowledge developed in our group we chose to operate with alkoxides and more precisely isopropoxides: $M^{n+}[O\text{-}iC_3H_7]_n$ where M = Ba^{2+}, Sr^{2+}, Ti^{4+} or Zr^{4+}.

From this choice of precursor results the type of solvents. It is well known that isopropoxides are reactive with water to undergo a sol-gel reaction; we must consequently prepare the precursors solutions in anhydrous alcohols. However, some water will have to be added at some point of the process to initiate the sol-gel reaction. This leads to the choice alcohol / water mixtures as solvent for the reaction, in particular the ethanol / water one. Moreover, it was shown that adjusting the molar ratio between ethanol and water enables to optimize the crystallinity of the synthesized nanoparticles. This adjusted ratio was $x_{ethanol}$ = 0.29 presenting a supercritical point at T_C= 305°C and 13 ≤ P_C≤ 17 MPa, than the one of pure water (Tc= 374◦C and Pc= 22.1 MPa) [173].

III.1.1.2 Method

III.1.1.2.1 Preparation of the precursors solution

Because of their water sensitivity, the alkoxides precursors are stored in a glove box. The precursors are weighted following a barium to titanium molar ratio of 1 and the concentration of the Ti^{4+} (or Ba^{2+}) in anhydrous ethanol can be varied at will. However, taking into account the processability, an optimized concentration in barium and titanium of 3.10^{-2} $mol.L^{-1}$ was chosen. The solution is stirred in a hermetically closed bottle for at least 30 minutes prior to the injection. This procedure is compulsory to avoid any contamination of the precursor or the initiation of the sol-gel reaction which would be incompatible with the injection system.

III.1.1.2.2 Experimental conditions

Two injection lines are necessary: one for the precursor solubilized in ethanol and the other for water. The water line was preheated at 150°C before being mixed with the precursor solution to faster the heating rate inside the reactor. However the precursor line was kept at room temperature to avoid side reactions. The temperature and pressure within the 24 m tubular reactor were respectively set at 400°C and 23 MPa. The flow rate of both injection lines was 6 $g.min^{-1}$ enabling to have a turbulent flow (Re > 3000) of a solvent mixture with $x_{ethanol}$ = 0.29 inside the reactor in order to synthesize fully crystallized nanoparticles (see section I.5.2) with a narrow size distribution (section II.1.2.3).

It is important to note that based on these flow rates, the concentration in precursor inside the reactor drops to approximately $1.3.10^{-2}$ $mol.L^{-1}$.

As we can see inFigure III-1, with an overall flow rate of 12 $g.min^{-1}$, experimentally, the temperature profile within the reactor first increased from 150 to 400 °C along the first six meters of the reactor and then stayed at 400 °C for the remaining 18 meters.

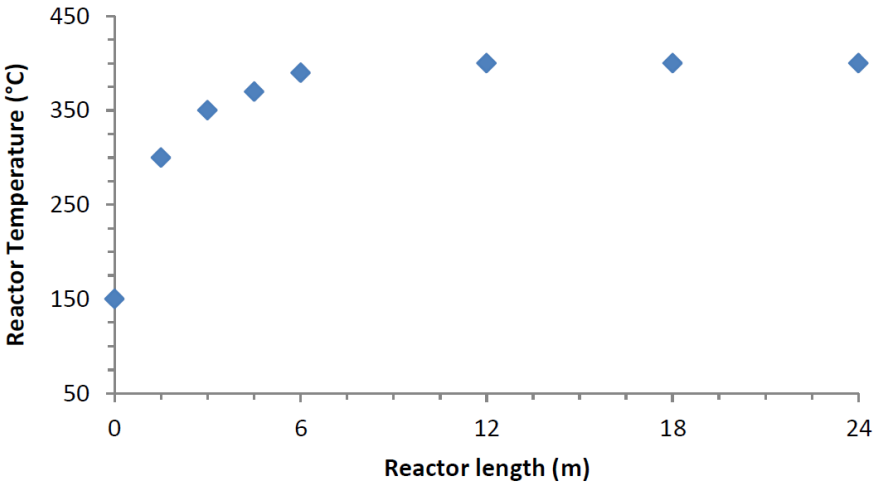

Figure III-1. Temperature profile within the reactor in our operating conditions

From this we were able to calculate, using the NIST software *Refprop*, the densities of the solvent for each temperature range and so the corresponding residence time with the equation (10) developed in section II.1.2.3.

Based on this, the overall residence time of the particles was estimated to be 53 seconds. In addition, using the viscosity values calculated with *AspenTech* software, we could estimate the variation of the Reynolds number. We can see that the flow type model is laminar in the first 1.5 m of the reactor, then it is intermediate (between 1.5 and 3 m) and finally it is turbulent from 3 m up to the outlet of the reactor.

Table III-1. Variation of solvent density across the reactor length with the corresponding residence time.

Reactor section (m)	Length (m)	Average temperature	Density ($kg.m^{-3}$)	Viscosity (Pa.s)	Reynolds number	Residence time (s)
0 – 1.5	1.5	230	719	$1.039.10^{-4}$	1561	10.4
1.5 – 3	1.5	330	483	$6.075.10^{-5}$	2670	7.0
3 – 4.5	1.5	360	253	$3.567.10^{-5}$	4548	3.7
4.5 – 6	1.5	380	194	$3.311.10^{-5}$	4899	2.8
6 -24	18	400	167	$3.311.10^{-5}$	4899	29.1
TOTAL	**24**	**/**	**/**	**/**	**/**	**53**

The powders are recovered directly in solution after the back pressure regulator and filtered, washed with ethanol and dried at room temperature before characterization. With such experimental conditions we are able to produce around 2 to 3 $g.h^{-1}$ of powder.

III.1.2 $BaTiO_3$ nanoparticle characterizations

Once the particles are synthesized we can then characterize their purity, crystallinity, defects and surface properties with the use of different analyses such as XRD, HRTEM, Raman and FTIR. In addition, combining these analyses with *in situ* synchrotron WAXS we can improve our understanding of the formation mechanism occurring in the supercritical reactor.

III.1.2.1 $BaTiO_3$ nanopowder characteristics

Figure III-2 presents the XRD pattern of the synthesized $BaTiO_3$ powder acquired with the monochromatic diffractometer apparatus. First of all, there are no extra peaks in the pattern confirming the synthesis of pure $BaTiO_3$. However, there is no splitting of the (002) / (200) peak at $2\Theta \approx 45°$ which tends to indicate a cubic structure. This is usually observed for $BaTiO_3$ nanoparticles where the size effect is generally considered as responsible for the loss of tetragonality. This last point will be discussed later in the study.

To have a better insight concerning the material purity FTIR analysis of the $BaTiO_3$ nanoparticles was performed (Figure III-3). First, we observe the presence of the $BaTiO_3$ fingerprint through the existence of two bands between 400 and 800 cm^{-1}. With this analysis we can also observe the presence of organics pollutions at the surface of our particles based on the presence of bands between 1000 – 1200 and 2800 – 3000 cm^{-1}. The organics traces result from the alkoxide precursors presenting a carbon skeleton which is partially deposit at the surface of the particles during the synthesis.

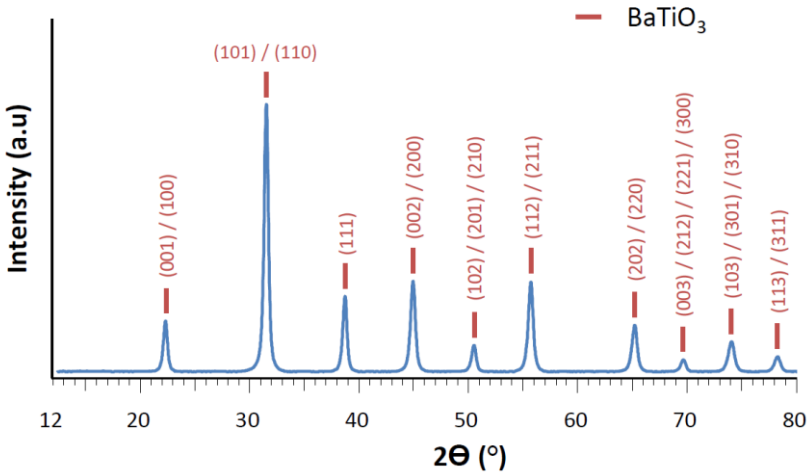

Figure III-2. XRD pattern of a typical $BaTiO_3$ powder synthesized in our supercritical conditions.

Moreover a band around 1440 cm^{-1} can be either attributed to a slight $BaCO_3$ pollution or to some organic pollution [96,117,155,159,216]. Finally the analysis probes the presence of –OH defects

which can be divided into two categories; (1) surface –OH defects with two narrow bands at 1350 and 1590 cm^{-1} and a wide band from 2600 to 3700 cm^{-1} and (2) structural –OH defects with two narrow bands at 1630 and 3520 cm^{-1}. It is not surprising to find these kinds of defects which are characteristic of the wet synthesis routes [99,124–126,128,133,137–142].

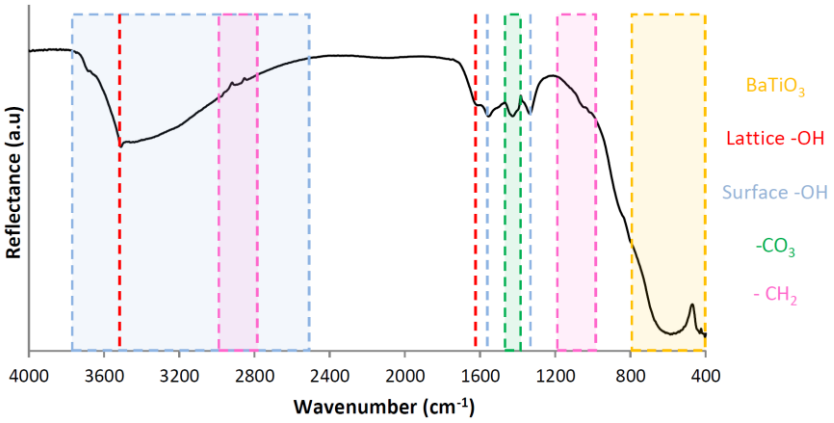

Figure III-3. FTIR spectrum of the $BaTiO_3$ powder synthesized in our supercritical conditions.

The HRTEM images Figure III-4a show that the produced $BaTiO_3$ nanoparticles are more or less spherical. The average size of the particles was estimated as being around 20 ± 6nm measuring over more than 150 particles on different TEM images (Figure III-4c). Finally, based on the HRTEM image Figure III-4b showing the presence of lattice fringe along the entire particles, we confirm taht the produced nanoparticles can be considered as monocrystalline.

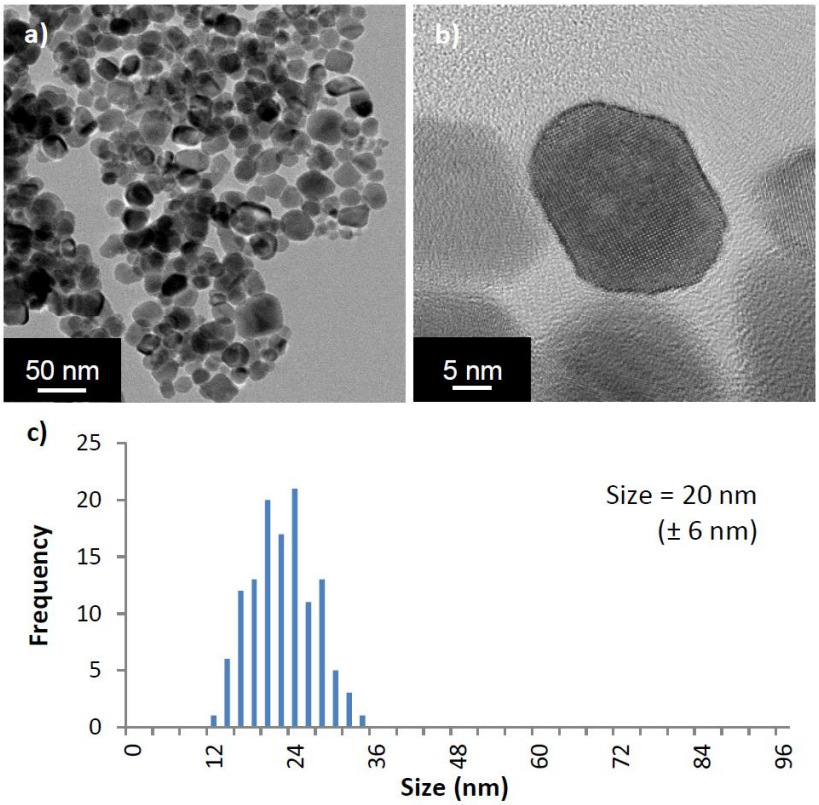

Figure III-4. a) and b) HRTEM images of the $BaTiO_3$ powder, c) average size and size distribution measured from TEM images.

Based on these analyses the $BaTiO_3$ particles can be considered as quasi pure with an average size of 20 ± 6 nm. However, complementary analyses are necessary to investigate the particles crystallinity and determine if, at this scale, the phase is cubic or pseudo cubic.

III.1.2.2 $BaTiO_3$ crystallite size

Figure III-5 presents a profile refinement, using the *FullProf Suite*, of a typical XRD pattern acquired on $BaTiO_3$ nanopowder and Table III-2 summarizes the results.

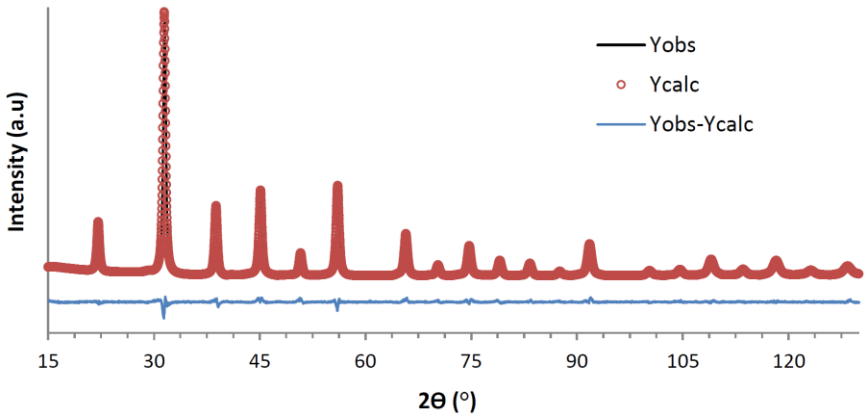

Figure III-5. *FullProf* profile refinement of the $BaTiO_3$ XRD pattern.

Even if the $BaTiO_3$ crystal structure appears to be cubic, knowing that the bulk $BaTiO_3$ is tetragonal at room temperature and, as mentioned in I.2.2.2, the literature being contradictory concerning the size effect on the material structure, especially concerning the size at which the nanoparticles lose their tetragonality, we decided to use the P4mm space group to describe the crystalline structure. In this case the lattice parameter c has a degree of freedom compared to the a and b parameters which must remain equals. A good match is observed between the XRD pattern in red and its fit in black. This confirms both, a high quality material and an accurate profile refinement.

Table III-2. Results obtained from the $BaTiO_3$ XRD pattern refinement compared with lattice parameters of the bulk $BaTiO_3$ from the (ICSD database reference 27974).

Parameters	Values	Uncertainties	Bulk $BaTiO_3$
Cell parameter (Å)	a = b = 4.0080	0.0001	a = b = 3.9923
	c = 4.0236	0.0001	c = 4.0349
	c / a = 1.0039	-	c / a = 1.0107
Scale factor	$1.0243.10^{-2}$	$3.5.10^{-5}$	-
Y	0.22708	0.00281	-
I_G	0.08715	0.00096	-
Overall B_{iso} (Å^2)	0.27176	0.01539	-
Bragg R-factor	2.39	-	-
Rf -factor	0.849	-	-
Chi2	2.71	-	-

Using the Y, σ_Y, I_G and σ_{IG} values in Table III-2 and the Scherrer equations developed in the section II.2.1.3, the crystallite size was estimated as being 19 nm with an error below the nanometer which is in very good agreement with the average size of 20 nm measured on the HRTEM images (Figure III-4 b).

Based on these results, it is possible to confirm that the particles are monocrystalline. However, the structure of the particles, which is dependent of the synthesis route used, remains unclear.

III.1.2.3 Study of the $BaTiO_3$ crystalline structure

III.1.2.3.1 Lattice distortion

On one hand, based on the *FullProf* profile refinement of the $BaTiO_3$ powder (Figure III-5 and Table III-2), the cell parameters were calculated as being a = b = 4.0084 Å and c = 4.0228 Å giving c/a ≈ 1.0039. On the other hand, If we look at the lattice parameter values of the bulk $BaTiO_3$ (ICSD database reference 27974), a = b = 3.9923 Å and c = 4.0349 Å giving c/a ≈ 1.0107. The decrease of c/a from 1.0107 to 1.0039 clearly confirms a loss of tetragonality. Indeed there is a broadening of the a and b parameters and a shrinkage of the c one. Smith and al. [89] studied this trend analyzing the c/a ratios variation for three different sizes of particles: 26, 45 and 75 also measured on TEM

images. Figure III-6 presents the corresponding c/a ratio evolution with $BaTiO_3$ nanoparticles size which is reported in green with in addition the case of our study in orange. This trend is confirmed, suggesting a loss of tetragonality decreasing the particles' size as mentioned in the literature and leading to the notion of pseudo cubic structure (see section I.2.2.2).

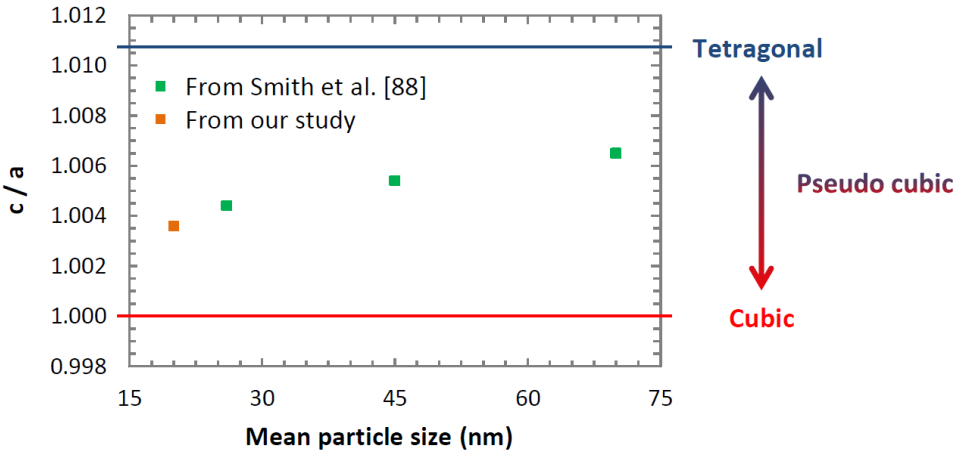

Figure III-6. c/a ratio evolution as a function of the $BaTiO_3$ particles size.

As already discussed in section II.2.3.1, contrary to the XRD analysis which represents an average response, the Raman technique enables a local analysis. It is a very sensitive method suitable to characterize crystal structures, especially to observe non centrosymmetric local structure in apparent an apparent pseudo-cubic nanopowders.

The Raman analysis of our $BaTiO_3$ nanoparticles is presented in Figure III-7. It exhibits the active modes at ≈ 305, 520 and 720 cm^{-1} characteristic of the tetragonal phase among other active modes at: 180, 270, 480 and 810 cm^{-1}. This is in agreement with other studies where the same active modes were identified [217–219]. Nevertheless, we do not observe the active mode around 1080 cm^{-1} characteristic of the $BaCO_3$ presence, identified with the FTIR analysis in Figure III-3.

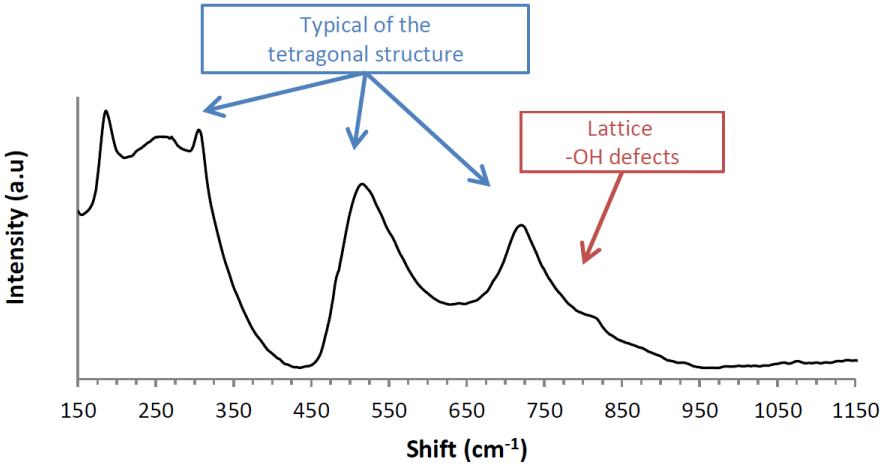

Figure III-7. Raman analysis of the $BaTiO_3$ powder exhibiting the existence of a tetragonal phase at room temperature.

As reported by Smith et al. [89], a part of the other active modes (180, 270 and 480 cm^{-1}) can be attributed to some disorder associated with the Ti off-centering. This off centering is associated to a high surface strain applied within the structure for particles at this size range. The disorder is illustrated Figure III-8 with the use of dark and bright field transmission electron microscopy (TEM) images [100]. There, the variations of contrast across a single particle corresponds to a variation of strain within it.

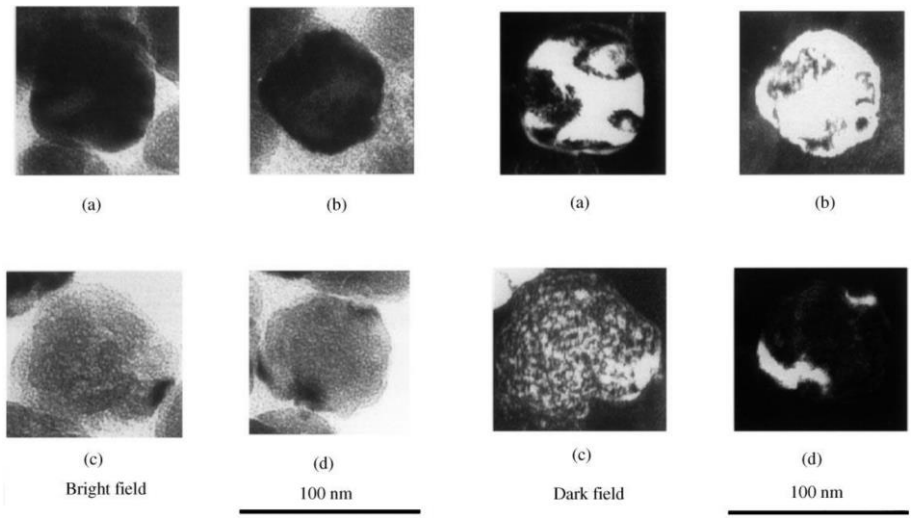

Figure III-8. TEM bright and dark field images of four individual $BaTiO_3$ nanocrystals with different contrasts: (a) nearly half-bright color and half-dark color contrast; (b) bright color dominant contrast; (c) equal bright-dark color contrast with nearly homogeneous distribution; and (d) dark color dominant contrast [100] Copyright © 2000, Elsevier.

Combining XRD with Raman analyses enables to demonstrate a coexistence of the cubic and tetragonal phases at the nanoscale. Subsequently, a core shell model was developed to present how these two phases are organized inside the particles.

From the literature, we know that the identified strain within nanoparticles of such size leads to changes in the domains structure, which is going to reduce the displacement ability of the titanium inside the cell [89–91]. This is a critical parameter concerning the intrinsic properties of the material since it will block the phase transitions and decrease the ferroelectric properties. Moreover, using FTIR (Figure III-3) and Raman (Figure III-7) analyses we pointed out the presence of –OH defects in our nanoparticles which are characteristic of wet synthesis routes such as sol-gel [220–222], hydrothermal [3,4,93,100,101,223] or supercritical [156–159,189] processes. They are reported as leading to the creation of barium vacancies at the surface of the particles in order to maintain the electroneutrality of the structure [94,95] which stabilize a cubic phase at the surface of the particles [96]. These observations tend to confirm the hypothesis of a core-shell model, where the core of the particle is tetragonal, surrounded with a cubic shell, also called “dead layer” (see the section I.2.2.2) [2,92,93]. Nevertheless, one question is remaining concerning the thickness of this dead layer. Indeed, since it depends on the vacancies, it also depends on the synthesis route. Moreover, we can find some extensions of this theory, in particular the notion of a lattice strain layer gradient leading to double layer configuration. In this case, the core of the particles is tetragonal and the external is shell cubic, with in between a gradient of lattice strain layer (GLSL) presenting a gradient of tetragonality [97,98].

The next step is then to achieve a deeper study in order to understand what are the key parameters governing the $BaTiO_3$ nanoparticles nucleation and growth in supercritical fluids.

III.1.3 Study of $BaTiO_3$ nanoparticles formation in supercritical fluid conditions

Working in collaboration with Prof. B. Iversen from Aarhus University (Denmark) and using the setup they developed (see section II.2.1.2) [214], we were able to achieve some *in situ* synchrotron WAXS analyses under high pressure and temperature conditions to observe how the particles grow during the supercritical synthesis.

III.1.3.1 Materials and method

Similarly to the section III.1.1, we used barium and titanium isopropoxides precursors and the reaction was carried out in an ethanol / water mixture ($x_{ethanol}$ = 0.29).

The parameters analyzed in this study were the synthesis temperature and precursor concentration effects on the growth behavior of the $BaTiO_3$ nanoparticles (Table III-3).

Table III-3. Experimental conditions for *in situ* synchrotron WAXS analysis of the $BaTiO_3$ synthesis.

Experiment n°	T (°C)	C (mol.L^{-1})	P (MPa)	Composition	Synthesis duration (min)
1	400	0.2	23	$BaTiO_3$	> 20
2	150	0.2			
3	400	0.04			
4	400	0.5			

III.1.3.2 Data integration

The first step of the data treatment is to integrate the raw 2D frames into 1D data using *Fit2D* [224]. As shown in Figure III-9a the data integration begins with the summation of all the powder diffraction patterns acquired during the experiment, in this case at least 250 frames (one frame being acquired every five seconds). Comparing with Figure III-9b we can see the diffraction circles of the $BaTiO_3$ nanoparticles formed during the synthesis, where the darker circles are the most intense ones, fit with the $BaTiO_3$ powder XRD pattern achieved in section III.1.2.1 (Figure III-2). This confirms the suitability of the protocol for the *in situ* study.

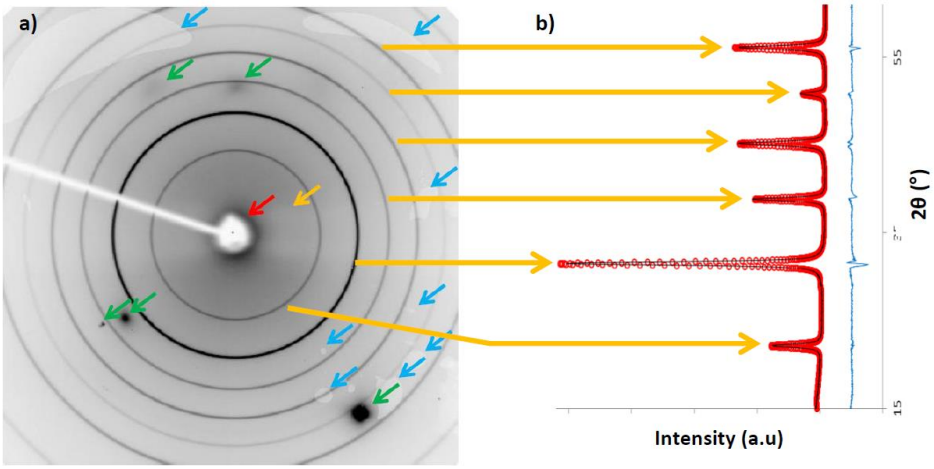

Figure III-9. a) Summation of the first 250 frames acquired in the case of $BaTiO_3$ synthesis at 400°C and 23 MPa (see experiment n°1 Table III-3) exhibiting extra shape classified with colored arrows. b) $BaTiO_3$ powder XRD pattern achieved in section III.1.2.1 (Figure III-2).

In addition some other shapes, which are not related to the $BaTiO_3$ diffraction pattern, appear and are marked with arrows of different colors:

- The red arrow is associated to the beam stop of the setup protecting the detector from the synchrotron beam center.
- The orange arrow shows the “shadow” from the sapphire capillary where the reaction is carried out.
- The green arrows are diffraction spots from the single crystalline sapphire capillary.
- The blue arrows are related to some extra “shadows”.

Because they do not belong to the $BaTiO_3$ diffraction pattern it is thus necessary to mask them before processing to the raw 2D frames integration into 1D data. Prior to the integration it is also necessary to set parameters such as the distance between the capillary and the detector, the coordinate of the synchrotron beam center, the wavelength of the synchrotron beam and the tilt angles which are required for the *Fit2D* data processing [224]. The sample to detector distance was calibrated fitting with an ellipsoid function the diffraction circles of a standard NIST LaB_6 capillary measured in the same position of the sapphire one. The three other parameters (the coordinate of the synchrotron beam center, the wavelength of the beam and the tilt angles) were determined fitting the most intense diffraction circle of the analyzed sample (the second one from the center). Once all these steps are fulfilled, it is then possible to proceed the data integration.

III.1.3.3 Data analysis

The data were then treated with the *FullProf Suite*. The profile refinements employed the 2θ-range from 12 to 38, with the background modeled using linear interpolation between 40 to 70 points with refinable height. The tetragonal cell being almost cubic (see section III.1.2.3) and the combination of the large instrumental broadening with broadness of the peaks from the particle size did not allow to distinguish between cubic and tetragonal space groups we thus chose to use the Pm3m one [225]. The Thompson-Cox-Hasting formulation of the pseudo-Voigt function was applied to describe the peak profiles [226]. Before analyzing the sample broadening, the total peak broadening was corrected from the instrumental contribution. It was determined by peak shape analysis of the diffraction pattern measured on a NIST LaB_6 sample. The particle size (<D>) was calculated with the Scherrer equations (see section II.2.1.3).

III.1.3.4 In situ study of the $BaTiO_3$ synthesis at 400°C and 23 MPa

This experiment corresponds to the n°1 of Table III-3, which mimic the pressure and temperature conditions of the flow reactor. However, the precursor concentration in the ethanol / water mixture (C in $mol.L^{-1}$) for the *in situ* study was higher than for the *ex situ* synthesis (see section III.1.1) in order to have a good scattering data. It is important to note that for the $BaTiO_3$ synthesis with the flow setup at ICMCB, the concentration cannot be as high to avoid clogging problems.

Figure III-10a is a 3D representation showing the superimposition of all the WAXS patterns acquired every five seconds during the experiment n°1 of Table III-3 ($BaTiO_3$: T = 400°C, P = 23MPa and C = 0.2 $mol.L^{-1}$) and Figure III-10b is the 2D representation of four diffraction patterns selected at a given time of the experiment (0, 5, 10 and 1200 seconds) after data integration.

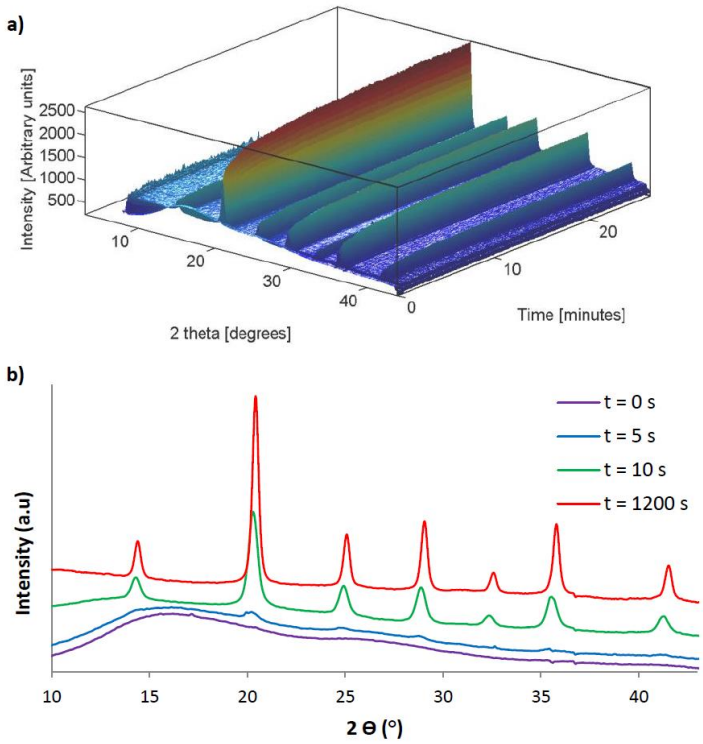

Figure III-10. Data processing in the case of the $BaTiO_3$ synthesis at T = 400°C, P = 23MPa and C = 0.2 $mol.L^{-1}$: a) 3D representation showing the superimposition of all the WAXS patterns, b) 2D representation of 4 WAXS patterns

At t = 0 seconds there are no diffraction pattern showing that the precursors are amorphous. However, after only five seconds, the $BaTiO_3$ diffraction peaks start to appear and after ten seconds the pattern is already well defined. Later in the experiment, after 20 minutes, the intensity of the pattern grew and the peak positions were shifted to higher 2Θ positions.

Figure III-11 highlights two examples of WAXS pattern refinements: after 10 seconds which correspond to the early stage of the $BaTiO_3$ nanoparticles formation (Figure III-11a and b) and after 20 minutes when the $BaTiO_3$ nanoparticles are supposed to be fully grown (Figure III-11c and d).

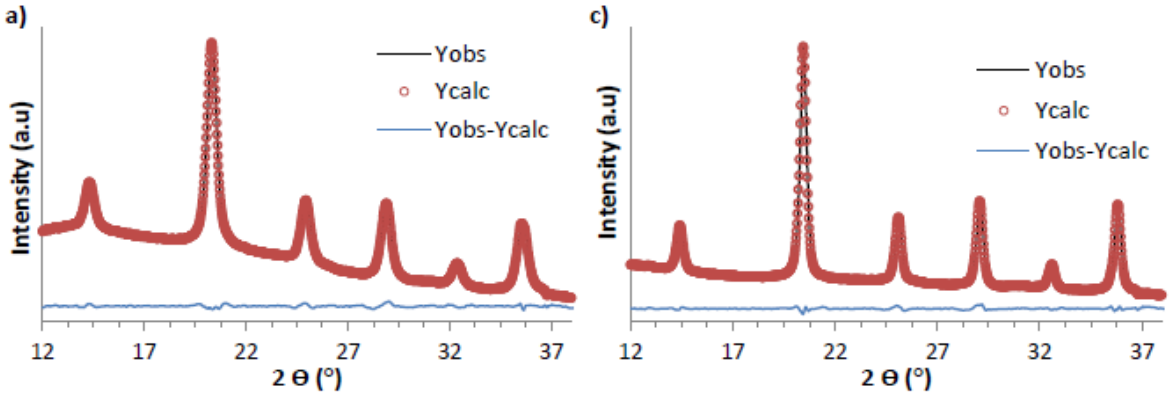

b)

Total number of parameters	46
Number of background	39
Cell parameter (Å)	4.0506
$\sigma_{\text{Cell parameter}}$ (Å)	0.0002
Scale factor	0.00064
$\sigma_{\text{Scale factor}}$	0.00001
Y	0.1601
σ_{Y}	0.0103
I_G	0.1553
σ_{IG}	0.0028
B_{iso} Ti (Å²)	4.02
$\sigma_{\text{Biso Ti}}$ (Å²)	0.10
R_Bragg (%)	0.1

d)

Total number of parameters	46
Number of background	39
Cell parameter (Å)	4.0251
$\sigma_{\text{Cell parameter}}$ (Å)	0.00001
Scale factor	0.00089
$\sigma_{\text{Scale factor}}$	0.00001
Y	0.1514
σ_{Y}	0.0038
I_G	0.0324
σ_{IG}	0.0008
B_{iso} Ti (Å²)	1.93
$\sigma_{\text{Biso Ti}}$ (Å²)	0.06
R_Bragg (%)	0.08

Figure III-11. $BaTiO_3$ a) *FullProf* profile refinement of the WAXS pattern after 10 seconds of analysis, b) corresponding refined parameters, c) *FullProf* profile refinement of the WAXS pattern after 1200 seconds of analysis, d) corresponding refined parameters.

Refining all the WAXS patterns acquired during the experiment enables to follow the variations of parameters such as: the scale factor, the unit cell parameter, the Gaussian and Lorentzian size broadening contributions (directly related to the particles size variation), the Debye-Waller-factors for barium and titanium and the instrumental zero point. Figure III-12 represents the evolution of some of these parameters with time.

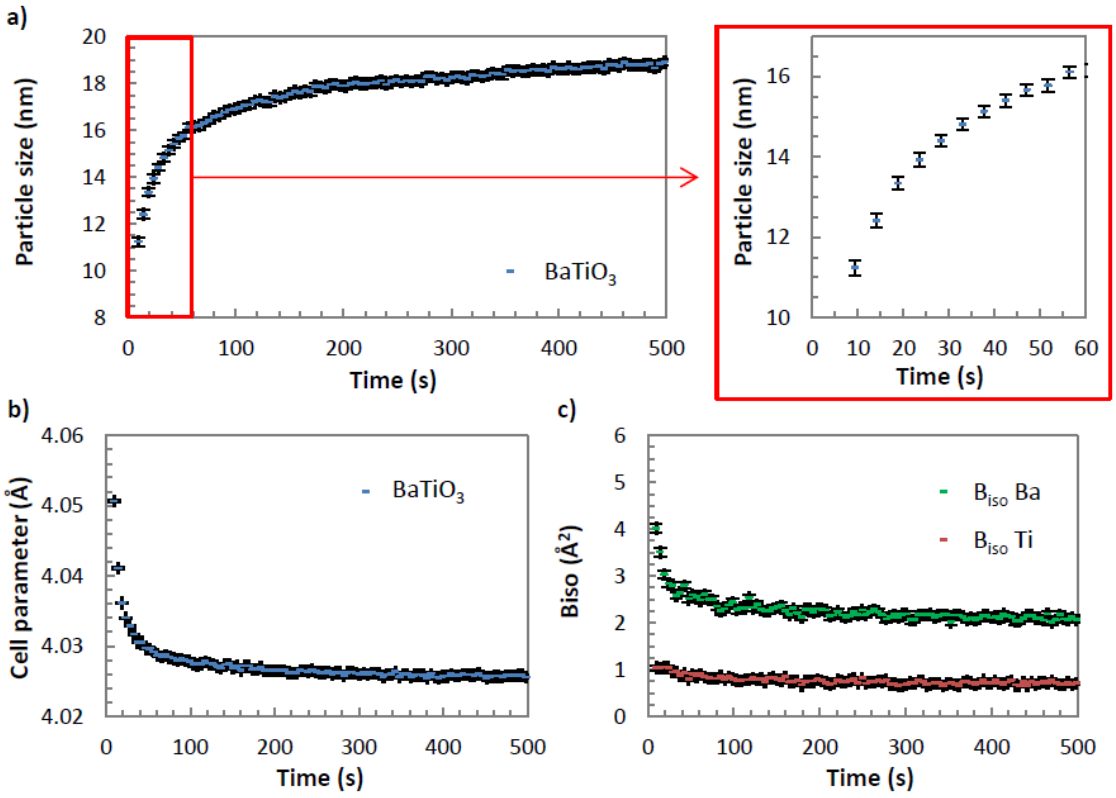

Figure III-12. *In* situ of the $BaTiO_3$ synthesis at 400°C and 23 MPa (experiment n°1 Table III-3): a) $BaTiO_3$ particles growth with time, b) $BaTiO_3$ cell parameter variation with time, c) Debye-Waller factor variation with time [204].

From Figure III-12a we can see that the main growth of the particles happens during the first 1-2 minutes, revealing a fast transformation of the precursor. Then a second growth regime, which is much slower, appears leading to particles with a final size of 19 nm. The zoom on the first 60 seconds demonstrates that, similarly to the *ex situ* crystallite size calculation, the estimated uncertainties remain small, below the nanometer. The secondary growth regime resulted from consumption of the remaining precursor according to Arrhenius law. In the literature different models exist to fit the growth of the particles, for example there is the Lifshitz Slyozov Wagner theory equation (22).

$$D(t) = D_0 + k.(t - t_0)^N \quad (22)$$

Where D_0 is the particle size at time t_0, k is a constant dependent on the microenvironment and N depends on the reaction mechanism. If it close to 1/3 the reaction is supposed to be limited by the diffusion and if it close to ½, the reaction is limited by the surface [227,228]. The problem of such model is that it is based on "classic" chemistry principles. However, in this case, it is well establish that the physical properties of the fluids change drastically making the model uncertain. On this

point, there are still efforts to make in order to develop new and reliable model adapted to these specific conditions. That is why in the case of this study we are just going to roughly determine the particles growth rate making linear regressions on the slopes of the curves. The growth evolution can be fitted with two linear regressions, from 0 to 60 seconds and 120 to 500 seconds, and in both cases the correlation coefficients were above 0.95. At the beginning (first minute), the synthesis is very fast with a growth rate estimated at a value around 8.9 nm/min but subsequently, it decreases down to 0.1 nm/min.

The disorder associated with the Ti off-centering to the size effect highlighted by Smith et al. [89] and observed with the Raman analysis in Figure III-7 was observed in the *in situ* study through the isotropic Debye-Waller factor (B_{iso}) evolution for the titanium atom (Figure III-12c). The titanium B_{iso} values were very high (around 4 $Å^2$) at the earlier stage of the synthesis then decreased rapidly towards a constant value around 2 $Å^2$. However this last value was still high compared to the barium B_{iso} and to the literature which gave values below 1 $Å^2$ for "bulk" $BaTiO_3$ [229–232]. This decrease of B_{iso} value for the titanium can be associated with an ordering of the $BaTiO_3$ nanoparticles structure illustrated in Figure III-12b through the decrease and stabilization of the cell parameter with time. It also explains the shift of the WAXS patterns to higher 2Θ during the synthesis (Figure III-10). Similarly to the crystallite size calculation, the uncertainties remain small, thus, in the following results, the uncertainties won't be plot.

III.1.3.5 Effect of experimental conditions on $BaTiO_3$ growth

Once the mimic of the flow reactor was achieved we studied the effect of other parameters such as the effect of the temperature or the precursor concentration on the $BaTiO_3$ growth (Table III-3 experiments n°2, 3 and 4). The main effect observed of these parameters on the $BaTiO_3$ nanoparticles synthesis was the particles growth behaviors (Figure III-13).

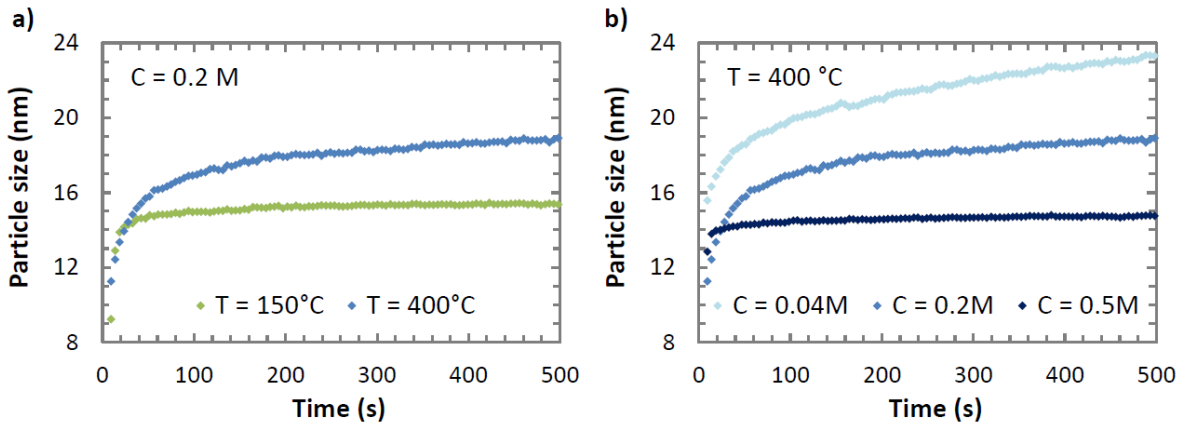

Figure III-13. *In situ* study of the $BaTiO_3$ particles growth with time according to a) the temperature and b) the precursor concentration.

Figure III-13a presents the $BaTiO_3$ nanocrystals growth according to two different temperatures: T = 150 °C leading to subcritical conditions (solvent's supercritical point at T = 305 °C and 13 ≤ P_C ≤ 17 MPa [173]), and T = 400 °C where the solvent is in supercritical conditions. As in the case of supercritical conditions already described, the growth in subcritical conditions is fast and after less than one minute the particles are fully grown. However, in the later cases, the final particle sizes is smaller (14 – 15 nm against 19nm) and the secondary growth regime becomes negligible suggesting that a part of the precursor did not react. Thus, the supercritical fluid conditions tend to favor the particles growth.

In the case of Figure III-13b it is the effect of the precursor concentration on the particles growth which is highlighted. It shows that increasing the precursor concentration from 0.04 to 0.5 $mol.L^{-1}$ tends to lower the growth of the particles. This trend can be explained by the nucleation and growth theory developed by V. LaMer and R. Dinegar [233] and illustrated in Figure III-14 [234]. For the three experiments, the concentration minimum (C_{min}) is reached enabling the $BaTiO_3$ nanoparticle nucleation.

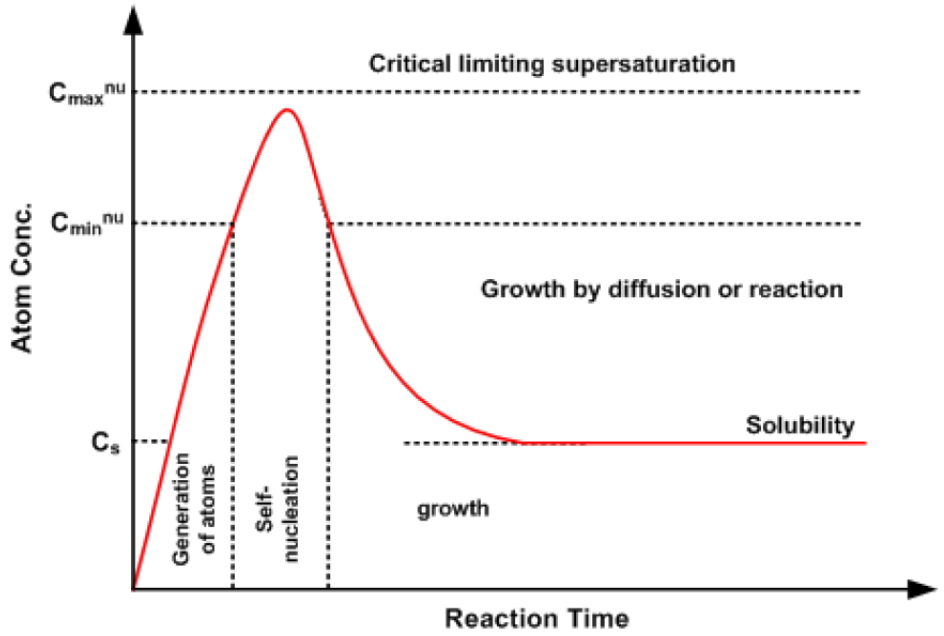

Figure III-14. Nucleation and growth theory [234].

While the nucleation occurs, the precursor concentration decreases, and if the starting concentration was just above C_{min}, the limit will be rapidly crossed back, stopping the nucleation. The particles growth can then take place consuming the remaining precursor, which is what happens for the experiment n°3 of the Table III-3 where the starting concentration is 0.04 mol.L^{-1}. If the starting concentration is increased, the nucleation will be more important, thus, more precursor will be involved in the nucleation mechanism decreasing the amount of remaining precursor contributing to the growth. Consequently the final size of the particles decreases (case of the experiment n°2 of the Table III-3 where the starting concentration is 0.2 mol.L^{-1}). Finally, if the starting concentration is too high, all the precursor will be consumed in the nucleation step leading to burst nucleation (case of the experiment n°4 of the Table III-3 where the starting concentration is 0.5 mol.L^{-1}).

III.1.4 Conclusion

Based on various *ex situ* characterization techniques we were able to demonstrate the synthesis of high quality $BaTiO_3$ nanoparticles using supercritical fluid technology. With XRD, FTIR and TEM analyses we were able to demonstrate the synthesis of pure and more or less spherical nanoparticles of 20 ± 6 nm. Then, combining the *FullProf* profile refinement of the XRD pattern with HR – TEM we could confirm that the particles were indeed monocrystalline. Finally, based on the *FullProf* profile refinement of the XRD pattern and Raman analysis we were able to observe a good

match between our nanoparticles structures and the core shell models developed in the literature and presented in the section I.2.2.2.

Then combining these results with *in situ* WAXS analyses we could get access to real time information concerning the nanoparticles formation in such conditions. We confirmed that the reaction kinetic was very fast, with nanoparticles fully grown in less than two minutes. In addition, we saw through the B_{iso} analysis that the titanium atoms are responsible for the structural disorder which is in agreement with the Raman analysis (Figure III-7) and Smith et al study [89]. We were also able to identify the temperature and concentration in precursor as being a key to control the size of the produced nanoparticles.

The next step of the study is now to extend these results concerning $BaTiO_3$ nanoparticles formation towards two of its solid solutions $Ba_{1-x}Sr_xTiO_3$ (with $0 \leq x \leq 1$ - BST) and $BaTi_{1-y}Zr_yO_3$ (with $0 \leq y \leq 1$).

III.2 Synthesis of $Ba_{1-x}Sr_xTiO_3$ (with $0 \leq x \leq 1$ - BST) nanoparticles

III.2.1 Experimental conditions

The synthesis procedure was identical to the one for $BaTiO_3$ nanoparticle synthesis (see section III.1.1) except that a part of the barium isopropoxide precursor was replaced with strontium isopropoxide. Table III-4 summarizes the different BST compositions which were produced where C is the concentration in $mol.L^{-1}$ of the titanium (or barium + strontium) inside the reactor.

Table III-4. Experimental conditions for $BaTiO_3$ – $SrTiO_3$ solid solution synthesis.

Experiment n°	Composition	Solvent	C ($mol.L^{-1}$)	T (°C)	P (MPa)	Residence time (s)
1	$BaTiO_3$	ethanol/water $x_{ethanol}$ = 0.29	0.013	400	23	53
2	$Ba_{0.8}Sr_{0.2}TiO_3$					
3	$Ba_{0.6}Sr_{0.4}TiO_3$					
4	$Ba_{0.4}Sr_{0.6}TiO_3$					
5	$Ba_{0.2}Sr_{0.8}TiO_3$					
6	$SrTiO_3$					

Changing the ratio between barium and strontium enables us to produce the entire solid solution, from $BaTiO_3$ to $SrTiO_3$.

III.2.2 BST nanoparticles characterization

III.2.2.1 BST solid solution synthesis

Figure III-15 presents the X-ray diffraction patterns normalized to the most intense peak of the synthesized nanoparticles. As expected, increasing the strontium content induces a regular shift of the pattern towards higher 2Θ angles. This is related to the volume variation of the cell, the cationic radius of Sr^{2+} (r_{Sr} = 1.32 Å) being smaller than the Ba^{2+} one (r_{Ba} = 1.49 Å) [67], increasing the amount of strontium induces a lattice parameter shrinkage. Based on Bragg's law ($2d \sin\theta = n\lambda$), the distance between plans decreasing, the 2θ position of the pattern shifts to higher angles.

These X-ray diffraction patterns were refined using the *FullProf* method to calculate their lattice parameters for each composition. As presented in section III.1.2.2, the $BaTiO_3$ structure at room temperature is tetragonal, however, in the case of bulk BST, we know from the literature that it is no longer the case for $x > 0.3$, where the structure becomes cubic at room temperature [74]. Consequently, in the case of $Ba_{0.8}Sr_{0.2}TiO_3$ we also used the P4mm space group to describe the structure but for all the others the chosen space group was Pm3m. That is why the comparisons between each samples are done on the lattice parameter "a".

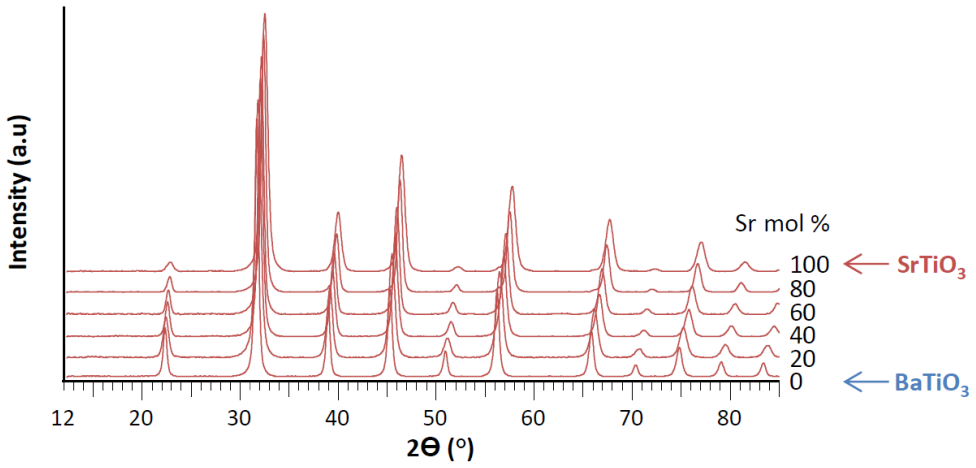

Figure III-15. XRD patterns of the BST solid solution exhibiting a regular shift towards higher 2Θ angles from $BaTiO_3$ to $SrTiO_3$.

Table III-5 summarizes the main parameters obtained from the *FullProf* profile refinement of BST XRD patterns. The Chi2 value being not being greater than 5 we can conclude that the fits are of good quality.

Table III-5. Results obtained from the BST XRD pattern refinement

Parameters	Compositions					
	$BaTiO_3$	$Ba_{0.8}Sr_{0.2}TiO_3$	$Ba_{0.6}Sr_{0.4}TiO_3$	$Ba_{0.4}Sr_{0.6}TiO_3$	$Ba_{0.2}Sr_{0.2}TiO_3$	$SrTiO_3$
Space group	P4mm	P4mm	Pm3m	Pm3m	Pm3m	Pm3m
Cell parameter (Å)	a = 4.0080	a = 3.9883	a = 3.9701	a = 3.9531	a = 3.9277	a = 3.9130
	b = 4.0080	b = 3.9883	b = 3.9701	b = 3.9531	b = 3.9316	b = 3.9130
	c = 4.0236	c = 4.0064	c = 3.9701	c = 3.9531	c = 3.9277	c = 3.9130
$\sigma_{Cell\ parameter}$ (Å)	a = 0.0001	a = 0.0001	a = 0.0001	a = 0.0001	a = 0.0001	a = 0.0001
	b = 0.0001	b = 0.0001	b = 0.0001	b = 0.0001	b = 0.0001	b = 0.0001
	c = 0.0001	c = 0.0002	c = 0.0001	c = 0.0001	c = 0.0001	c = 0.0001
Scale factor	$1.024.10^{-2}$	$1.111.10^{-2}$	$3.956.10^{-2}$	$3.544.10^{-2}$	$6.093.10^{-2}$	$8.743.10^{-2}$
$\sigma_{Scale\ factor}$	4.10^{-5}	3.10^{-5}	12.10^{-5}	12.10^{-5}	18.10^{-5}	19.10^{-5}
Y	0.22708	0.39356	0.32294	0.32560	0.31126	0.41297
σ_Y	0.00281	0.00369	0.00163	0.00182	0.00148	0.00148
I_G	0.08715	0.15647	0.15450	0.12967	0.11423	0.24343
σ_{IG}	0.00096	0.00193	0.00128	0.00142	0.00119	0.00170
Bragg R-factor	2.39	3.83	3.97	2.12	3.38	3.58
Rf -factor	0.849	1.86	2.24	3.87	1.57	1.88
Chi2	2.71	3.06	3.94	4.02	4.16	3.58

From the various profile refinements we can, for example, plot the variation of the calculated lattice parameter “a” according to the amount of barium substituted with strontium (Figure III-16). It shows that the lattice parameter “a” decreases linearly with the increase of strontium content (R^2 = 0.999).

Knowing this and based on Vegard's law it is then possible to confirm the synthesis of the entire solid solution (from $BaTiO_3$ to $SrTiO_3$).

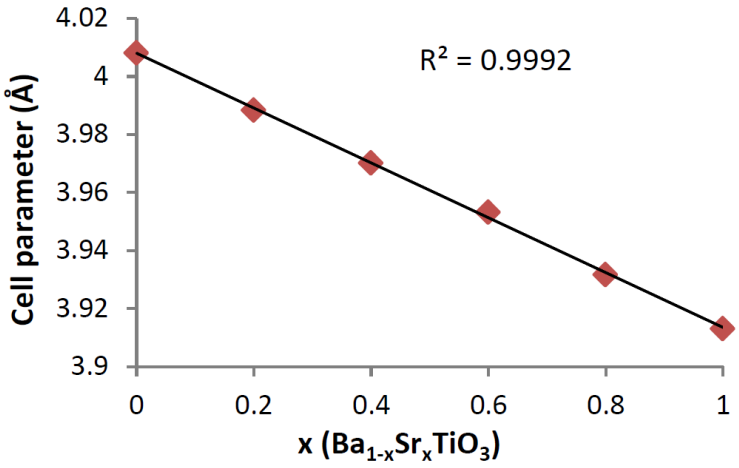

Figure III-16. Linear variation of the lattice parameter from $BaTiO_3$ to $SrTiO_3$ confirming the synthesis of the entire solid solution.

In addition, no extra peaks were observed on the XRD patterns of the Figure III-15 which indicates that the purity of the $BaTiO_3$ based nanoparticles is preserved along the entire solid solution.

III.2.2.2 Evolution of particle size with the composition

The TEM images (Figure III-17) of all the BST particles synthesized according to the conditions of Table III-4 show that in all cases the particles are more or less spherical with a narrow size distribution. Indeed, looking at the corresponding histograms plotted from the particles measurements on TEM images (every time more than 150 particles were measured over different images) we can see that, as soon as some barium is substituted with strontium, the average size and size distribution of the particles decreases from 20 ± 6 nm for $BaTiO_3$ nanoparticles to 12 ± 2 nm for $SrTiO_3$ ones.

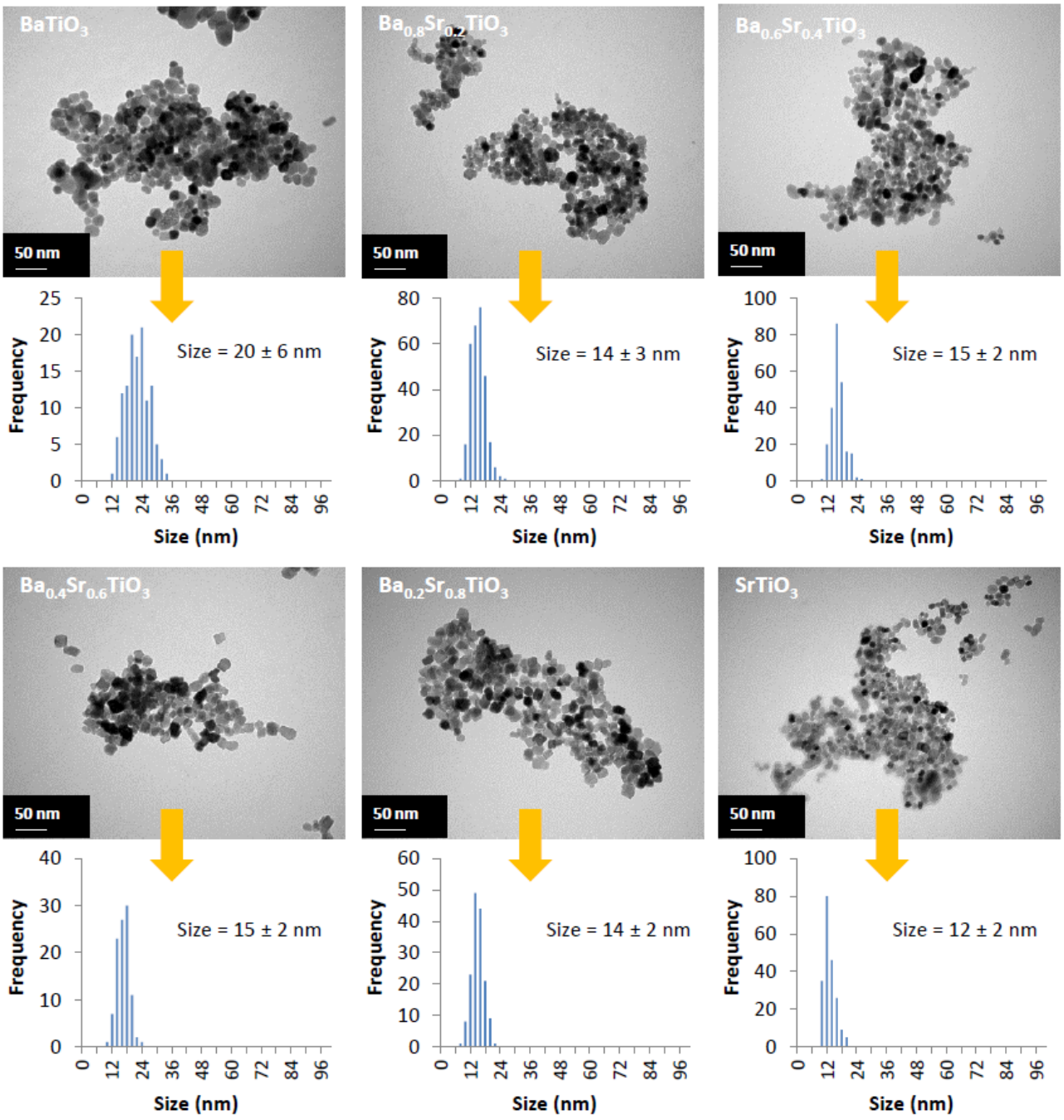

Figure III-17. TEM images of BST nanoparticles synthesize according to the material composition.

Based on the TEM analysis we can conclude that the barium substitution with strontium influences the particles growth. Indeed, since some strontium is added, the particles become smaller, and even though the Sr^{2+} cations are smaller the Ba^{2+} ones (r_{Sr} = 1.32 Å and r_{Ba} = 1.49 Å [67]), this difference is not sufficient to justify this size variation.

III.2.2.3 Crystallite sizes

Table III-6 describes both, the particles size measured from the TEM images and the crystallites size calculated with the *FullProf* profile refinement of the XRD patterns (Figure III-2).

Table III-6. Comparison between the BST particles sizes measured from TEM images and their crystalline size estimated with Scherrer equation using XRD patterns refinements.

Composition	Particles size from TEM (nm)	Crystallite size from XRD (nm)
$BaTiO_3$	20 ± 6	19
$Ba_{0.8}Sr_{0.2}TiO_3$	14 ± 3	13
$Ba_{0.6}Sr_{0.4}TiO_3$	15 ± 2	14
$Ba_{0.4}Sr_{0.6}TiO_3$	15 ± 2	15
$Ba_{0.2}Sr_{0.8}TiO_3$	14 ± 2	16
$SrTiO_3$	12 ± 2	11

If we compare the average size of the particles with the crystallites size, both being close, we can conclude that, similarly to $BaTiO_3$ case, the particles are monocrystalline along the entire solid solution. In addition, the size distribution decreasing, it indicates an improvement of the samples homogeneity.

If we focus on the specific composition of $Ba_{0.6}Sr_{0.4}TiO_3$ (Figure III-18), comparing the average size and size distribution (Figure III-18a and c) to the HRTEM image Figure III-18b shows the presence of lattice fringe along the entire particle which confirms that the produced particles are monocrystalline.

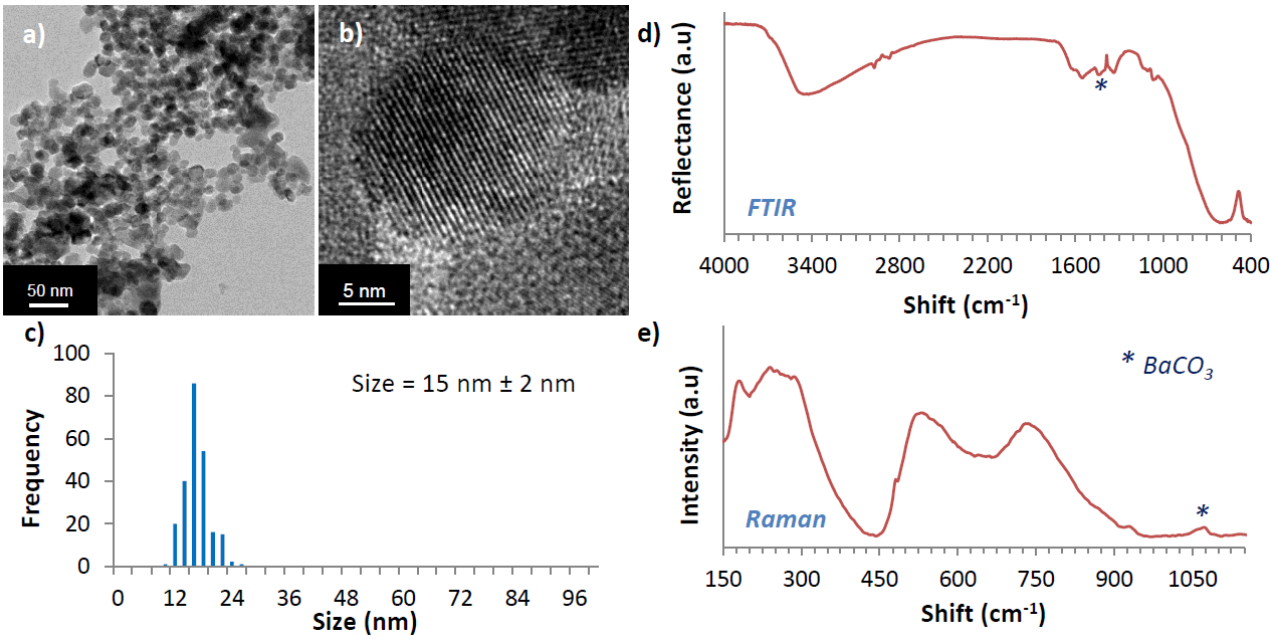

Figure III-18. a) and b) HRTEM images of the $Ba_{0.6}Sr_{0.4}TiO_3$ powder, c) average size and size distribution of $Ba_{0.6}Sr_{0.4}TiO_3$ 15 ± 2 nm measured from TEM images, d) FTIR and e) Raman analyses.

Concerning FTIR and Raman analyses (Figure III-18d and e), the profiles remains similar to the $BaTiO_3$ powder (see section III.1.2). As expected, in the specific case of Raman analysis the intensity of the modes is weaker, especially the one at 307 cm^{-1} which is characteristic to the tetragonal phase. The main difference concerns the $BaCO_3$ contamination. In the case of $BaTiO_3$ study the interpretation was not clear, even if FTIR could presume it, the Raman analysis did not show the corresponding active mode. Nevertheless, in this case there is no longer a doubt concerning this since it is visible on both analyses.

From this we can confirm that the barium substitution with strontium does not impact the material quality in terms crystallinity, but it increases slightly the amount of $BaCO_3$ which is now visible with Raman spectroscopy.

It is important to note that the FTIR analysis appears to be more sensitive that the Raman one towards $BaCo_3$ detection.

III.2.2.4 Conclusion

In this part we showed that using the supercritical fluid technology it was possible to synthesize the entire solid solution from $BaTiO_3$ to $SrTiO_3$ just by adjusting the precursor ratio to target the expected composition. In addition, the quality of the nanoparticles established in the case of $BaTiO_3$ synthesis is almost preserved for all the other compositions. Indeed, there are no extra phases

visible on the XRD patterns and the BST particles are still monocrystalline nevertheless the $BaCO_3$ contamination is slightly higher and can be detected with Raman spectroscopy.

However a size variation was observed between $BaTiO_3$ and BST nanoparticles. That is why, in the following part, we propose to answer to the following question: “Why does the growth change with the substitution of barium with strontium?” and this will be done coupling *ex situ* with *in situ* analyses.

III.2.3 Study of the BST particles size variation according to their composition

To investigate this size variation we focus first on the *in situ* study considering the case of $Ba_{0.6}Sr_{0.4}TiO_3$ nanoparticles growth compared to $BaTiO_3$ ones.

III.2.3.1 In situ analysis

Figure III-19 shows the effect of barium substitution with strontium one on the growth profiles. $BaTiO_3$ growth was compared to the $Ba_{0.6}Sr_{0.4}TiO_3$ one for syntheses achieved at T = 400°C and P = 23 MPa. Similarly to the experiment n°1 of Table III-3, the concentration in precursor was set at 0.2 $mol.L^{-1}$ in an ethanol / water mixture of 0.29. As already discussed, the $BaTiO_3$ particles grow up to 19 nm, but the $Ba_{0.6}Sr_{0.4}TiO_3$ growth was limited at 15 nm. Even if the *in situ* setup differs from the *ex situ* one this confirms the trend observed concerning the size variation comparing $BaTiO_3$ with $Ba_{0.6}Sr_{0.4}TiO_3$ at the beginning of the discussion (20 ± 6 nm for $BaTiO_3$ versus 15 ± 2 nm for $Ba_{0.6}Sr_{0.4}TiO_3$).

However, to give further explanations of this behavior, complementary *ex situ* analyses were performed on BST (with $0 \leq x \leq 1$) nanoparticles synthesized with the continuous setup.

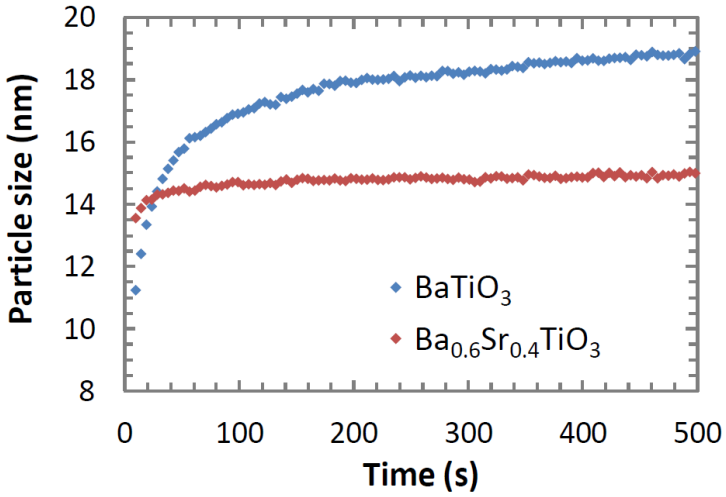

Figure III-19. *In situ* study of the strontium effect on particles growth at T = 400 °C and P = 23 MPa.

III.2.3.2 Complementary ex situ analyses

As presented in Table III-4 the entire solid solution of $Ba_{1-x}Sr_xTiO_3$ (with x = 0, 0.2, 0.4, 0.6, 0.8, 1) was produced at 400°C and 23 MPa with the flow reactor. Figure III-20 shows the Raman spectra of the samples, exhibiting the effect of barium substitution with strontium on the BST structure.

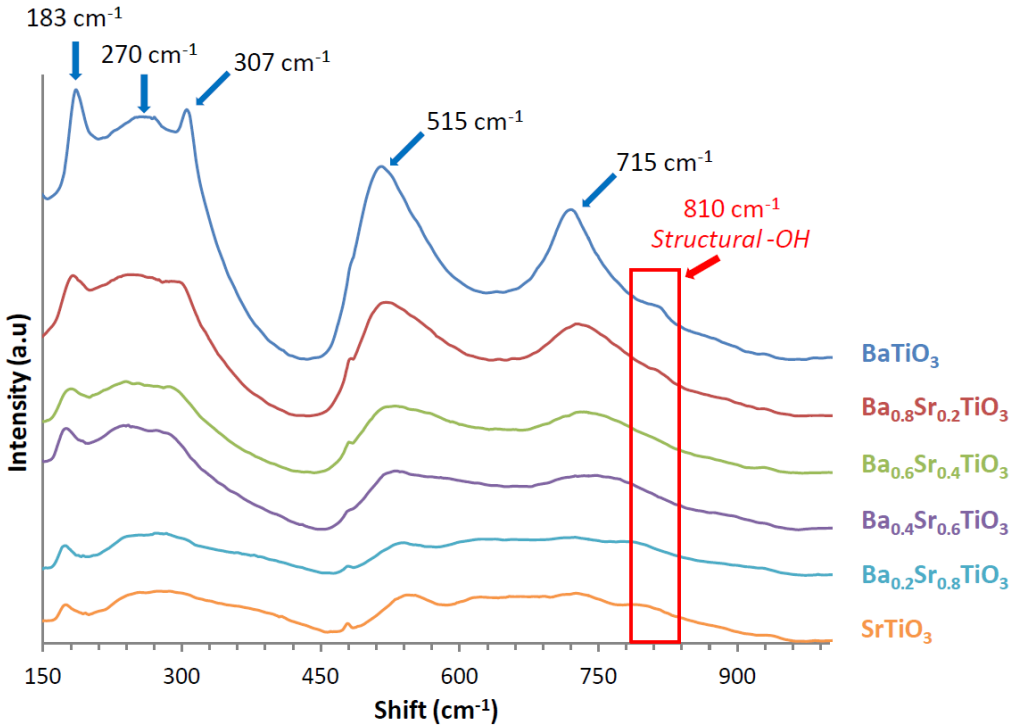

Figure III-20. Raman spectra showing the BST structure variation according to the amount of strontium.

In the case of $BaTiO_3$ (Figure III-7), several longitudinal and transversal Raman modes were activated (183 to 715 cm^{-1}) which can be explained by a structural disorder of the synthesized nanoparticles at

this size range. However, with strontium substitution, the Raman response changes; the peak intensities decrease while their widths increase. In addition the Raman peak at 810 cm^{-1}, which is related to the presence of structural –OH defects, presents an intensity decrease with the increase of strontium substitution [235]. This shows a structural stabilization related to the substitution of barium with strontium.

The FTIR analysis Figure III-21 confirms that the purity of the material along the entire solid solution is close to the $BaTiO_3$ one. In addition, similarly to the Raman analysis Figure III-20, increasing the strontium content, the band related to structural –OH defects disappears.

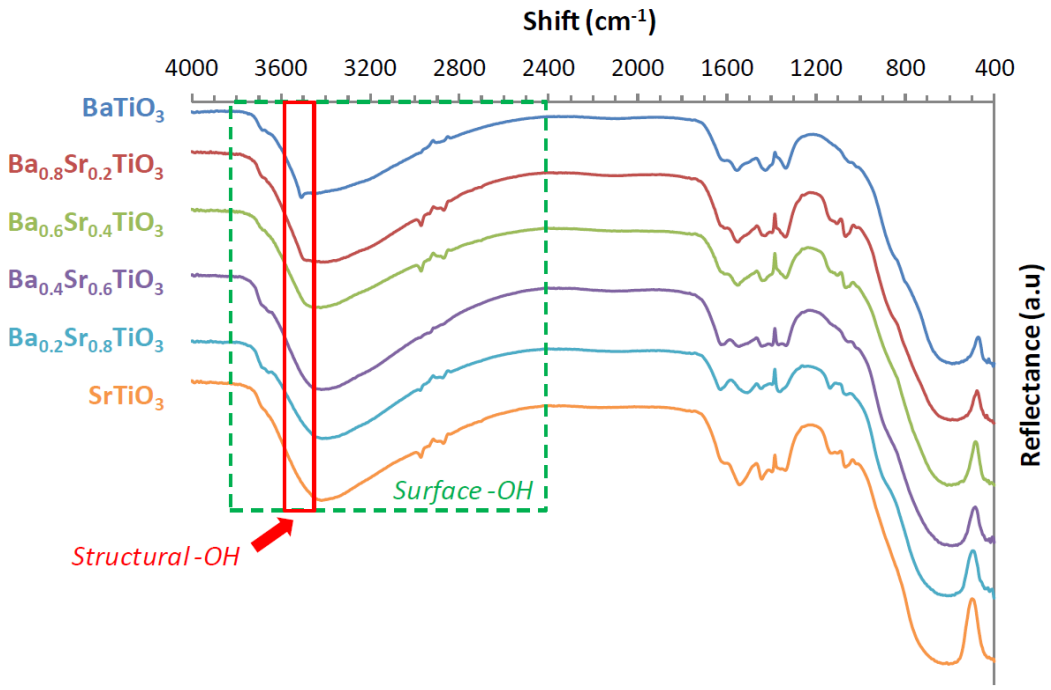

Figure III-21. FTIR spectra of the various BST compositions confirming the $BaTiO_3$ purity preservation and exhibiting the presence of surface and structure –OH defects

However, the FTIR analysis does not enable us to have a more precise idea concerning the variation of the surface –OH defects with the strontium content. To have this information it is necessary to perform an O 1s XPS analysis of the BST powders (Figure III-22). Although this type of analysis does not enable a precise quantification, it is still possible to see a trend comparing the variation of the area ratio between the peak related to surface –OH and the one related to structural $–O^-$ [236].

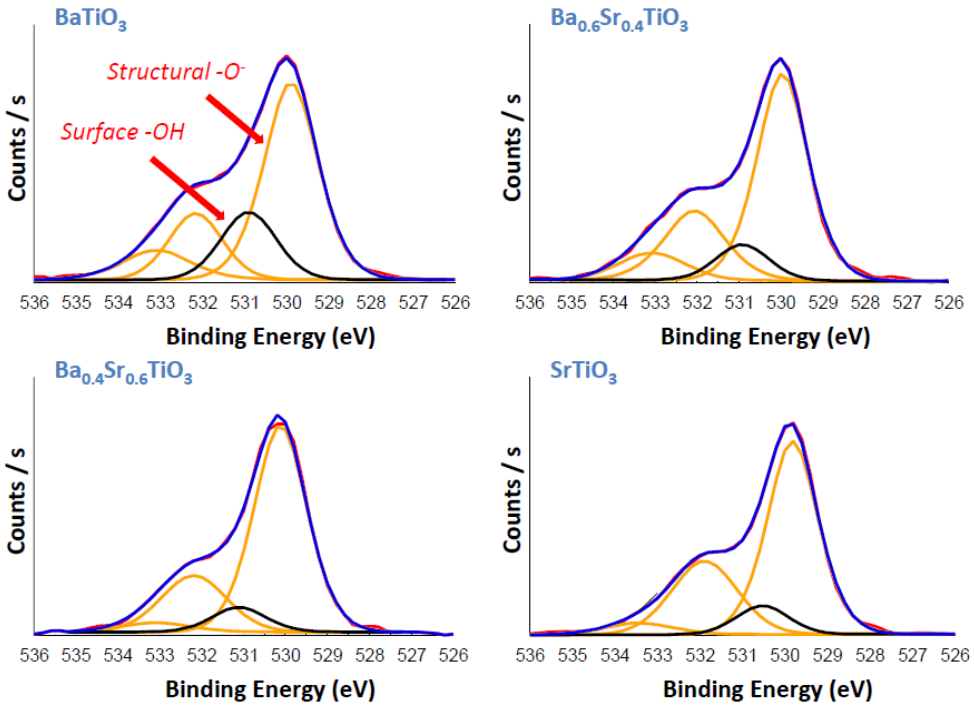

Figure III-22. O 1s XPS response of the BST particles surface enabling to quantify the variation of surface –OH compared to $–O^-$ atoms within the structure.

Table III-7 shows that increasing the strontium content, the quantity of surface –OH significantly decreases. Indeed if a value of 1 is attributed to the peak area related to structural $–O^-$ (around 530 eV), the area ratio of the peak linked to surface –OH (around 531 eV) decreases from 0.34 for $BaTiO_3$ to values between 0.12 - 0.17 for $Ba_{0.6}Sr_{0.4}TiO_3$, $Ba_{0.4}Sr_{0.6}TiO_3$, and $SrTiO_3$.

Table III-7. Area ratios from O 1s XPS analysis of the BST powders

		Area ratio			
Experiment n°	Composition	Structural -O ≈ 530 eV	Surface –OH ≈ 531 eV	O=C ≈ 532 eV	O-C ≈ 533 eV
1	$BaTiO_3$	1	0.34	0.34	0.19
3	$Ba_{0.6}Sr_{0.4}TiO_3$	1	0.17	0.34	0.13
4	$Ba_{0.4}Sr_{0.6}TiO_3$	1	0.12	0.27	0.05
6	$SrTiO_3$	1	0.15	0.38	0.06

The two other peaks around 532 and 533 eV are related to carbon contamination (O=C and O-C, respectively). This contamination which remains constant for each composition could result from the precursors as identified in the FTIR analyses.

III.2.3.3 Conclusion

The *ex situ* analyses thus provide important information concerning the strontium effect on the BST nanoparticles characteristics. It was observed that increasing the strontium content reduces the disorder within the material. The decrease of disorder due to Ti off centering identified with Raman

analysis could be related to the difference of atomic size between barium (r_{Ba} = 1.49 Å) and strontium (r_{Sr} = 1.32 Å). Indeed the strontium being smaller it tends to decrease the tetragonal distortion within the structure. Concerning structure and surface –OH defects, their presence is clearly identified into the literature and attributed to the dissolution of the barium ions. This could be explained through theoretical calculations based on the first principles indicating that Ti-O chemical bond are more covalent and that Ba-O and Sr-O ones are more ionic [237–239]. In consequence, barium and strontium ions tend to be dissolved under aqueous conditions leading to the apparition of –OH defects. In addition, other numerical studies compared the stability of Ba-O to Sr-O; they concluded that Sr-O is more stable than Ba-O [240]. This is in agreement with the Raman FTIR and XPS results showing a decrease of surface and structure –OH defects increasing with the strontium amount.

This decrease of surface –OH with the increase of strontium content can explain the variations in growth profiles between $BaTiO_3$ and $Ba_{0.6}Sr_{0.4}TiO_3$ identified in the *in situ* synchrotron WAXS study (Figure III-23).

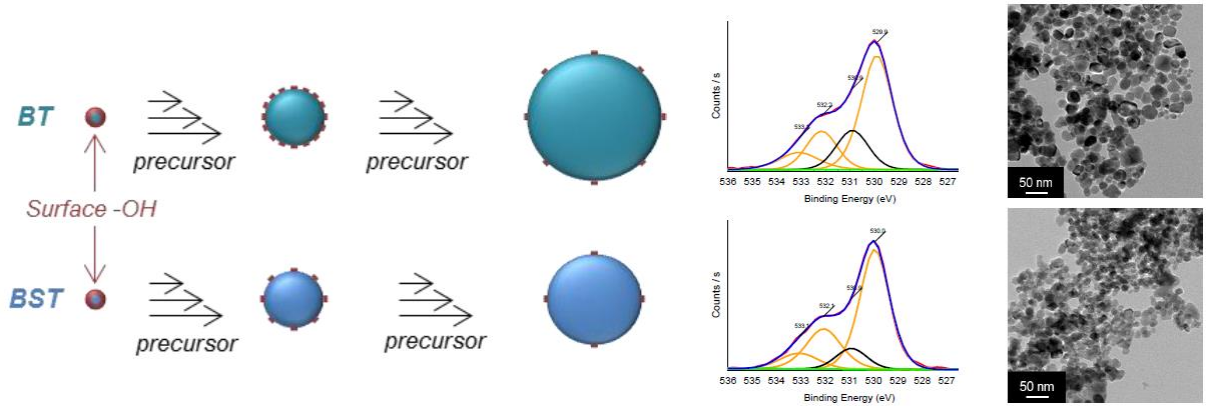

Figure III-23. Sketch illustrating why BST nanoparticles grow less than $BaTiO_3$ ones [204] Copyright © 2014, Elsevier.

If the growth is based on a sol-gel mechanism, a reduction of the surface –OH amount means that the quantity of precursor able to react at the surface of the particles decreases. This explains why the BST nanoparticles grow less than the $BaTiO_3$ ones.

III.2.4 Conclusion

Through this study we confirmed that the supercritical fluid technology enables the production of high quality BST nanoparticles in a very short time scale. The coupling of *in situ* synchrotron powder diffraction with *ex situ* spectroscopy analyses leads to a better understanding of the particles growth behavior highlighting the composition effect. The presence of surface –OH was identified as the key

parameter for the particle growth. The presence of strontium decreasing the quantity of surface – OH explains why BST particles grow less than $BaTiO_3$ ones.

Now that the study concerning $BaTiO_3$ and BST nanoparticles formation of in supercritical fluid conditions is achieved, in the following part we are going to move towards the study of the B site substitution through the example of titanium substitution with zirconium.

III.3 Synthesis of $BaTi_{1-y}Zr_yO_3$ (with $0 \leq y \leq 1$ - BTZ) nanoparticles

The main synthesis route used to produce BTZ is the solid state one which consists in mixing $BaCO_3$, ZrO_2 and TiO_2 powders and heat treat them at high temperature (1000 – 1600°C) for several hours (4 – 6h) [81,241–245]. Although this simple method enables a large scale production of material, it is time and energy consuming. In addition, the produced material usually presents impurities and inhomogeneity [8]. Some other alternative methods can be found in the literature such as the chemical solution deposition [80,246] or the hydrothermal one [247,248]. Among these methods only the one based on a modified vapor diffusion sol-gel process is reported as enabling the synthesis of the BTZ entire solid solution [82]. However, this last method only enables the synthesis of a small quantity of BTZ nanoparticles and goes through several steps which make it time consuming and unsuitable for a transfer towards industrial production.

In this part we are first going to demonstrate de feasibility of this synthesis using supercritical fluid technology, then, associate the results to an *in situ* synchrotron WAXS study to better understand the material's growth.

III.3.1 Experimental conditions

The synthesis procedure was identical to the one for BST nanoparticles synthesis, except that now it is a part of the titanium isopropoxide precursor which is replaced with zirconium isopropoxide as presented in Table III-8 where C is the concentration in $mol.L^{-1}$ of the barium (or titanium + zirconium) precursor in the ethanol / water mixture ($x_{Ethanol} = 0.29$) inside the reactor.

Table III-8. Experimental conditions for $BaTiO_3$ – $BaZrO_3$ solid solution synthesis

Experiment n°	Composition	Solvent	C ($mol.L^{-1}$)	T (°C)	P (MPa)	Residence time (s)
1	$BaTiO_3$	ethanol/water $x_{Ethanol} = 0.29$	0.015	400	23	53
2	$BaTi_{0.8}Zr_{0.2}O_3$					
3	$BaTi_{0.6}Zr_{0.4}O_3$					
4	$BaTi_{0.4}Zr_{0.6}O_3$					
5	$BaTi_{0.2}Zr_{0.8}O_3$					
6	$BaZrO_3$					

Changing the ratio between barium and zirconium enables us to produce the entire solid solution, from $BaTiO_3$ to $BaZrO_3$.

III.3.2 BTZ nanoparticles characterization

III.3.2.1 BTZ solid solution synthesis

Figure III-24 presents the X-ray diffraction patterns normalized to the most intense peak of the synthesized nanoparticles. As expected, increasing the zirconium content induces a regular shift of the peaks towards lower angle. This is related to the volume variation of the cell, the cationic radius of Zr^{4+} (r_{Zr} = 0.86 Å) being bigger than the Ti^{4+} one (r_{Ti} = 0.75 Å) [67], increasing the amount of zirconium induces a cell distortion resulting in its swelling. Based on Bragg's law ($2d \sin\theta = n\lambda$), the distance between plans increasing, the 2Θ position of the pattern shifts towards smaller angles. Nevertheless, it is important to note a slight contamination for the $BaZrO_3$ case which was not identified.

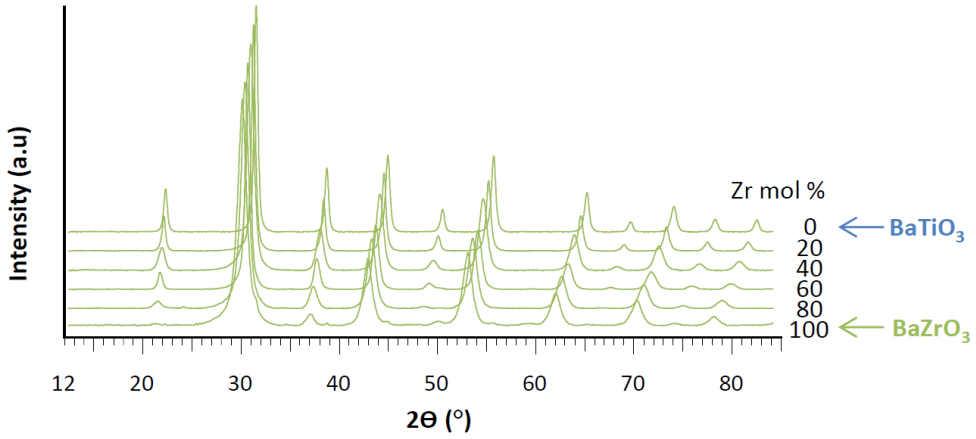

Figure III-24. XRD patterns of the BTZ solid solution exhibiting a regular shift towards smaller 2Θ angles from $BaTiO_3$ to $BaZrO_3$.

These X-ray diffraction patterns were refined using the *FullProf* method to calculate their lattice parameters for each composition. As presented in section III.1.2.2, the $BaTiO_3$ structure at room temperature is tetragonal, however, as reported in the literature for bulk BTZ, since y > 0.05, the structure becomes pseudo cubic up to y = 0.15 and finally cubic [81,82]. In this study $BaTiO_3$ structure was described in the space group P4mm and all the others in the Pm3m one. That is why, similarly to BST, the comparisons between each samples were made on the lattice parameter "a".

Table III-9 summarizes the main parameters obtained from the *FullProf* profile refinement of BTZ XRD patterns. We can see that the Chi2 value is a bit high in the case of $BaTi_{0.8}Zr_{0.2}O_3$ and $BaTi_{0.4}Zr_{0.6}O_3$. For the first case, it is around this composition that the material goes from ferroelectric to relaxor which is associated to structural variations [81,242–245]. Combining this to the lattice distortion due to surface strain at this scale can explain why the Chi2 increases for this

specific composition. But so far, we cannot explain why it is also high for the second case. Deeper analyses are needed concerning the materials morphology and structure.

Table III-9. Results obtained from the BTZ XRD pattern refinements

Parameters	Compositions					
	$BaTiO_3$	$BaTi_{0.8}Zr_{0.2}O_3$	$BaTi_{0.6}Zr_{0.4}O_3$	$BaTi_{0.4}Zr_{0.6}O_3$	$BaTi_{0.2}Zr_{0.8}O_3$	$BaZrO_3$
Space group	P4mm	Pm3m	Pm3m	Pm3m	Pm3m	Pm3m
Cell parameter (Å)	a = 4.0080	a = 4.0481	a = 4.0892	a = 4.1223	a = 4.1602	a = 4.1969
	b = 4.0080	b = 4.0481	b = 4.0892	b = 4.1223	b = 4.1602	b = 4.1969
	c = 4.0236	c = 4.0481	c = 4.0892	c = 4.1223	c = 4.1602	c = 4.1969
$\sigma_{Cell\ parameter}$ (Å)	a = 0.0001	a = 0.0001	a = 0.0001	a = 0.0001	a = 0.0001	a = 0.0001
	b = 0.0001	b = 0.0001	b = 0.0001	b = 0.0001	b = 0.0001	b = 0.0001
	c = 0.0001	c = 0.0002	c = 0.0001	c = 0.0001	c = 0.0001	c = 0.0001
Scale factor	$1.024.10^{-2}$	$6.226.10^{-2}$	$2.344.10^{-2}$	$5.965.10^{-2}$	$5.323.10^{-2}$	$4.563.10^{-2}$
$\sigma_{Scale\ factor}$	4.10^{-5}	14.10^{-5}	5.10^{-5}	14.10^{-5}	12.10^{-5}	11.10^{-5}
Y	0.22708	0.35965	0.37783	0.45098	0.72736	1.05916
σ_Y	0.00281	0.00207	0.00350	0.00453	0.00408	0.00541
I_G	0.08715	0.04797	0.14860	0.14217	0.19089	0.00329
σ_{IG}	0.00096	0.00080	0.00165	0.00219	0.00250	0.00035
Bragg R-factor	2.39	2.29	3.8	2.58	1.16	1.50
Rf -factor	0.849	2.39	2.33	1.98	0.961	1.08
Chi2	2.71	7.75	3.22	8.79	2.65	3.34

Figure III-25 is the plot of the calculated lattice parameter “a” variation according to the material composition. It is observed that “a” increases linearly with the increase of zirconium content (R^2 = 0.999). Knowing this and based on Vegard’s law it is then possible to confirm the synthesis of the entire solid solution (from $BaTiO_3$ to $BaZrO_3$).

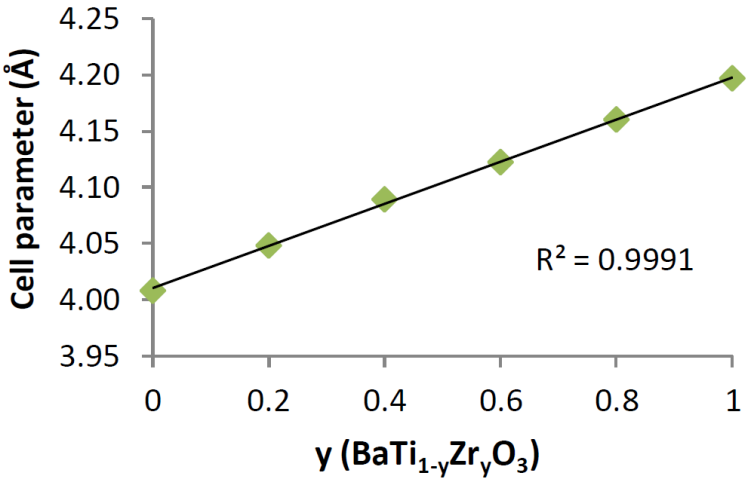

Figure III-25. Linear variation of the lattice parameter from $BaTiO_3$ to $BaZrO_3$ confirming the synthesis of the entire solid solution

In addition (Figure III-24), no extra peaks were observed on the XRD patterns, except for $BaZrO_3$, indicating that the purity of the $BaTiO_3$ based nanoparticles is mainly preserved along the entire solid solution.

III.3.2.2 Particles size

The TEM images of all the BTZ particles synthesized according to the conditions of Table III-8 (Figure III-26) show that in all cases the particles are more or less spherical with a narrow size distribution. Indeed, looking at the plotted histograms from the particles measurements (every time more than 150 particles measures over different TEM images), we can see a size variation depending on the composition of the samples.

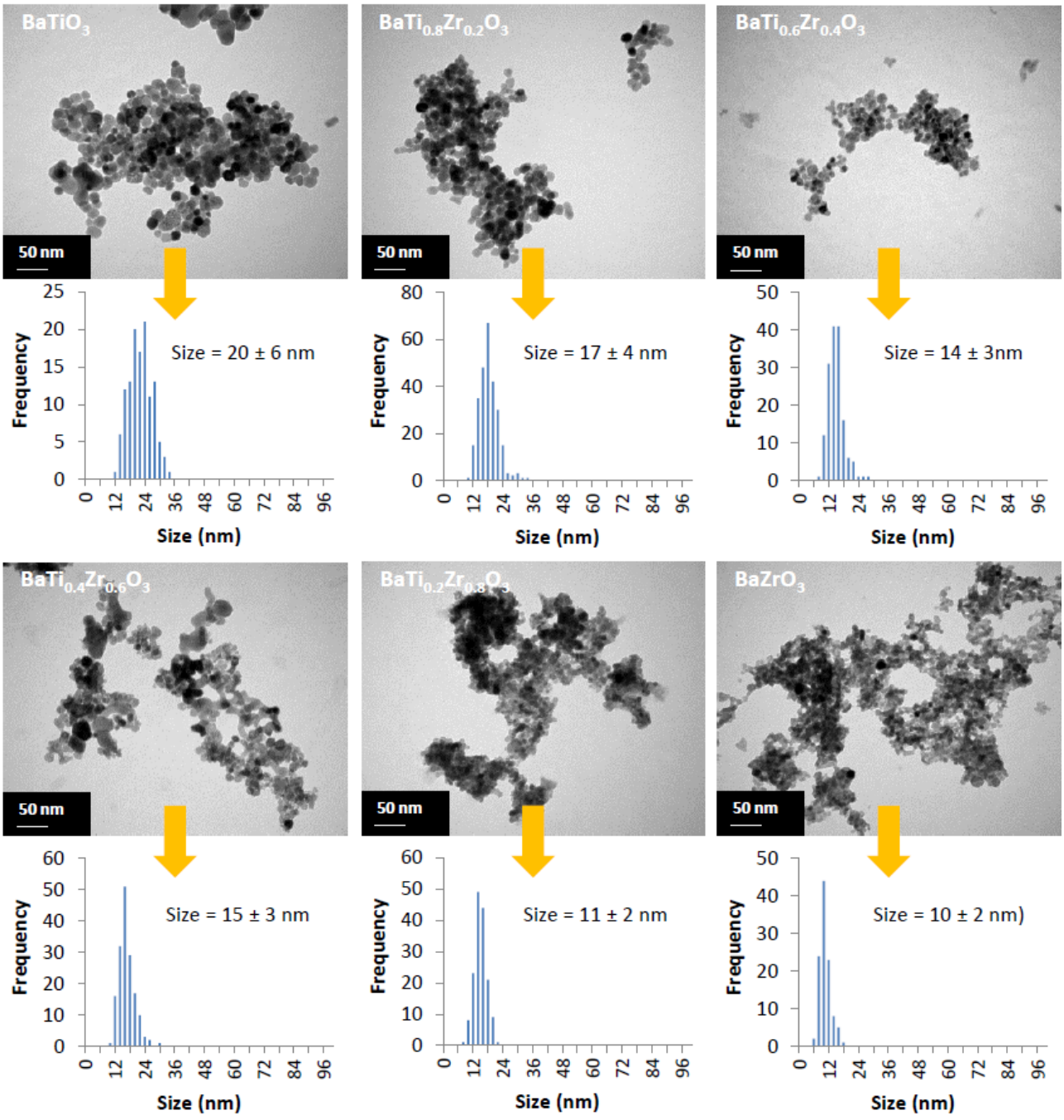

Figure III-26. TEM images of BTZ nanoparticles synthesized according to the material composition.

For $BaTiO_3$ nanoparticles the average size was measured as being 20 ± 6 nm; increasing zirconium amount to $BaTi_{0.4}Zr_{0.6}TiO_3$ induces an average size decrease down to 15 ± 3 nm and for $BaZrO_3$ nanoparticles the average size reaches 10 ± 2 nm. This confirms that not only the average size decreases with zirconium content but its size distribution as well. However, looking carefully to Figure III-26, we can see that in the specific case of $BaTi_{0.4}Zr_{0.6}TiO_3$ there are some particles which are much bigger than the average size of 15 nm. As there are only few of them, they weren't considered

in the average size calculation. This secondary population can have an effect on the XRD pattern which would explain the increase of the Chi2 value of observed in Table III-5.

III.3.2.3 Crystallites size

Table III-10 presents both, the particles size measured from the TEM images and the crystallites size calculated with the *FullProf* profile refinement of the XRD patterns.

Table III-10. Comparison between the BTZ particles sizes measured from TEM images and their crystallite sizes estimated with Scherrer equation using XRD patterns refinements.

Composition	Particles size from TEM (nm)	Crystallite size from XRD (nm)
$BaTiO_3$	20 ± 6	19
$BaTi_{0.8}Zr_{0.2}O_3$	17 ± 4	18
$BaTi_{0.6}Zr_{0.4}O_3$	14 ± 3	13
$BaTi_{0.4}Zr_{0.6}O_3$	15 ± 3	12
$BaTi_{0.2}Zr_{0.8}O_3$	11 ± 2	9
$BaZrO_3$	10 ± 2	8

If we compare the average size of the particles with the crystallites size, both being close, we can conclude that the particles are monocrystalline along the entire solid solution.

Indeed, if we focus on the specific case of $BaTi_{0.8}Zr_{0.2}O_3$ (Figure III-27), comparing the average size and size distribution (Figure III-27a and c) to the HRTEM image Figure III-27b, which shows the presence of lattice fringe along the entire particles, confirms that the produced particles are monocrystalline.

The FTIR analysis (Figure III-27c) remains similar to the one of $BaTiO_3$ (Figure III-3) giving some insight concerning the presence of $BaCO_3$ but this time, the Raman analysis (Figure III-27e) does not indicate the presence of $BaCO_3$ which might be below the detection limit. Nevertheless, the activation of the modes is different from the $BaTiO_3$case (Figure III-7). Indeed, the modes at 183 cm^{-1} combined with 307 cm^{-1} and 715 cm^{-1} ones indicate the presence of a long-range ferroelectric order within the material [81,249–253]. Again, this is in agreement with the variation of Chi2 value observed Table III-5 and attributed to structural variation. As already explained, this variation was expected since the BTZ phase changes around this composition.

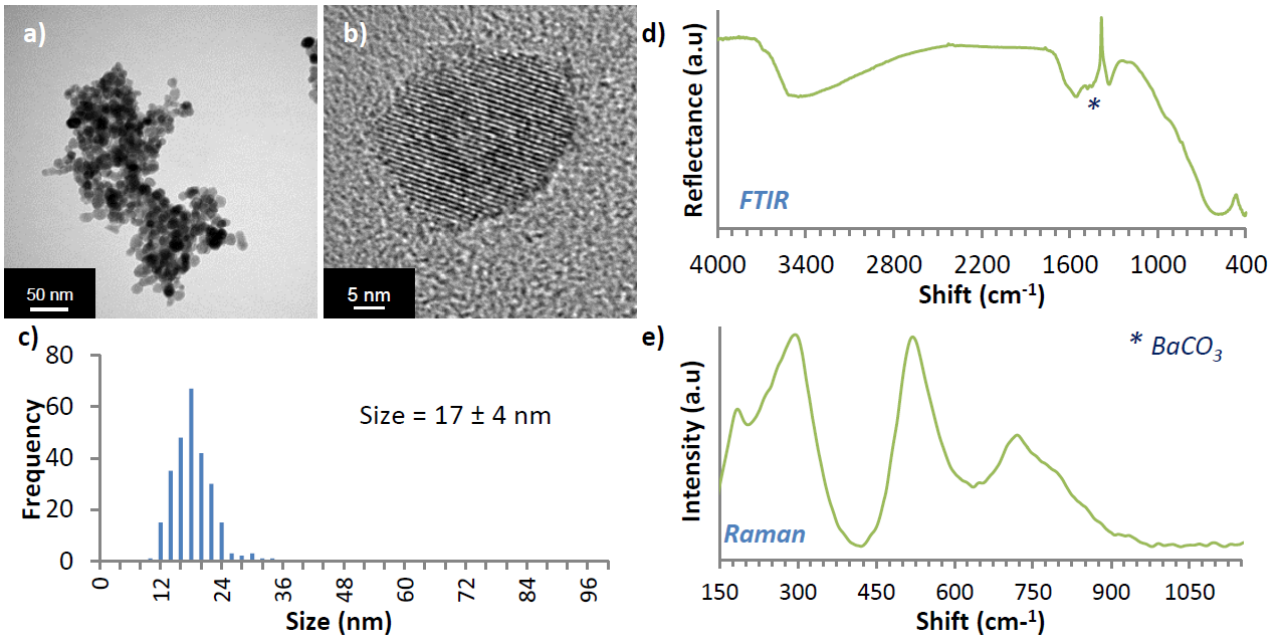

Figure III-27 a) and b) HRTEM images of the $BaTi_{0.8}Zr_{0.2}TiO_3$ powder, c) average size and size distribution of 17 ± 4 nm measured from TEM images, d) FTIR and e) Raman analyses.

III.3.2.4 Conclusion

In this part we showed that based on this synthesis process it was also possible to synthesize the entire solid solution from $BaTiO_3$ to $BaZrO_3$ only by adjusting the precursor ratios to the targeted composition. In addition, the quality of the nanoparticles established in the case of $BaTiO_3$ is preserved, there are no extra phases visible on the XRD patterns and the particles are still monocrystalline. Nevertheless, we observed a slight contamination in the $BaZrO_3$ XRD pattern which remains unidentified. The synthesis procedure might need some optimization for this specific composition.

To better understand the BTZ particles formation, similarly to the BST case, it is important to perform first, a deep *ex situ* study of the materials structure and surface properties, prior to the *in situ* one.

III.3.3 Structural and surface properties

III.3.3.1 Structural analysis

The XRD analysis giving an average response on the material structure, Raman analyses of the BTZ powders produced according to Table III-8 conditions were achieved (Figure III-28). In comparison to the BST solid solution (Figure III-20), the titanium substitution with zirconium impacts more drastically the structure of the material. Indeed, on Figure III-28 we can see that the active modes of

the $BaTiO_3$ structure defined in section III.1.2.1 change already a lot for $BaTi_{0.8}Zr_{0.2}O_3$ and almost disappear for further titanium substitution with zirconium.

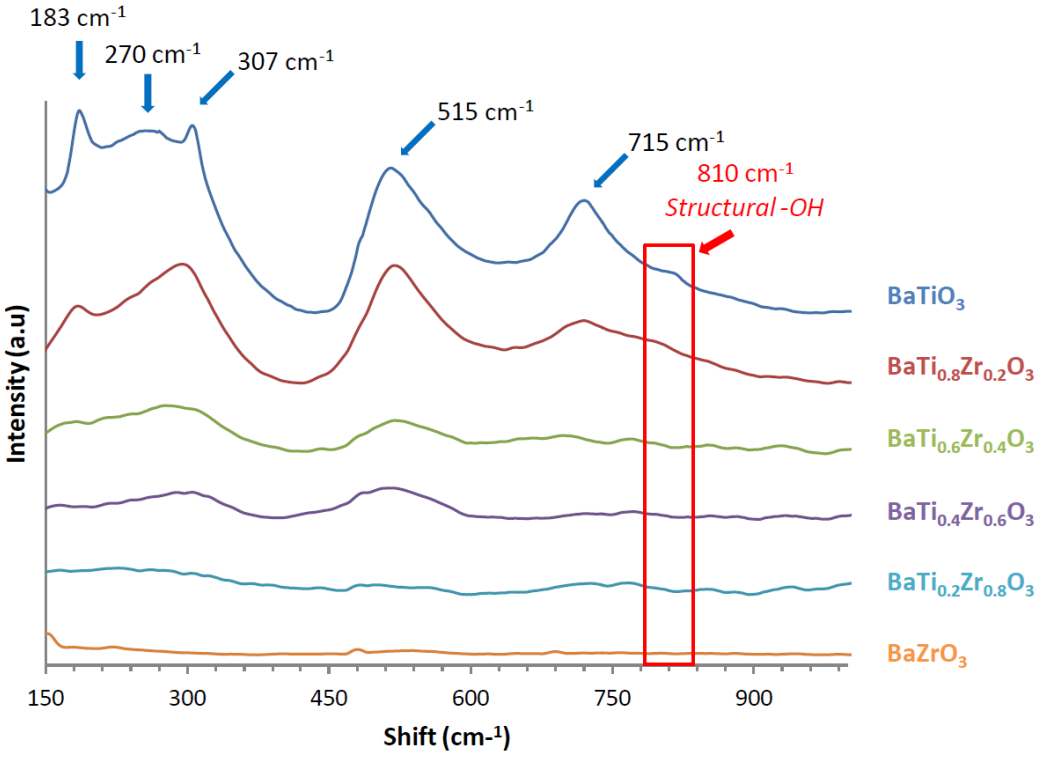

Figure III-28. Raman spectra showing the BTZ structure variation according to the amount of zirconium

In the case of $BaTi_{0.8}Zr_{0.2}O_3$, the modes at 183 cm^{-1} combined with the 307 cm^{-1} and 715 cm^{-1} ones indicate the presence of a long-range ferroelectric order within the material [81,249–253]. This is in agreement with the variation of Chi2 value observed Table III-5 and attributed to structural variation. However, since we reach $y \geq 0.4$ there is no more ferroelectricity. Only two broad bands around 300 and 500 cm^{-1} remain for $BaTi_{0.6}Zr_{0.4}O_3$ which are characteristic of the Pm3m paraelectric space group. These two bands become broader and broader for $BaTi_{0.4}Zr_{0.64}O_3$ and $BaTi_{0.2}Zr_{0.8}O_3$ and almost disappear for $BaZrO_3$ indicating an increase of structural symmetry and thus order towards the cubic Pm3m space group, which is Raman inactive. Nevertheless, for $BaZrO_3$, the presence of modes at 150 and 660 cm^{-1} (and a one at 1080 cm^{-1} which is not shown in this figure) are related to a $BaCO_3$ contamination. Similarly to the BST study (Figure III-20), the Raman analyses exhibit the presence of structural –OH defects which tend to decrease increasing the rate of titanium substitution with zirconium.

III.3.3.2 Analysis of the BTZ particles surface properties

The FTIR analysis enables to complete the Raman one of the previous section. Figure III-29 confirms the presence of structural –OH defects which tend to decrease increasing the zirconium substitution

rate. In addition we can observe a higher $BaCO_3$ contamination in the case of $BaZrO_3$. Since this solid solution is new, the process might not be fully optimized and, similarly to H. Reverón et al study concerning the $BaTiO_3$ supercritical fluid synthesis [159], it might be important to investigate the influence of the ethanol / water ratio. Indeed they show that optimizing this ratio enables both; to make monocrystalline nanoparticles and lower the $BaCO_3$ contamination. This might also prevent the contamination observed in $BaZrO_3$ XRD pattern. In addition, similarly to the BST case, the presence of surface –OH is detected through the broad band between 2500 and 3700 cm^{-1} and the narrow one at 1560 cm^{-1}.

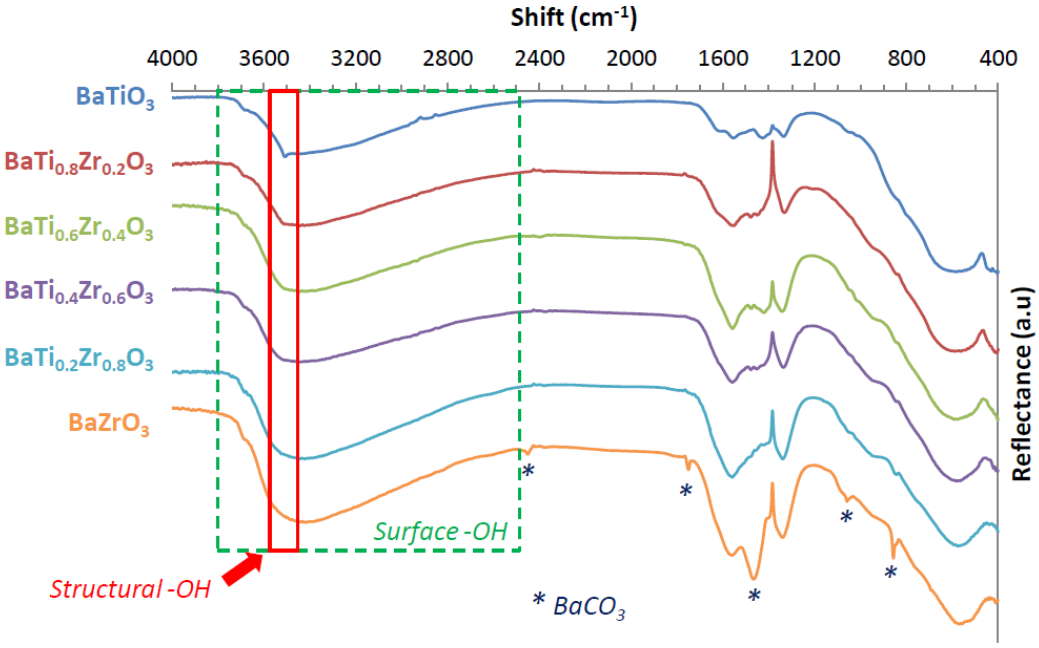

Figure III-29. FTIR of the various BTZ compositions confirming the $BaTiO_3$ purity preservation excepts for $BaZrO_3$ where a $BaCO_3$ contamination is observed, and exhibiting the presence of surface and structure –OH defects

Complementary XPS analyses of the particles surface are necessary to have a better idea concerning their surface properties (Figure III-30).

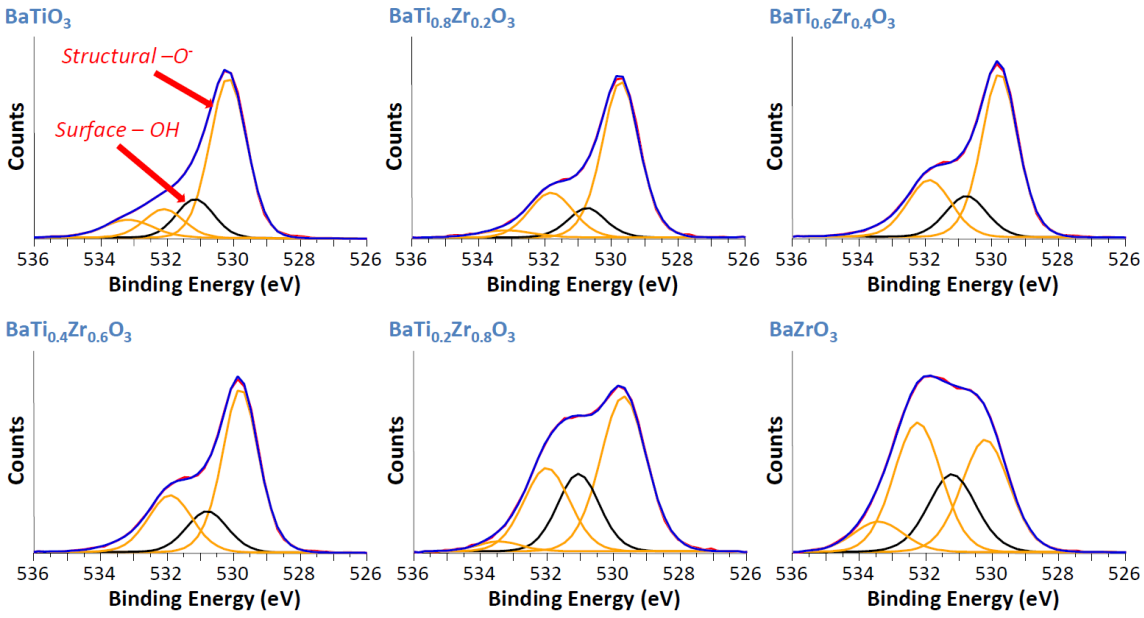

Figure III-30. O 1s XPS response of the BTZ particles surface enabling to quantify the variation of surface –OH compared to $–O^-$ atoms within the structure.

Similarly to BST, Table III-11 presents the relative variation of surface –OH and carbon contamination compared to the amount of structural $–O^-$. It is important to note that the XPS analyses in the present case were not performed with the same equipment than for the BST study. Consequently, we cannot compare the values of both studies, only the trends. The amount of surface –OH being directly related to the barium dissolution, as the quantity of barium is constant; it is surprising to observe an increase of them since $y \geq 0.4$. However, knowing from the literature that it is difficult to replace more than 40 – 50 % of titanium with zirconium, crossing this value could lead to structures which are less stable. Consequently this could decrease the ionic bond strength of Ba-O, favoring the barium dissolution. Nevertheless, based on the hypothesis concerning the BST growth behavior (see conclusion III.2.3.3), this result does not fit with the decrease of particles size increasing the zirconium amount observed in Figure III-26.

Table III-11. Area ratios O 1s from XPS analysis of the BTZ powders

		Area ratio			
Experiment n°	Composition	Structural -O ≈ 530 eV	Surface –OH ≈ 531 eV	O=C ≈ 532 eV	O-C ≈ 533 eV
1	$BaTiO_3$	1	0.24	0.18	0.15
2	$BaTi_{0.8}Zr_{0.2}O_3$	1	0.19	0.33	0.07
3	$BaTi_{0.6}Zr_{0.4}O_3$	1	0.28	0.43	0.07
4	$BaTi_{0.4}Zr_{0.6}O_3$	1	0.33	0.50	0.12
5	$BaTi_{0.2}Zr_{0.8}O_3$	1	0.45	0.53	0.06
6	$BaZrO_3$	1	0.69	1.14	0.27

Table III-11 also confirms the presence of $BaCO_3$ contamination in the case of $BaZrO_3$ where both, the O=C and O-C ratios are much higher than for the other compositions. We can also note that, for the compositions where the $BaCO_3$ contamination is lower ($BaTiO_3$ to $BaTi_{0.2}Zr_{0.8}O_3$), the amount of O=C gradually increases compared to the O-C amount which can be considered as constant. This trend can be associated to an increase of carbon contamination at the surface of the particles increasing the amount of zirconium. This increasing contamination may limit the accessibility of the precursors to the surface –OH which thus "quench" the BTZ particles growth.

III.3.3.3 Conclusion

The use of Raman spectroscopy enables to get more precise information concerning the materials structure with the presence of a long range ferroelectricity up to 20 % of zirconium. Coupling Raman and FTIR highlighted a decrease of structural –OH defects increasing the amount of zirconium. We also observed the presence of a higher $BaCO_3$ contamination for the $BaZrO_3$ powder. However the study also triggered some questions: (1) Knowing that the amount of surface –OH defects is stable up to 40% of zirconium and then increase: why the BTZ particles size decreases increasing the rate of zirconium substitution? and (2) why the carbon contamination at the surface increases with the amount of substituted zirconium?

In order to answer these questions an *in situ* analysis, similar to the BST one, is necessary to have a look at the growth behaviors and the kinetics of the syntheses.

III.3.4 *In* situ study of BTZ nanoparticles formation in supercritical fluid conditions

Table III-12 summarizes the four *in situ* experiments we did concerning the BTZ solid solution. In addition to the $BaTiO_3$ case, three other compositions were targeted: $BaTi_{0.8}Zr_{0.2}O_3$, $BaTi_{0.4}Zr_{0.6}O_3$ and $BaTi_{0.2}Zr_{0.8}O_3$.

Table III-12. Experimental conditions for *in situ* synchrotron WAXS BTZ solid solution synthesis

Experiment n°	Composition	Solvent	C (mol.L^{-1})	T (°C)	P (MPa)	Synthesis duration (min)
1	$BaTiO_3$	ethanol/water $x_{Ethanol}$ = 0.29	0.2	400	23	> 20
2	$BaTi_{0.8}Zr_{0.2}O_3$					
3	$BaTi_{0.4}Zr_{0.6}O_3$					
4	$BaTi_{0.2}Zr_{0.8}O_3$					

In each cases the temperature and pressure were respectively set at 400 °C and 23 MPa and the precursor concentration at 0.2 mol.L^{-1}.

III.3.4.1 Case of $BaTi_{0.4}Zr_{0.6}O_3$

The *in situ* analysis of this specific case presents unusual powder diffraction patterns during the growth. As presented in the Figure III-31, in the first part of the synthesis a splitting of the diffraction peaks appears, especially at high 2Θ (Figure III-31a). However, while the material is forming, a continuous decrease of the splitting is observed (Figure III-31b and c) to finally disappear (Figure III-31d) and present a diffraction pattern similar to the one of the *ex situ* study (Figure III-24).

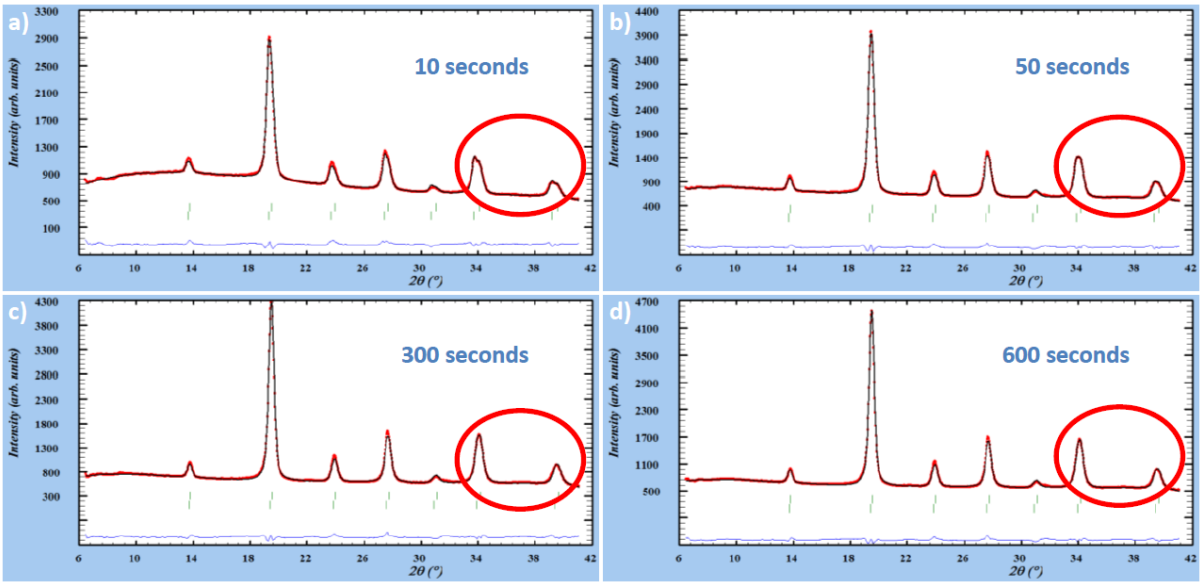

Figure III-31. *In situ* studies of the $BaTi_{0.4}Zr_{0.6}O_3$ synthesis: decrease of the powder diffraction pattern splitting with time.

This behavior can be explained by the production of $BaTi_{0.4}Zr_{0.6}O_3$ particles with initially two size distributions due to the mentioned carbon contamination which might disrupts the nucleation. Indeed, at this size range, the surface strain which strongly depends on the particles size has a significant effect of the lattice distortions, which can induce shifts of the XRD patterns. Moreover, the splitting decreasing with time and the presence of few bigger particles being observe on the TEM image (Figure III-26) for this specific composition strengthened this hypothesis. Thus, we conclude that this phenomenon was due to the presence of two size populations of $BaTi_{0.4}Zr_{0.6}O_3$ particles. With time, and probably due to Ostwald ripening, the size difference between the two populations decreased leading to the disappearance of the peaks splitting.

Consequently the profile refinement in this specific case was performed considering two phases of $BaTi_{0.4}Zr_{0.6}O_3$ with two different lattice parameters. This observation is also in agreement with the increased Chi2 value observed in the Table III-9.

III.3.4.2 Composition effect on particles growth

Figure III-32 shows the particles size variation for each compositions according to the synthesis duration. In this case we can see that the results are different to the particles size variation observed from TEM images (Figure III-26). Indeed, in the case of BTZ particles synthesized with the flow process, we saw that the average particles size tended to decrease increasing the amount of zirconium. However, in the case of the *in situ* study it is different; for $BaTiO_3$ and $BaTi_{0.8}Zr_{0.2}O_3$ compositions the growth are close but for $BaTi_{0.4}Zr_{0.6}O_3$ and $BaTi_{0.2}Zr_{0.8}O_3$ the particles size increases with the amount of zirconium while the kinetics tend to slow down.

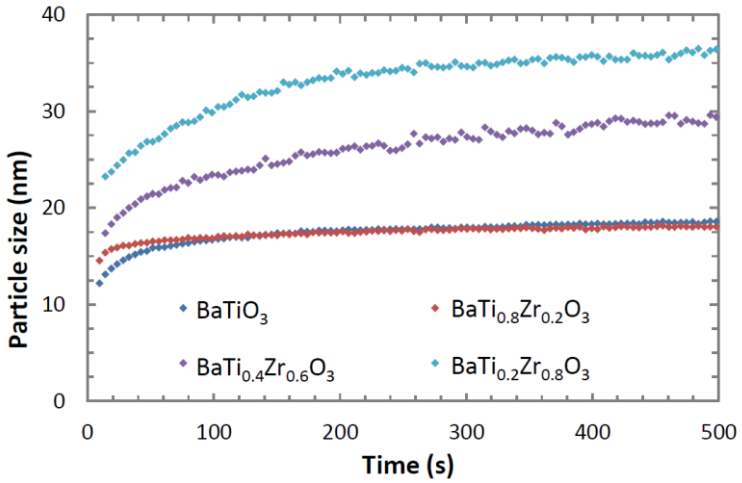

Figure III-32. *In situ* study of the zirconium effect on to particles growth at T = 400 °C and P = 23 MPa.

Even though this result seems in contradiction with the particles size from the TEM study, it is in agreement with the XPS one (Figure III-30) where more surface –OH were observe, confirming the BST growth theory where the surface –OH amount drives the particles growth. Indeed we showed that first the amount of surface –OH was constant then increases with the amount of zirconium and in the case of the *in situ* study we can see that first the particle size remains constant then increase too with the amount of zirconium.

If we do not observe the same trend with the flow synthesis it is because the growth kinetics became slower increasing the amount of zirconium. In contrary to the BST synthesis, the zirconium atom is bigger than the titanium one and the substitution site is no longer at the corner of the cell but at the center inducing strain within the structure which might slow down the reaction kinetics. Consequently, the residence time being constant, the size of the particles decreases.

This also explains the increase of surface –OH observed in XPS study, the kinetics being slower, more barium is dissolved producing more surface –OH defects.

III.3.5 Conclusion

Based on XRD, HRTEM, FTIR and Raman analyses we can confirm that the quality of the $BaTiO_3$ nanoparticles is mainly preserved along the entire BTZ solid solution. The exception concerns the $BaZrO_3$ case, where both; a secondary phase and a higher $BaCO_3$ contamination were observed. This was probably due to a slower reaction kinetic favoring the carbonation and other side reactions. That is why it would be interesting to optimize the synthesis procedure in order to lower these defects.

Similarly to the BST study, coupling *in situ* and *ex situ* analyses enabled us to better understand the growth behavior of the BTZ particles. The surface –OH defects amount is still a key parameter, nevertheless, the growth kinetic is a second aspect which has to be taken into account for explaining the growth trends.

III.4 Conclusion of the Chapter 3

Along this chapter we were able to demonstrate step by step the strengths of the supercritical fluid technology towards synthesis of high quality nanoparticles with the example of $BaTiO_3$ ones. The versatility of this process was also exhibited with the synthesis of both $BaTiO_3$ – $SrTiO_3$ and $BaTiO_3$ – $BaZrO_3$ entire solid solutions keeping the high quality of the $BaTiO_3$ based material. This is especially noteworthy in the case of the BTZ solid solution where we are, to our knowledge, the first to demonstrate the entire solid solution synthesis in supercritical fluids and the second among the various synthesis routes. Moreover, we were the first to exhibit such level of quality in terms of crystallinity but also potential amount of production. Nevertheless, the $BaZrO_3$ synthesis has to be optimized.

The use of *in situ* synchrotron WAXS analyses, combined with *ex situ* ones, were a very important asset to better understand the growth behaviors of these materials in such conditions. This enabled us to develop a growth mechanism where the amount of surface –OH drives the particles growth. This statement was verified in both solid solutions BST and BTZ, even though in the BTZ case, the growth kinetics plays also a preponderant role.

Now that the controlled synthesis of $BaTiO_3$ based nanoparticles is demonstrated the next step is to characterize their intrinsic properties, especially their ferroelectricity, to strengthen the potential of such nanomaterials synthesis route.

Chapter IV. Ceramics and hybrids processing and characterizations

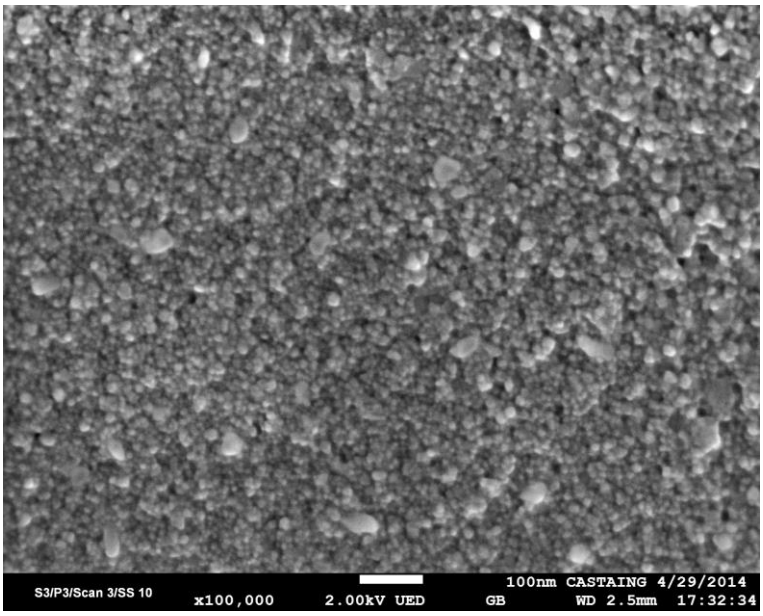

Ferroelectric materials are very attractive in many fields of applications, however, since 20 years there have been many discussions concerning the size effect on both structure and intrinsic dielectric properties of these materials. For example many studies predict the disappearance of the ferroelectricity with the materials downscaling but none agreed on a specific critical size. This is mainly due to: (1) the capability to produce crystallized particles of tens of nanometers without any amorphous shell, and (2) to the ability of processing them into dense and nanostructured ceramics while keeping their initial grain size while controlling the composition and crystallinity. The first challenge is now answered thanks to the supercritical fluid synthesis of high quality nanoparticles. Concerning the second one, the development of fast sintering processes these last ten years with especially the spark plasma sintering (SPS) technique, enables now to produce dense nanostructured ceramics for answering it [254–257].

This chapter will be first devoted to the processing of dense and nanostructured $Ba_{0.6}Sr_{0.4}TiO_3$ ceramics keeping the initial grain size and starting material quality. Then we will focus on the influence of SPS processing parameters, in particular the pressure effect on the properties. Finally we will analyze the size effect on the intrinsic dielectric properties of the BST ceramics. In a second section we will also study the densification of BTZ nanopowders and characterize their intrinsic properties. To do this, specific compositions were selected to study the transition from a ferroelectric behavior to a relaxor one in order to prove the accuracy of the synthesis route in terms of composition control. In a last part we will introduce the development of hybrids embedded passives and / or flexible electronic (BT particles dispersed into a polymeric matrix) with especially the development of a procedure to characterize their dielectric properties at high frequencies.

IV.1 BST processing into dense and nanostructured ceramics

Obtaining nanostructured and dense ceramics with grains size below 20 nm is a difficult task and thus a great challenge. Conventional sintering processes does no enable to achieve this aim. That is why, in this part, we are going to study fast sintering technologies, especially the spark plasma sintering (SPS) one in collaboration with Dr. Claude Estournes at “Centre Interuniversitaire de Recherche et d’Ingénierie des Matériaux - Plateforme Nationale CNRS de Frittage Flash” (CIRIMAT – PNF2) located at Paul Sabatier University in Toulouse. Then we will characterize the ceramics in terms of structure, nano/microstructure and dielectric properties et ICMCB.

IV.1.1 Materials and method

IV.1.1.1 Materials

In the framework of this study we focused our research on $Ba_{0.6}Sr_{0.4}TiO_3$ nanoparticles produced in supercritical fluids with the process and conditions detailed in Chapter I. Figure IV-1 is a reminder of the particles morphology, size and size distribution that we are going to use. We can see that the particles have an average size of 16 ± 2 nm.

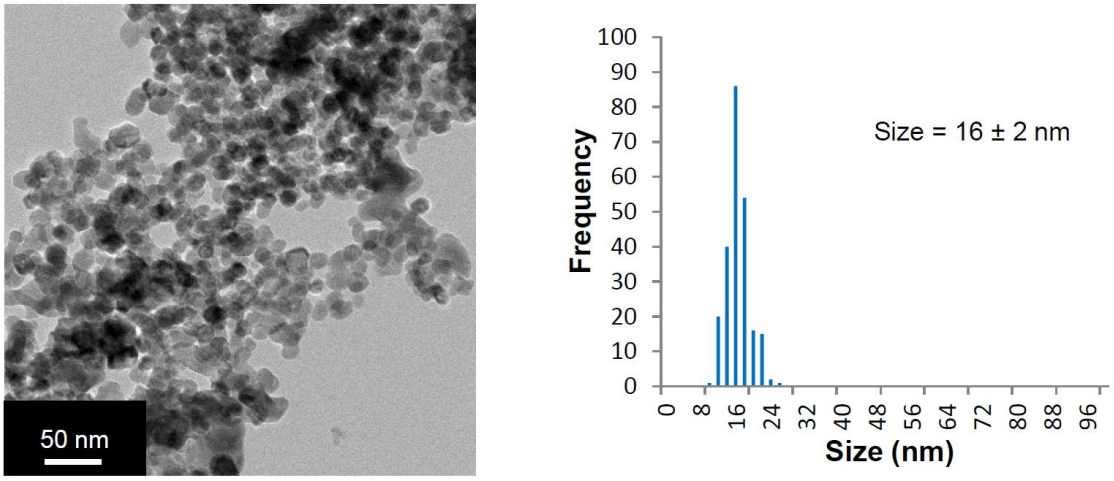

Figure IV-1. TEM image of $Ba_{0.6}Sr_{0.4}TiO_3$ nanoparticles produced in supercritical fluids showing their morphology, size and size distribution.

IV.1.1.2 Method

The samples were sintered using a Dr Sinter 2080 SPS apparatus (SPS Syntex Inc., Tokyo Japan), 400 mg of powder (without any binder) were loaded onto a 8 mm inner diameter cylindrical tungsten carbide die, covered with a graphite foil. The sintering temperature was 750°C, holding time 2 minutes while an uniaxial pressure of 300MPa was applied. Figure IV-2 presents the pressure and temperature profiles during of 32 minutes sintering cycle.

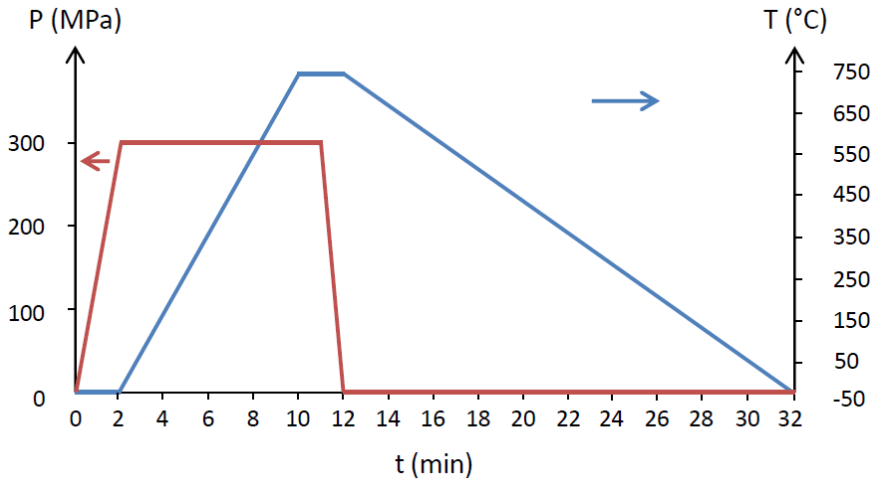

Figure IV-2. SPS pressure and temperature cycles of the $Ba_{0.6}Sr_{0.4}TiO_3$ powder processing into ceramics

At such small size range, the surface reactivity of the powder is very high, it is thus necessary to apply the pressure at the beginning of the cycle at room temperature in order to prevent any grain growth. Then, this applied pressure is slowly removed before cooling down the sample to lower the strain within the ceramic.

The specificity of our process lies in the atmosphere in which the sintering is achieved. Indeed, the SPS processing of titanium oxide based nanoparticles, such as TiO_2 or $BaTiO_3$, has been studied for around ten years now and the reported works showed that the chosen atmosphere inside the chamber is of main importance regarding the material defects chemistry. Sintering is usually performed under vacuum and in such conditions of low oxygen partial pressure atmosphere, the Ti^{4+} cations tend to be reduced into Ti^{3+} ones. As a result associated oxygen vacancies induce conductivity within the samples [86,258–261]. In our case, in order to avoid these extrinsic defects, the BST sintering is achieved in air and because it is an oxidant atmosphere, the die in tungsten carbide cannot handle temperatures exceeding 800 to 900°C. That is why the sintering is achieved at relatively low temperature (750°C). To balance this and to obtain an efficient densification, a high pressure of 300 MPa is applied.

IV.1.2 Ceramic characterization

IV.1.2.1 Grain size and density

Figure IV-3 shows high resolution SEM (HRSEM) images from the fractured cross section of the ceramic.

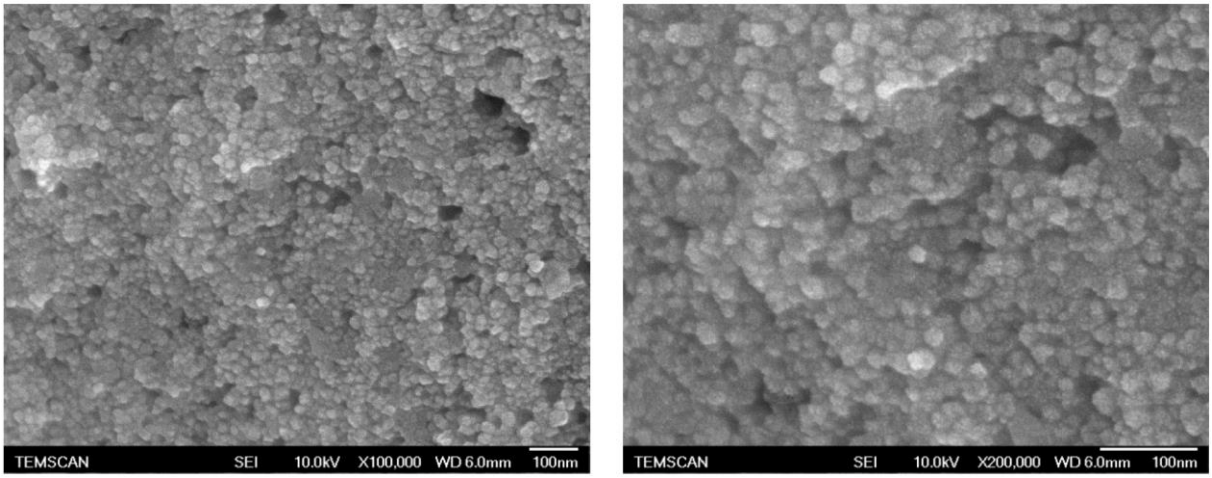

Figure IV-3. HRSEM images (JEOL JSM 6700F at UMS Raimond Castaing) of the $Ba_{0.6}Sr_{0.4}TiO_3$ powder processed with SPS two minutes at 300 MPa and 750°C exhibiting no grain growth.

Compared to the Figure IV-1, the first observation which can be done is that the initial grains size is preserved, except in local area where the particles aggregation led to a slight growth. Moreover, the pellets density estimated at 86 % using a pycnometer was in agreement with the HRSEM analysis showing some porosity within the ceramic. In addition the particles remain spherical and no differential sintering is observed despite the initial nanosized powder.

IV.1.2.2 Structural analysis

It is important to compare the XRD patterns of the material before and after the SPS processing to check if the sintering step did not induced neither secondary phases nor grain growth. In Figure IV-4, the XRD patterns of the raw powder in black and of the ceramic in red are superimposed.

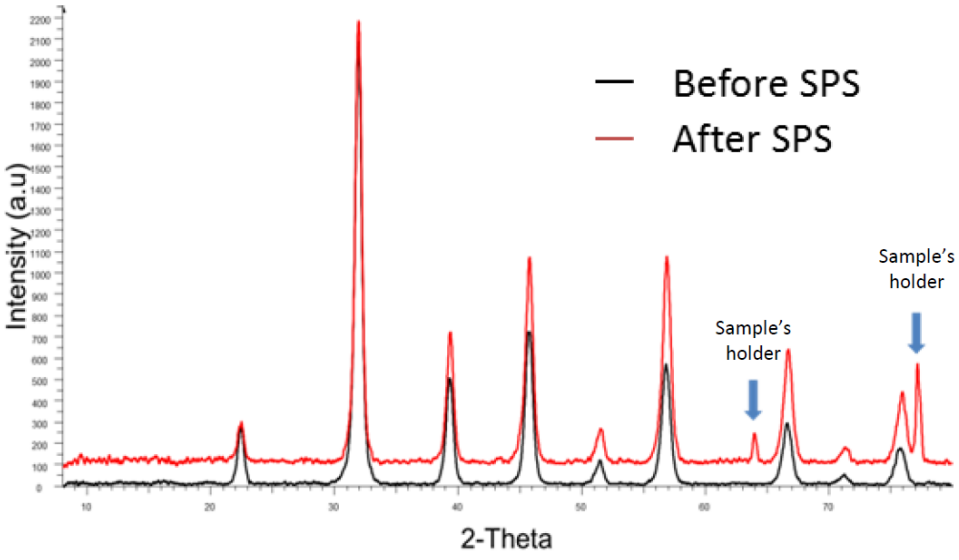

Figure IV-4. XRD patterns of the BST powder before and after SPS processing. The peaks position and width did not change confirming both : no grain growth and purity preserved

From these patterns we can first see that the peaks position did not change indicating that the processing did not affect the material stoichiometry. In addition, their widths are also constant confirming that there was no grain growth during the sintering as observed on the HRSEM images (Figure IV-3). Finally there are no extra peaks in the patterns, except the ones from the sample holder, confirming that no extra phases were formed. All together, we can conclude that the SPS sintering performed in these specific conditions enables to process nanostructured ceramics while keeping the characteristics of the starting powder in terms of size and crystallinity.

An average cubic structure is revealed by XRD in both; the powder and ceramic. Indeed no splitting of the pseudo cubic (200) into tetragonal (200) and (002) reflections appears after sintering. A deeper structural investigation would require high quality X-rays diffraction measurements performed on powders. Because our aim was to probe the properties of the ceramic proceeded under high pressure, we have chosen to use Raman spectroscopy offering the advantage to be accurate either on powder or ceramic. In addition, this very sensitive tool, suitable to characterize crystal structures, enables to detect the local dynamic symmetry with a coherence length lower than 2 nm which is not possible using XRD [262,263].

IV.1.2.3 Raman analysis for studying structural variation

As it was shown on the raw powder (Chapter I), at this size range there is a structural disorder, especially related to Ti off centering due to the high surface strain. It is now interesting to see if the high pressure applied during SPS processing had an impact on such called “size effect”. Figure IV-5 shows the resulting Raman analysis and first of all, it is important to precise that the differences observed between this powder spectrum and the one (previously shown on Figure III-7) arise from a slight modification of the apparatus after a failure.

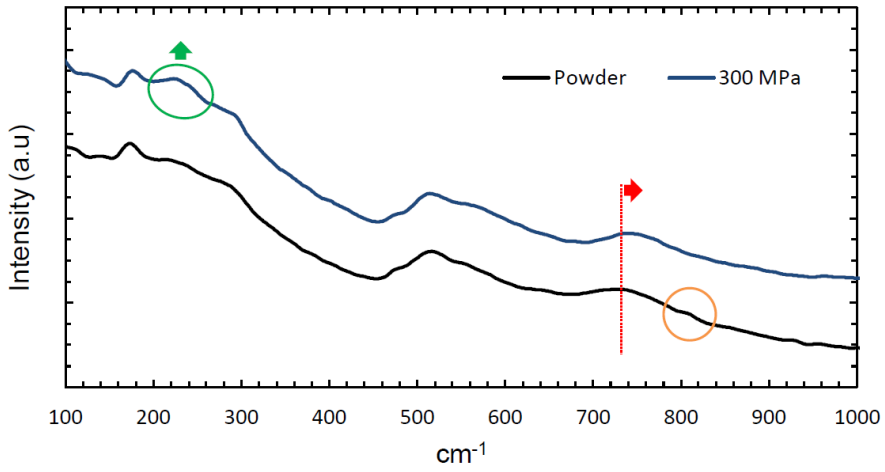

Figure IV-5. Room temperature Raman analysis of the BST powder before and after SPS processing.

Very interesting information could be pulled of this analysis and compared to the literature [264]:

- The peaks around 175 cm^{-1} and 480 cm^{-1}, observed in both; powder and ceramic, were already reported in literature and are ascribed to a strain induced orthorhombic phase, which can be locally stabilized at room temperature in nanosized ferroelectrics [265,266].

- The A_1(TO) peak around 230 cm^{-1} becomes more visible after the SPS step. This is ascribed to an increase of the tetragonality. However the signature of the pseudo cubic character is still present in both the powder and the ceramic (280 cm^{-1}).

- The E(TO) and A_1(TO) modes between 500-600 cm^{-1} which can be related to the crystalline structure do not show any frequency shift after SPS sintering under pressure.

- Blueshift of the A_1(LO3) peak at 730 cm^{-1} towards 760cm^{-1}. This phenomenon can be related to a compressive stress and can originate from the uniaxial pressure applied during SPS. This can also be a result of the release of surface stress resulting from the departure of surface and lattice hydroxyl groups after thermal treatment (the peak at 810cm^{-1} assigned to the lattice -OH is no more visible in the ceramic).

The interpretation of the results remains difficult since different contributions have to be considered when the powder and the ceramic are compared. Indeed, the strain arising from the size effect (effective in the two samples), the external compressive stress applied during the sintering at this grain size can have a strong influence. As a result, in the ceramic case, the competition between the internal stress due to size effect (coexistence of a cubic surface layer and tetragonal grain core) and the arising one from sintering make difficult the discrimination of the specific contributions which

affect the crystal structure (off centering of the Ti, distortion of the unit cell). In addition, it should be mentioned that the contribution of defects, such as –OH groups present in the powder and released in the ceramic, can affect the stabilization of the long range tetragonal structure.

IV.1.2.4 Dielectric properties

From the literature it is well known that the T_{Curie} can be tuned by (1) the cationic substitution on either the A site (Ba^{2+} with Sr^{2+}) or the B site (Ti^{4+} with Zr^{4+}) and (2) the grain size effect. For the specific case of $Ba_{0.6}Sr_{0.4}TiO_3$, V. Hornebecq et al [88] already studied the size effect on the Curie temperature variation. Indeed, we can see in Figure IV-6 that once the particles size goes below 150 nm the value of T_{Curie} decreases.

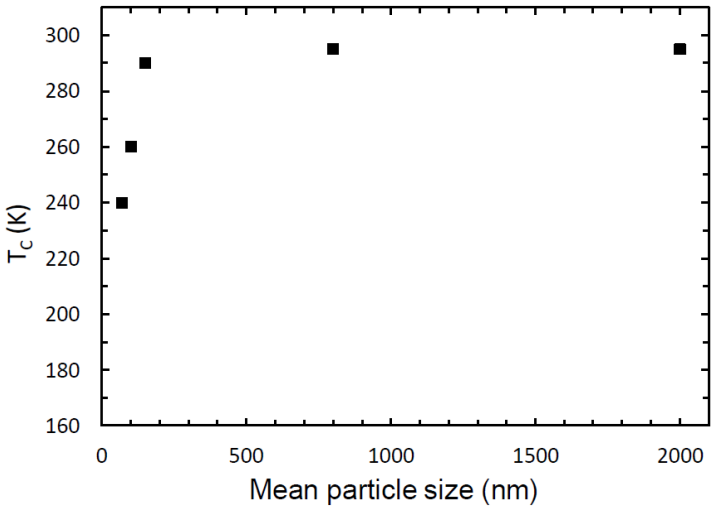

Figure IV-6. Variation of T_{Curies} according to the particles size based on V. Hornebecq et al study [88].

Now that we confirmed the processing of dense and nanostructured ceramics, keeping the starting particles characteristics in terms of size, purity and structure, we can complete the study analyzing dielectric properties of the ceramic made of 20 nm grain size. To do that we study the thermal variation of the dielectric permittivity in a temperature window from 100 to 400 K and for frequencies ranging from 0.1 to 200 kHz and Figure IV-7 presents the materials response at 1 kHz.

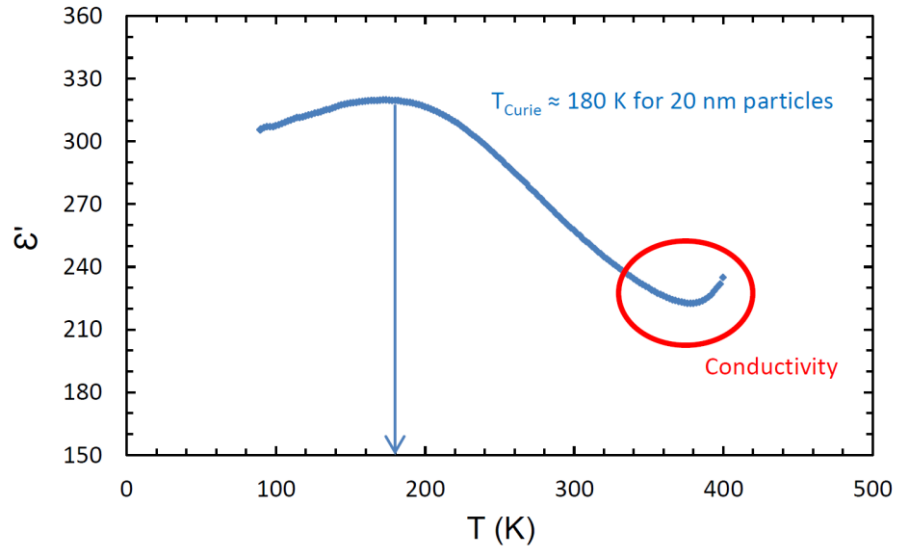

Figure IV-7. Dielectric permittivity variation according to the temperature for a BST ceramic processed with SPS (300MPa, 750°C).

Even though the dielectric permittivity is low (< 350) compared to bulk material reported in the literature (>10 000), a maximum can be observed. In contrary to the bulk, at this size range the transition from the paraelectric to the ferroelectric phase is broad and, as a result, the T_{Curie} is more difficult to define precisely; in this case it was estimated at 180 K.

In addition, at high temperature we observe the apparition of a slight conductivity. This is explained with the slight blue color from the reduced state of titanium after SPS, even if the sintering was achieved under air. This is due to a very high reactivity of the powders related to their nanozize. To make sure that this phenomenon does not impact the value of T_{Curie} the ceramic was annealed ten hours at 700°C to eliminate oxygen vacancies. The annealing temperature is below the sintering one to prevent any grain growth. After this step, the ceramic recovers a white color confirming its reoxydation.

To check that no grain growth occurs after the annealing at 700°C, we performed a SEM analysis of a fractured ceramic cross section. As shown in Figure IV-8, the average grain size remains close to 20 nm. Only a slight growth of few grains can be observed due to aggregation and in terms. In of density, the annealing step at 700°C slightly increased it from 86 to 89 %.

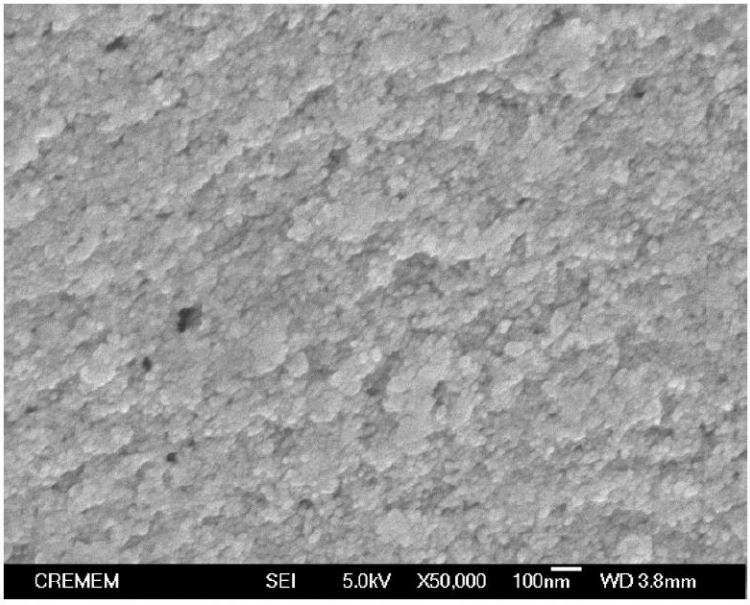

Figure IV-8. HRSEM image (JEOL JSM 6700F at PLACAMAT) of the ceramic processed with SPS at 300 MPa, 750 °C and annealed 10 hours at 700 °C.

In Figure IV-9 we now compare the variation of the dielectric permittivity of the ceramic before and after the post thermal treatment. The position of T_{Curie} did not change after the annealing, however the conductivity disappears confirming the efficiency of this reoxydation step.

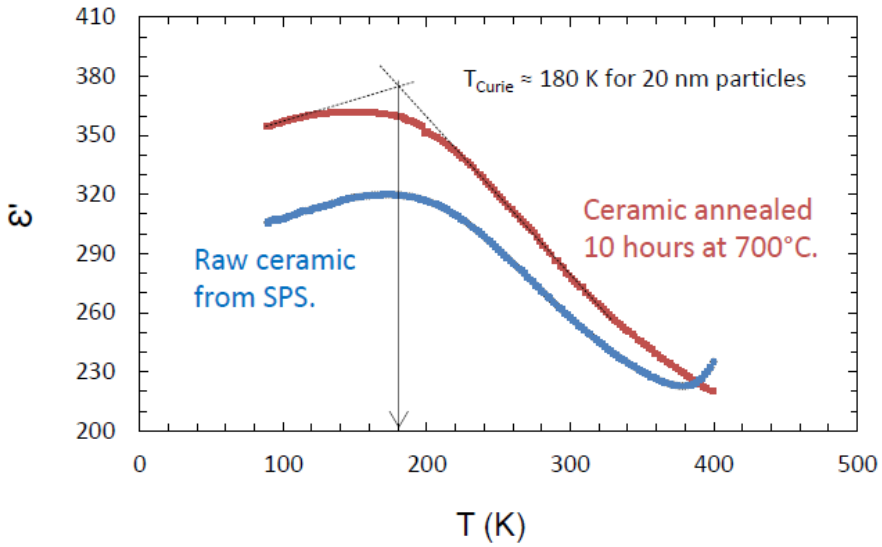

Figure IV-9. Effect of the annealing step at 700°C to reoxidize the ceramic.

The dielectric permittivity value is also slightly higher after reoxydation which can be attributed to the increase in density.

This result allows to complete V. Hornebecq et al. study [88] (Figure IV-10) with an additional T_{Curie} point at 180 K corresponding to $Ba_{0.6}Sr_{0.4}TiO_3$ particles of 20 nm. We can see in Figure IV-6 that a very good agreement is obtained with the evolution reported by the authors.

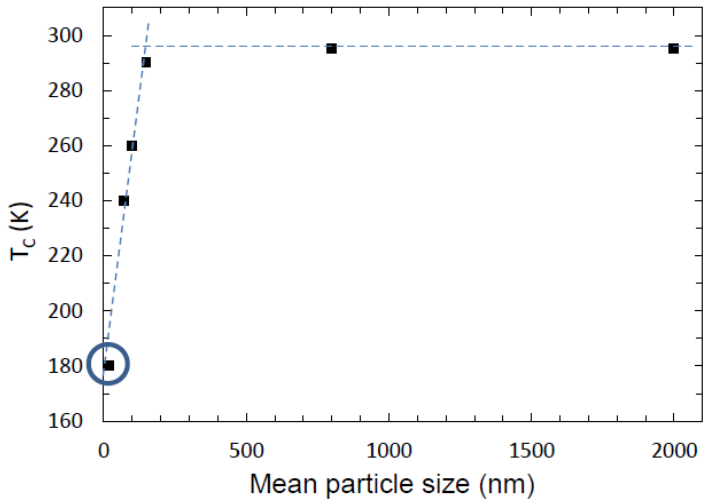

Figure IV-10. Variation of T_{Curie} according to the particles size based on V. Hornebecq et al study [88] and complete with ours

Figure IV-11 represents the thermal variation of the dielectric losses (tan δ) in the case of the ceramic annealed at 700°C.

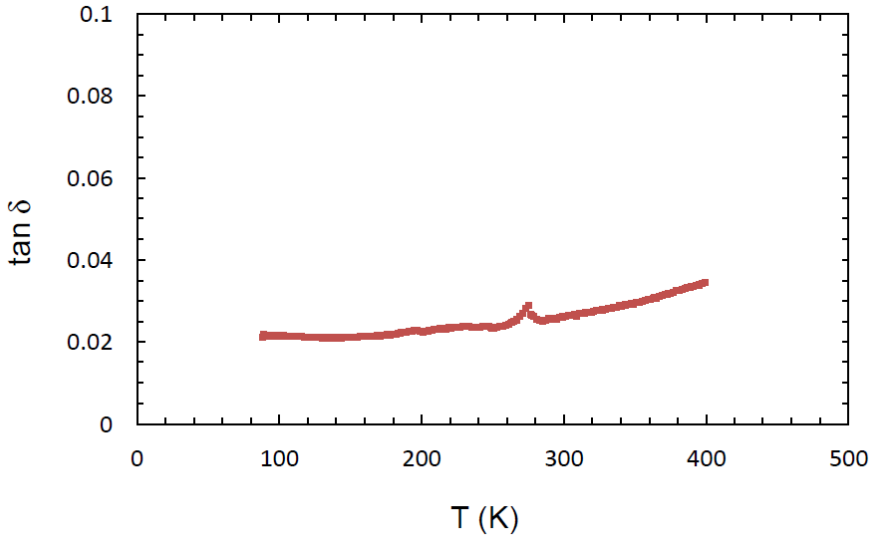

Figure IV-11. Loss (tan δ) variation according to the temperature for a BST ceramic processed with SPS (300MPa, 750°C) and annealed at 700°C.

We can note that tan δ values are in the range of 0.02 to 0.04 for temperatures between 100 to 400K and exhibit a good thermal stability. Such values are quite low considering the high density of grain boundaries and confirm that the macroscopic properties are not dominated by extrinsic

contributions. Indeed grain boundaries in nanostructured ceramics can be defect rich regions. This is in good agreement with the low permittivity values obtained which are not artificially raised by such extrinsic contributions. The stabilization of the losses in the overall temperature range can be highlighted. The maximum of losses (usually between 4 and 6%), occurring in the vicinity of the transition temperature in bulk BST, is not observed. This absence of a step the losses the thermal variations can be correlated to the specific ferroelectric domains configuration in ultrafine ferroelectric grains. Indeed, grains of 20nm size are not able to develop the formation of 90° ferroelastic- ferroelectric domains which are required to minimize the elastic energy resulting from the mechanical stress associated with the deformation of the unit cell at T_{Curie}. As a result the domain walls present within the grains are those whose displacement contributes only to the polarization (180° domains) and considering the very small size of the grains, this contribution is rather low. The losses resulting from the domain walls motion in the ferroelectric state (below T_{Curie}) are thus suppressed. Such a minimization of losses through domain structure engineering can be of considerable practical interest in many applications.

Note that the peak observed at T = 273 K is related to residual water in the dielectric cell during cooling even the measurement.

IV.1.2.5 Conclusion

Using the SPS technology we were able to process nanostructured $Ba_{0.6}Sr_{0.4}TiO_3$ ceramics made of 20 nm grain size with a density value close to 86% just after SPS and 89 % after a post thermal treatment performed at a temperature lower to the sintering temperature. Raman and XRD analyses allowed confirming that the quality of the starting materials in terms of size and purity was preserved. However the Raman analysis also pointed out a structural variation that can be related to a complex competition between different strain and stress effects arising from surface properties, size and pressure applied during sintering. It also appears that even if the sintering was conducted in air, the ceramic is slightly reduced and an annealing step at 700°C enables to reoxydize it. Finally, the dielectric characterizations allowed to determine the Curie temperature, the obtained value complement the studies in literature and proves that even at 20 nm the ferroelectric transition can be observed. Even though the value of the dielectric permittivity is quite low (< 350) compared to the literature (> 10 000), this can still be high enough according to the type of application targeted. In addition, the broadening of the transition from the paraelectric to the ferroelectric phase is strengthen in terms of thermal stability of the material properties. Finally the dielectric losses are low and remain stable over all the studied temperature range. The inhibition of the maximum of dielectric loss values near T_{Curie} reflects the minimization of domain walls contribution due to the

specific domain configuration in such nanometric grain size. These results emphasize the limited contribution of both extrinsic defects and domain walls motion to the dielectric response and valid the combination of the supercritical fluid synthesis and the Spark Plasma Sintering as a promising approach to perform functional nanostructured ceramics.

IV.1.3 Pressure effect during SPS processing

In the following part we are going to discuss the impact of the SPS processing parameters, especially the pressure, on the material's structure and consequently its dielectric characteristics.

IV.1.3.1 Materials and method

Similarly to the previous part, all the experiments were conducted with the same starting material: $Ba_{0.6}Sr_{0.4}TiO_3$ nanoparticles produced in supercritical fluids. Table IV-1 shows the experimental conditions we studied; all the parameters remain constant to the ones presented in the section IV.1.1, except the applied pressure.

Table IV-1. Experimental conditions for the study of the pressure effect during SPS processing

Experiment n°	Pressure (MPa)	Temperature (°C)	Duration (minutes)
1	300	750	2
2	350		
3	400		
4	500		
5	600		

These ceramics will be characterized in terms of density, structure and dielectric properties as a function of the applied pressure.

IV.1.3.2 Density

Figure IV-12 represents the HRSEM study of the fractured cross section of the ceramics processed at 300, 400, 500 and 600 MPa where we can see that increasing the pressure the density of the ceramic tends to increase.

Nevertheless, the metallization step prior to the analysis can affect the accuracy of the SEM analysis. To overcome this issue, first tests were performed on the ceramic sintered at 500 MPa with a JEOL JSM 7800F (at UMS Raimond Castaing) without metallization and at 2 kV.

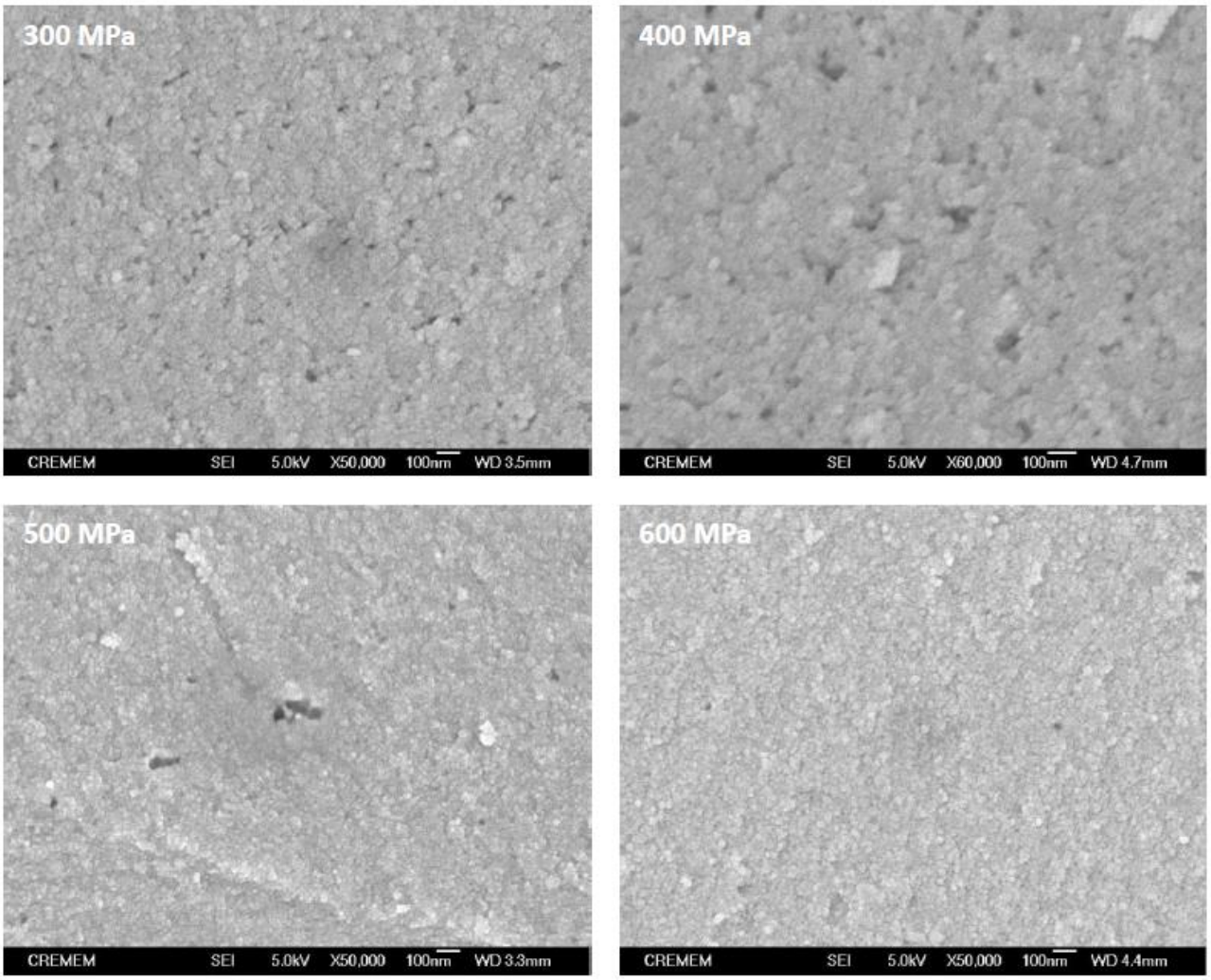

Figure IV-12. HRSEM images (JEOL JSM 6700F at PLACAMAT) of the BST ceramics processed with SPS at 300, 400, 500 and 600 MPa.

As expected (Figure IV-13) this enables us to have an HRSEM image with a better resolution, confirming that the size of the $Ba_{0.6}Sr_{0.4}TiO_3$ nanoparticles (16 ± 2 nm) was preserved during the sintering. Moreover, similarly to Figure IV-3, we can observe local areas where the particles aggregation led to a slight growth.

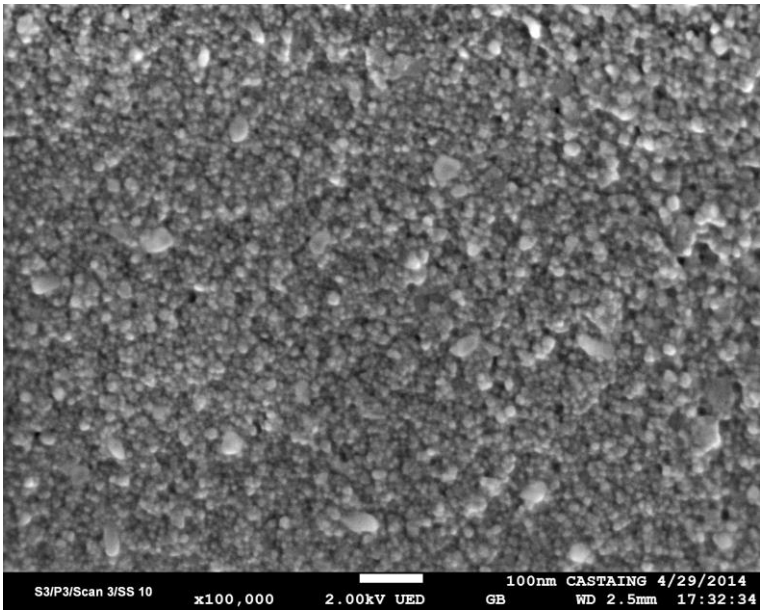

Figure IV-13. HRSEM images (JEOL JSM 7800F at UMS Raimond Castaing) of the $Ba_{0.6}Sr_{0.4}TiO_3$ powder processed with SPS two minutes at 500 MPa and 750°C without metallization.

Figure IV-14 presents the variation of the density according to the applied pressure during the SPS processing before and after the annealing at 700°C.

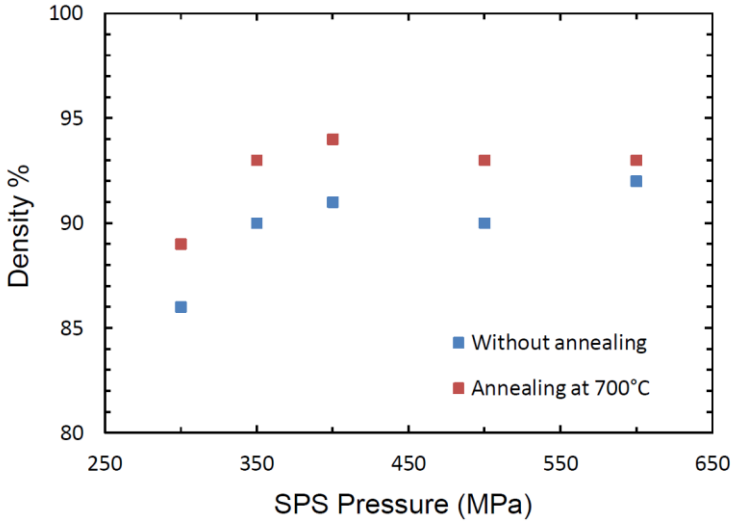

Figure IV-14. Effect of SPS pressure and annealing at 700°C on the ceramics' density.

For each pressure a slight increase in density (1-3%) is observed after annealing. The most noticeable impact of the pressure on densification lies between 300 and 400MPa: the density value increases from 86 to 91% without subsequent annealing and from 89 up to 93% after the thermal treatment. Note that this last value is quite high when considering nanostructured ceramics with grain size below 50 nm. However, increasing the SPS pressure from 400 to 600 MPa does not allowed a significant further density improvement.

IV.1.3.3 Structural analysis

IV.1.3.3.1 Effect of pressure on material's purity

A superimposition of the XRD patterns corresponding to each SPS pressure condition is shown in Figure IV-15.

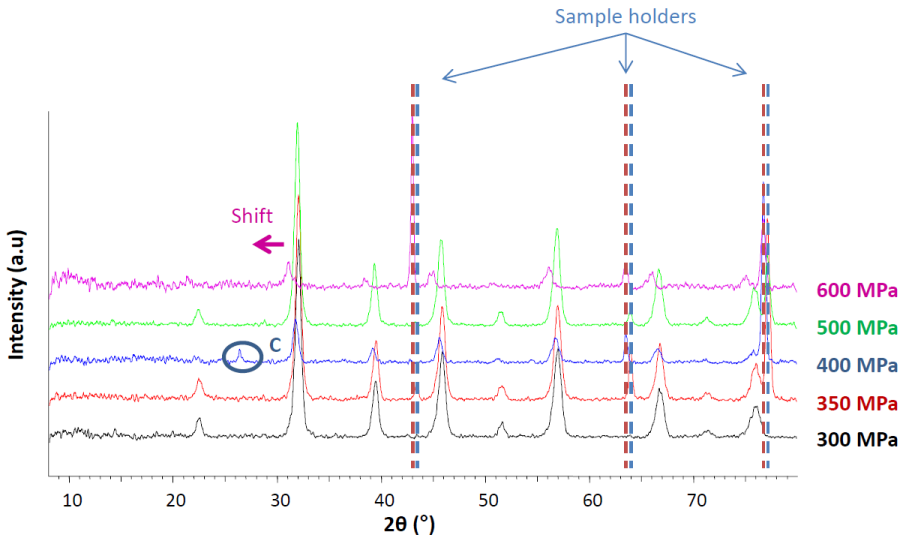

Figure IV-15. XRD patterns of the BST ceramics processed at different pressures (from 300 to 600 MPa).

Some shifts between the different patterns occur especially at 600 MPa but it is difficult to conclude unambiguously on that point. Indeed, increasing the SPS pressure, the pellets tended to broke in several pieces which is problematic in the case of XRD measurements since the surface to analyze becomes smaller. Moreover, considering this in the case of ceramics, the resolution is already not accurate enough to reasonably to go further in the structural analysis considering these patterns. However, this analysis enables us to confirm that no secondary phases are induced with SPS. Except in the case of the ceramic made at 400 MPa where we can see some carbon which is due to the graphite foil used during the SPS processing. Finally the width of the peaks remains similar confirming thus the absence of grain growth whatever the pressure applied.

Figure IV-16 shows the XRD patterns of the BST powder obtained after grinding of the ceramics made at 300 and 600 MPa. They are still "noisy" due to the small amount of powder used.

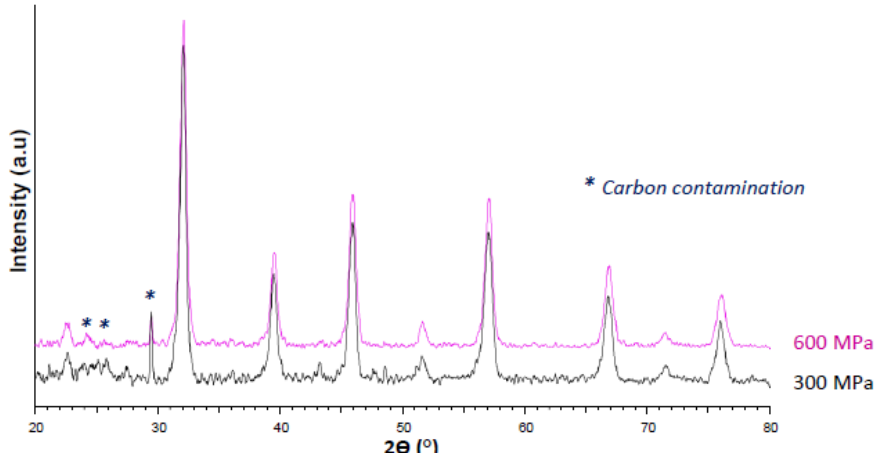

Figure IV-16. XRD patterns of the BST powder from the ceramics made at 300 and 600 MPa then milled.

We can see that the shift between the XRD patterns of the ceramics made at 300 and 600 MPa observed in Figure IV-15 is not anymore observed. Two hypotheses can be proposed: (1) a part of the stress within the material due to SPS and leading to a cell distortion, and so a peak shift, was released when the ceramics are crushed or (2) the shift was only due to an artefact of the measurement. No secondary phases are detected, only some traces of carbon contamination are still observed. Finally, the absence of grain growth which is the most important feature is here confirmed.

To go deeper in the structural characterization, we use again the Raman analysis which is not sensitive to the sample size.

IV.1.3.3.2 Effect of pressure on material structure

In Figure IV-17, we compare the spectra of the starting powder with the ones of the ceramics made at different SPS pressures.

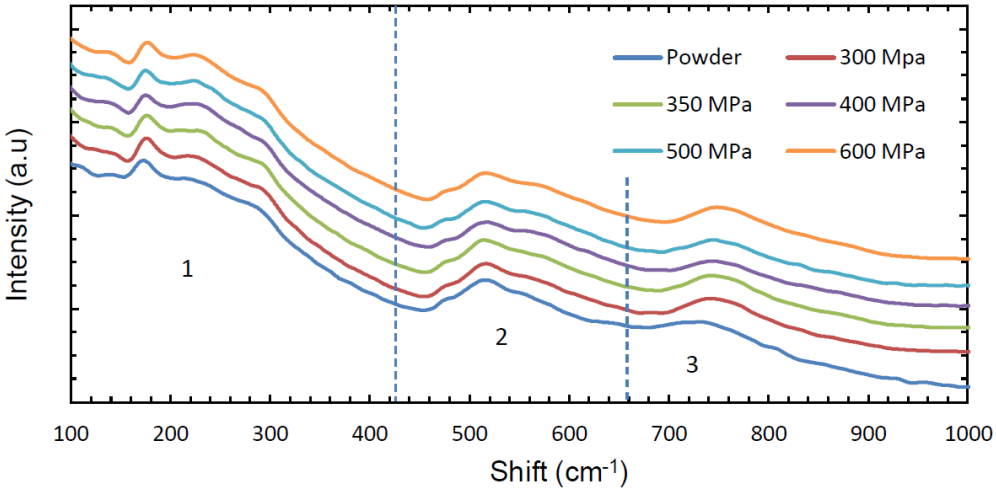

Figure IV-17. Comparisons of the Raman spectra between the $Ba_{0.6}Sr_{0.4}TiO_3$ starting powder and the ceramics made at different pressures

Similarly to the Figure IV-5, the Raman spectra can be divided into 3 main domains; 100 - 420 cm^{-1}, 420 - 660 cm^{-1} and 660 – 1000 cm^{-1}. For each applied pressure the spectra appear to be similar with the presence of a blueshift in the third area confirming the apparition of a compressive stress due to the SPS processing. However no significant evolution of this blue shift can be noticed when increasing the pressure.

IV.1.3.3.3 Conclusion

From the XRD analysis we can confirm that the SPS processing, at any pressure, does not change the purity and the grain size of the starting powder. From Raman analysis, it appears that the blueshift A_1(LO3) peak at 730 cm^{-1} towards 760cm^{-1} is observed for all the SPS ceramics but does not evolve significantly when the pressure is increased.

IV.1.3.4 Dielectric characterizations

The dielectric measurements were performed on the SPS ceramics annealed at 700°C for 10 hours in order to avoid the contribution of the conductivity (see section IV.1.2.4). Figure IV-18 shows the thermal variation of the dielectric permittivity according to the pressure applied during the SPS processing.

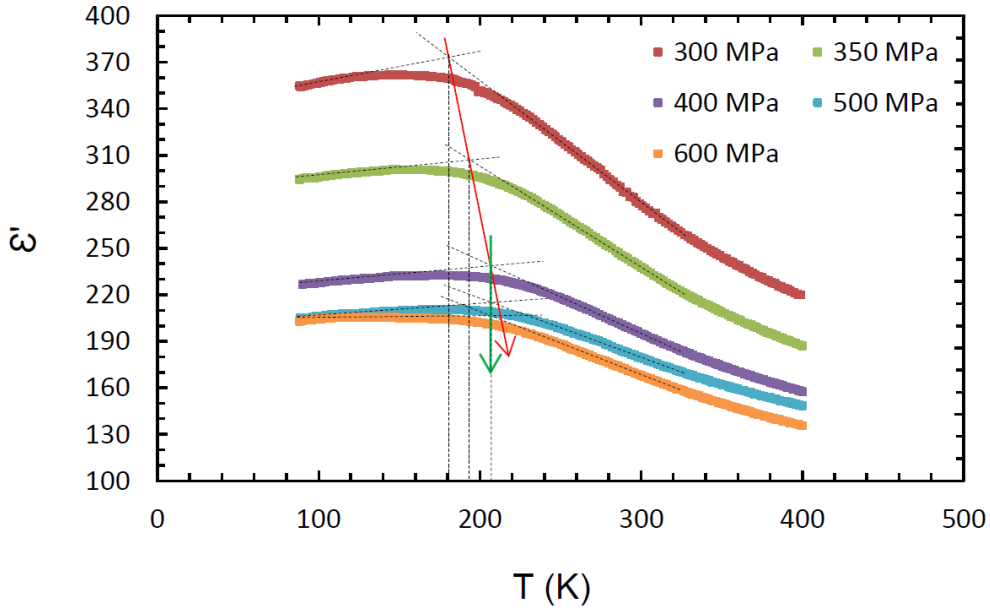

Figure IV-18. Variation of the dielectric permittivity response of the ceramics according to the pressure applied during the SPS processing

Increasing the pressure during the sintering leads to two noticeable effects: (1) a decrease of the permittivity values despite the increase in density (Figure IV-19) and (2) a variation of the Curie temperature. The transition becomes broader when increasing the pressure (Figure IV-18) and the determination of the T_{Curie} position is more difficult. This broadening is illustrated Figure IV-20 which is the superimposition of the linear regressions from the different dielectric curves (Figure IV-18), where the crossing angle between the two linear fits of each curve increases when increasing the SPS pressure.

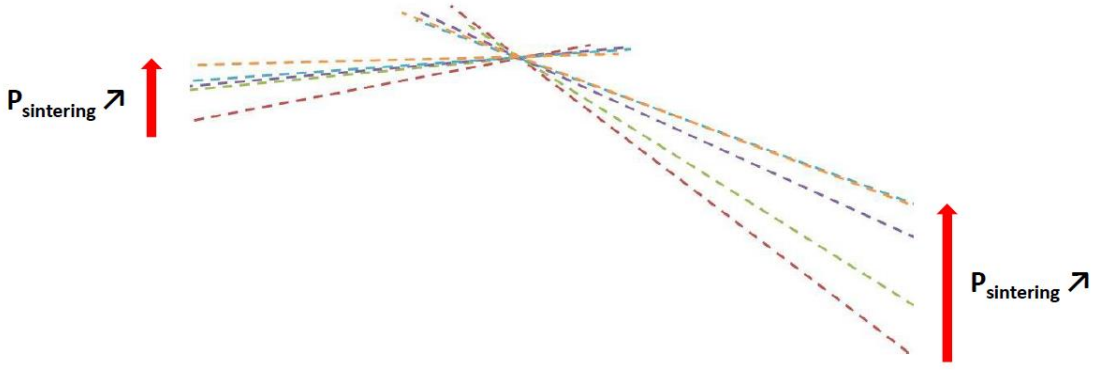

Figure IV-20. Superimposition of the fits of Figure IV-18 for determining the position of the T_{Curie}.

Reporting the T_{Curie} as a function of the applied pressure during sintering (Figure IV-21) evidences an increase of the transition temperature from ≈ 180 K up to ≈ 207 K when the pressure increases respectively from 300 to 400MPa and then remains stable in a second regime from 400 to 600 MPa.

Such an evolution can be hardly compared to the studies in literature reporting on the pressure effect on T_{Curie}. Indeed most of the studies refer to either $BaTiO_3$ or $SrTiO_3$ and concerns mainly crystals [75,267].

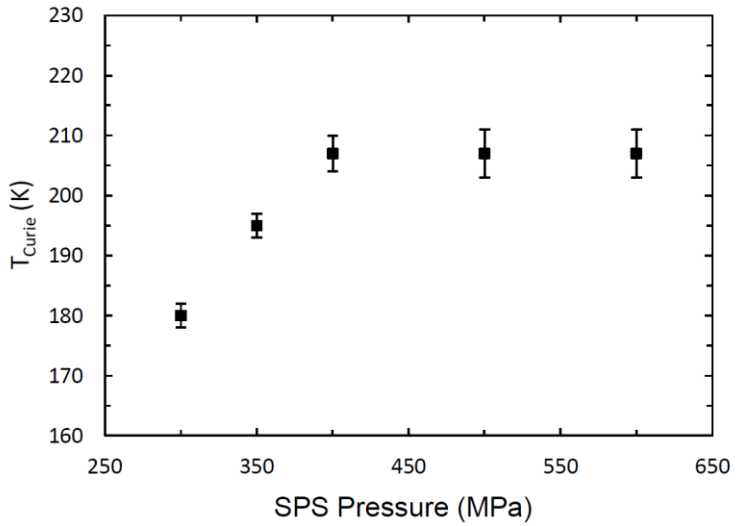

Figure IV-21. Variation of the T_{Curie} according to the pressure applied during the SPS processing.

In parallel the maximum of permittivity at T_{Curie} can be plotted as a function of the applied pressure (Figure IV-22).

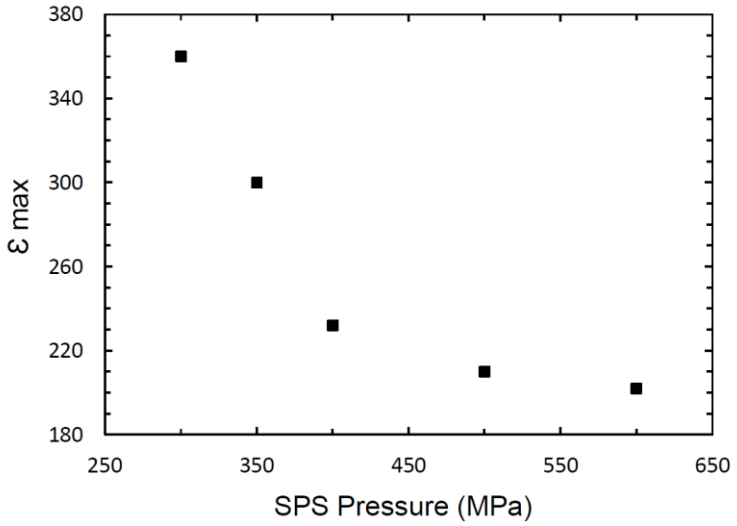

Figure IV-22. Variation of ε_{max} according to the pressure applied during the SPS processing.

Similarly to the Figure IV-21 two regimes can be distinguished, the ε_{max} values decrease up to a SPS pressure of 400MPa, and then stabilized with a further increase of pressure up to 600 MPa. As a result, the evolutions of T_{Curie} and ε_{max} observed can be thus correlated. An assumption, schematically illustrated in Figure IV-23a, can be proposed: in the first regime when the applied pressure is increased from 300 to 400MPa, the stress induced can be considered as a competitive

external stress which stands the surface strain due to size effect, leading to a decrease of the paraelectric shell contribution and thus to an increase of T_{Curie}. The remaining lateral strain forces the polarization along the direction of the applied pressure. As a result, because the electric field is applied in the direction parallel to the pressure (Figure IV-23b), the measured permittivity is lowered in a similar way than observed in crystals. At pressure values higher than 400 MPa a balance is reached between the external stress and the internal surface strain and a further increase of the pressure does not affect anymore both the permittivity and T_{Curies} values.

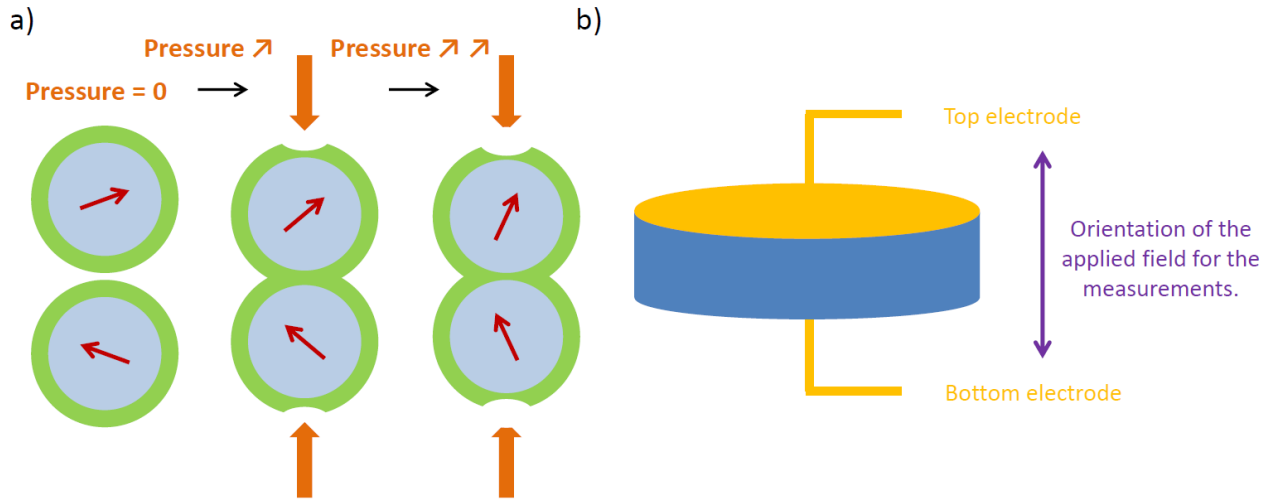

Figure IV-23. a) Effect of SPS pressure on long range polarization of the material through lowering of the paraelectric shell and b) direction of applied electric field during dielectric measurements.

IV.1.3.5 Conclusion

In this part we have shown that increasing the SPS pressure from 300 to 400 MPa enables to increase the density of the material from ≈ 86 % up to ≈ 91 % keeping the purity and the initial size of the starting powder. A further increase up to 600M Pa does not improve the density but the grain size remains close to 20 nm in the final ceramic. Whatever the applied SPS pressure the annealing step at 700°C not only enables the reoxydation of the material (conductivity is suppressed) but slightly increases the ceramics density. From a structural point of view, no obvious evolution as a function of the increased pressure was evidenced from both XRD and Raman investigations. However we highlight the impact of the SPS pressure onto the dielectric properties. Increasing the applied pressure during SPS lead to a broadening of the transition and to an increase of T_{Curie} value from 180 K (300 MPa) up to 207 K (400 MPa). A further increase of pressure up to 600 MPa does not affect anymore the transition temperature. In parallel, the evolution of the maximum of dielectric permittivity as a function of the applied pressure during SPS can be correlated to the T_{Curie} variation. As result we consider that the principal impact of the sintering pressure increase is to compensate

the surface strain induced by size effect. Such effect remains weak, that is probably why it is not observed with Raman analysis.

IV.1.4 Grain size effect

In this part, thermal treatments are performed on the ceramics in order to obtain grain growth and to probe the impact of such grain size increase on the dielectric properties. In particular the aim is to follow the evolution of T_{Curie}.

IV.1.4.1 Materials and method

To do this we use the ceramic describe in the Table IV-1, made at 750°C and applying, for two minutes, a pressure of 300 MPa. The ceramic is annealed up to 1100°C with a heating rate of 100°C/h, then is kept at this temperature for 10 hours before being cooled down to room temperature with a cooling rate of 100 °C/h. From the HRSEM image in Figure IV-24 we can observe, with this heat treatment, a grain growth from 20 to around 100 nm.

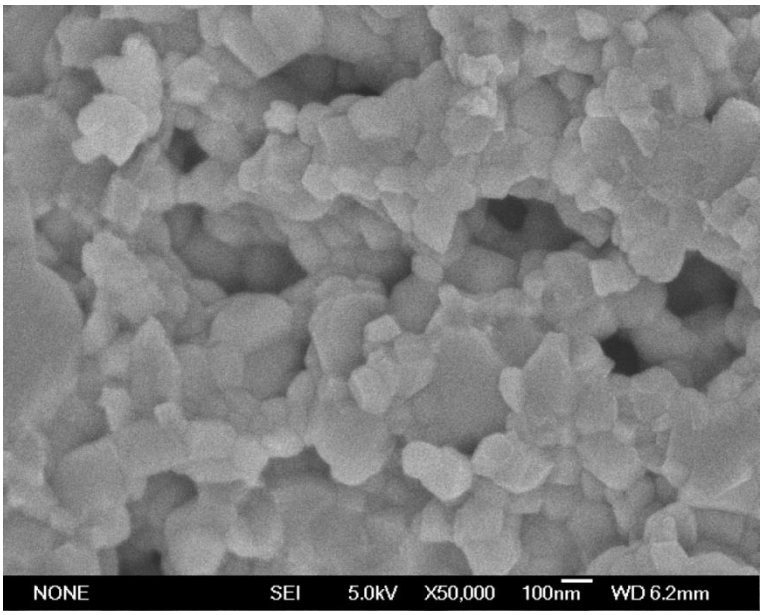

Figure IV-24. HRSEM image (JEOL JSM 6700F at PLACAMAT) of the BST ceramic SPS processed at 300 MPa and annealed 10 hours at 1100 °C.

IV.1.4.2 Structural variation and dielectric properties

Raman analysis was performed in order to probe the structural variation induced by the post sintering thermal treatment. In Figure IV-25 we superimpose the Raman spectra of the $Ba_{0.6}Sr_{0.4}TiO_3$ raw ceramics from SPS, heat treated at 700°C and 1100 °C, in parallel the corresponding thermal variations of dielectric permittivity are presented.

In Figure IV-25a, as expected, before and after the annealing at 700°C, there are no visible variations in the structure. However, once the ceramic is heated up to 1100°C for 10 hours the Raman spectrum changes significantly: the peak at 175 cm^{-1} attributed to the orthorhombic phase is no more visible. Rather a negative peak is observed suggesting that the local symmetry is more tetragonal. This is in agreement with the increased intensity of the A1(TO) peak at 230 cm^{-1}. In parallel the A_1(LO3) band around 760cm^{-1} attributed to asymmetric structure vanished reflecting a more cubic structure. We can thus conclude that the BST annealed at 1100°C (100nm grain size) exhibits at room temperature a less “distorted” cubic phase than the sample obtained just after SPS (or annealed at 700°C) with in addition the signature of local tetragonal symmetry. This can be explained by the effect of grain growth which suppresses the contribution of the strong surface strain observed in the ceramic made of 20 nm grains size. This is supported by the blueshift of the E(TO) and A_1(TO) modes between 500-600 cm^{-1} [265].

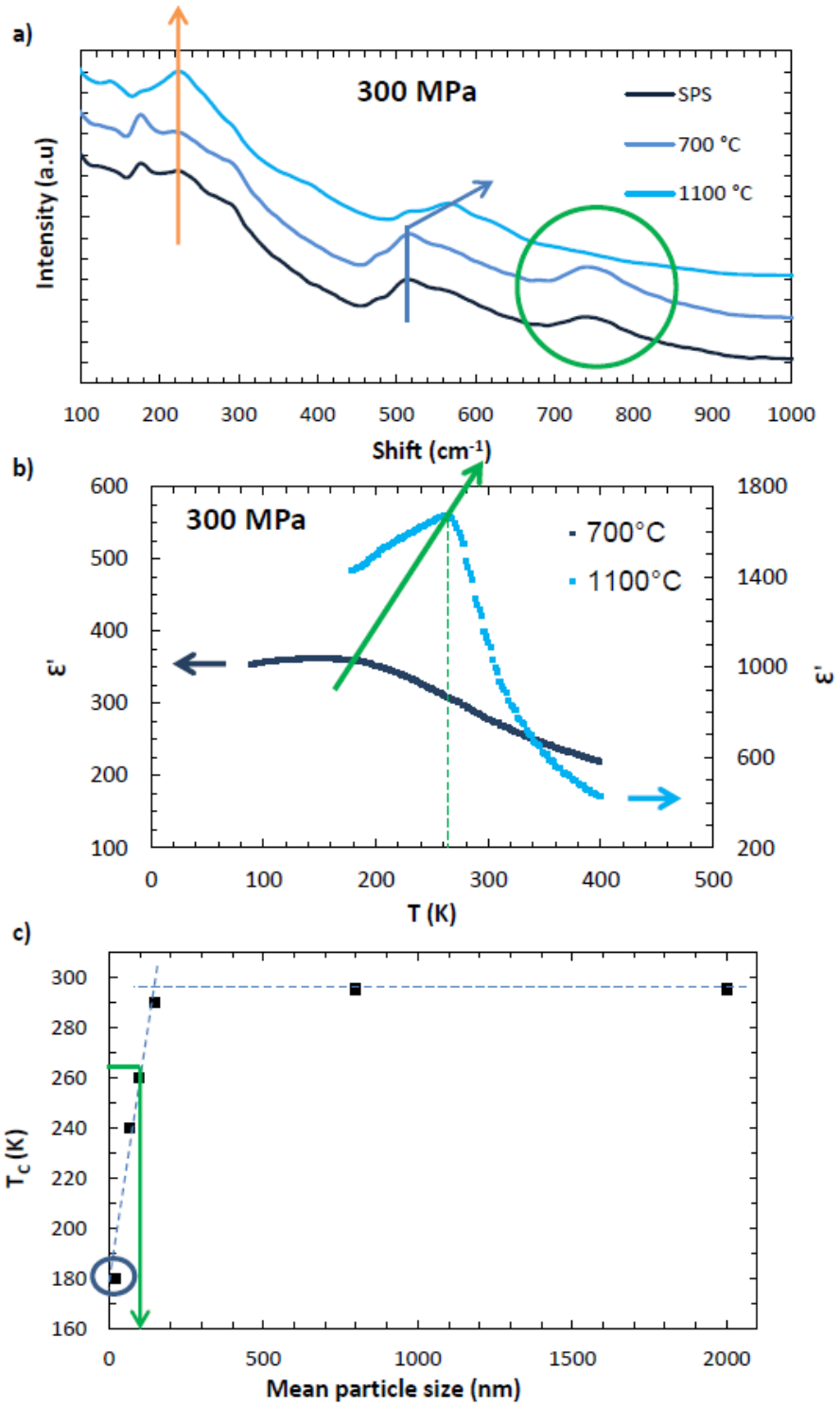

Figure IV-25. a) Raman analysis of the ceramics made with SPS at 300 MPa each before the annealing at 700°C, after it and after a heat treatment at 1100°C, b) and c) corresponding dielectric curves and T_{Curie}.

In Figure IV-25b, the dielectric permittivity is drastically increased, the transition from paraelectric to ferroelectric phase becomes sharper and the T_{Curie} is shifted towards higher temperatures. This behavior is in agreement with what we were expecting. Indeed, with a grain growth, we tend to reduce the surface strain due to the size effect. This is confirmed in Figure IV-25c with the data

reported by V. Hornebecq et al [88] (completed with our result for a grain size of 20 nm). According to this study such value of $T_{curie} \approx 263$ K corresponds to a value of grain size around 100 nm which is in very good agreement with the grain size deduced from HRSEM study. These results allow to confirm the grain size dependence on the Curie temperature in the specific case of $Ba_{0.6}Sr_{0.4}TiO_3$. Contrary to $BaTiO_3$, few studies report on the grain size effect in BST.

IV.1.4.3 SPS pressure effect

In order to highlight the effect of the pressure on the dielectric properties, a similar experiment was carried out on a ceramic sintered at 600MPa and the results were compared to those obtained for the 300MPa ceramic (Figure IV-26).

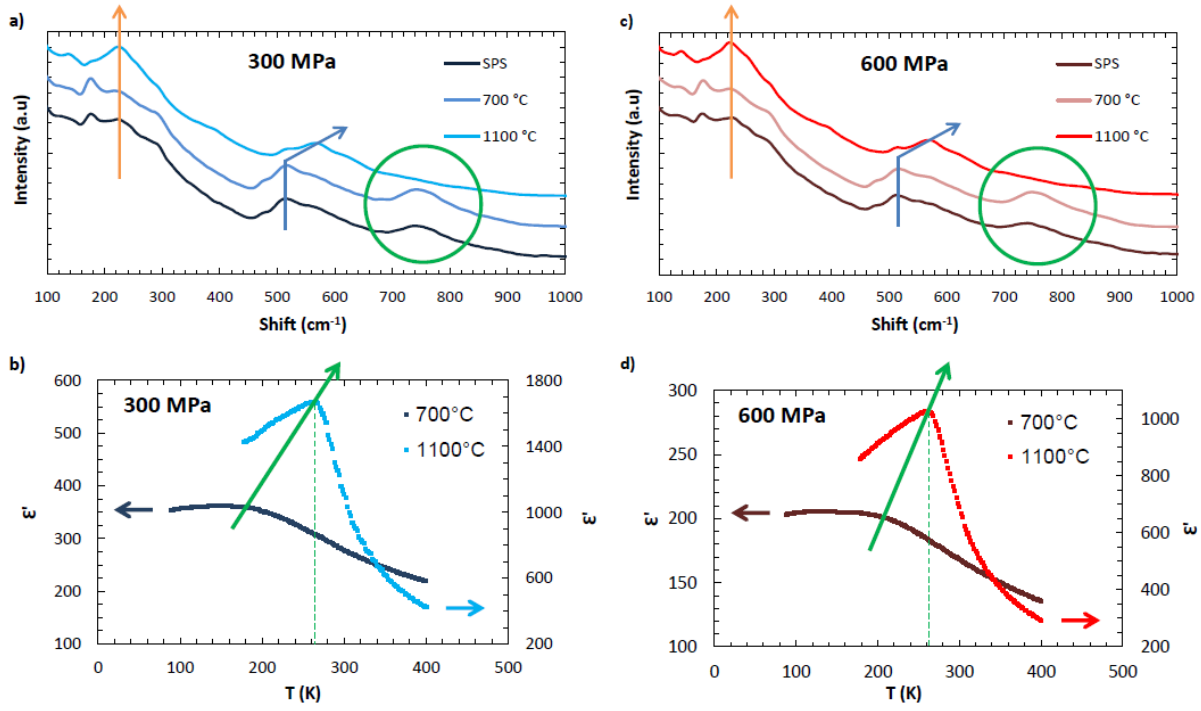

Figure IV-26. a) and c) Raman analysis of BST ceramics processed with SPS at 300 and 600 MPa and annealed at 700 and 1100 °C, b) and d) corresponding dielectric curves.

From Raman analyses (Figure IV-26a and c) we can notice that the Raman spectra are similar for both ceramics. In Figure IV-26b and d, similarly to the 300 MPa ceramic, the dielectric permittivity of the 600 MPa ceramic is drastically increased and the transition from paraelectric to ferroelectric phase becomes sharper. Moreover, it is very interesting to note that the T_{Curie} values, which were not the same for both ceramics at a similar grain size of 20 nm (180 K for the 300 MPa ceramics against 207 for the 600 MPa one), become identical (260 K) after an annealing at 1100 °C. Indeed, for the 600 MPa ceramic, after the 1100 °C annealing, the grains also have a size around 100 nm (Figure IV-27), meaning that in the latter case some residual structural strain was released.

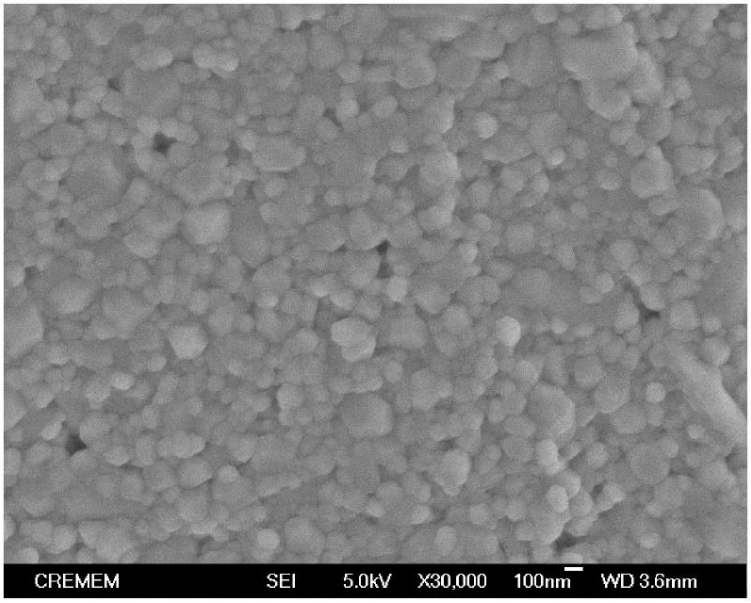

Figure IV-27. HRSEM image (JEOL JSM 6700F at PLACAMAT) of the BST ceramic SPS processed at 600 MPa and annealed 10 hours at 1100°C.

This confirms that the pressure applied during SPS can affect the structural distortion within the 20 nm grain size. Nevertheless, when the surface strain is relaxed thought the grain growth such additional stress does not have any impact on the Curie temperature.

IV.1.4.4 Conclusion

An annealing performed at 1100 °C for 10 hours enables to grow the grain size from ≈ 20 to ≈ 100 nm. However, based on Raman analysis we showed that it leads to important structural variations with the coexistence of both cubic and a more tetragonal phases. Dielectric measurements performed on the annealed ceramics exhibit an increase of the permittivity, a narrow phase transition from the paraelectric to the ferroelectric and a shift of the T_{Curie} towards higher values. All these features are ascribed to a grain growth. After the thermal treatment and whatever the pressure initially applied during SPS, the ceramic grains size reaches ≈ 100 nm and the T_{Curie} merge in a same value, confirming thus that the difference of T_{Curie} observed in the 20 nm ceramics grains size is directly related to the external stress induced by the SPS pressure. Finally, the good agreement obtained between the data reported by V. Hornebecq et al study [88] and our results confirm the possibility to predict the T_{Curie} according to the particles size in BST.

IV.1.5 Conclusion

In this part we showed that using SPS, we were able to process nanostructured $Ba_{0.6}Sr_{0.4}TiO_3$ ceramics keeping the starting particles size of ≈ 20 nm as well as the material purity with a density

ranging from 86 to 93 %. We demonstrated that, at such small grain size, the ferroelectric transition can be observed. The permittivity value is quite low (≈ 350) but a remarkable good thermal stability is obtained due to the diffuse character of the paraelectric-ferroelectric transition. In addition the dielectric losses remain stable and low all over the temperature range with in particular the absence of the maximum occurring usually at T_{Curie}. Such features are interesting regarding the aimed applications. Adjusting the pressure applied during SPS enables a further control of the dielectric parameters with in particular the possibility to increase T_{Curie} while decreasing the permittivity when the SPS pressure is increased. In a first approximation, such evolutions can be related to a competitive effect between the size effect on the intrinsic properties due to the surface strain and the external compressive stress. However further work is needed to confirm this assumption. Finally we showed that the T_{Curie} can also be tuned by increasing the ceramic grain size through post thermal annealing. Our results have allowed not only to confirm but also to complete previous results in literature devoted to grain size effect in BST.

In the next section we are going to study the processing BTZ nanoparticles produced in supercritical fluids into ceramics and their ferroelectric / relaxor properties.

IV.2 BTZ ceramics

The objective of this part is to prove the accuracy and the reliability of the supercritical fluid synthesis in terms of control of composition when applied to the solid solution $BaTi_{1-y}Zr_yO_3$ (with $0 \leq y \leq 1$). The strategy is to compare the ferroelectric properties obtained on the ceramics performed using our powder with those reported in literature. To this aim we select two compositions x = 0.15 and 0.3 for which the dielectric properties are supposed to change from ferroelectric to relaxor behavior [268]. Through the determination of both T_{Curie} and T_m the dielectric characterizations will be used as a macroscopic probe for the composition. In this part it is important to note that the aim is different from the BST study as our objective is not to keep the initial nanometric grain size but to characterize the ferroelectric behavior according to the composition and independently of any size effect.

IV.2.1 Materials and method

To fulfill this objective, the most suitable and the simplest way to perform ceramics is to use the "conventional process" (see section II.3.1.1.1). Raw pellet were pressed under an uniaxial pressure and then sintered in air in a furnace. From the literature it appears that the BTZ ceramics are usually sintered at temperatures ranging between 1200 - 1900°C and for 4 to 8 hours [81,85,253,269,270]. The BTZ nanoparticles sizes we produced in supercritical fluids are very small (≈ 15 ± 3 nm) and present a high surface reactivity. We thus estimate that a lower sintering temperature may be sufficient to reach a correct densification. In our case, after a dwell of one hour at 450°C to burn the binder we chose to perform a dwell time of 4 hours at 1200°C for both compositions. The heating rates were 100°C/hour to reach the 450°C plateau then increased up to 200°C/min to reach the second one at 1200°C and the cooling rate was 200°C/min to reach room temperature.

IV.2.2 Ceramics characterization

IV.2.2.1 Density and purity

The densities of the obtained ceramics were close to only 65% for each. Considering such high level of porosity, the dielectric characteristics will not be discussed in terms of permittivity values in this section. However the transition temperature being an intrinsic parameter, independent on the density of the ceramic, we will focus on the determination of ferroelectric and relaxor behaviors.

Figure IV-28 shows that the peak positions did not change between the starting powder and the ceramic confirming that the phase compositions were preserved. In addition we can see that the

widths of the peaks for the ceramics are thinner indicating that, as expected, a grain growth occurred during sintering.

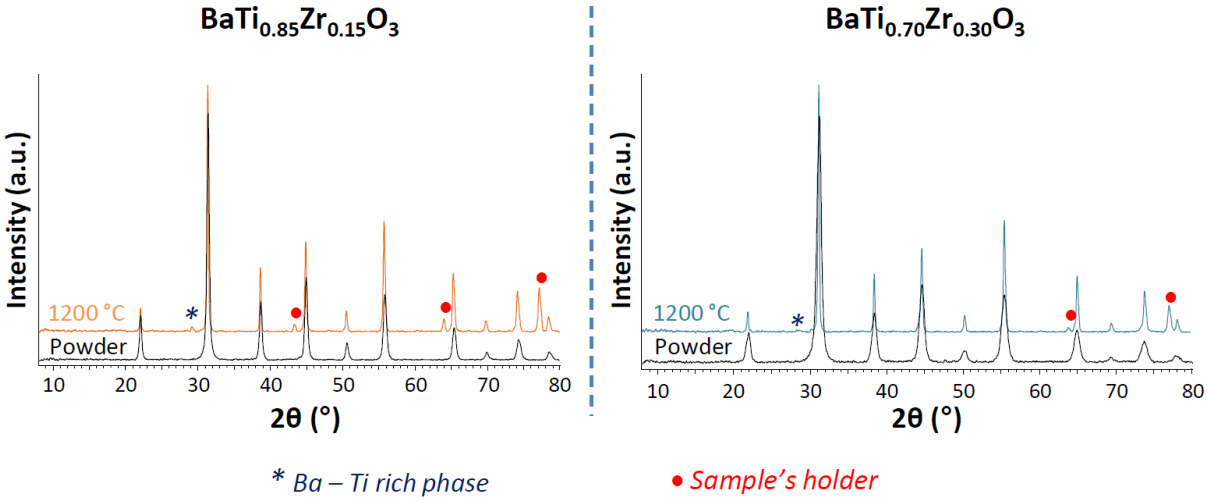

Figure IV-28. XRD patterns of $BaTi_{0.85}Zr_{0.15}O_3$ and $BaTi_{0.7}Zr_{0.3}O_3$ powders and ceramics sintered at 4 hours at 1200°C.

However, in addition to the sample holder peaks, we can observe few weak extra peaks, especially at 29°. This extra phase was difficult to identify but appears to be a rich barium and titanium phase. This secondary phase being in minority we chose to go further into the ceramic characterization.

IV.2.2.2 Microstructure

IV.2.2.2.1 Microstructure of the sintered ceramic

The ceramic microstructures were investigated by SEM using secondary electrons detectors. Whatever the composition, inhomogeneous microstructures were observed (Figure IV-29).

In both cases, in addition to a grain growth from the initial nanosize up to the micrometer scale, exaggerated anisotropic grain growth is evidenced. This phenomena is more pronounced when increasing the zirconium content (case of y = 30). These anisotropic grains are randomly oriented throughout the ceramic and their dimensions can be estimated as 1 µm wide and tens µm length.

This observation is surprising considering that no significant extra phase was detected by XRD after sintering. In addition such microstructure evolution in BTZ was never reported in literature. Backscattered electrons detector was thus used to probe the change in chemical composition through the sample.

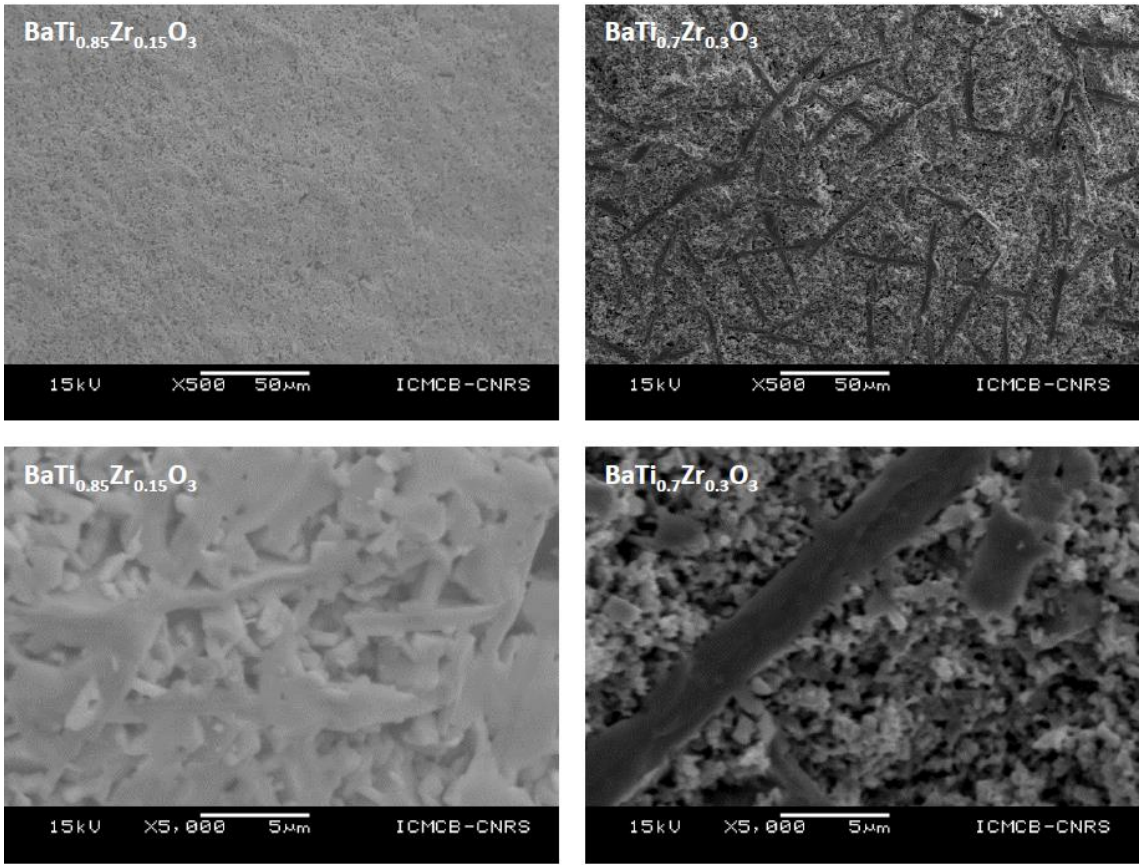

Figure IV-29. SEM images (JEOL 6360A at ICMCB) of the $BaTi_{0.85}Zr_{0.15}O_3$ and $BaTi_{0.7}Zr_{0.3}O_3$ ceramics sintered at 1200 °C.

IV.2.2.2.2 Chemical composition of the sintered ceramic

The use of backscattered electrons, from which the energy depends on the nature of elements exposed to the electron beam, enable a chemical analysis of specific areas of the ceramic cross section, giving more local information than XRDs. Indeed, the darker zones correspond to lighter elements.

Using this analysis (Figure IV-30), we can see that the anisotropic grains do not seem homogeneous in composition. Referring to the chemical contrast, the edges of these anisotropic grains should correspond to a barium - richer phase compared to their center which appear darker. This qualitative observation implies different migration rates between the cations involved in the diffusion process occurring during the sintering, in particular a slower migration of Zr^{4+} and Ti^{4+} in comparison to diffusion of the alkaline-earth cation. Such diffusion -related phenomena can be assimilated or compared to the Kirkendall effect which, in addition, is known to be favored by the presence of defects [271]. The amount of defects is greater in the initial powder when increasing the zirconium content and as observed the effect is enhanced for the $BaTi_{0.7}Zr_{0.3}O_3$ ceramic.

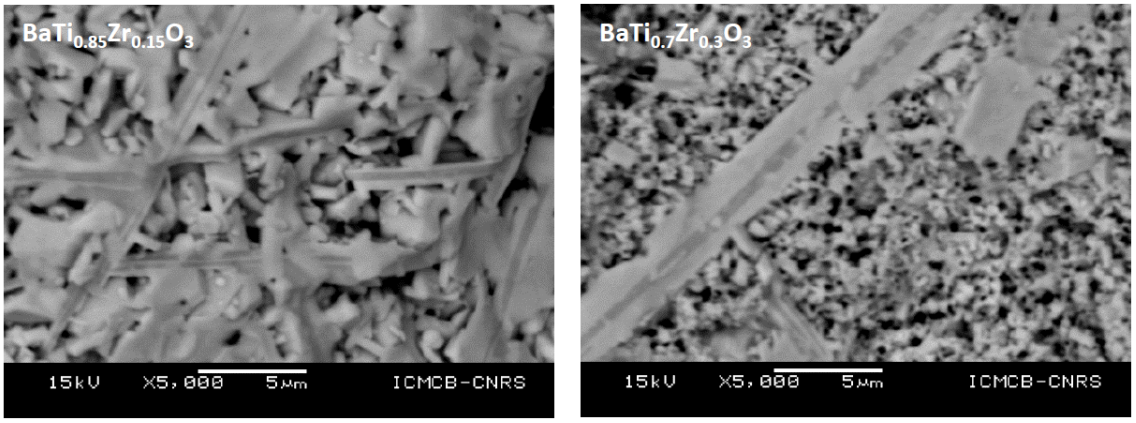

Figure IV-30. Backscattered electron images (JEOL 6360A at ICMCB) of the $BaTi_{0.85}Zr_{0.15}O_3$ and $BaTi_{0.7}Zr_{0.3}O_3$ ceramics sintered at 1200 °C.

To go deeper in the chemical analysis of the ceramics energy-dispersive X-ray spectroscopy (EDS) cartography of the $BaTi_{0.7}Zr_{0.3}O_3$ ceramic was performed (Figure IV-31).

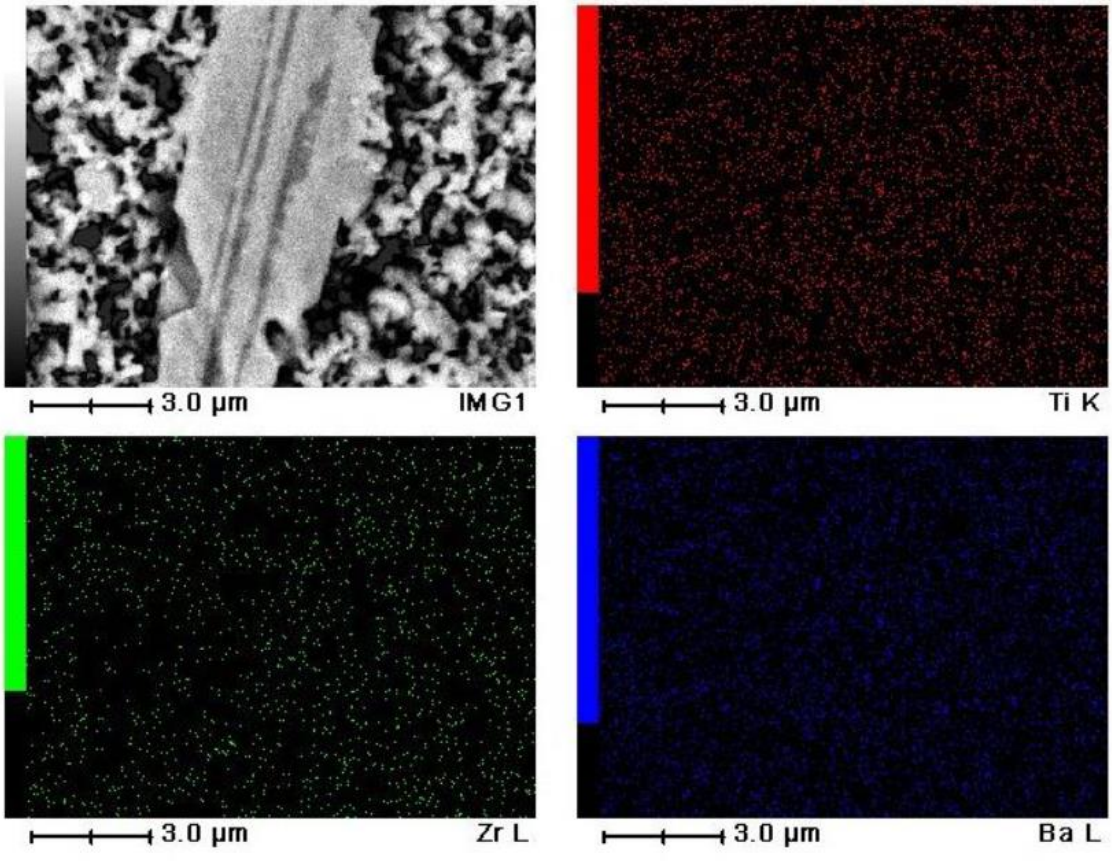

Figure IV-31. EDS cartography (JEOL 6360A at ICMCB) of the $BaTi_{0.7}Zr_{0.3}O_3$ ceramic sintered at 1200 °C.

From these images we can see that the overall composition appears homogeneous, however, this does not enable to get more precise information about an eventual composition gradient within the anisotropic grains. Indeed, when we compare the resolution of the analysis (1 μm^3) to the width of

the anisotropic grains around 1 µm, it is not accurate enough to be able to conclude. In addition, the energy of the photon collected for the barium and titanium being very close it is not possible to quantify both elements.

In conclusion, even if we observe the presence of inhomogeneous anisotropic grains (1 µm wide and tens µm long) randomly oriented throughout the ceramic, the overall compositions of the ceramics tend to be homogeneous. An additional indirect way to probe the chemical composition is to perform dielectric measurements as the transition temperature is very sensitive to the composition. Then, comparing the values to the literature, we will be able to see if the presence of anisotropic grains has an impact on the ferroelectric / relaxor properties.

IV.2.2.3 Dielectric characterizations of the ceramics

From Figure IV-32 we can distinguish two different behaviors according to the composition; the ceramic corresponding to y = 0.15 exhibits a ferroelectric behavior with a T_{Curie} ≈ 335 K independent of the frequency while the ceramic corresponding to y = 0.30 behaves as a relaxor with T_m ≈ 295 K at 100 Hz.

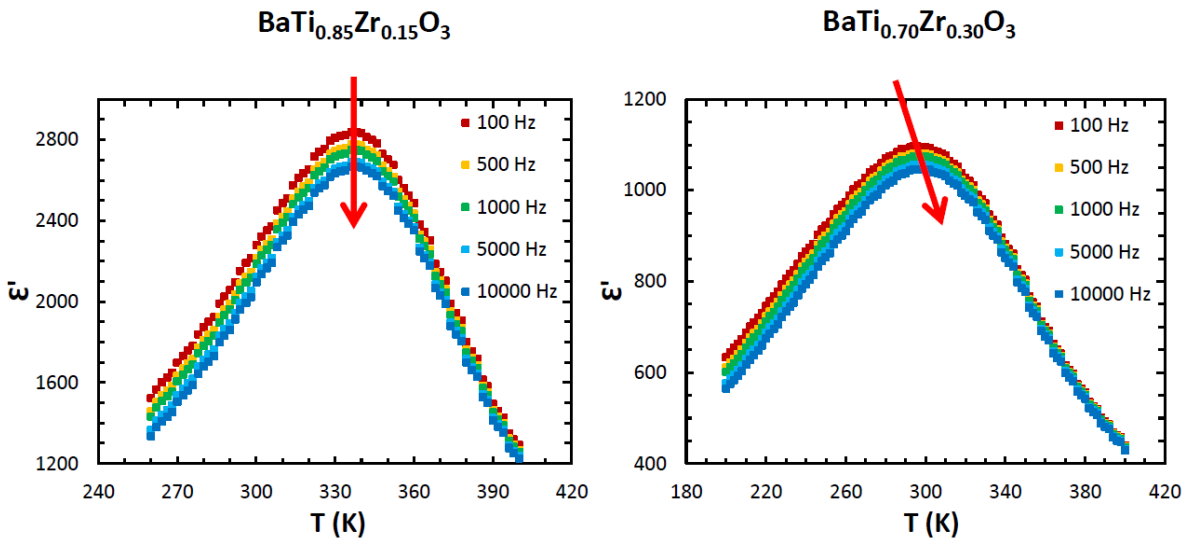

Figure IV-32. Dielectric measurements of the $BaTi_{0.85}Zr_{0.15}O_3$ and $BaTi_{0.7}Zr_{0.3}O_3$ ceramics sintered at 1200 °C.

Comparing these values to the literature we can note that T_{Cure} (when y = 0.15) has the expected value, whereas, T_m (y = 0.30) is slightly higher than expected [253,272]. However for this case, it is important to underline the spreading of values of T_m reported in literature, ranging from 220 to 270 K. However the higher T_m value obtained in this work might be related to the presence of these inhomogeneous anisotropic grains, it is thus necessary to deeply investigate their formation and

composition, especially for the higher zirconium content composition ($BaTi_{0.7}Zr_{0.3}O_3$) for which the impact on the dielectric properties is the most visible.

IV.2.3 Study of anisotropic grains formation

To better understand the complex microstructure of the studied ceramics, we focused on $BaTi_{0.7}Zr_{0.3}O_3$ for which the effect is more pronounced. The first experiment consisted in an increase of the sintering temperature up to 1400°C, keeping the other sintering parameters constant, in order to favor this anisotropic growth and identify more precisely the occurrence of extra phases by XRD. As expected, in Figure IV-33a we can clearly observe this secondary phase were the peak at 29°, previously identified, is the most intense one. This is indeed a phase reach in barium and titanium which can be identified as $BaTi_2O_5$, Ba_2TiO_4, $BaTi_6O_{13}$, $Ba_2Ti_9O_{20}$, etc. Moreover, a zirconium oxide phase starts to appear. In addition, we can note on the SEM images in Figure IV-33b and c that the anisotropic grains are still present for the ceramic sintered at 1400°C.

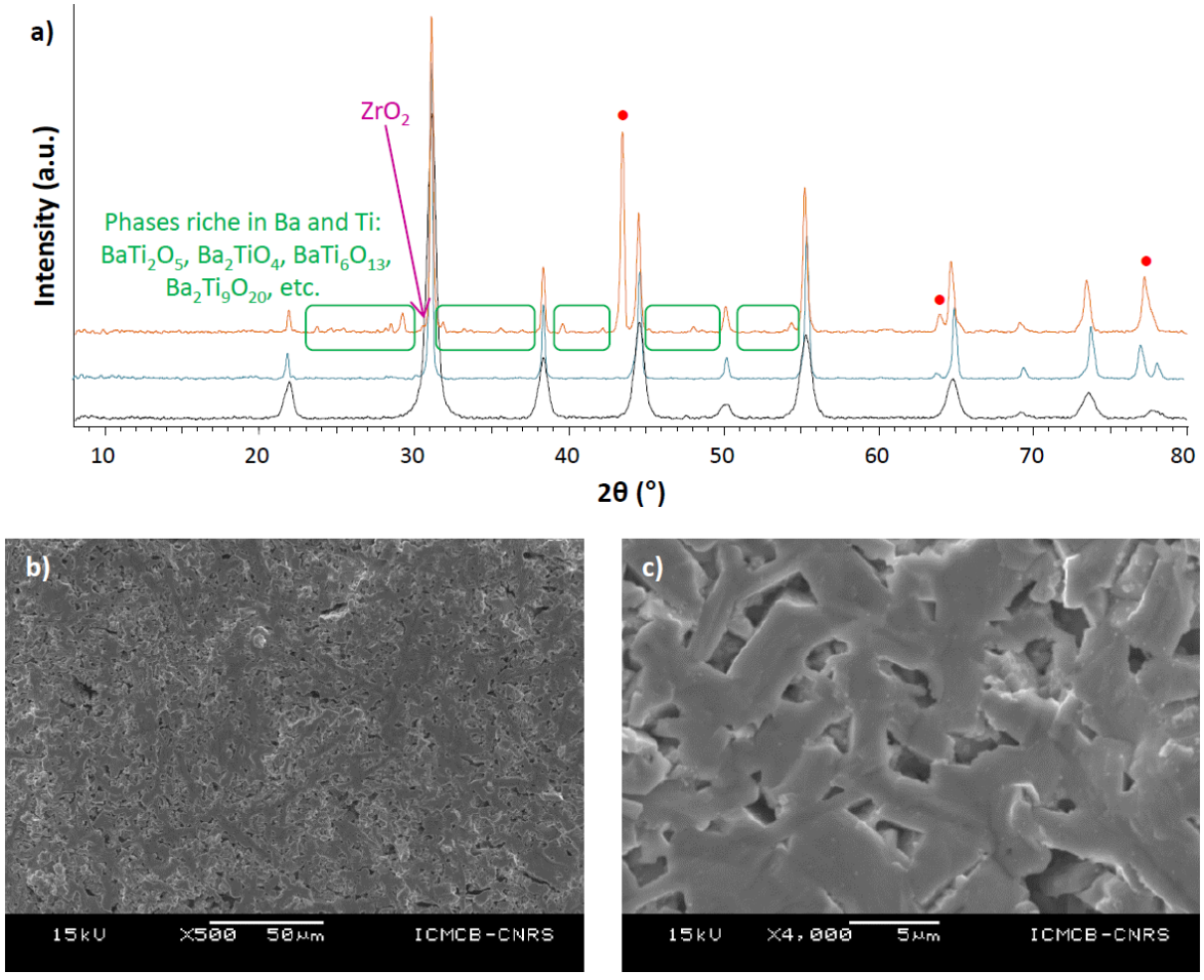

Figure IV-33. a) XRD analysis of the sintering effect temperature on $BaTi_{0.7}Zr_{0.3}O_3$, b) and c) SEM images (JEOL 6360A at ICMCB) of the $BaTi_{0.7}Zr_{0.3}O_3$ ceramic sintered at 1400 °C.

This experiment gives us some insights concerning the composition of the anisotropic grains. Indeed, we saw in Figure IV-30 (ceramic sintered at 1200°C) that the sides of the anisotropic grains were brighter; this can be associated to the barium and titanium rich phases, the barium being the heavier element. The center which is darker would thus be associated to the zirconium oxide one.

The next step of this investigation is to modify the cooling rate since crystallization process can be favored during the cooling step. We thus proceed to a quenching in an ice bath of a ceramic sintered at 1200°C in order to check if the growth of the elongated grains could be avoided. We decided to not lower the sintering temperature in order to keep as much as possible all the others parameters constant. In addition, the density of the ceramic being already very low at 1200 °C (≈ 65%), a further decrease in sintering temperature would have been detrimental regarding densification.

Unfortunately, we can observe on the SEM images from Figure IV-34 that this anisotropic growth still occurs.

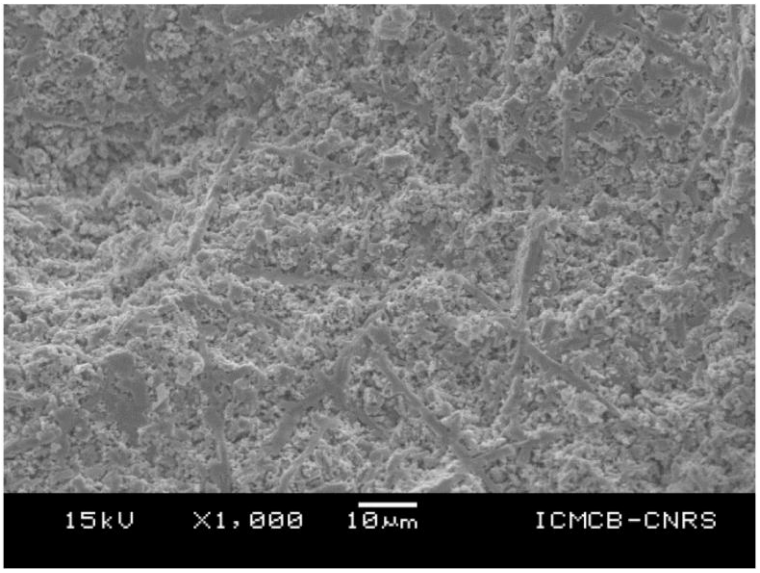

Figure IV-34. SEM image (JEOL 6360A at ICMCB) of the $BaTi_{0.7}Zr_{0.3}O_3$ ceramic sintered at 4 hours at 1200 and quenched.

The conventional process does not seems to be the most suitable for sintering the BTZ nanoparticles, we thus decided to change drastically the sintering kinetics and use fast sintering processes. Again, we used spark plasma sintering (SPS), which enables to significantly shorten the sintering cycle (dwell of few minutes, high heating and cooling rates) compared to conventional sintering and thus to limit the diffusion processes. For this, we used the apparatus available at ICMCB, a Dr. Sinter 515S machine.

In this experiment the heating rate was 100°C/min and a pressure of 100 MPa was applied three minutes at 1200°C before cooling down switching off the electric current. This enables both, fast heating and cooling. In addition the sintering was performed under vacuum and the 8 mm die was in graphite.

First of all a drastic improvement of density was obtained using SPS, indeed the density was estimated at 90 %. From the SEM images Figure IV-35 we can observe a very homogeneous microstructure without abnormal grain growth. However, the ceramic is made of fine grains with an average size below 200nm. Nevertheless, the poor resolution does not enable us to have a more precise value of the grains size. To improve this it would be necessary to use a HRSEM.

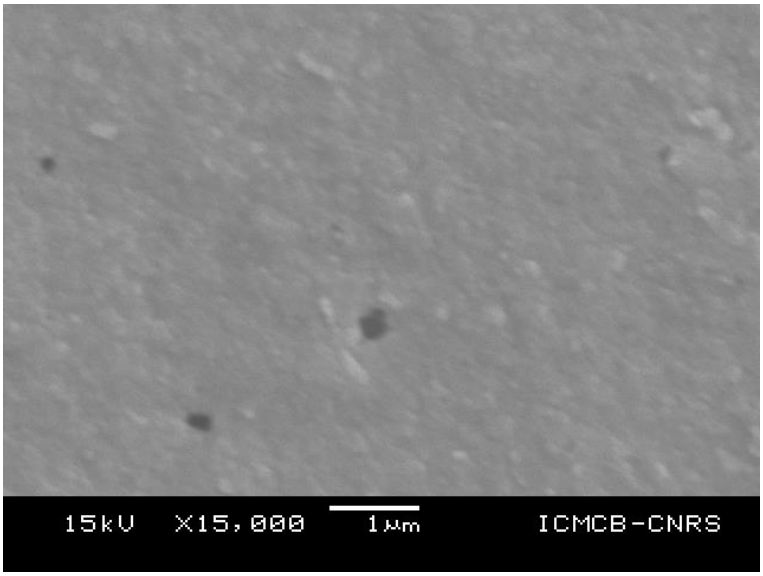

Figure IV-35. SEM image (JEOL 6360A at ICMCB) of the $BaTi_{0.7}Zr_{0.3}O_3$ ceramic sintered with SPS (3 minutes at 1200°C and 100 MPa).

If we check the purity of the ceramic using XRD (Figure IV-36), we can confirm that there are no extra phases and a slight grain growth since the width of the peaks is narrower.

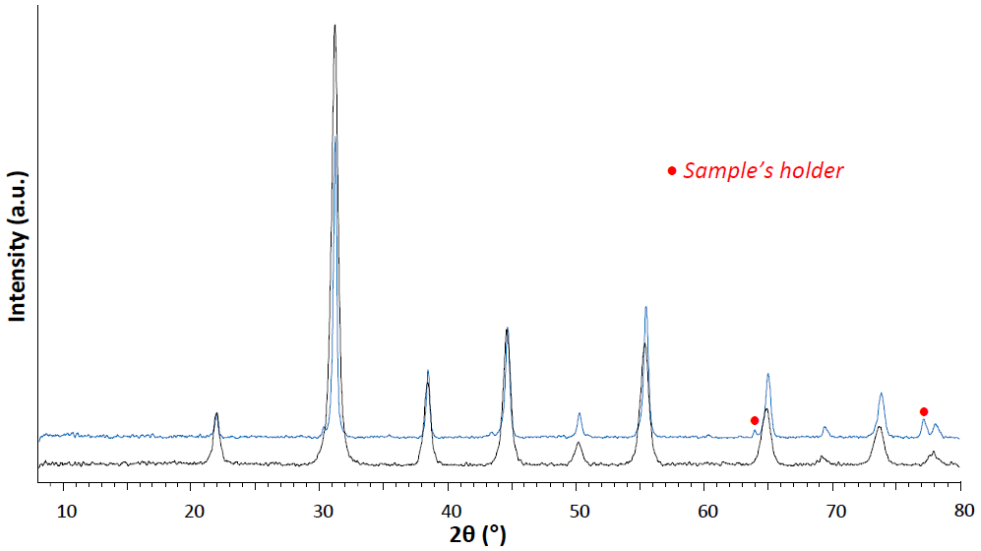

Figure IV-36. XRD pattern of the $BaTi_{0.7}Zr_{0.3}O_3$ powder (black) ceramic (blue) sintered with SPS (3 minutes at 1200°C and 100 MPa).

Now that the ceramic does not present any anisotropic grains we can measure the dielectric properties of the ceramic (Figure IV-37) which, similarly to the BST study, might be affected by the particles size effect. Prior to this an annealing step in air at 1000°C was performed in order to reoxidize the ceramic. The annealing temperature is higher than for BST since BTZ starting powder presents more defects which can be trapped during the SPS processing due to carbon contamination (see section III.3.3.2).

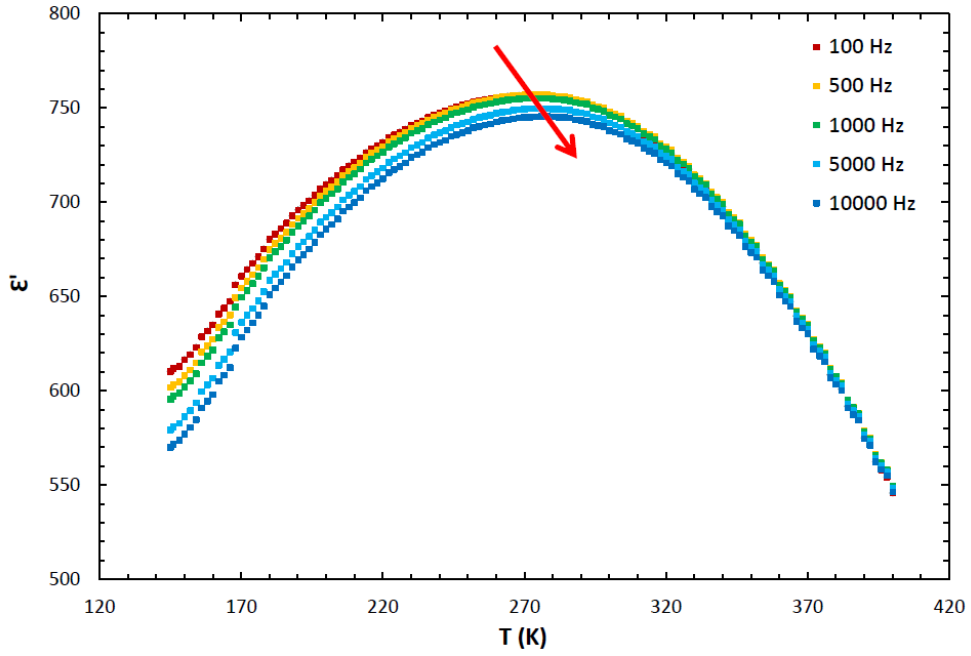

Figure IV-37. Dielectric measurement of the $BaTi_{0.7}Zr_{0.3}O_3$ ceramic sintered with SPS (3 minutes at 1200°C and 100 MPa).

As expected, a relaxor behavior is observed, with a $T_m \approx 270$ K at 100 Hz which is in better agreement with the values reported in literature. Nevertheless, compared to ceramic conventionally sintered, the transition is broader and the permittivity decreased, despite a higher density in this SPS ceramic. These features can also be ascribed to a size effect. Few studies are reported in literature on the influence of the grain size on BTZ, it thus difficult to conclude on a possible relation between the grain size and the change in temperature T_m. However, the observed grain size by SEM is believed to be above a critical size regarding the transition temperature.

IV.2.4 Conclusion

In this study we were able to confirm, through the ferroelectric / relaxor properties, that our supercritical fluids synthesis of BTZ was accurate. Moreover, based on XRD and EDS cartography, the overall ceramic appeared to be homogeneous, however, using backscattered electrons, a complex microstructure made of anisotropic grains and local inhomogeneity can be observed. The edges of the anisotropic grains present a barium and titanium rich phase and the core a zirconium rich one. This can be linked to the high reactivity of the powder due to its initial nanosize, together with –OH defects (observed in the Chapter I) creating vacancies and thus diffusion pathways. Adjusting the kinetics by using fast sintering processes such as SPS was shown to be efficient for both the improvement of densification and the limitation of diffusion process leading to solid state reaction or crystallization process. From this we can conclude that, even if the composition can be controlled in all the solid solution, further improvement of the synthesis would imply to lower the amount of defects which become critical during the ceramic sintering. In addition in the BTZ system the reactivity of the powder seems to be critical during the sintering and the kinetics of the thermal treatment is a key point to avoid the formation of secondary phases.

In the next part we are going to expose the preliminary work performed on hybrids materials

IV.3 Hybrids materials

In this section we expose a preliminary work, in collaboration with Dr. I. Bord-Majek and M. Wade at the institute of Integration Materials to System in Bordeaux (IMS - CNRS) and with Prof. R. Jakoby, Dr. Yuliang Zheng and L. Donghang, in order to see if it is possible to measure the dielectric properties of a composite at high frequency using an Inter Digital Capacitor (IDC) structure (see section II.3.2).

IV.3.1 Materials and method

We dispersed $BaTiO_3$ nanoparticles we produced using the supercritical fluids technology in a polyester matrix. The ratio of $BaTiO_3$ nanoparticles over the polyester was 30 wt %. The mixture was then sonicated 30 minutes in order to have a homogeneous dispersion. The composite is then screen printed on a glass substrate where the gold IDC structure is patterned.

We chose this particle loading in order to keep a good processability of the composite while increasing the starting polymer dielectric properties.

Figure IV-38a shows the IDC structure used which is made of four fingers with a 30 micron gap between each. The four fingers are similar with a width of 30 micron and a length of 1170 micron.

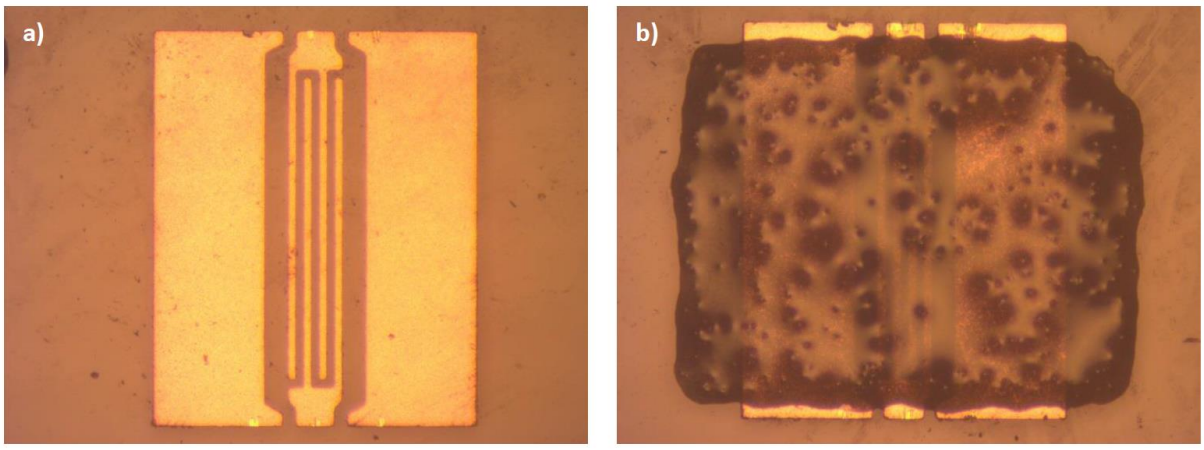

Figure IV-38. a) Picture of the IDC structure, b) picture of the IDC structure with the composite.

In Figure IV-38b, we can note that the composite layer is well aligned with a free space to make the measurements. However we can see that the composite presents roughness and is not homogeneous but we can use it to see if the measurement procedure is suitable.

IV.3.2 Characterization

Because we study the stability of our composite at high frequency, the measurements are thus performed at a constant temperature (room temperature) for frequencies ranging from 1 up to 10 GHz. Measuring the capacitance of the IDC and knowing the dielectric constant it is then possible to extract the real part of the composite permittivity using a model developed by Igreja et al. [273].

In Figure IV-39 we compare the variation of the dielectric permittivity of the $BaTiO_3$ / polyester composite with the theoretical value of the polyester which is around 3.

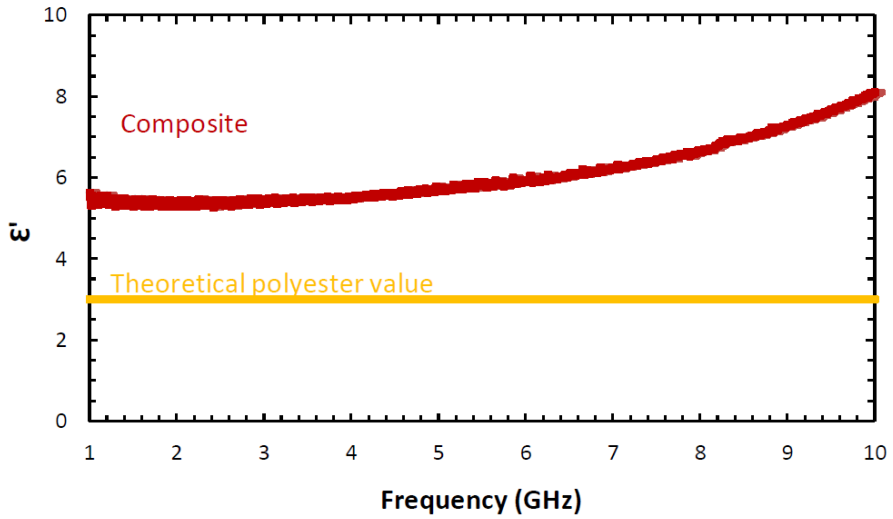

Figure IV-39. High frequency measurement of the $BaTiO_3$ / polymer composite.

We can see that we double the permittivity of the starting polymer and the value remains stable from 1 up to 10 GHz. From this measurement it is possible to calculate the quality factor (Q) of the capacitor (equation (23)).

$$Q = \frac{1}{\omega . C . R} \tag{23}$$

Where ω is the angular frequency and C is the capacitance of the structure with the composite and R is the series equivalent resistance. If the quality factor is above 80 - 100 it means that the material has a difference between its dielectric permittivity and its losses suitable for integration. In Figure IV-40 is presented the quality factor variation of the IDC structure with the composite.

We can see that up to 2 GHz, the quality factor is good enough however, with a further increase of frequency, the value drops to 20 for 10 GHz.

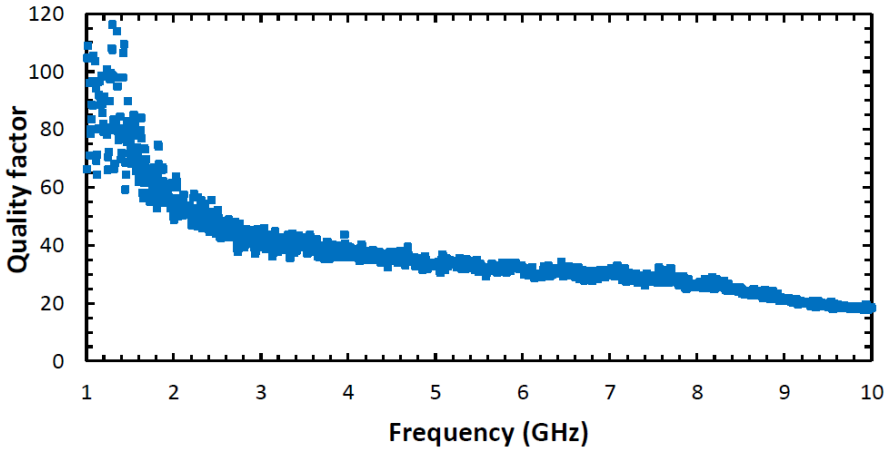

Figure IV-40. Variation of the IDC quality factor.

IV.3.3 Conclusion

In this section we were able to demonstrate the suitability of the composite characterization strategy, nevertheless the value of dielectric permittivity remains quite low even if the quality factor is good up to 2 GHz.

The next step will be to focus on the composite elaboration and deposit. Indeed, we saw in Figure IV-38b that the dispersion was not homogeneous and the particles were aggregated. To improve this it is necessary to work of the particles surface functionalization which will prevent the aggregation and favor the dispersion in the matrix. This will enable to improve the dielectric permittivity of the composite. Moreover, to further improve the permittivity, it will be necessary to work on the particles loading and the nature of the polymeric matrix.

IV.4 Conclusion of Chapter 4

Across this chapter we processed and characterized different types of materials. First we studied the intrinsic properties of the $Ba_{0.6}Sr_{0.4}TiO_3$ nanoparticles produced in supercritical fluids using SPS which enabled us to make dense ceramics keeping the starting grains size. We were able to demonstrate that even at 20 nm the $Ba_{0.6}Sr_{0.4}TiO_3$ still presented ferroelectricity. Nevertheless, due to the size effect, the transition from the ferroelectric phase to the paraelectric one was broad. Moreover, T_{Curie} was lower than the bulk but in agreement with V. Hornebecq et al. study [88]. We were also able to demonstrate the effect of SPS processing, especially the applied pressure, which can balance the contribution from the paraelectric shell.

In a second part we focused on ceramics made with BTZ nanoparticles and evidenced the accuracy of the synthesis through the bulk ferroelectric / relaxor properties. However we observed the apparition of local inhomogeneity through the growth of anisotropic grains. The phenomenon is related to the high reactivity of the nanopowders and to the presence of –OH defects in the starting powder, crating vacancies and thus diffusion pathways ionic diffusion. It is thus necessary to optimize the powder synthesis prior to their processing in order to reduce these defects and thus the creation of anisotropic grains.

Finally we validated our composites characterization procedure using IDC structure basing our demonstration on a $BaTiO_3$ / polyester composite. Nevertheless the dielectric permittivity remained low, now that we can properly characterize the composite, the next step is to improve their properties improving the particles dispersion through surface functionalization and varying the amount of particles or the nature of the matrix.

General conclusion

In the context of producing more compact and multifunctional devices, electronic industries have to face new challenges. Passives components and more precisely capacitor being space consuming their size have to be reduced while increasing their volume efficiency. In the case of capacitors such as MLCCs, to achieve this they have to decrease the dielectric layers thickness and thus use high quality $BaTiO_3$ nanoparticles (tens of nanometers) with a narrow size distribution. However using conventional production routes such as solid state or sol-gel syntheses, it is not possible to meet these expectations.

It is thus necessary to develop other synthesis processes and across this PhD work we were able to highlight the strength of the supercritical fluid technology for this specific need:

- We first focused on the study of high quality $BaTiO_3$ based nanoparticles formation in supercritical fluids:

  - In the case of $BaTiO_3$, using conventional *ex situ* analyses such as XRD, FTIR, Raman, TEM and XPS we were able to fully characterize the nanoparticles at different levels. With XRD and TEM we proved that the particles were monocrystalline. With Raman spectroscopy we evidenced the coexistence of a tetragonal phase with cubic one. This was in agreement with the core shell theory developed to explain the size effect on the crystalline structure. In additions we observed a Ti off centering due to the surface strain at this scale. Adding the FTIR and XPS analyses to the Raman one we were able to identify the presence of structural and surface –OH defects.

  - Then, we were able to extend the synthesis procedure and powder characterizations towards both $BaTiO_3$ – $SrTiO_3$ and $BaTiO_3$ – $BaZrO_3$ entire solid solutions. This was especially interesting since, to our knowledge, we were the first to demonstrate the synthesis of the entire BTZ solid solution in supercritical fluid conditions and the second among all studies, based on different synthesis routes, reported in the literature.

  - Finally, we combined the different conventional *ex situ* powder characterization techniques listed above with *in situ* synchrotron WAXS analyses in order to follow in real time the formation of $BaTiO_3$ based nanoparticles in supercritical fluid conditions. From this we were able to propose a growth mechanism where the amount of surface –OH drives the particles growth. This statement was verified in both solid solutions even though, in the BTZ case, the growth kinetics also play a preponderant role.

- Once the formation mechanism of the $BaTiO_3$ based nanoparticles in supercritical conditions was identified we produced them in a larger scale for processing them into ceramics and characterize their ferroelectric properties:

  - Through the example of $Ba_{0.6}Sr_{0.4}TiO_3$ and using SPS we first evidence the processing of these nanoparticles into dense and nanostructured ceramics with a density up to ≈ 95 % and keeping the starting grains size. This enabled us the study the intrinsic ferroelectric properties of the $Ba_{0.6}Sr_{0.4}TiO_3$ nanoparticles at the nanoscale. We thus proved the existence of a broad ferroelectric transition even for 20 nm size nanoparticles. Nevertheless the measured T_{Curie} was lower than the bulk (180 K instead of 300 K) which completed V. Hornebecq et al. study [88]. Finally, we evidenced the SPS pressure effect which can balance the paraelectric shell contribution on the ferroelectric properties.

  - Concerning the BTZ, making ceramics with the conventional process enabled us, on one hand, to confirm the accuracy of the synthesis in terms of stoichiometry through the ferroelectric / relaxor properties of $BaTi_{0.85}Zr_{0.15}O_3$ and $BaTi_{0.7}Zr_{0.3}O_3$. However, on the other hand, we saw that the presence of –OH defects in the produced powders opening pathways for the ionic diffusion, leading to the formation of anisotropic grains. We were able to prevent their formation using SPS which is a sintering process well known for limiting the ionic diffusion. Nevertheless it would be very interesting to optimize the BTZ supercritical fluid synthesis in order to lower the presence of -OH defects and thus enable a homogeneous sintering with conventional methods.

- Finally, through the example of $BaTiO_3$ nanoparticles produced in supercritical fluids and dispersed in a polyester matrix, we were able to demonstrate that the choice of an IDC structure for determining the dielectric properties of a composite at the GHz range was suitable. At this point the dielectric permittivity of the composite remains low but stable up to 10 GHz. This stability is directly related to the intrinsic properties of the produced particles which present a broad ferroelectric to paraelectric phase transition.

This last point is very interesting as it opens new perspectives to the TU Darmstadt – Bordeaux University collaboration. Indeed, the work of the PhD to understand the formation of $BaTiO_3$ based nanoparticles produced in supercritical fluids and characterize their intrinsic ferroelectric properties was an essential step prior to the development of hybrid nanocomposites. Now that this part is achieved it would be interesting to focus on the composite formulation such as the composition and amount of inorganic nanoparticles we disperse, the homogeneity of the dispersion through surface

functionalization and the nature of the polymeric matrix. This would enable to get closer to the final aim which is the integration of these dielectric nanocomposites into PCBs.

References

[1] L. Huang, Z. Chen, J.D. Wilson, S. Banerjee, R.D. Robinson, I.P. Herman, et al., Barium titanate nanocrystals and nanocrystal thin films: Synthesis, ferroelectricity, and dielectric properties, Journal of Applied Physicsp. 100 (2006) 034316 1–10.

[2] S. Wada, T. Hoshina, K. Takizawa, M. Ohishi, H. Yasuno, H. Kakemoto, et al., Origin of Ultrahigh Dielectric Constants for Barium Titanate Nanoparticles, Journal of the Korean Physical Society. 51 (2007) 878.

[3] X. Zhu, Z. Zhang, J. Zhu, S. Zhou, Z. Liu, Morphology and atomic-scale surface structure of barium titanate nanocrystals formed at hydrothermal conditions, Journal of Crystal Growth. 311 (2009) 2437–2442.

[4] X. Zhu, J. Wang, Z. Zhang, J. Zhu, S. Zhou, Z. Liu, et al., Atomic-Scale Characterization of Barium Titanate Powders Formed by the Hydrothermal Process, Journal of the American Ceramic Society. 91 (2008) 1002–1008.

[5] Y. Zhang, X. Wang, Z. Tian, K.-H. Hur, L. Li, Preparation of BME MLCC Powders by Aqueous Chemical Coating Method, Journal of the American Ceramic Society. 94 (2011) 3286–3290.

[6] Y. Zhang, X. Wang, J. Kim, J.-R. Kim, K.-H. Hur, L. Li, Uniform Coating of BaTiO3 -Dy2O3 - SiO2 Compound Nano Layer on Ni Particles for MLCC Electrode, Journal of the American Ceramic Society. 96 (2013) 2163–2166.

[7] J.A. Dahl, B.S. Maddux, J.E. Hutchison, Toward greener nanosynthesis, Journal of Chemical Reviews. 107 (2007) 2228–2269.

[8] G.H. Haertling, Ferroelectric Ceramics: History and Technology, Journal of the American Ceramic Society. 82 (1999) 797–818.

[9] M.M. Vijatovic, J.D. Bobic, B.D. Stojanovic, History and challenges of barium titanate: Part I, Science of Sintering. 40 (2008) 155–165.

[10] M.M. Vijatovic, J.D. Bobic, B.D. Stojanovic, History and challenges of barium titanate: Part II, Science of Sintering. 40 (2008) 235–244.

[11] F. Wan, J. Han, Z. Zhu, Dielectric response in ferroelectric BaTiO3, Physics Letters A. 372 (2008) 2137–2140.

[12] D.D. Lu, C.P. Wong, Materials for advanced packaging, 2009.

[13] C. Hunter, Three issues in the miniature capacitor market, SMT Surface Mount Technology Magazine. 20 (2006) 12.

[14] J. Ho, T.R. Jow, S. Boggs, Historical Introduction to Capacitor, IEEE Electrical Insulation Magazine. 26 (2010) 20–25.

[15] T.F. Hellmann, G., Winkler, J. H., Franklin, B., Dalibard, Ueber Luftelektricität 1746-1753: Mit einer einleitung, A. Asher & Company, Berlin, 1898.

[16] G.W.A. Drummer, Electronic Inventions and Discoveries: Electronics from its earliest beginnings to the present day, Institute of Physics Publishing, Bristol and Philadelphie, 1997.

[17] G.N. Howatt, R.G. Breckenridge, J.M. Brownlow, Fabrication of thin ceramic sheets for capacitors, Journal of the American Ceramic Society. 30 (1947) 237–242.

[18] D. Yoon, Tetragonality of barium titanate powder for a ceramic capacitor application, Journal of Ceramic Processing Research. 4 (2006) 343–354.

[19] M.-J. Pan, C.A. Randall, A Brief Introduction to Ceramic Capacitors, IEEE Electrical Insulation Magazine. 26 (2010) 44–50.

[20] F.C. Krebs, Fabrication and processing of polymer solar cells: A review of printing and coating techniques, Solar Energy Materials and Solar Cells. 93 (2009) 394–412.

[21] D.D. Lu, C.P. Wong, Materials for advanced packaging, 2009.

[22] P.A. Sandborn, A review of the economics of embedded passives, in: International Electronic Packaging Conference and Exhibition, 2003.

[23] M. a. Alam, M.H. Azarian, M. Osterman, M. Pecht, Temperature and voltage aging effects on electrical conduction mechanism in epoxy-BaTiO3 composite dielectric used in embedded capacitors, Microelectronics Reliability. 51 (2011) 946–952.

[24] C.-S. Hsi, F.-M. Hsieh, H.-P. Chen, Characteristics of thick film resistors embedded in low temperature co-fired ceramic (LTCC) substrates, Journal of the European Ceramic Society. 27 (2007) 2779–2784.

[25] D. Majumdar, W. Borland, O. Renovales, M. Doyle, U.K. Bs, Ceramic thick-film capacitor for embedded passives in printed circuit boards, in: Packaging Technical Conference and Exhibition, 2003.

[26] W. Jillek, W.K.C. Yung, Embedded components in printed circuit boards: a processing technology review, The International Journal of Advanced Manufacturing Technology. 25 (2004) 350–360.

[27] S. Liang, S.R. Chong, E.P. Giannelis, Barium Titanate/Epoxy Composite Dielectric Materials for Integrated Thin Film Capacitors, in: Electronic Componenets and Technology Conference, 1998: pp. 171–175.

[28] D. Street, Polymer - ceramic composite materials with high dielectric constants, Thin. 158 (1988) 93–105.

[29] Y. Bai, Z.-Y. Cheng, V. Bharti, H.S. Xu, Q.M. Zhang, High-dielectric-constant ceramic-powder polymer composites, Applied Physics Letters. 76 (2000) 3804.

[30] Y. Rao, C.P. Wong, Material Characterization of a High-Dielectric-Constant Polymer – Ceramic Composite for Embedded Capacitor for RF Applications, Journal of Applied Polymer Science. 92 (2004) 2228–2231.

[31] M. Arbatti, X. Shan, Z.-Y. Cheng, Ceramic–Polymer Composites with High Dielectric Constant, Advanced Materials. 19 (2007) 1369–1372.

[32] P. Kim, S.C. Jones, P.J. Hotchkiss, J.N. Haddock, B. Kippelen, S.R. Marder, et al., Phosphonic Acid-Modified Barium Titanate Polymer Nanocomposites with High Permittivity and Dielectric Strength, Advanced Materials. 19 (2007) 1001–1005.

[33] T. Hu, J. Juuti, H. Jantunen, T. Vilkman, Dielectric properties of BST/polymer composite, Journal of the European Ceramic Society. 27 (2007) 3997–4001.

[34] R. Yeetsorn, M. Fowler, C. Tzoganakis, A Review of Thermoplastic Composites for Bipolar Plate Materials in PEM Fuel Cells, in: J. Cuppoletti (Ed.), Nanocomposites with Unique Properties and Applications in Medicine and Industry, InTech, 2011: pp. 317–344.

[35] Z.-M. Dang, Y. Shen, C.-W. Nan, Dielectric behavior of three-phase percolative Ni–BaTiO[sub 3]/polyvinylidene fluoride composites, Applied Physics Letters. 81 (2002) 4814.

[36] J. Xu, M. Wong, C.P. Wong, Super high dielectric constant carbon black-filled polymer composites as integral capacitor dielectrics, in: Proceedings - Electronic Components and Technology Conference, 2004: pp. 536–541.

[37] J. Xu, C.P. Wong, Low-loss percolative dielectric composite, Applied Physics Letters. 87 (2005) 082907.

[38] L. Qi, B.I. Lee, S. Chen, W.D. Samuels, G.J. Exarhos, High-Dielectric-Constant Silver-Epoxy Composites as Embedded Dielectrics, Advanced Materials. 17 (2005) 1777–1781.

[39] C.P. Wong, Development of Novel Silver Nanoparticles/Polymer Composites as High K Polymer Matrix by In-situ Photochemical Method, 56th Electronic Components and Technology Conference 2006. (2006) 1841–1846.

[40] J. Lu, K.-S. Moon, J. Xu, C.P. Wong, Synthesis and dielectric properties of novel high-K polymer composites containing in-situ formed silver nanoparticles for embedded capacitor applications, Journal of Materials Chemistry. 16 (2006) 1543.

[41] Y. Shen, Y. Lin, M. Li, C.-W. Nan, High Dielectric Performance of Polymer Composite Films Induced by a Percolating Interparticle Barrier Layer, Advanced Materials. 19 (2007) 1418–1422.

[42] B.C. Pecharromµn, J.S. Moya, Experimental Evidence of a Giant Capacitance in Insulator - Conductor Composites at the Percolation Threshold, Advanced Materials. 12 (2000) 294–297.

[43] A. Bunde, W. Dieterich, Percolation in Composites, Journal of E. 5 (2000) 81–92.

[44] Z.-M. Dang, Y. Shen, C.-W. Nan, Dielectric behavior of three-phase percolative Ni–BaTiO3/polyvinylidene fluoride composites, Applied Physics Letters. 81 (2002) 4814.

[45] J. Xu, M. Wong, C.P. Wong, Super high dielectric constant carbon black-filled polymer composites as integral capacitor dielectrics, in: Proceedings - Electronic Components and Technology Conference, 2004: pp. 536–541.

[46] C.P. Wong, Dielectric loss control of high-K polymer composites by coulomb blockade effects of metal nanoparticles for embedded capacitor applications, Proceedings. International Symposium on Advanced Packaging Materials: Processes, Properties and Interfaces, 2005. (2005) 237–242.

[47] J. Xu, C.P. Wong, Low-loss percolative dielectric composite, Applied Physics Letters. 87 (2005) 082907.

[48] L. Qi, B.I. Lee, S. Chen, W.D. Samuels, G.J. Exarhos, High-Dielectric-Constant Silver-Epoxy Composites as Embedded Dielectrics, Advanced Materials. 17 (2005) 1777–1781.

[49] C.P. Wong, Development of Novel Silver Nanoparticles/Polymer Composites as High K Polymer Matrix by In-situ Photochemical Method, 56th Electronic Components and Technology Conference 2006. (2006) 1841–1846.

[50] Y. Shen, Y. Lin, M. Li, C.-W. Nan, High Dielectric Performance of Polymer Composite Films Induced by a Percolating Interparticle Barrier Layer, Advanced Materials. 19 (2007) 1418–1422.

[51] C.-W. Nan, Y. Shen, J. Ma, Physical properties of composites near percolation, Annual Review of Materials Research. 40 (2010) 131–151.

[52] Z.-M. Dang, J.-K. Yuan, J.-W. Zha, T. Zhou, S.-T. Li, G.-H. Hu, Fundamentals, processes and applications of high-permittivity polymer–matrix composites, Progress in Materials Science. 57 (2012) 660–723.

[53] J. Curie, P. Curie, Développement par pression de l'électricité polaire dans des crystaux hémiédriques à faces inclinées, Comptes Rendus de l'Académie Des Sciences. (1880) 294–295.

[54] D. Brewster, Observation on the Pyro-Electricity in Minerals, The Edinburgh Journal of Science. 1 (1824) 208–218.

[55] G. Busch, P. Scherrer, Eine neue seignette-elektrische Substanz, Naturwissenschaften. 23 (1935) 737.

[56] J. Valasek, Piezoelectric and allied phenomena in Rochelle salt, Physical Review. (1920) 537.

[57] E. Schrödinger, Studien über Kinetik der Dielektrika, dam Schmelzpunkt, Pyro-und Piezoelektrizität, S. B. Akad. Wiss. Wien. (1912) 1937–1972.

[58] L.E. Cross, R.E. Newnham, History of Ferroelectrics, in: E. Lense (Ed.), Ceramics and Civilization, Volume III: High Technology Ceramics: Past, Present, and Future : The Nature of Innovation and Change in Ceramic Technology, The American Ceramic Society, 1987: pp. 289–305.

[59] R. López-juárez, F. González, M.-E. Villafuerte-Castrejón, Lead-Free Ferroelectric Ceramics with Perovskite Structure, in: M. Lallart (Ed.), Ferroelectrics - Material Aspects, InTech, Rijeka, 2011: pp. 305–330.

[60] B.M. Wul, I.M. Goldman, Dielectric Constants of Titanates of Metals of the Second Group, Doklady Akademii Nauk SSSR. (1945) 139–142.

[61] T.-C. Huang, M.-T. Wang, H.-S. Sheu, W.-F. Hsieh, Size-dependent lattice dynamics of barium titanate nanoparticles, Journal of Physics: Condensed Matter. 19 (2007) 476212 1–12.

[62] L. Bourgeois, Sur les titanates cristallins de baryum et strontium, Comptes Rendus de l'Académie Des Sciences de Paris. 103 (1886) 141–144.

[63] B.M. Wul, M. Goldman, Dielectric Constants of Titanates of Metals of the Second Group, Doklady Akademii Nauk SSSR. 46 (1945) 139.

[64] a. von Hippel, R.G. Breckenridge, F.G. Chesley, L. Tisza, High dielectric constant ceramics, Industrial & Engineering Chemistry. 38 (1946) 1097–1109.

[65] G. Philippot, C. Elissalde, M. Maglione, C. Aymonier, Supercritical fluid technology: A reliable process for high quality BaTiO3 based nanomaterials, Advanced Powder Technology. (2014) DOI: 10.1016/j.apt.2014.02.016.

[66] J. Varghese, R.W. Whatmore, J.D. Holmes, Ferroelectric nanoparticles, wires and tubes: synthesis, characterisation and applications, Journal of Materials Chemistry C. 1 (2013) 2618.

[67] R.D. Shannon, Revised effective ionic radii and systematic studies of interatomic distances in halides and chalcogenides, Acta Crystallographica Section A. 32 (1976) 751–767.

[68] K.M. Rabe, C.H. Ahn, J.-M. Triscone, Physics of ferroelectrics: a modern perspective (Vol. 105), Springer, 2007.

[69] A. Safari, Piezoelectric and Acoustic Materials for Transducer Applications, Springer US, Boston, MA, 2008.

[70] W.D. Dong, D.M. Pisani, C.S. Lynch, A finite element based phase field model for ferroelectric domain evolution, Smart Materials and Structures. 21 (2012) 094014.

[71] M. Foeth, Determination of the Thermal Broadening of Ferroelectric Domain Walls using Quantitative Transmission Electron Microscopy, École polytechnique fédérale de Lausanne, 1999.

[72] D. Damjanovic, Ferroelectric , dielectric and piezoelectric properties of ferroelectric thin films and ceramics, Reports on Progress in Physics. 61 (1998) 1267–1324.

[73] A.K. Tagantsev, V.O. Sherman, K.F. Astafiev, J. Venkatesh, N. Setter, Ferroelectric Materials for Microwave Tunable Applications, Journal of Electroceramics. 11 (2003) 5–66.

[74] H. Frayssignes, B.L. Cheng, G. Fantozzi, T.W. Button, Phase transformation in BST ceramics investigated by internal friction measurements, Journal of the European Ceramic Society. 25 (2005) 3203–3206.

[75] T. Ishidate, S. Abe, H. Takahashi, N. Môri, Phase Diagram of BaTiO3, Physical Review Letters. 78 (1997) 2397–2400.

[76] Z. Yu, C. Ang, R. Guo, a. S. Bhalla, Piezoelectric and strain properties of Ba(Ti1−xZrx)O3 ceramics, Journal of Applied Physics. 92 (2002) 1489.

[77] I.-K. Jeong, C.Y. Park, J.S. Ahn, S. Park, D.J. Kim, Ferroelectric-relaxor crossover in BaTi1−xZrxO3 studied using neutron total scattering measurements and reverse Monte Carlo modeling, Physical Review B. 81 (2010) 214119.

[78] C. Kajtoch, Influence of Zr-substitution on phase transitions character in polycrystalline Ba(Ti1−xZrx)O3, Journal of Materials Science. 46 (2010) 1469–1473.

[79] J. Bera, S.K. Rout, On the formation mechanism of BaTiO3–BaZrO3 solid solution through solid-oxide reaction, Materials Letters. 59 (2005) 135–138.

[80] J.F. Ihlefeld, J.-P. Maria, W. Borland, Dielectric and microstructural properties of barium titanate zirconate thin films on copper substrates, Journal of Materials Research. 20 (2011) 2838–2844.

[81] S. Miao, J. Pokorny, U.M. Pasha, O.P. Thakur, D.C. Sinclair, I.M. Reaney, Polar order and diffuse scatter in Ba(Ti1−xZrx)O3 ceramics, Journal of Applied Physics. 106 (2009) 114111.

[82] F. a Rabuffetti, R.L. Brutchey, Local structural distortion of BaZr(x)Ti(1-x)O3 nanocrystals synthesized at room temperature., Chemical Communications (Cambridge, England). 48 (2012) 1437–9.

[83] T. Maiti, R. Guo, a. S. Bhalla, Evaluation of Experimental Resume of BaZrxTi1-xO3 with Perspective to Ferroelectric Relaxor Family: An Overview, Ferroelectrics. 425 (2011) 4–26.

[84] D. Nuzhnyy, J. Petzelt, M. Savinov, T. Ostapchuk, V. Bovtun, M. Kempa, et al., Broadband dielectric response of Ba(Zr,Ti)O_{3} ceramics: From incipient via relaxor and diffuse up to classical ferroelectric behavior, Physical Review B. 86 (2012) 014106.

[85] W. Kleemann, S. Miga, J. Dec, J. Zhai, Crossover from ferroelectric to relaxor and cluster glass in BaTi1−xZrxO3 (x = 0.25–0.35) studied by non-linear permittivity, Applied Physics Letters. 102 (2013) 232907.

[86] S. Yoon, J. Dornseiffer, Y. Xiong, D. Grüner, Z. Shen, S. Iwaya, et al., Spark plasma sintering of nanocrystalline BaTiO3-powders: Consolidation behavior and dielectric characteristics, Journal of the European Ceramic Society. 31 (2011) 1723–1731.

[87] S. Lin, T. Lü, C. Jin, X. Wang, Size effect on the dielectric properties of BaTiO3 nanoceramics in a modified Ginsburg-Landau-Devonshire thermodynamic theory, Physical Review B. 74 (2006) 134115 1–5.

[88] V. Hornebecq, C. Huber, M. Maglione, M. Antonietti, C. Elissalde, Dielectric Properties of Pure (BaSr)TiO3 and Composites with Different Grain Sizes Ranging from the Nanometer to the Micrometer, Advanced Functional Materials. 14 (2004) 899–904.

[89] M.B. Smith, K. Page, T. Siegrist, P.L. Redmond, E.C. Walter, R. Seshadri, et al., Crystal Structure and the Paraelectric-to-Ferroelectric Phase Transition of Nanoscale BaTiO3, Journal of American Chemical Society. 130 (2008) 6955–6963.

[90] T. Hoshina, K. Takizawa, J. Li, T. Kasama, H. Kakemoto, T. Tsurumi, Domain Size Effect on Dielectric Properties of Barium Titanate Ceramics, Japanese Journal of Applied Physics. 47 (2008) 7607–7611.

[91] C. Fang, L. Chen, Study of ferroelectric nanodomains and the effect of grain size in BaTiO3 ceramics, Philosophical Magazine Letters. 92 (2012) 37–41.

[92] S. Aoyagi, Y. Kuroiwa, A. Sawada, H. Kawaji, T. Atake, Size effect on crystal structure and chemical bonding nature in BaTiO3 nanopowder, Journal of Thermal Analysis and Calorimetry. 81 (2005) 627–630.

[93] H.-W. Lee, S. Moon, C.-H. Choi, D.K. Kim, Synthesis and Size Control of Tetragonal Barium Titanate Nanopowders by Facile Solvothermal Method, Journal of the American Ceramic Society. 95 (2012) 2429–2434.

[94] G. Busca, V. Buscaglia, M. Leoni, P. Nanni, Solid-state and Surface Spectroscopic Characterization of BaTiO3, Chemistry of Materials. 6 (1994) 955–961.

[95] R. Waser, Solubility of Hydrogen Defects in Doped and Undoped BaTi03, Journal of American Ceramic Society. 71 (1988) 58–63.

[96] E. Shi, C. Xia, W. Zhong, B. Wang, C. Feng, Crystallographic Properties of Hydrothermal Barium Titanate Crystallites, Journal of American Ceramic Society. 80 (1997) 1567–1572.

[97] C. Fang, D. Zhou, S. Gong, Core-shell structure and size effect in barium titanate nanoparticle, Physica B: Condensed Matter. 406 (2011) 1317–1322.

[98] T. Hoshina, Size effect of barium titanate: fine particles and ceramics, Journal of the Ceramic Society of Japan. 121 (2013) 156–161.

[99] Z. Zhao, V. Buscaglia, M. Viviani, M. Buscaglia, L. Mitoseriu, A. Testino, et al., Grain-size effects on the ferroelectric behavior of dense nanocrystalline BaTiO3 ceramics, Physical Review B. 70 (2004) 024107.

[100] S.W. Lu, B.I. Lee, Z.L. Wang, W.D. Samuels, Hydrothermal synthesis and structural characterization of BaTiO3 nanocrystals, Journal of Crystal Growth. 219 (2000) 269–276.

[101] L. Qi, B.I. Lee, P. Badheka, L.-Q. Wang, P. Gilmour, W.D. Samuels, et al., Low-temperature paraelectric–ferroelectric phase transformation in hydrothermal BaTiO3 particles, Materials Letters. 59 (2005) 2794–2798.

[102] V. Petkov, M. Gateshki, M. Niederberger, Y. Ren, Atomic-Scale Structure of Nanocrystalline BaxSr1-xTiO3 (x = 1, 0.5, 0) by X-ray Diffraction and the Atomic Pair Distribution Function Technique, Chemistry of Materials. 18 (2006) 814–821.

[103] C.J. Xiao, Z.H. Chi, W.W. Zhang, F.Y. Li, S.M. Feng, C.Q. Jin, et al., The phase transitions and ferroelectric behavior of dense nanocrystalline BaTiO3 ceramics fabricated by pressure assisted sintering, Journal of Physics and Chemistry of Solids. 68 (2007) 311–314.

[104] S. Wada, H. Yasuno, T. Hoshina, H. Kakemoto, Y. Kameshima, T. Tsurumi, Size dependence of THz region dielectric properties for barium titanate fine particles, Journal of Electroceramics. 21 (2007) 198–201.

[105] X. Tian, J. Li, K. Chen, J. Han, S. Pan, Y. Wang, et al., Nearly Monodisperse Ferroelectric BaTiO3 Hollow Nanoparticles: Size-Related Solid Evacuation in Ostwald-Ripening-Induced Hollowing Process, Crystal Growth & Design. 10 (2010) 3990–3995.

[106] A. Schilling, S. Prosandeev, R.G.P. McQuaid, L. Bellaiche, J.F. Scott, J.M. Gregg, Shape-induced phase transition of domain patterns in ferroelectric platelets, Physical Review B. 84 (2011) 064110 1–5.

[107] K. Suzuki, K. Kijima, Well-crystallized barium titanate nanoparticles prepared by plasma chemical vapor deposition, Materials Letters. 58 (2004) 1650–1654.

[108] K. Suzuki, K. Kijima, Size driven phase transition of barium titanate nanoparticles prepared by plasma chemical vapor deposition, Journal of Materials Science. 40 (2005) 1289–1292.

[109] M. Vehkamäki, T. Hatanpää, M. Ritala, M. Leskelä, S. Väyrynen, E. Rauhala, Atomic Layer Deposition of BaTiO3 Thin Films—Effect of Barium Hydroxide Formation, Chemical Vapor Deposition. 13 (2007) 239–246.

[110] J. Zeng, H. Wang, M. Wang, S. Shang, Z. Wang, C. Lin, Preparation and ferroelectric properties of BaTiO3 thin films by atmospheric-pressure metalorganic chemical vapor deposition, Thin Solid Films. 322 (1998) 104–107.

[111] K.M. Ring, K.L. Kavanagh, Substrate effects on the ferroelectric properties of fine-grained BaTiO3 films, Journal of Applied Physics. 94 (2003) 5982.

[112] L. Qiao, X. Bi, Microstructure and ferroelectric properties of BaTiO3 films on LaNiO3 buffer layers by rf sputtering, Journal of Crystal Growth. 310 (2008) 2780–2784.

[113] L. Qiao, X. Bi, Domain configuration and phase transition for BaTiO3 thin films on tensile Si substrates, Journal of Crystal Growth. 310 (2008) 5327–5330.

[114] B. Li, W. Shang, Z. Hu, N. Zhang, Template-free fabrication of pure single-crystalline BaTiO3 nano-wires by molten salt synthesis technique, Ceramics International. 40 (2014) 73–80.

[115] V. a. Zhabrev, L.P. Efimenko, V.G. Baryshnikov, I.G. Polyakova, a. V. Gumennikov, Synthesis of BaTiO3 powders of different dispersities by the exchange reactions in molten salts, Glass Physics and Chemistry. 34 (2011) 91–96.

[116] D. Lv, R. Zuo, S. Su, Processing and Morphology of (111) BaTiO3 Crystal Platelets by a Two-Step Molten Salt Method, Journal of the American Ceramic Society. 95 (2012) 1838–1842.

[117] Y. Zhang, L. Wang, D. Xue, Molten salt route of well dispersive barium titanate nanoparticles, Powder Technology. 217 (2012) 629–633.

[118] N. Kumada, A. Miura, T. Takei, I.B. Adilina, S. Shimazu, Low temperature synthesis of ATiO3 (A : Mg , Ca , Sr , Ba) by using molten salt, Journal of the Ceramic Society of Japan. 121 (2013) 74–79.

[119] L.J. McGilly, a Schilling, J.M. Gregg, Domain bundle boundaries in single crystal BaTiO3 lamellae: searching for naturally forming dipole flux-closure/quadrupole chains., Nano Letters. 10 (2010) 4200–5.

[120] D. Hennings, S. Schreinemacher, H. Schreinemacher, Solid-State Preparation of BaTiO3 - Based Dielectrics, Using Ultrafine Raw Materials, Journal of American Ceramic Society. 84 (2001) 2777–2782.

[121] C. Pithan, D. Hennings, R. Waser, Progress in the Synthesis of Nanocrystalline BaTiO3 Powders for MLCC, International Journal of Applied Ceramic Technology. 2 (2005) 1–14.

[122] M.T. Buscaglia, M. Bassoli, V. Buscaglia, R. Alessio, Solid-State Synthesis of Ultrafine BaTiO3 Powders from Nanocrystalline BaCO3 and TiO2, Journal of the American Ceramic Society. 88 (2005) 2374–2379.

[123] R. Yanagawa, M. Senna, C. Ando, H. Chazono, H. Kishi, Preparation of 200 nm BaTiO3 Particles with their Tetragonality 1.010 Via a Solid-State Reaction Preceded by Agglomeration-Free Mechanical Activation, Journal of the American Ceramic Society. 90 (2007) 809–814.

[124] L.L. Hench, J.K. West, The sol-gel process, Chemical Reviews. 90 (1990) 33–72.

[125] O.A. Harizanov, Sol – gel BaTiO3 from a peptized solution, Materials Letters. 34 (1998) 232–236.

[126] L. Wang, L. Liu, D. Xue, H. Kang, C. Liu, Wet routes of high purity BaTiO3 nanopowders, Journal of Alloys and Compounds. 440 (2007) 78–83.

[127] K. Byrappa, M. Yoshimura, Handbook of Hydrothermal Technology, Noyes Publications, Norwich, New York, USA, n.d.

[128] W. Suchanek, M. Lencka, R. Riman, Hydrothermal synthesis of ceramic materials, in: D.. Palmer, R. Fernandez-Prini, A.. Harvey (Eds.), Aqueous Systems at Elevated Temperatures and Pressures: Physical Chemistry in Water, STeam and Hydrothermal Solutions, 1st ed., Elsevier Ltd, London, UK, 2004: pp. 717–744.

[129] R.I. Walton, F. Millange, R.I. Smith, T.C. Hansen, D. O'Hare, Real time observation of the hydrothermal crystallization of barium titanate using in situ neutron powder diffraction., Journal of the American Chemical Society. 123 (2001) 12547–12555.

[130] R.I. Walton, Subcritical solvothermal synthesis of condensed inorganic materials, Chemical Society Reviews. 31 (2002) 230–238.

[131] M. Lin, Z.Y. Fu, H.R. Tan, J.P.Y. Tan, S.C. Ng, E. Teo, Hydrothermal Synthesis of CeO2 Nanocrystals : Ostwald Ripening or Oriented Attachment ?, Crystal Growth & Design. (2012) 3296 – 3303.

[132] M. Mohammadikish, Hydrothermal synthesis, characterization and optical properties of ellipsoid shape α-Fe2O3 nanocrystals, Ceramics International. (2013) 1–8.

[133] Z. Shao, W. Zhou, Z. Zhu, Advanced synthesis of materials for intermediate-temperature solid oxide fuel cells, Progress in Materials Science. 57 (2012) 804–874.

[134] R.M. Piticescu, R.R. Piticescu, D. Taloi, V. Badilita, Hydrothermal synthesis of ceramic nanomaterials for functional applications, Nanotechnology. 14 (2003) 312–317.

[135] A. Habib, R. Haubner, N. Stelzer, Effect of temperature, time and particle size of Ti precursor on hydrothermal synthesis of barium titanate, Materials Science and Engineering: B. 152 (2008) 60–65.

[136] J. Ovenstone, K.C. Chan, C.B. Ponton, Hydrothermal processing and characterisation of doped lanthanum chromite for use in SOFCs, Journal of Materials Science. 37 (2002) 3315–3322.

[137] S. Sōmiya, R. Roy, Hydrothermal synthesis of fine oxide powders, Bulletin of Materials Science. 23 (2000) 453–460.

[138] K. Byrappa, T. Adschiri, Hydrothermal technology for nanotechnology, in: Progress in Crystal Growth and Characterization of Materials, 2007: pp. 117–166.

[139] R. Asiaie, W. Zhu, S.A. Akbar, P.K. Dutta, Characterization of Submicron Particles of Tetragonal, Chemistry of Materials. (1996) 226–234.

[140] M.-S. Zhang, Z. Yin, Q. Chen, W. Zhang, W. Chen, Study of structural and photoluminescent properties in barium titanate nanocrystals synthesized by hydrothermal process, Solid State Communications. 119 (2001) 659–663.

[141] H. Xu, L. Gao, Tetragonal Nanocrystalline Barium Titanate Powder : Preparation, Characterization, and Dielectric Properties, Journal of American Ceramic Society. 86 (2003) 203–205.

[142] L. Guo, H. Luo, J. Gao, L. Guo, J. Yang, Microwave hydrothermal synthesis of barium titanate powders, Materials Letters. 60 (2006) 3011–3014.

[143] N. Nuraje, K. Su, a. Haboosheh, J. Samson, E.P. Manning, N. -l. Yang, et al., Room Temperature Synthesis of Ferroelectric Barium Titanate Nanoparticles Using Peptide Nanorings as Templates, Advanced Materials. 18 (2006) 807–811.

[144] X. Wu, Z. Chen, Z. Cui, Low temperature synthesis of cubic BaTiO3 nanoparticles, The 8th Annual IEEE International Conference on Nano/Micro Engineered and Molecular Systems. 1 (2013) 399–402.

[145] A.R. Tao, K. Niesz, D.E. Morse, Bio-inspired nanofabrication of barium titanate, Journal of Materials Chemistry. 20 (2010) 7916.

[146] S. O'Brien, L. Brus, C.B. Murray, Synthesis of Monodisperse Nanoparticles of Barium Titanate: Toward a Generalized Strategy of Oxide Nanoparticle Synthesis, Journal of American Chemical Society. 123 (2001) 12085–12086.

[147] T. Adschiri, Y. Hakuta, K. Arai, Hydrothermal Synthesis of Metal Oxide Fine Particles at Supercritical Conditions, Industrial & Engineering Chemistry Research. 39 (2000) 4901–4907.

[148] T. Adschiri, Y. Hakuta, K. Sue, K. Arai, Hydrothermal synthesis of metal oxide nanoparticles at supercritical conditions, Journal of Nanoparticle Research. 3 (2001) 227–235.

[149] M. Atashfaraz, M. Shariatyniassar, S. Ohara, K. Minami, M. Umetsu, T. Naka, et al., Effect of titanium dioxide solubility on the formation of BaTiO3 nanoparticles in supercritical water, Fluid Phase Equilibria. 257 (2007) 233–237.

[150] C. Aymonier, A. Loppinet-Serani, H. Reverón, Y. Garrabos, F. Cansell, Review of supercritical fluids in inorganic materials science, The Journal of Supercritical Fluids. 38 (2006) 242–251.

[151] J.F. Bocquet, K. Chhor, C. Pommier, Barium titanate powders synthesis from solvothermal reaction and supercritical treatment, Materials Chemistry and Physics. 57 (1999) 273–280.

[152] B. Chevalier, A. Demourgues, J. Etourneau, C. Even, A. Tressaud, Y. Garrabos, et al., Supercritical fluid processing: a new route for materials synthesis, Journal of Materials Chemistry. 9 (1999) 67–75.

[153] Y. Hakuta, H. Ura, H. Hayashi, K. Arai, Effect of water density on polymorph of BaTiO3 nanoparticles synthesized under sub and supercritical water conditions, Materials Letters. 59 (2005) 1387–1390.

[154] Y. Hakuta, H. Hayashi, K. Arai, Fine particle formation using supercritical fluids, Current Opinion in Solid State and Materials Science. 7 (2003) 341–351.

[155] Y. Hakuta, H. Ura, H. Hayashi, K. Arai, Continuous Production of BaTiO3 Nanoparticles by Hydrothermal Synthesis, Industrial & Engineering Chemistry Research. 44 (2005) 840–846.

[156] H. Hayashi, Y. Hakuta, Hydrothermal Synthesis of Metal Oxide Nanoparticles in Supercritical Water, Materials. 3 (2010) 3794–3817.

[157] H. Hayashi, T. Noguchi, N.M. Islam, Y. Hakuta, Y. Imai, N. Ueno, Hydrothermal synthesis of organic hybrid BaTiO3 nanoparticles using a supercritical continuous flow reaction system, Journal of Crystal Growth. 312 (2010) 3613–3618.

[158] K. Matsui, T. Noguchi, N. Islam, Y. Hakuta, H. Hayashi, Rapid synthesis of BaTiO3 nanoparticles in supercritical water by continuous hydrothermal flow reaction system, Journal of Crystal Growth. 310 (2008) 2584–2589.

[159] H. Reverón, C. Aymonier, A. Loppinet-Serani, C. Elissalde, M. Maglione, F. Cansell, Single-step synthesis of well-crystallized and pure barium titanate nanoparticles in supercritical fluids, Nanotechnology. 16 (2005) 1137–1143.

[160] R. Sui, P. Charpentier, Synthesis of Metal Oxide Nanostructures by Direct Sol−Gel Chemistry in Supercritical Fluids, Journal of Chemical Reviews. 112 (2012) 3057–3082.

[161] C. Gomez-Yanez, C. Benitez, H. Balmori-Ramirez, Mechanical activation of the synthesis reaction of BaTiO3 from a mixture of BaCO3 and TiO2 powders, Ceramics International. 26 (2000) 271–277.

[162] V. Berbenni, A. Marini, G. Bruni, Effect of mechanical milling on solid state formation of BaTiO3 from BaCO3 ± TiO2 (rutile) mixtures, Thermochimica Acta. 374 (2001) 151–158.

[163] L. Kong, J. Ma, H. Huang, R. Zhang, W. Que, Barium titanate derived from mechanochemically activated powders, Journal of Alloys and Compounds. 337 (2002) 226–230.

[164] E. Brzozowski, M.S. Castro, Lowering the synthesis temperature of high-purity BaTiO3 powders by modifications in the processing conditions, Thermochimica Acta. 398 (2003) 123–129.

[165] M.T. Buscaglia, M. Bassoli, V. Buscaglia, R. Vormberg, Solid-State Synthesis of Nanocrystalline BaTiO3 : Reaction Kinetics and Powder Properties, Journal of the American Ceramic Society. 91 (2008) 2862–2869.

[166] M.T. Buscaglia, V. Buscaglia, R. Alessio, Coating of BaCO3 Crystals with TiO2: Versatile Approach to the Synthesis of BaTiO3 Tetragonal Nanoparticles, Chemistry of Materials. 19 (2007) 711–718.

[167] F. Cansell, C. Aymonier, A. Loppinet-Serani, Review on materials science and supercritical fluids, Current Opinion in Solid State and Materials Science. 7 (2003) 331–340.

[168] E. Reverchon, R. Adami, Nanomaterials and supercritical fluids, The Journal of Supercritical Fluids. 37 (2006) 1–22.

[169] F. Cansell, C. Aymonier, Design of functional nanostructured materials using supercritical fluids, The Journal of Supercritical Fluids. 47 (2009) 508–516.

[170] C. Morin, A. Loppinet-Serani, F. Cansell, C. Aymonier, Near- and supercritical solvolysis of carbon fibre reinforced polymers (CFRPs) for recycling carbon fibers as a valuable resource: State of the art, The Journal of Supercritical Fluids. 66 (2012) 232–240.

[171] A. Loppinet-Serani, C. Aymonier, F. Cansell, Supercritical water for environmental technologies, Journal of Chemical Technology & Biotechnology. 85 (2010) 583–589.

[172] A. Laaksonen, P.G. Kusalik, I.M. Svishchev, Three-Dimensional Structure in Water - Methanol Mixtures, The Journal of Physical Chemistry A. 101 (1997) 5910–5918.

[173] A.R. Bazaev, I.M. Abdulagatov, E.A. Bazaev, A. Abdurashidova, (p,v,T,x) Measurements of {(1−x)H2O+xC2H5OH} mixtures in the near-critical and supercritical regions, The Journal of Chemical Thermodynamics. 39 (2007) 385–411.

[174] W.L. Marshall, E. V Jones, Liquid-vapor critical temperatures of several aqueous-organic and organic-organic solution systems, Journal of Inorganic and Nuclear Chemistry. 36 (1974) 2319–2323.

[175] J. Griswold, J.D. Haney, V.A. Klein, Ethanol-water system: Vapor-Liquid Properties at High Pressures, Industrial and Engineering Chemistry. 35 (1943) 701–704.

[176] F. Barr-David, B. Dodge, Vapor-Liquid Equilibrium at High Pressures: The Systems Ethanol-Water and 2-Propanol- Water, Journal of Chemical and Engineering Data. 4 (1959) 107–121.

[177] T. Adschiri, K. Kanazawa, K. Arai, Crystalization of Metal Oxide Particle through Hydrolysis in Supercritical Water, in: World Congress of Chemical Engineering, 1991.

[178] T. Adschiri, K. Kanazawa, K. Arai, Rapid and continuous hydrothermal crystallization of metal oxide particles in supercritical water, Journal of the American Ceramic Society. 75 (1992) 1019–1022.

[179] T. Adschiri, K. Kanazawa, K. Arai, Rapid and Continuous Hydrothermal Synthesis of Boehmite Particles in Subcritical and Supercritical Water, ChemInform. 75 (1992) 2615–2618.

[180] Y. Hakuta, K. Seino, H. Ura, T. Adschiri, H. Takizawa, K. Arai, Production of phosphor (YAG : Tb) fine particles by hydrothermal synthesis in supercritical water, Journal of Materials Chemistry. 9 (1999) 2671–2674.

[181] J.D. Holmes, K.J. Ziegler, R.C. Doty, L.E. Pell, K.P. Johnston, B. a Korgel, Highly luminescent silicon nanocrystals with discrete optical transitions., Journal of the American Chemical Society. 123 (2001) 3743–8.

[182] S. Desmoulins-Krawiec, C. Aymonier, F. Weill, S. Grosse, J. Etourneau, F. Cansell, et al., Synthesis of nanostructured materials in supercritical ammonia: nitrides, metals and oxides, Journal of Materials Chemistry. 14 (2004) 228.

[183] J.J. Watkins, J.M. Blackburn, T.J. McCarthy, Chemical Fluid Deposition: Reactive Deposition of Platinum Metal from Carbon Dioxide Solution, Chemistry of Materials. 11 (1999) 213–215.

[184] P.S. Shah, J.D. Holmes, R.C. Doty, K.P. Johnston, B.A. Korgel, Steric Stabilization of Nanocrystals in Supercritical CO2 Using Fluorinated Ligands, Journal of American Chemical Society. 122 (2000) 4245–4246.

[185] P.S. Shah, S. Husain, K.P. Johnston, B.A. Korgel, Nanocrystal Arrested Precipitation in Supercritical Carbon Dioxide, The Journal of Physical Chemistry B. 105 (2001) 9433–9440.

[186] P.S. Shah, S. Husain, K.P. Johnston, B.A. Korgel, Role of Steric Stabilization on the Arrested Growth of Silver Nanocrystals in Supercritical Carbon Dioxide, The Journal of Physical Chemistry B. 106 (2002) 12178–12185.

[187] A. Kameo, T. Yoshimura, K. Esumi, Preparation of noble metal nanoparticles in supercritical carbon dioxide, Colloids and Surfaces A: Physicochemical and Engineering Aspects. 215 (2003) 181–189.

[188] M.C. McLeod, W.F. Gale, C.B. Roberts, Metallic nanoparticle production utilizing a supercritical carbon dioxide flow process., Langmuir : The ACS Journal of Surfaces and Colloids. 20 (2004) 7078–82.

[189] H. Reverón, C. Elissalde, C. Aymonier, C. Bousquet, M. Maglione, F. Cansell, Continuous supercritical synthesis and dielectric behaviour of the whole BST solid solution, Nanotechnology. 17 (2006) 3527–3532.

[190] H. Reverón, C. Elissalde, C. Aymonier, O. Bidault, M. Maglione, F. Cansell, Supercritical fluid route for synthesizing crystalline Barium Strontium Titanate nanoparticles., Journal of Nanoscience and Nanotechnology. 5 (2005) 1741–1744.

[191] C. Slostowski, S. Marre, O. Babot, T. Toupance, C. Aymonier, Near- and supercritical alcohols as solvents and surface modifiers for the continuous synthesis of cerium oxide nanoparticles., Langmuir : The ACS Journal of Surfaces and Colloids. 28 (2012) 16656–63.

[192] Y. Hakuta, S. Onai, H. Terayama, T. Adschiri, K. Arai, Production of ultra-fine ceria particles by hydrothermal synthesis under supercritical conditions, Journal of Materials Science Letters. 17 (1998) 1211–1213.

[193] J. Lu, K. Minami, S. Takami, T. Adschiri, Rapid and continuous synthesis of cobalt aluminate nanoparticles under subcritical hydrothermal conditions with in-situ surface modification, Chemical Engineering Science. 85 (2013) 50–54.

[194] A.I. Cooper, Recent Developments in Materials Synthesis and Processing Using Supercritical CO2, Advanced Materials. 13 (2001) 1111–1114.

[195] T. Gendrineau, S. Marre, M. Vaultier, M. Pucheault, C. Aymonier, Microfluidic synthesis of palladium nanocrystals assisted by supercritical CO2: tailored surface properties for applications in boron chemistry., Angewandte Chemie (International Ed. in English). 51 (2012) 8525–8.

[196] K.S. Morley, P.C. Marr, P.B. Webb, A.R. Berry, F.J. Allison, G. Moldovan, et al., Clean preparation of nanoparticulate metals in porous supports: a supercritical route, Journal of Materials Chemistry. 12 (2002) 1898–1905.

[197] V. Pessey, R. Garriga, F. Weill, B. Chevalier, J. Etourneau, F. Cansell, Control of particle growth by chemical transformation in supercritical CO2/ethanol mixtures, Journal of Materials Chemistry. 12 (2002) 958–965.

[198] E. Reverchon, G. Caputo, S. Correra, P. Cesti, Synthesis of titanium hydroxide nanoparticles in supercritical carbon dioxide on the pilot scale, The Journal of Supercritical Fluids. 26 (2003) 253–261.

[199] W.E. Stallings, H.H. Lamb, N. Carolina, Synthesis of Nanostructured Titania Powders via Hydrolysis of Titanium Isopropoxide in Supercritical Carbon Dioxide, Langmuir. 19 (2003) 2989–2994.

[200] A. Cabañas, M. Poliakoff, The continuous hydrothermal synthesis of nano-particulate ferrites in near critical and supercritical water, Journal of Materials Chemistry. 11 (2001) 1408–1416.

[201] R. Garriga, V. Pessey, F. Weill, B. Chevalier, J. Etourneau, F. Cansell, Kinetic study of chemical transformation in supercritical media of bis(hexafluoroacetylacetonate)copper (II) hydrate, The Journal of Supercritical Fluids. 20 (2001) 55–63.

[202] E. Grigorova, F. Cansell, B. Chevalier, A ddition of nanosized Cr2O3 to magnesium for improvement of the hydrogen sorption properties, Journal of Alloys and Compounds. 351 (2003) 217–221.

[203] E.S. Ilin, S. Marre, V. Jubera, C. Aymonier, Continuous supercritical synthesis of high quality UV-emitting ZnO nanocrystals for optochemical applications, Journal of Materials Chemistry C. 1 (2013) 5058.

[204] G. Philippot, K.M.Ø. Jensen, M. Christensen, C. Elissalde, M. Maglione, B.B. Iversen, et al., Coupling in situ synchrotron radiation with ex situ spectroscopy characterizations to study the formation of Ba1−xSrxTiO3 nanoparticles in supercritical fluids, The Journal of Supercritical Fluids. 87 (2014) 111–117.

[205] Y. Roig, S. Marre, T. Cardinal, C. Aymonier, Synthesis of exciton luminescent ZnO nanocrystals using continuous supercritical microfluidics., Angewandte Chemie (International Ed. in English). 50 (2011) 12071–4.

[206] K. Sue, K. Murata, K. Kimura, K. Arai, Continuous synthesis of zinc oxide nanoparticles in supercritical water, Green Chemistry. 5 (2003) 659.

[207] T. Adschiri, Y.-W. Lee, M. Goto, S. Takami, Green materials synthesis with supercritical water, Green Chemistry. 13 (2011) 1380–1390.

[208] L. Matějová, Z. Matěj, R. Fajgar, T. Cajthaml, O. Šolcová, TiO2 powders synthesized by pressurized fluid extraction and supercritical drying: Effect of water and methanol on structural properties and purity, Materials Research Bulletin. 47 (2012) 3573–3579.

[209] C. Elissalde, H. Reverón, C. Aymonier, D. Michau, F. Cansell, M. Maglione, The ferroelectric transition temperature as an intrinsic probe for sintered nanocrystalline BaTiO3 synthesized under supercritical conditions, Nanotechnology. 16 (2005) 797–802.

[210] O. Fouassier, L. Guitton, T. Meral, F. Cansell, C. Aymonier, Procédé de synthèse de poudres nanométriques en milieux fluides supercritiques, MATERIAUX. (2006) 13–17.

[211] C. Bousquet, Chimie en milieux supercritiques pour l'élaboration de céramiques ferroelectriques nanostructurées, Bordeaux University, ICMCB - CNRS, Supercritical fluid group, 2008.

[212] Y. Cerenius, K. Ståhl, L. a Svensson, T. Ursby, a Oskarsson, J. Albertsson, et al., The crystallography beamline I711 at MAX II., Journal of Synchrotron Radiation. 7 (2000) 203–8.

[213] M. Knaapila, C. Svensson, J. Barauskas, M. Zackrisson, S.S. Nielsen, K.N. Toft, et al., A new small-angle X-ray scattering set-up on the~crystallography beamline I711 at MAX-lab, Journal of Synchrotron Radiation. 16 (2009) 498–504.

[214] J. Becker, M. Bremholm, C. Tyrsted, B. Pauw, K.M.Ø. Jensen, J. Eltzholt, et al., Experimental setup for in situ X-ray SAXS/WAXS/PDF studies of the formation and growth of nanoparticles in near- and supercritical fluids, Journal of Applied Crystallography. 43 (2010) 729–736.

[215] C. Bousquet, Chimie en milieux fluides supercritiqes pour l'élaboration de céramiques ferroelectriques nanostructurées, Université de Bordeaux, 2008.

[216] H. Zheng, K. Zhu, Q. Wu, J. Liu, J. Qiu, Preparation and characterization of monodispersed BaTiO3 nanocrystals by sol–hydrothemal method, Journal of Crystal Growth. 363 (2013) 300–307.

[217] W.-S. Cho, Structural Evolution and Caracterization of BaTiO3 Nanoparticles Synthesized from Polymeric Precursor, Journal of Physics and Chemistry of Solid. 59 (1998) 659–666.

[218] I.J. Clark, T. Takeuchi, N. Ohtoric, D.C. Sinclaira, Hydrothermal synthesis and characterisation of BaTiO3 fine powders: precursors, polymorphism and properties, Journal of Materials Chemistry. 9 (1999) 83–91.

[219] E. Chávez, S. Fuentes, R. a. Zarate, L. Padilla-Campos, Structural analysis of nanocrystalline BaTiO3, Journal of Molecular Structure. 984 (2010) 131–136.

[220] B. Lee, J. Zhang, Preparation , structure evolution and dielectric properties of BaTiO3 thin films and powders by an aqueous sol . gel process, Thin Solid Films. 388 (2001) 107–113.

[221] T. Makino, M. Arimura, K. Fujiyoshi, Y. Yamashita, M. Kuwabara, Crystallinity of Barium Titanate Nanoparticles Synthesized by Sol-Gel Method, Key Engineering Materials. 350 (2007) 31–34.

[222] S. Fuentes, E. Chávez, L. Padilla-Campos, D.E. Diaz-Droguett, Influence of reactant type on the Sr incorporation grade and structural characteristics of Ba1−xSrxTiO3 (x=0−1) grown by sol–gel-hydrothermal synthesis, Ceramics International. 39 (2013) 8823–8831.

[223] X. Zhu, J. Zhu, S. Zhou, Z. Liu, N. Ming, D. Hesse, BaTiO3 nanocrystals: Hydrothermal synthesis and structural characterization, Journal of Crystal Growth. 283 (2005) 553–562.

[224] A.P. Hammersley, S.O. Svensson, M. Hanfland, A.N. Fitch, D. Hausermann, Two-dimensional detector software: From real detector to idealised image or two-theta scan, High Pressure Research. 14 (1996) 235–248.

[225] J. Rodríguez-Carvajal, Recent advances in magnetic structure determination by neutron powder diffraction, Physica B: Condensed Matter. 192 (1993) 55–69.

[226] P. Thompson, D.E. Cox, J.B. Hastings, Rietveld Refinement of Debye-Scherrer Synchrotron X-ray Data from A1203, Journal of Applied Physics. 20 (1987) 79–83.

[227] I.M. Lifshitz, V. V Slyozov, The kinetics of precipitation from supersaturated solid solutions, Journal of Physics and Chemistry of Solids. 19 (1961) 35–50.

[228] C.N.R. Rao, A. Müller, A.K. Cheetham, Nanomaterials Chemistry: Recent Developments and New Directions, 2007.

[229] Y. Kim, S. Nahm, Structural refinement of nano BaTiO3 powder using X-ray diffraction data, Journal of Materials Science. 39 (2004) 4363–4366.

[230] J.-S. Park, Y.-H. Lee, K.-B. Kim, Y.-I. Kim, Structural study of Ca doped barium titanate, Nuclear Instruments and Methods in Physics Research B. 284 (2012) 44–48.

[231] S. Aoyagi, Y. Kuroiwa, A. Sawada, I. Yamashita, T. Atake, Composite Structure of BaTiO3 Nanoparticle Investigated by SR X-Ray Diffraction, Journal of the Physics Society Japan. 71 (2002) 1218–1221.

[232] N. Hirose, J.M.S. Skakle, A.R. West, Doping Mechanism and Permittivity Correlations in Nd-Doped BaTiO3, Journal of Electroceramics. 3 (1999) 233–238.

[233] V. LaMer, R. Dinegar, Theory, production and mechanism of formation of monodispersed hydrosols, Journal of. 72 (1950) 4847–4854.

[234] T.-D. Nguyen, T.-O. Do, Size- and Shape-Controlled Synthesis of Monodisperse Metal Oxide and Mixed Oxide Nanocrystals, in: Y. Masuda (Ed.), Nanotechnology and Nanomaterials, 2011.

[235] Y. Shiratori, C. Pithan, J. Dornseiffer, R. Waser, Raman scattering studies on nanocrystalline BaTiO3 Part II – consolidated polycrystalline ceramics, Journal of Raman Spectroscopy. 38 (2007) 1300–1306.

[236] S.K. Patil, F.D. Blum, Fourier transform infrared analysis of hydroxyl content of hydrothermally processed heteroepitaxial barium titanate films, Journal of Materials Research. 20 (2005) 3312–3319.

[237] H. Salehi, M. Hosseini, N. Shahtahmasebi, First-Principles Study of the Electronic Structure of BaTiO3 using Different Approximations, Chinese Journal of Physics. 42 (2004) 619–628.

[238] X.Y. Xue, C.L. Wang, W.L. Zhong, The atomic and electronic structure of the TiO2- and BaO-terminated BaTiO3(001) surfaces in a paraelectric phase, Surface Science. 550 (2004) 73–80.

[239] S. Qin, D. Liu, H. Liu, Z. Zuo, Size-Dependent Selective Etching Mechanism: Cavity Formation on Barium Titanate Nanocubes, Journal of Physical Chemistry C. 112 (2008) 17171–17174.

[240] G.-Z. Wang, C.-R. Li, J. Cui, Z.-Y. Man, Ab initio study of ATiO3 (001) surfaces, Surface and Interface Analysis. 41 (2009) 918–923.

[241] D. Nuzhnyy, J. Petzelt, I. Rychetsky, V. Buscaglia, M.T. Buscaglia, P. Nanni, THz and IR dielectric response of BaTiO 3 core–shell composites: evidence for interdiffusion, Journal of Physics D: Applied Physics. 42 (2009) 155408.

[242] N. Sawangwan, J. Barrel, K. MacKenzie, T. Tunkasiri, The effect of Zr content on electrical properties of Ba(Ti1-xZrx)O3 ceramics, Applied Physics A. 90 (2007) 723–727.

[243] C. Ciomaga, M. Viviani, M.T. Buscaglia, V. Buscaglia, L. Mitoseriu, A. Stancu, et al., Preparation and characterisation of the Ba(Zr,Ti)O3 ceramics with relaxor properties, Journal of the European Ceramic Society. 27 (2007) 4061–4064.

[244] S. Mahajan, O.P. Thakur, D.K. Bhattacharya, K. Sreenivas, Study of Structural and Electrical Properties of Conventional Furnace and Microwave-Sintered BaZr 0.10 Ti 0.90 O 3 Ceramics, Journal of the American Ceramic Society. 92 (2009) 416–423.

[245] C.E. Ciomaga, M.T. Buscaglia, V. Buscaglia, L. Mitoseriu, Oxygen deficiency and grain boundary-related giant relaxation in Ba(Zr,Ti)O3 ceramics, Journal of Applied Physics. 110 (2011) 114110.

[246] S. Halder, T. Schneller, U. Böttger, R. Waser, Fabrication and electrical characterisation of Zr-substituted BaTiO3 thin films, Applied Physics A. 81 (2004) 25–29.

[247] T. Kawano, K. Hashimoto, A. Nishida, T. Tsuchiya, Preparation and Electrical Properties of Ba(Ti1-xZrx)O3 Thin Films by Hydrothermal Method, Journal of the Ceramic Society of Japan. 110 (2002) 530–534.

[248] X. Wu, J. Chen, Z. Shi, H. Huang, L. Liu, J. Yu, et al., Hydrothermal synthesis and photoluminescence properties of BaZr1−xTixO3 hollow nanospheres, Materials Letters. 86 (2012) 21–24.

[249] R. Farhi, M. El Marssi, A. Simon, J. Ravez, A Raman and dielectric study of ferroelectric Ba(Ti1−xZrx)O3 ceramics, 604 (1999) 599–604.

[250] N.K. Karan, R.S. Katiyar, T. Maiti, R. Guo, a. S. Bhalla, Raman spectral studies of Zr 4+ rich BaZrxTi1−xO3 ($0.5 \leq x \leq 1.00$) phase diagram, Journal of Raman Spectroscopy. 40 (2009) 370–375.

[251] M. El Marssi, Y. Gagou, J. Belhadi, F. De Guerville, Y.I. Yuzyuk, I.P. Raevski, Ferroelectric BaTiO3/BaZrO3 superlattices: X-ray diffraction, Raman spectroscopy, and polarization hysteresis loops, Journal of Applied Physics. 108 (2010) 084104.

[252] L.R. Macario, M.L. Moreira, J. Andrés, E. Longo, An efficient microwave-assisted hydrothermal synthesis of BaZrO3 microcrystals: growth mechanism and photoluminescence emissions, CrystEngComm. 12 (2010) 3612.

[253] M. Deluca, C. a. Vasilescu, A.C. Ianculescu, D.C. Berger, C.E. Ciomaga, L.P. Curecheriu, et al., Investigation of the composition-dependent properties of BaTi1−xZrxO3 ceramics prepared by the modified Pechini method, Journal of the European Ceramic Society. 32 (2012) 3551–3566.

[254] T. Hungrı, M. Alguero, A.B. Hungrı, Dense , Fine-Grained Ba1-x SrxTiO3 Ceramics Prepared by the Combination of Mechanosynthesized Nanopowders and Spark Plasma Sintering, Chemistry of Materials. 17 (2005) 6205–6212.

[255] T. Hungría, J. Galy, A. Castro, Spark Plasma Sintering as a Useful Technique to the Nanostructuration of Piezo-Ferroelectric Materials, Advanced Engineering Materials. 11 (2009) 615–631.

[256] T. Hungría, H. Amorín, M. Algueró, a. Castro, Nanostructured ceramics of BiScO3–PbTiO3 with tailored grain size by spark plasma sintering, Scripta Materialia. 64 (2011) 97–100.

[257] F. Maglia, I.G. Tredici, U. Anselmi-Tamburini, Densification and properties of bulk nanocrystalline functional ceramics with grain size below 50nm, Journal of the European Ceramic Society. 33 (2013) 1045–1066.

[258] J.H. Noh, K.S. Hong, H.S. Jung, J.-K. Lee, Dielectric properties of nanocrystalline TiO2 prepared using spark plasma sintering, Journal of Electroceramics. 17 (2006) 913–917.

[259] J.H. Noh, H.S. Jung, J.-K. Lee, J.-R. Kim, K.S. Hong, Microwave dielectric properties of nanocrystalline TiO2 prepared using spark plasma sintering, Journal of the European Ceramic Society. 27 (2007) 2937–2940.

[260] Z. Valdez-Nava, C. Tenailleau, S. Guillemet-Fritsch, N. El Horr, T. Lebey, P. Dufour, et al., Structural characterization of dense reduced BaTiO3 and Ba0.95La0.05TiO3 nanoceramics showing colossal dielectric values, Journal of Physics and Chemistry of Solids. 72 (2011) 17–23.

[261] Z. Valdez-Nava, S. Guillemet-Fritsch, C. Tenailleau, T. Lebey, B. Durand, J.Y. Chane-Ching, Colossal dielectric permittivity of BaTiO3-based nanocrystalline ceramics sintered by spark plasma sintering, Journal of Electroceramics. 22 (2008) 238–244.

[262] T. Sakashita, M. Deluca, S. Yamamoto, H. Chazono, G. Pezzotti, Stress dependence of the Raman spectrum of polycrystalline barium titanate in presence of localized domain texture, Journal of Applied Physics. 101 (2007) 123517.

[263] M. Deluca, L. Stoleriu, L.P. Curecheriu, N. Horchidan, A.C. Ianculescu, C. Galassi, et al., High-field dielectric properties and Raman spectroscopic investigation of the ferroelectric-to-relaxor crossover in BaSnxTi1−xO3 ceramics, Journal of Applied Physics. 111 (2012) 084102.

[264] S.Y. Wang, B.L. Cheng, C. Wang, S.Y. Dai, K.J. Jin, Y.L. Zhou, et al., Raman spectroscopy studies of Ce-doping effects on Ba[sub 0.5]Sr[sub 0.5]TiO[sub 3] thin films, Journal of Applied Physics. 99 (2006) 013504.

[265] M. Frey, D. Payne, Grain-size effect on structure and phase transformations for barium titanate., Physical Review. B. 54 (1996) 3158–3168.

[266] A. Gajović, J.V. Pleština, K. Žagar, M. Plodinec, S. Šturm, M. Čeh, Temperature-dependent Raman spectroscopy of BaTiO3 nanorods synthesized by using a template-assisted sol-gel procedure, Journal of Raman Spectroscopy. 44 (2013) 412–420.

[267] M. Guennou, P. Bouvier, J. Kreisel, D. Machon, Pressure-temperature phase diagram of SrTiO3 up to 53 GPa, Physical Review B. 81 (2010) 054115.

[268] A. Simon, J. Ravez, M. Maglione, The crossover from a ferroelectric to a relaxor state in lead-free solid solutions, Journal of Physics: Condensed Matter. 16 (2004) 963–970.

[269] X. Chou, J. Zhai, X. Yao, Relaxor Behavior and Dielectric Properties of MgTiO 3 -Doped BaZr 0.35 Ti 0.65 O 3 Composite Ceramics for Tunable Applications, Journal of the American Ceramic Society. 90 (2007) 2799–2801.

[270] P.S. Dobal, A. Dixit, R.S. Katiyar, Z. Yu, R. Guo, a. S. Bhalla, Micro-Raman scattering and dielectric investigations of phase transition behavior in the BaTiO3–BaZrO3 system, Journal of Applied Physics. 89 (2001) 8085.

[271] M.T. Buscaglia, M. Viviani, Z. Zhao, V. Buscaglia, P. Nanni, D. Pad, et al., Synthesis of BaTiO3 Core - Shell Particles and Fabrication of Dielectric Ceramics with Local Graded Structure, Chemistry of Materials. 18 (2006) 4002–4010.

[272] Z. Sun, Y. Pu, Z. Dong, Y. Hu, X. Liu, P. Wang, Effect of Zr4+ content on the TC range and dielectric and ferroelectric properties of BaZrxTi1−xO3 ceramics prepared by microwave sintering, Ceramics International. 40 (2014) 3589–3594.

[273] R. Igreja, C.J. Dias, Analytical evaluation of the interdigital electrodes capacitance for a multi-layered structure, Sensors and Actuators A: Physical. 112 (2004) 291–301.

Titre : Synthèse en milieux supercritiques de nanoparticules à base de $BaTiO_3$: étude des mécanismes de formation, mise en forme des poudres et ferroélectricité

Résumé : Dans un contexte où l'électronique est au centre de notre société, la production d'appareils de plus en plus compacts et multifonctionnels concentre les efforts en recherche et développement. Pour répondre à cette attente, une des options est d'augmenter le rendement volumique des composants passifs tels que les condensateurs, en se basant sur l'utilisation de nanoparticules diélectriques du type $BaTiO_3$. Dans un premier temps, l'objectif est d'optimiser la synthèse des nanoparticules de $BaTiO_3$ et de comprendre leurs mécanismes de formation en milieux fluides supercritiques. Pour ce faire nous avons combiné des méthodes d'analyses *ex situ* telles que la microscopie électronique, la diffraction des rayons X, et les spectroscopies Raman ou infra rouge à des mesures *in situ* synchrotron de diffraction des rayons X aux grands angles. L'étude a par la suite été transposé à l'élaboration de la totalité des solutions solides$Ba_{1-x}Sr_xTiO_3$ ($0 \leq x \leq 1$) et $BaTi_{1-y}Zr_yO_3$ ($0 \leq y \leq 1$). Une fois les synthèses optimisées, l'utilisation du spark plasma sintering (SPS) nous a permis de mettre en œuvre des céramiques denses et nanostructurées, préservant la taille initiale des particules (20 nm), ceci afin d'étudier les propriétés intrinsèques des matériaux à l'échelle nanoscopique. Enfin, connaissant les propriétés de base de ces nanomatériaux, nous avons pu commencer à développer des matériaux hybrides diélectriques pour l'électronique flexible.

Mots clés : Diélectrique, fluides supercritiques, $BaTiO_3$, céramiques nanostructurées, hybrides.

Title : Supercritical fluids synthesis of $BaTiO_3$ based nanoparticles: study of the particles growth mechanisms, powder processing and ferroelectric properties

Abstract : In a context where the electronic is at the center of our society, the production of more compact and multifunctional devices focuses the research efforts. To answer to the expectations, one option is to improve the volume efficiency of passive components such as capacitors using dielectric nanoparticles such as $BaTiO_3$. First, the objective is to optimize the synthesis of $BaTiO_3$ nanoparticles and understand their formation in supercritical fluids. To do this, we combined conventional *ex situ* analyses such as X-ray diffraction, electronic microscopy, infrared and Raman spectroscopies with *in situ* synchrotron wide angle X-ray scattering analyses. This was then transferred to the development of $Ba_{1-x}Sr_xTiO_3$ ($0 \leq x \leq 1$) and $BaTi_{1-y}Zr_yO_3$ ($0 \leq y \leq 1$) solid solutions. Once the syntheses were optimized, using spark plasma sintering (SPS), we processed the powders into dense and nanostructured ceramics keeping the starting particles size (20 nm), to study the materials intrinsic properties at the nanoscale. Finally, knowing the nanoparticles properties, we could start to develop hybrid dielectric materials for flexible electronics.

Keywords : Dielectric, supercritical fluids, $BaTiO_3$, nanostructures ceramics, hybrids.

Unité de recherche

ICMCB–CNRS, UPR9048, 87 Av. du Dr. Schweitzer, 33608 Pessac cedex (France)

TU Darmstadt, IMP, Merckstr. 25, 64283 Darmstadt (Germany)